Electron Beam Melting of Titanium Aluminides; Process Development and Material Properties Optimisation

Lampros Kourtis

Doctor of Philosophy in Materials Science and Engineering

JULY 2017

I. SUMMARY

Additive Manufacturing (AM) process development was conducted to the production of high-Niobium Titanium Aluminide components with properties suitable for structural aerospace applications. Computational analysis of experimental data from statistically designed experiments and numerical heat source modelling revealed the effect of key Electron Beam Melting (EBM) process parameters on the melting response of γ- Titanium Aluminides.

Dimensionless terms for melt pool depth and operational parameters for various literature data and experimental data from this study show a very good fitting; which proves that predictive models and process windows could be generated and used to rapidly and efficiently develop process themes for a given material and required melting response. Heating, preheating and melting EBM process themes were developed for fabricating simple geometries. Using a Design of Experiments (DOE) approach melting (hatching) process themes were optimised for surface finish, maximum component density without process defects and minimum Aluminium evaporation loss. Post-processing for eliminating defects and porosity from the bulk and surface was performed by machining and hot isostatic pressing (HIP). Optimum HIP treatment conditions were identified. Microstructural analysis and mechanical properties were investigated for the as-built and HIPed specimens at room and elevated temperatures.

Excess Aluminium evaporation loss was identified as the main issue during the process development of this study. Evaporation per surface area, during EBM processing, from a metallic substrate mainly depends on surface temperature, heating time and chamber pressure and is a function of material properties and operational parameters. The main parameters affecting evaporation were investigated by numerical modelling using a modified Rosenthal equation. Impeding pressure for suppressing Aluminium evaporation versus surface temperature was also investigated.

II. CONTENTS

I TABLE OF CONTENTS

III. LIST OF FIGURES

IV. LIST OF TABLES

V. NOMENCLATURE

Terminology	Description	Units
2D	Two - dimensional	-
3D	Three - dimensional	-
A	Surface area	m^2
A, B, C	Antoine's coefficients	-
a, c	Unit cell lattice parameters	nm
AFM	Atomic force microscopy	-
AM	Additive manufacturing	-
ANOVA	Analysis of variance	-
bcc	Body centred cubic	-
bct	Body centred tetragonal	-
BS-SEM	Back scattered scanning electron microscopy	-
CAD	Computer aided design	-
CCD	Central composite design	-
CCT	Continuous cooling transformation diagram	-
CNC	Computer numerical control machining	-
CP	Commercial purity	-
C_p	Specific heat capacity	$J \cdot g^{-1} \cdot K^{-1}$
CV-EBM	Controlled vacuum electron beam melting	-
D	Melt pool depth	μm
D_b	Beam diameter	μm
DFL	Degraded fully lamellar microstructure	-
DOE	Design of experiments	-
E	Young's modulus	GPa
E_0	Energy density	$J \cdot m^{-2}$
EB	Electron beam	-
EBM	Electron beam melting	-
EBW	Electron beam welding	-
EDX	Energy-dispersive X-ray	-
EIGA	Electrode induction gas atomisation	-
E_L	Line energy density	$J \cdot m^{-1}$

ELI	Extra low interstitial	-
E_R	Relative evaporation rate	-
fcc	Face centred cubic	-
fct	Face-centred tetragonal	-
FFF	Freeform fabrication	-
FL	Fully lamellar microstructure	-
FO	Focus offset	mA
G	Temperature gradient	$K \cdot m^{-1}$
GA	Gas atomised	-
hcp	Hexagonal close packed	-
HIP	Hot isostatic pressing	-
HT	Heat treated	-
HV	High voltage	-
HV	Vickers hardness	HV
I	Current	mA
I_b	Beam current	mA
ICP	Inductively coupled plasma mass spectrometry	-
IM	Investment casting	-
ISM	Induction skull melting	-
J_i	Evaporation rate of component i	$kg \cdot sec \cdot m^2$
k	Thermal conductivity	$W \cdot m^{-1} \cdot K^{-1}$
L	Liquid phase	-
L	Scan length	mm
L	Profile length	mm
LCF	Low cycle fatigue	-
LMD	Laser metal deposition	-
LOF	Line offset	mm
LPT	Low pressure turbine	-
M	Molar mass of the evaporating species	$g \cdot mole^{-1}$
MIM	Metal injection molding	-
MMC	Metal matrix composite	-
n	Dimensionless operating parameter	-
NL	Nearly lamellar microstructure	-

ODS	Oxide dispersion-strengthened	-
P	Power	W
PAM	Plasma arc remelting	-
PIGA	Plasma inert gas atomisation	-
PM	Powder metallurgy	-
PREP	Plasma rotating electrode process	-
PRS	Powder recovery system	-
PSD	Powder size distribution	-
p_v	partial pressure of component i	mBar, Pascal
Q	Electron beam power	W
R&D	Research and development	-
R_a	Surface roughness	μm
R_g	Ideal gas constant	$J \cdot K^{-1} \cdot mol^{-1}$
RSM	Response surface method	-
RT	Room Temperature	-
S_a	Surface roughness	μm
SEM	Scanning electron microscopy	-
SF	Speed function	-
SLA	Stereolithography	-
SLM	Selective laser melting	-
SPS	Spark Plasma Sintering	-
SS	Stainless steel	-
ST	Surface temperature - EBM process parameter	-
STL	Standard triangulation language	-
T	Temperature	°C, K
t	time	sec
T_0	Substrate temperature	°C, K
T_{build}	Build temperature	°C, K
T_c	Critical Temperature	°C, K
TEM	Transmission electron microscopy	-
TiGA	Titanium gas atomisation	-
T_m	Melting point	°C, K
T_β	Beta transus temperature	°C, K

UAM	Ultrasonic additive manufacturing	-
UC	Ultrasonic consolidation	-
UTS	Ultimate tensile strength	MPa
V	Accelerating voltage	V
VAR	Vacuum arc remelting	-
v_b	Beam velocity	m/s
W	Melt pool width	μm
x, y, z	Orthogonal coordinates	-
x_i	Molar fraction of component i	-
XRD	X-ray diffraction	-
XRF	X-ray fluorescence	-
YS	Yield strength	MPa
α	HCP alpha phase	-
α	Thermal diffusivity	$m^2 \cdot s^{-1}$
α_2	Hexagonal ordered alpha 2 (Ti_3Al) phase	-
β	BCC beta phase	-
β	Efficiency parameter	-
γ	Gamma intermetallic phase	-
γ_i	Activity coefficient of component i	-
γ_m	Massively transformed gamma phase	-
λ	Lamellar spacing	μm
ρ	Density	$g \cdot cm^{-3}$
σ_0, κ_λ	Material constants	-
σ_y	Yield strength	MPa
φ	Porosity or void fraction	%, or 0-1
ω	Diffusionless hexagonal omega phase	-

VI. ACKNOWLEDGEMENTS

I would like to thank everyone who has helped for the completion of this Thesis. There are far too many people to name individually but their work and support in whatever capacity is very much appreciated. Above all I would like to offer special thanks to the following people;

I thank my Supervisors Prof Iain Todd and Prof Mark Rainforth for giving me the opportunity to work on this interesting project, as well as their guidance and support throughout its completion.

I would like to acknowledge the financial support of Mercury Centre, who have funded this work.

I thank all my colleagues at the University of Sheffield; all the Academic Staff and Students, and especially Everth Hernandez-Nava, Dr. Fatos Derguti, Chris Smith and Sam Tammas-Williams for all the support and the fun we had working together.

I also thank the Academic staff and students at the Edward P. Fitts Department of Industrial and Systems Engineering, North Carolina State University, NC, USA, where I spent 5 five weeks for this work as a visiting researcher, and especially Dr Ola Harrysson, Tim Horn and Joakim Karlson.

I thank my family, who I have missed so much, for supporting me throughout and being patient to this very difficult period for me.

My friends that have been so patient and supporting all this period. Especially, Fotini, who has been there for me during the very difficult last year.

Laura, I am not sure if I can ever be able to thank you enough. Without you I wouldn't be able to complete this. You were always there for me, giving me courage and love when I needed it. I am looking forward to all the great adventures that we are now free to have.

1 Introduction

1.1 Motivation

Light-weight, heat resistant materials are required for increasing the efficiency of the next-generation gas turbine engines by replacing the currently used heavier Ni-base Superalloys. γ-Titanium Aluminide (γ-TiAl) intermetallics have been extensively investigated during the last two decades, due to their remarkable high temperature properties that make them very attractive candidates for aero-engine applications. However, until just recently there have not been any aerospace commercial applications developed using this alloy. The reason for this is that they exhibit very low fracture toughness and room temperature ductility, which makes the manufacture of TiAl parts with required properties, in desired shapes and acceptable final costs very challenging using any of the known conventional routes, such as extrusion and forging, casting and powder metallurgy.

Electron beam melting (EBM), which is a near-net shape, powder bed, Additive Manufacturing (AM) technology was considered as an alternative processing route in this research project to achieve γ-TiAl structures with required properties and performance. In powder bed, AM technologies, fully dense structural parts are made straight from powder feedstock, just with some extra surface finishing machining and usually after HIP and/or heat treatments. Each layer is selectively melted to the desired, complex geometry defined by a 3D-CAD model. In the EBM machine, patented from the Swedish company Arcam, which was used for this project the melting and the consolidation of the layers is being done using the energy of an electron beam. The whole building process takes place in a high vacuum chamber. The operational principles of an EBM are similar to a Scanning Electron Microscope (SEM). Electrons are emitted from a tungsten filament, accelerated through an anode to hit and melt the powder by the transformation of their kinetic energy into heat. Magnetic lenses are used to focus and control the movement of the beam.

Core benefits of EBM AM processing [1]–[5] are: i) design freedom, which allows formability issues of TiAl to be overcome and complex parts to be produced with limited post processing, ii) low "buy-to-fly ratio", as the powder not used for the final material can be recycled and reused up to 95%, iv) high vacuum, which leads to very low impurities (O, N) pick up, v) higher speed and efficiency than laser-based AM methods, vi) very fine microstructures are produced, due to the intrinsic rapid solidification conditions of EBM, vii) resultant properties

superior to cast and comparable to wrought materials. It is expected that formability and cost issues, resulting from very low ductility and fracture toughness, will be overcome, as well as an increase in in-service ductility and fracture toughness due to the microstructure's refinement and the very low O pick up.

Nevertheless, there are some disadvantages related to EBM and AM in general. The main barriers for metal-based AM are the high cost of the platforms and the availability, cost and quality of metallic powders. Furthermore, AM is still a relatively immature manufacturing route when compared with the well-established conventional manufacturing routes, there are not comprehensive property databases and there is also an inconsistency of properties between different builds and/or different platforms. Other concerns are related to the available build sizes, generation of thermal stresses and columnar microstructures. Finally, a drawback of the EBM process compared with laser based techniques is the poor (quite rough) surface finish, which requires post machining. [1]–[8]

1.2 Project Aims and Objectives

The main **Aim** of this project is to investigate and develop the Electron Beam Melting (EBM) direct manufacturing process to produce high niobium Titanium Aluminide (TNB-TiAl) components with properties suitable for structural aerospace applications. The authors believe that an AM method and specifically EBM is probably the only viable manufacturing route to achieve this. The specific objectives of this work are:

i. To review and critically assess the current state of knowledge on TiAl metallurgy and EBM and identify the gaps in literature

ii. To investigate the literature and assess the feasibility and requirements for EBM processing of TiAl based alloys and identify any potential related issues

iii. To design and document a process development route for developing novel alloys by EBM process

iv. To investigate and identify the optimum powder manufacturing route for sourcing the suitable TiAl powder feedstock

v. To use statistically designed experiments to investigate, analyse and model the effect of key EBM process variables on selected response variables

vi. To establish the TNB-TiAl EBM process window for optimum performance and material properties

<ol type="i" start="7">
To develop the main EBM process themes for producing TNB-TiAl components with optimum properties
To investigate post-processing techniques, such as HIP and/or heat treatments to further optimise material properties
To perform comprehensive material properties characterisation at all stages from powder feedstock to final as-built and post-processed components
To investigate the evaporation phenomena during vacuum EBM processing of TNB-TiAl alloys and the effect of Aluminium content variation on mechanical properties

1.3 Thesis Outline

Chapter 2 is a review of the literature discussing the general metallurgy of Titanium Aluminide intermetallics, their importance and challenges for commercial use, the main commercial and R&D alloy systems and current processing routes and applications. A dedicated section gives an overview of AM processes and goes through the recent literature for TiAl processing by AM with a focus on EBM.

Chapter 3 explains the challenges during EBM process development and the methodology designed to overcome those challenges and accomplish the aims and objectives of this study. Design of experiments (DOE), manufacturing and post-manufacturing processes, as well as the sample preparation and characterisation techniques used for this study are documented. Heat source modelling methodology for calculating surface temperature and weld pool dimensions is described in this chapter as well.

Chapter 4 discusses the results of preliminary characterisation and parametrical studies for investigating the effect of key EBM process parameters on melting response of single weld tracks scanned on pre-sintered substrates of varied density. Regression analysis, statistical multivariate analysis using Pearson's coefficients, dimensionless analysis by plotting material properties normalised terms and analytical heat source modelling are used.

Chapter 5 describes the experimental methodology followed for the EBM process development of the TNB-TiAl alloys and discusses the effect of key melting process theme variables on selected response variables. HIP study and mechanical property results and microstructures for the as-build and HIPed samples are all discussed.

Chapter 6 discusses the evaporation phenomena during vacuum EBM processing of TNB-TiAl alloys and the effect of Aluminium content variation on mechanical properties. Measured Aluminium evaporation losses are correlated with estimated surface temperatures and evaporation rates during vacuum EBM processing. EBM process parameters affecting evaporation are discussed. Impeding pressures for suppressing volatilisation has been investigated.

Chapter 7 documents the key conclusions from this study and suggests some further work.

2 LITERATURE REVIEW

2.1 γ- Titanium Aluminide Intermetallics

2.1.1 Importance and Challenges

Titanium Aluminide based (TiAl) intermetallics have been extensively investigated during the last 2 decades for potential aerospace and automotive applications [9]–[22]. They have been mainly considered as an alternative, light-weight material option to the heavier nickel-based superalloys, currently used for aircraft applications and especially for the low pressure (LPT) turbine blades, as shown in Figure 2-1. The density of TiAl-based alloys ($3.9 - 4.2$ g/cm^3) is about half of the Nickel-based ones and with comparable or even superior high temperature performance [18]. Total weight reduction of a gas turbine engine has been estimated [23] to be up to 30%. GEnx^{TM} [24] by GE is the first and only until now commercial turbine engine that is announced to fly with TiAl LPT blades (at stages 6 and 7), reducing weight by approximately 180 kg. This significant weight reduction results in increased propulsion efficiency and a 20% reduction in fuel consumption, a 50% reduction in noise and an 80% reduction in NOx emissions [25].
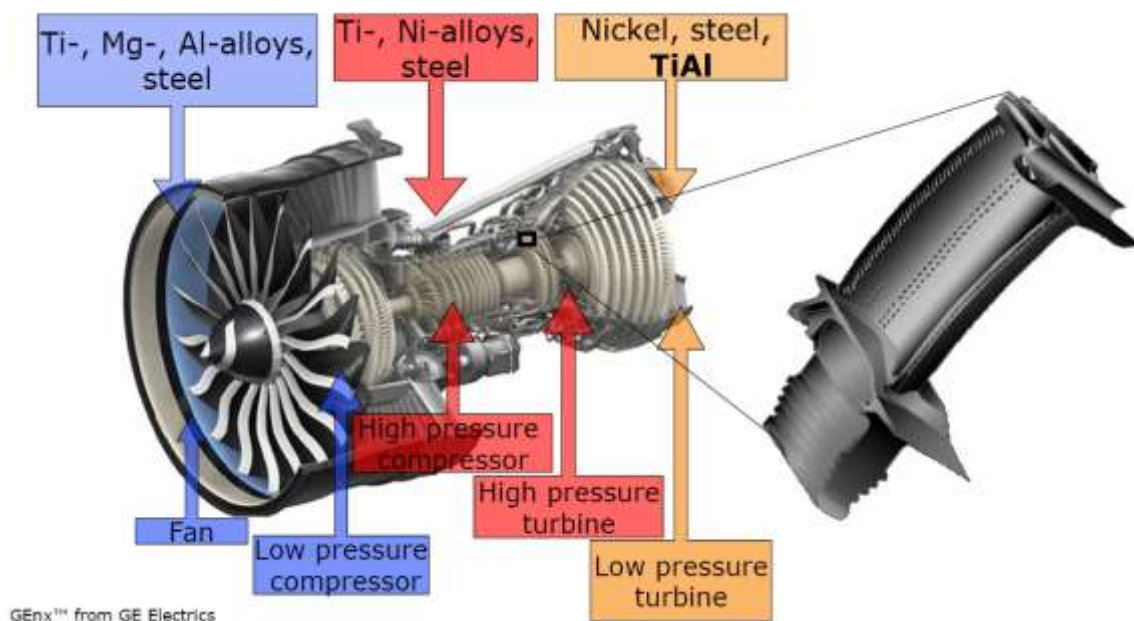
Figure 2-1. Jet engine layout and material families used at different stages [26]

TiAl-based alloys exhibit remarkable high temperature thermo-physical and mechanical properties, such as high density-normalized strength (similar to Nickel- based alloys), high stiffness, very good oxidation and corrosion resistance, low thermal expansion coefficient, high thermal conductivity and high ignition temperature. Some of the critical properties of TiAl-based alloys and compared with other competing alloy families are shown in Figure 2-3 and Figure 2-2. The properties shown in those graphs are representative for more generic alloy families rather for some specific alloys. Despite the excellent properties and after decades of research and development only recently [24] has been announced a commercial aircraft application for those alloys. This is mainly due to the extremely low room temperature ductility (Figure 2-3-d) and low fracture toughness, which makes it very difficult for TiAl components to be formed with required properties, in desired shapes and with acceptable final costs by any of the known conventional routes, such as extrusion and forging, casting and powder metallurgy. [6], [18]
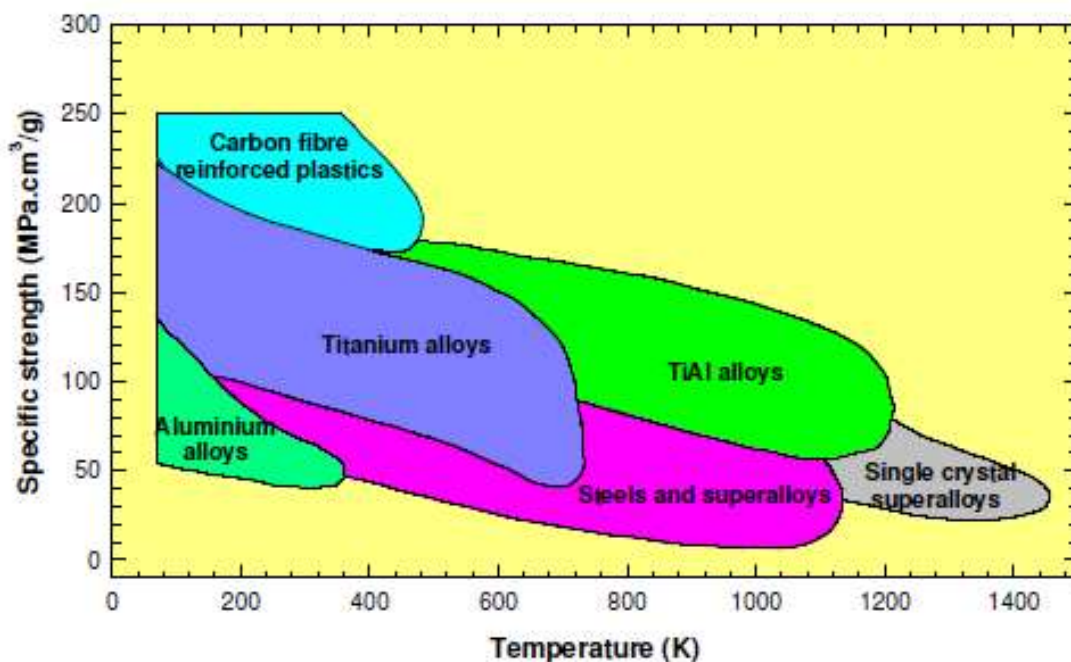
Figure 2-2. Specific strength of various materials versus temperature [19]
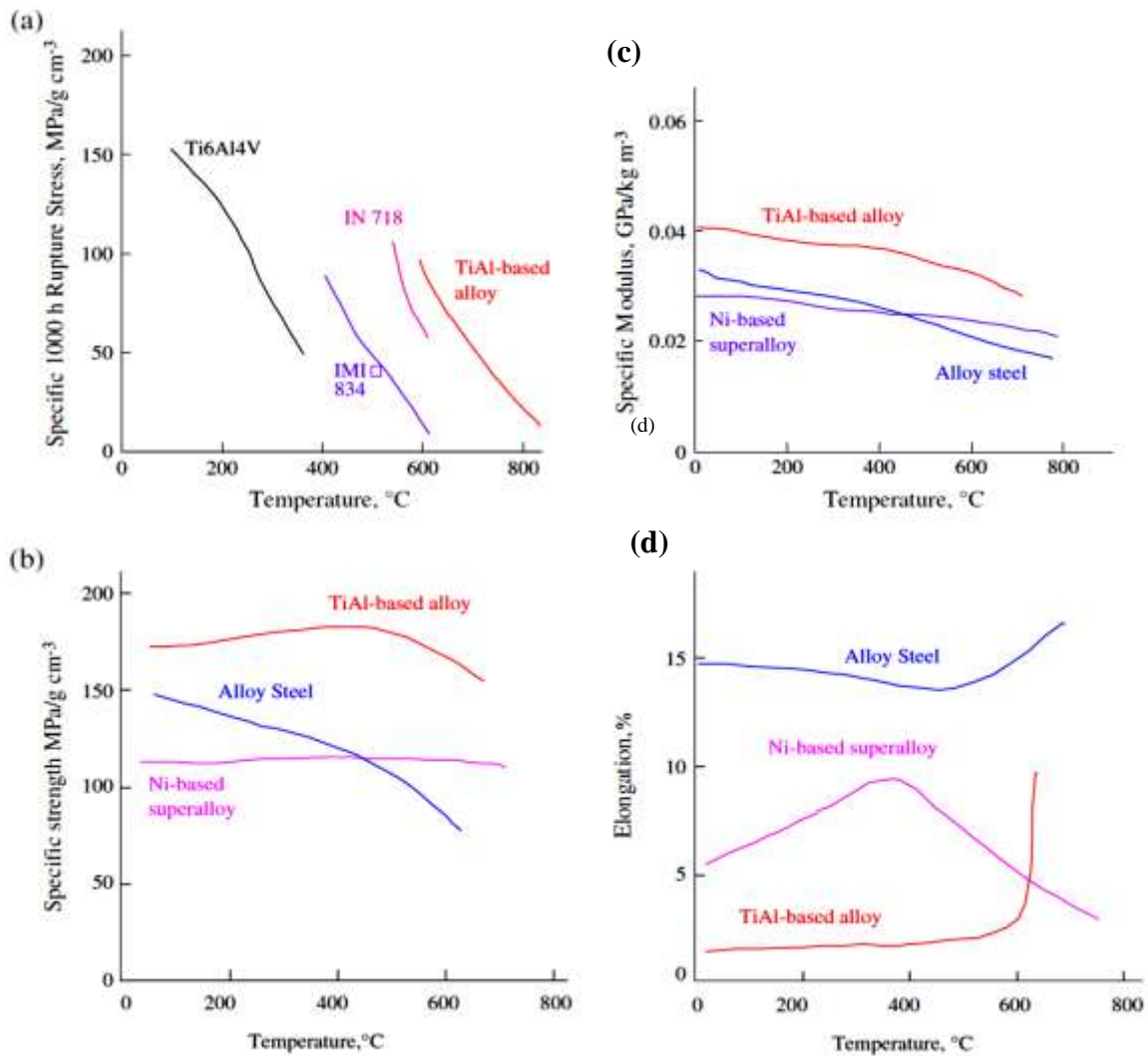
Figure 2-3. Comparison of a generic TiAl based-alloy with other engineering alloys for (a) rupture strength vs. temperature (b) specific strength vs. temperature, (c) specific modulus vs. temperature, and (d) elongation vs. temperature [18]

2.1.2 Intermetallics

Titanium Aluminide properties are closely related to their intermetallic nature. Intermetallics are the result of the combination of two or more metallic elements and sometimes with the addition of some non-metallic element additions [27]. Those different elements are of unlike atoms and this is the effect which leads to much stronger bonding than when like atoms are combined. Intermetallics exhibit properties between ceramic and metallic materials due to the covalent or part ionic nature of their bonding, compared with metallic solid solutions. The resulting solid phases are different from the individual elements regarding crystal structures and physical or mechanical properties. In intermetallics the different constituent elements are

26

ordered on a precise sub-lattice. This long-range ordering exists up to a critical temperature, T_c, which sometimes could be as high as the melting temperature, T_m. Long range ordering results in restrictions being introduced on deformation modes, which in due course, usually has an effect of increased strength but leads also to decreased room temperature ductility and fracture toughness. [27], [28]

Important structural intermetallics that have been considered for applications include Aluminides, (e.g. TiAl, NiAl and FeAl-based), Silicides (e.g. NbSi-based), Nickel Titanium (NiTi based), etc. [29]. A lot of research has been performed during the last 30 years to develop intermetallic alloys for jet engine applications, but like the TiAl-based alloys this has been proved to be very challenging as a result of the intrinsic material properties (i.e. low ductility and fracture toughness) and manufacturing related issues (i.e. challenging and costly processing) [30]. It has been reported [31] that low ductility and fracture toughness in several Aluminides and Silicides is a result of extrinsic environmental factors and those properties could be improved by alloying, microstructural control or by coating.

2.1.3 Ti-Al Binary Phase Diagram and Effect of Aluminium Content

Figure 2-4 shows the full Ti-Al binary phase diagram while Figure 2-5 demonstrates a more detailed version of its central section. Between the various existing intermetallic compounds, the main ones for engineering applications are the α_2- Ti_3Al and the γ- TiAl phases [27], [32].
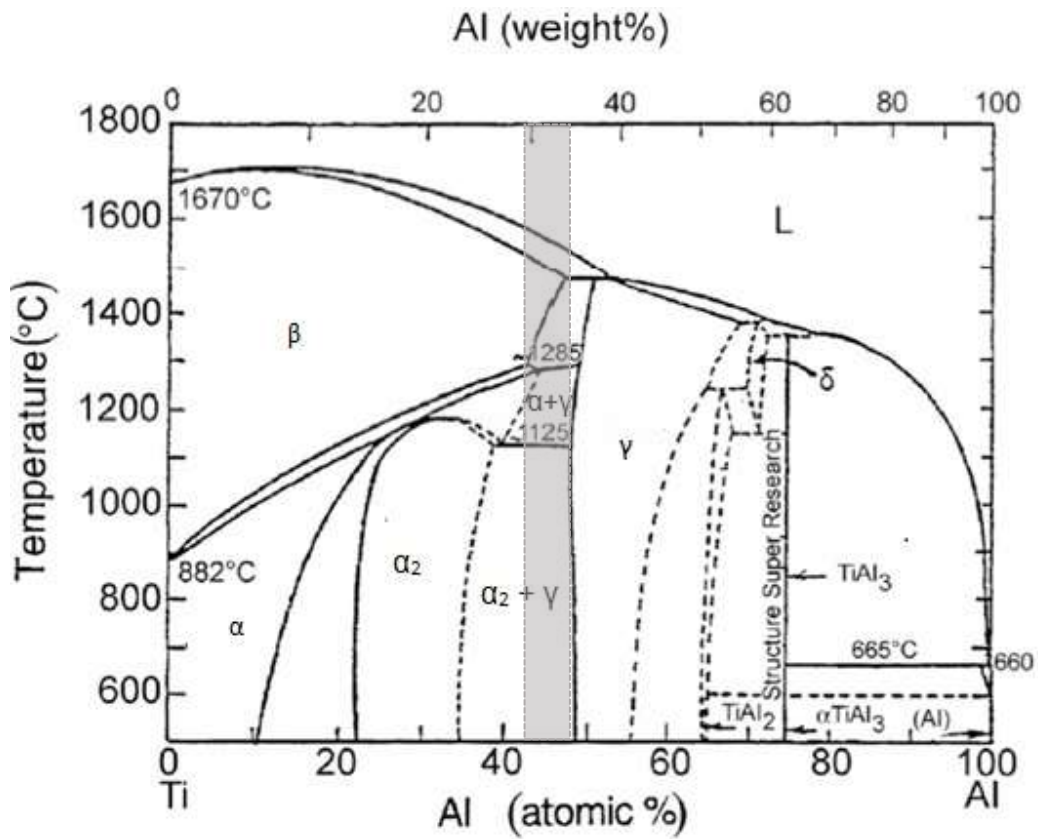
Figure 2-4. Ti-Al binary phase diagram. Typical range for engineering γ- based alloys is highlighted [28]
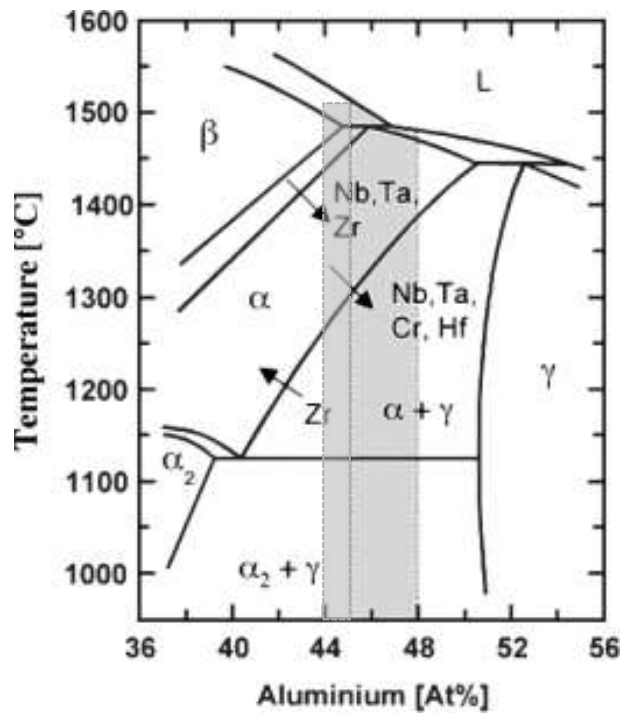
Figure 2-5. Central section of the Ti-Al binary phase diagram. Typical range for engineering γ- based alloys is highlighted [18]

α_2- Ti_3Al phase has an hexagonal DO_{19} ordered structure and its lattice parameters are a= 0.58 nm and c= 0.48 nm, resulting in a c/a ratio of 0.8. At room temperature, α_2 phase is homogeneous at Aluminium contents between 23 - 35 at % and it remains ordered up to 1180 ^{o}C for an Aluminium content of 32 at %, where it disorders into an hcp α- phase. During heating at higher temperatures α- phase transforms to a bcc β- Ti phase. [32], [33]

γ- TiAl has an ordered face-centred (fct) tetragonal structure and its lattice parameters are a= 0.40 nm and c= 0.41 nm, resulting in a c/a ratio of 1.02. At room temperature, γ- phase is homogeneous at Aluminium contents between 48 - 53 (at %). Its maximum homogeneity range is 48 – 68 Al at% at 1390 ^{o}C. It disorders at 1440 ^{o}C with a peritectic reaction to α + Liquid at 54 Al at %. [32], [33]

Between 35 - 48 (at %) Al content there is an area in the phase diagram in which the two phases, α_2 and γ coexist. In this area, there is one peritectic reaction at 1500 °C and 46 at % Al in which α disordered phase incongruently melts in β + Liquid. At 40 at % Al content the mixture of γ + α_2 forms into α phase at 1100 °C by a eutectoid reaction. [32], [33]

None of the above described single phases have the required properties for industrial applications, mainly due to the very low room temperature ductility and fracture toughness. More specifically, the ductility of alloys based on α_2- Ti_3Al phase is low at about 3%. With the introduction of β- stabilising elements a RT ductility up to 8% could be achieved [32]. An issue with these alloys is environmental embrittlement due to oxygen and hydrogen absorption at temperatures higher than 600 to 700 ^{o}C [19], [34]–[37]. γ- TiAl based alloys have much higher temperature strength and oxidation resistance, they are less prone to environmental embrittlement, but they suffer from extremely low RT ductility [32]. Therefore, the alloys typically used are slightly off- stoichiometric in the Ti-rich area. Most of the alloys are based on the binary Ti- 44-48 at % Al with some extra element additions [18]. As shown in Figure 2-6, the most balanced properties for the binary alloy are at an Al content of 48%, in the α_2 + γ region and typically thermo-mechanically processed to achieve fine grains and/or lamellar spacing [27].
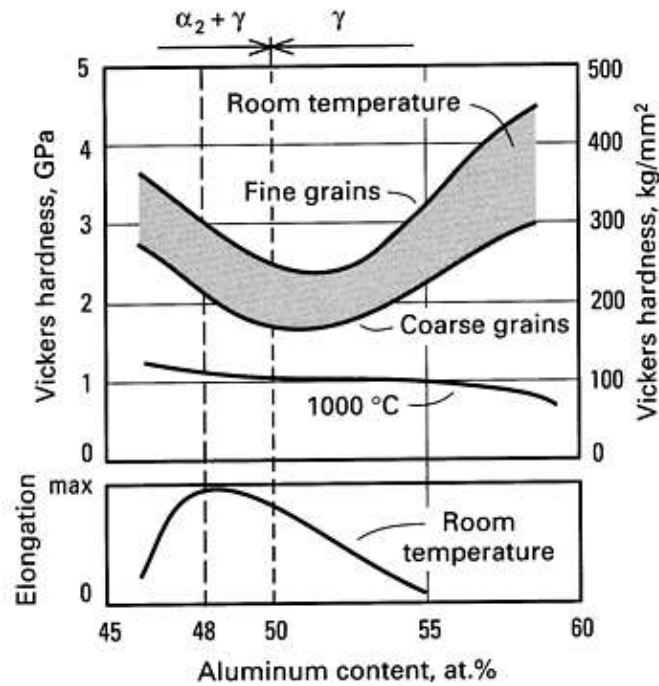
Figure 2-6. Tensile Properties vs. Al content [27]

In the literature, there are plenty of information for the binary TiAl alloys with Aluminium content between 45 – 50 at % and even up to 55-60%, as shown in Figure 2-6. On the other hand, the authors couldn't find any about the mechanical properties of alloys with Aluminium content less than 45 at% other than Figure 2-7. The data in this figure [38] are based on two typical cast γ-based engineering alloys, rather the binary alloy; the GE 48-2-2 and the GKSS TAB. Both alloys and its properties are summarised in more details in Table 2-1. The GE 48-2-2 alloy data by Austin and Kelly, which were replotted in this graph by Apel and Oehring [38], are showing a significant effect of Aluminium content on the strength and ductility for Aluminium content between 45-48 at%. The GKSS TAB alloy data are showing a similar strengthening effect by reducing the Aluminium content; an effect which seems to plateau below 44 at%. This could not be different for the ductility, as the alloy seems to have zero plastic elongation for an Aluminium content below 43 at%. [38]
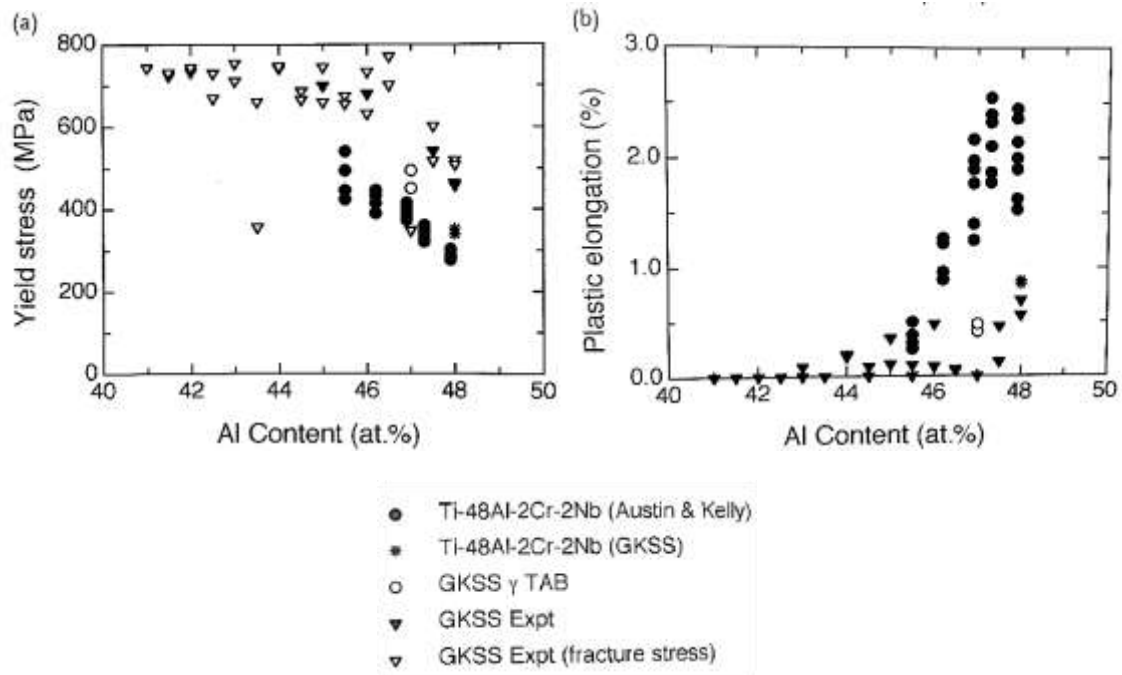
Figure 2-7. Effect of Aluminium content on the a) yield stress (0.2% flow) and b) plastic elongation to failure, of the GE 48-2-2 (Ti-48Al-2Cr-2Nb) and GKSS TAB cast alloys [38]

Liu [39] has investigated the influence of Nb and Al content on the microstructures and properties of TiAl based alloys. They suggest that the yield stress (σ_y), at 900°C of TiAl alloys follows a Hall-Petch relationship $\sigma_{0.2}=\sigma_0+\kappa_\lambda\lambda^{-1/2}$, where $\sigma_{0.2}$ is the yield strength, σ_0 and κ_λ are material constants and λ is the lamellar spacing. TiAl alloys strengthen with decreasing Al content and/or an increase in Nb content, but Aluminium content is the main factor which influences lamellar spacing, as shown in Figure 2-8. Decreasing Al content increases α_2 volume fraction (Figure 2-9-a), which results in a linear decrease of the lamellar spacing (Figure 2-9-b), which thereafter results in increasing the strength. As shown in Figure 2-10, and regardless the microstructure the yield stress (σ_y), at 900°C increases linearly by reducing the Al content.
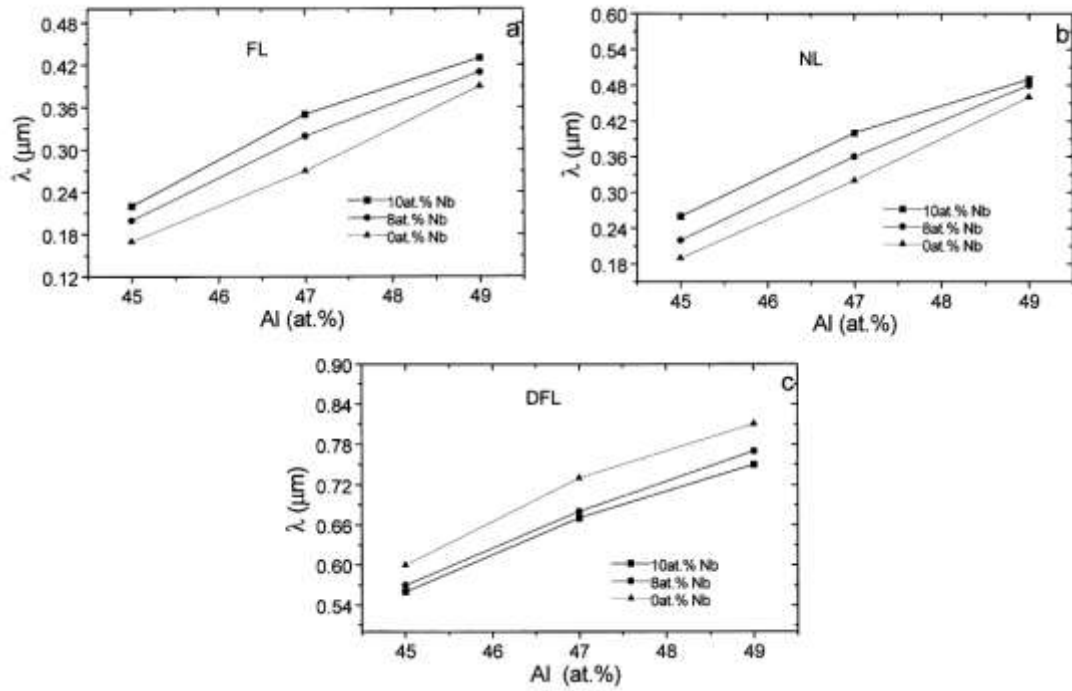
Figure 2-8. Effect of Aluminium and Nb contents on the lamellar spacing of a) fully lamellar (FL), b) nearly lamellar (NL) and c) degraded fully lamellar (DFL) microstructures [39]
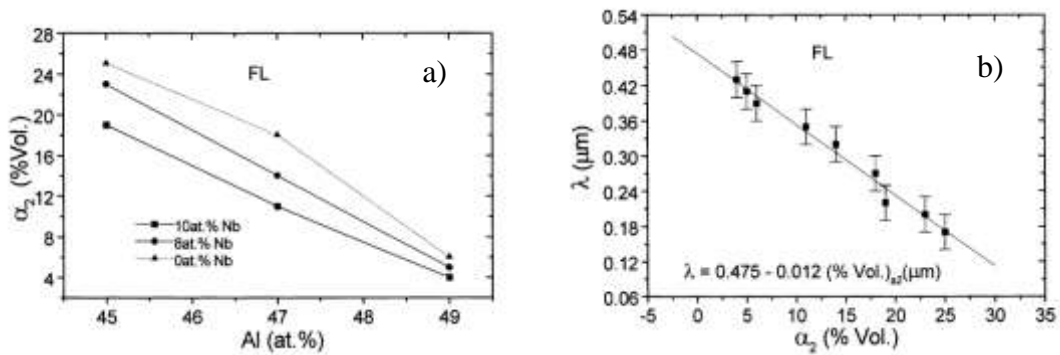
Figure 2-9. a) Effect of Nb and Al contents on the volume fraction of α_2 phase and b) Statistic relationship between lamellar spacing and the volume fraction of α_2 [39]
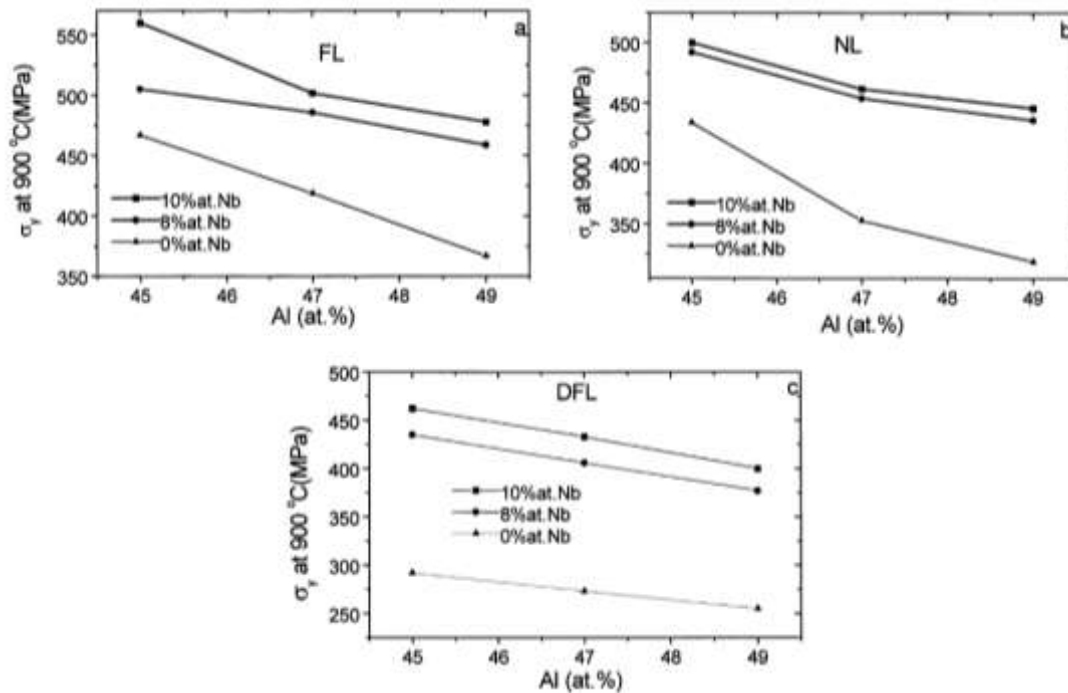
Figure 2-10. Effect of Nb and Al on the high temperature strength of TiAl alloys; for a) fully lamellar (FL), b) nearly lamellar (NL) and c) degraded fully lamellar (DFL) microstructures [39]

2.1.4 Microstructures and their Effect on Mechanical Properties

As noted above, mechanical properties of the $\alpha_2 + \gamma$ TiAl alloys are very sensitive to aluminium content and other minor or major element additions, as well as the microstructure of the alloy. Different microstructures result depending on thermo-mechanical processing. There are four main types of microstructures as shown below in Figure 2-11; a) the relatively coarse fully lamellar (alternate $\alpha_2//\gamma$ colonies) microstructure resulting from cooling down from the high temperature α phase region, b) the fine equiaxed (fine γ grains with α_2 precipitates at grain boundaries) microstructure resulting from lower temperature heat-treatment in the $\alpha_2 + \gamma$ region, c) the fine duplex (mixture of fine $\alpha2//\gamma$ lamellas and fine equiaxed γ grains) microstructure resulting from heat-treatment in the $\alpha + \gamma$ region, and d) the nearly lamellar (mostly lamellar and some equiaxed γ grains) microstructure resulting from heat treating at higher than duplex temperatures and in the $\alpha + \gamma$ region. Figure 2-12 displays a CCT diagram showing resulting microstructures as a function of cooling rate for a high-Niobium massively transformed [17] TiAl based alloy, when cooling starts at temperatures above the α- transus. For the specific alloy system the resulting microstructure changes from fully lamellar at very low cooling rates, to duplex at intermediate and faster cooling rates and finally to fine equiaxed at much faster cooling rates. [11], [17], [23], [32]
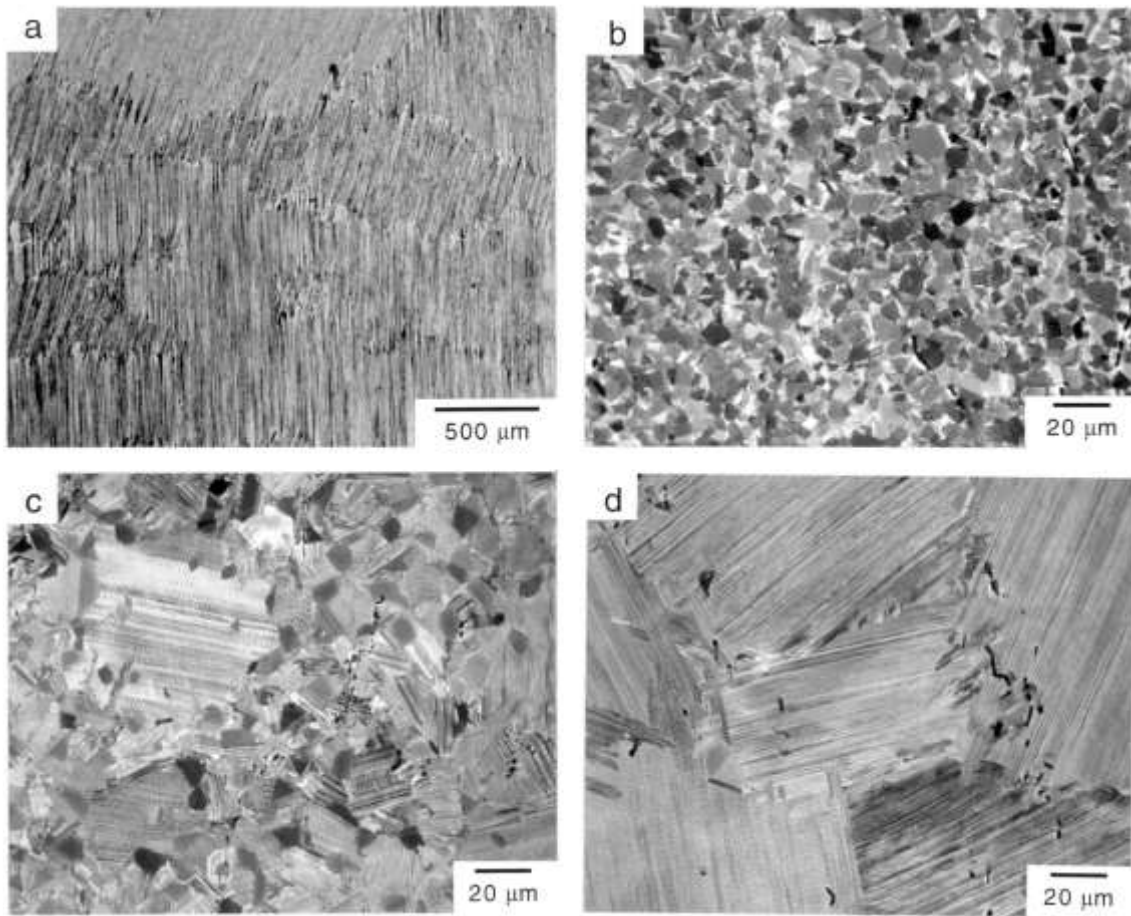
Figure 2-11. Typical γ- TiAl microstructures alloy a) Coarse nearly lamellar, b) equiaxed, c) duplex and d) lamellar [11]
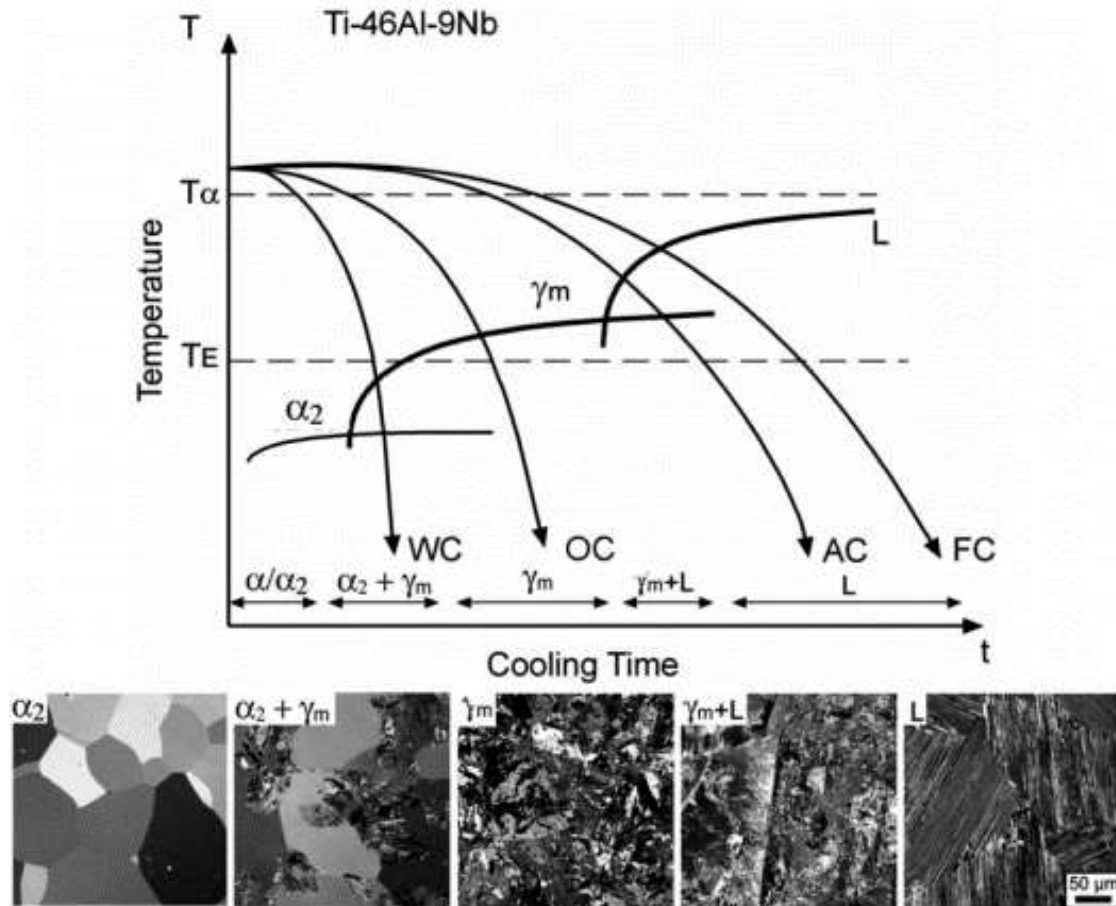
Figure 2-12. CCT diagram for a high Nb TiAl based alloy, showing the resulting microstructures of various cooling rates when furnace cooling, air cooling, oil cooling and water cooling [17]

Figure 2-13 [28] schematically shows some of the key mechanical properties of TiAl based alloys as a function of microstructure. As often the case is, there is no optimal microstructure that exhibits the best performance for all the required properties. Typically, it is considered [6], [7], [18], [32] that the duplex (II) microstructure exhibits the most balanced performance, including higher strength and RT elongation, due to the very fine microstructural characteristics (γ grain size, lamellar grain size and lamellar spacing), following a Hall-Petch strengthening relationship. Where creep resistance and fracture toughness are required, as in high temperature turbine engine parts, the coarse characteristics of fully lamellar microstructures (IV) could be more beneficial. It is implied [32] that refining the microstructural features of fully lamellar (lamellar grain size and spacing) components will improve this microstructure for higher elongations and high temperature strength, as well.
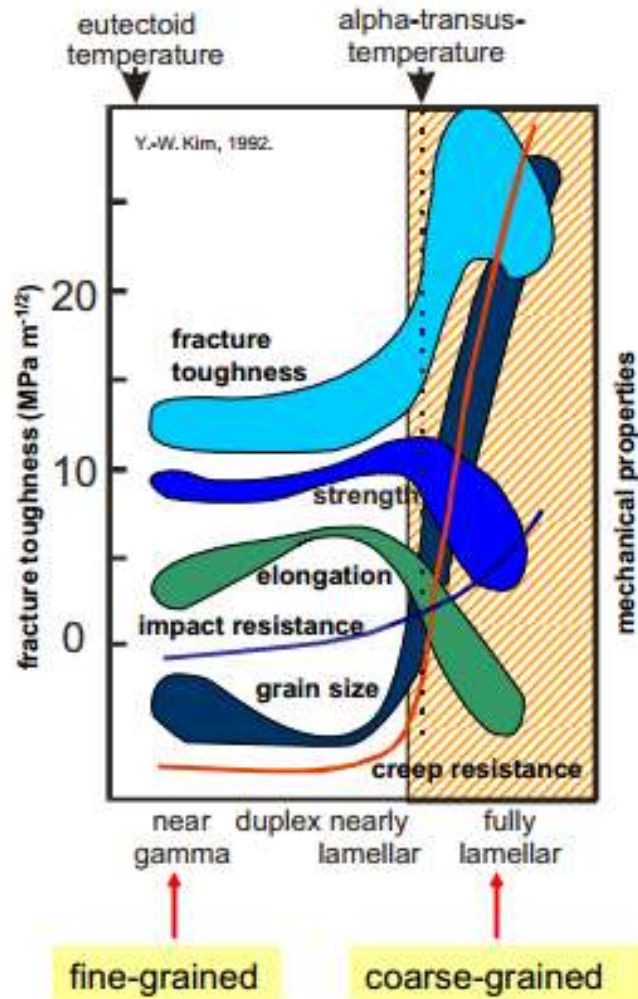
Figure 2-13. Mechanical and tensile properties vs. microstructure [28]

2.1.5 Alloy Design and Classification of Main TiAl based Intermetallics

During the last decades, numerous investigations have been performed in order to optimise performance and properties of TiAl based alloys by alloying and microstructural control. Several alloying elements have been used to achieve the most suitable properties depending on the specific application. A general formula of the alloys typically used can be summarised as below:

$$Ti- (42-49) Al – (1-10) Nb, Ta – (0-4) X – (0-1) Y – (0-1) Z \text{ [40]} \qquad (2.1)$$
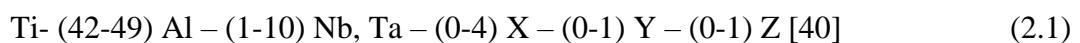
Where X= Cr, Mn, Ta, V, Mo; Y= W, Hf, Zr; and Z= C, B, Si, N

Figure 2-5 shows how those additions are expected to affect the binary phase diagram. Y group elements are used to increase ductility in two phase alloys and in most cases about 2% Cr is used. Z group elements, in small additions, improve creep and/or oxidation resistance and they are also used for microstructural refinement and/or precipitation hardening. Nb is used in almost all cases at contents higher than 2%. Addition of Nb is typically used to increase oxidation and creep resistance at lower concentrations and to increase high temperature strength at higher concentrations. [18], [32], [40]

The most researched alloys of the last 10 years are the so-called 2nd generation alloys and especially the GE 48-2-2 developed by GE [41] with a composition of Ti-48Al-2Cr-2Nb and the Ti-45Al-2Nb-2Mn plus 0.8 vol. % TiB2 introduced by Howmet-Pratt and Whitney [42]. GE 48-2-2, as earlier mentioned in this Chapter, is the first γ-TiAl based alloy to be used for a commercial jet engine application [24]. 1st generation alloys are mainly binary alloys with a varying Al content and with some minor element additions. 2nd generation alloys are typically low alloyed with additions typically lower than 5 at %. [6], [7], [16], [38], [43]–[46]

1st and 2nd generation alloys are also classified as conventional alloys [38]. Other alloys in this category contain the γ-TAB (Ti-47Al-4(Nb, Cr, Mn, Si, B)) developed by GKSS [47] and the γ-MET (Ti-46.5Al-4(Nb, Cr, Ta, B)) developed by Plansee [48]. The alloy design at this time was more focused to achieve maximum ductility and that's why most of the alloys were developed to be close to the optimum 48 at % Al concentration and to have a duplex $\alpha_2 + \gamma$ microstructure. On the other hand high-temperature strength, oxidation and creep resistance of those alloys is found [38] to be much lower than Ni-based superalloys at temperatures higher than 700 °C. To increase high temperature strength and oxidation during, the last decade, a 3rd and 4th generation of TiAl based alloys with much higher (5-10 at %) 3rd element additions (Nb, Mo and Ta) have been developed. The main 3rd and 4th generation alloy families are the β- solidifying, the high-Niobium and the massively transformed ones. [17], [19], [23], [38], [49], [50]

β- Solidifying alloys contain relatively high contents of β- stabilisers, such as W, Re, Fe, Mo, Cr, Nb and Ta and typically a lower content of Al and so they solidify via a β solidification path (L+β → β → β+α → β+α+γ → α_2+α+β+γ → α_2+β+γ). β to α transformation by precipitation at lower temperatures during cooling or heat treatments it can be achieved in up to 12 different orientation variants, compared with only one available orientation relationship between γ and α for the typical solidification path when cooling or heat treating γ-based TiAl

alloys (L+β → α → α+γ → α₂+γ) [17], [38]. So, β- solidifying alloys are shown to exhibit increased grain refining of the cast structure with improved wrought processing capability and balanced mechanical properties when appropriately heat-treated. On the other hand, most of those alloys exhibit unacceptable creep resistance and/or low room temperature elongation, due to the intrinsic low ductility of the Al-rich low temperature β_2 phase and due to the brittle ω phase transformation during prolonged high temperature exposure. The most promising alloys of this category are the TNM alloys developed by Clemens [17] at the University of Leoben, Austria with collaboration with MTU Aero Engines and GfE in Germany. Those multicomponent alloys contain balanced amounts of Nb and Mo β- stabilisers. A typical formula for those alloys is Ti-(42-45)Al-(3-5)Nb-(0.1-2)Mo-(0.1-1)B. TNM alloys have been reported to be under both 3rd and 4th generation classification. [17], [51]–[54]

Massively transformed alloys have been investigated mainly by the IRC in Birmingham [55]. The typical formula for those alloys is Ti-46Al-8(Nb, Ta). Depending on Oxygen content and cooling rate Ti46Al8Nb can transform into a massive gamma (γ_m) phase, as shown in Figure 2-12, when cooling in oil from temperatures higher than the α- transus. When those components are appropriately heat treated in the α + γ region, a very fine microstructure is formed consisting of α_2 plates into γ matrix and exhibiting balanced good properties. 4th generation alloys containing Ta instead of Nb (Ti46Al8Nb) have been developed by the IRC, which can undergo the massive gamma (γ_m) phase transformation at even lower cooling rates (air cooling) when casting 25 mm diameter bars. [17], [19], [38], [55]

High niobium alloys are considered to exhibit improved creep and oxidation resistance, as well as high temperature strength. As earlier mentioned in this Section, Nb is considered to enhance those properties, especially at concentrations over 5 at%. Furthermore, an increase of Nb content changes the phase equilibria of the Ti-Al (Figure 2-14) system. by i) increasing the eutectoid and melting temperature, ii) shifting α and β phases to higher Al concentrations and iii) decreasing α and β transus temperatures. Figure 2-15 a) and b) shows the isopleth phase diagrams for 45% Al and 8% Nb for the ternary Ti-Al-Nb alloy systems, respectively, as developed by Witusiewicz, [56] by experimental and theoretical modelling work. [18], [32], [39], [40], [57]
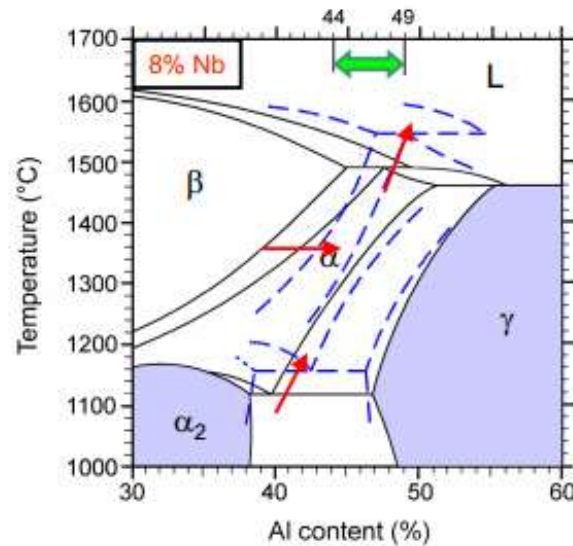
Figure 2-14. Isopleth phase diagram section for 8% Nb for the ternary Ti-Al-Nb alloy system [58]
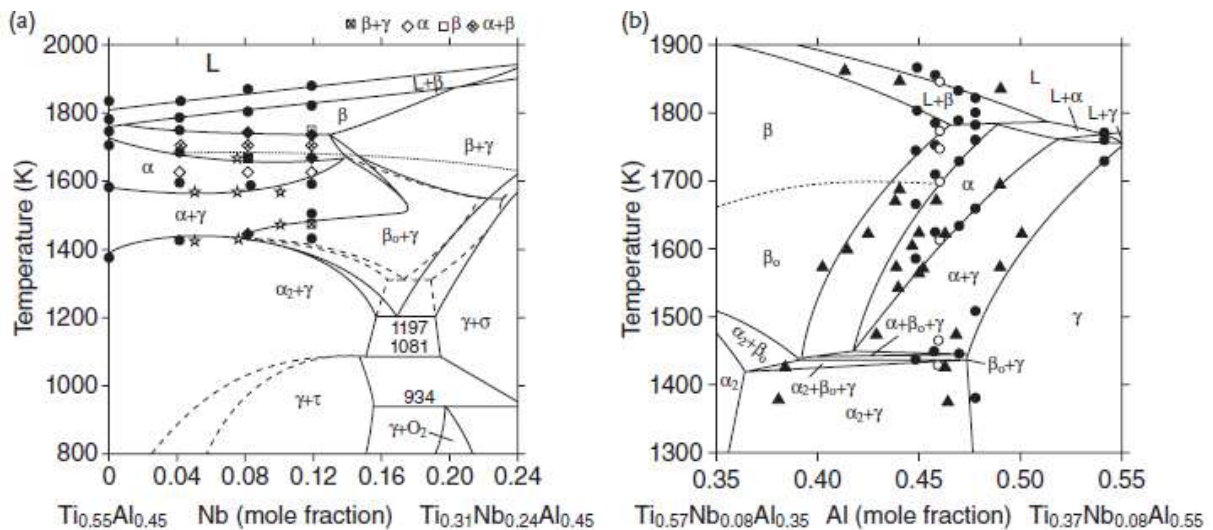
Figure 2-15. Isopleth phase diagram sections for (a) 45% Al and (b) 8% Nb, for the ternary Ti-Al-Nb alloy system, respectively, developed by experimental and theoretical modelling work [56]

Chladil [57] have investigated the effect of Nb and Carbon on the equilibria of the TiAl system. As shown in Figure 2-16 additions of Carbon have an even stronger effect on increasing the eutectoid temperature. Their results, also, show that Nb or C additions do not significantly affect the α-transus. Eutectoid and α-transus are very important for subsequent heat and/or HIP treatments [58]. As also reviewed in section 2.1.3, Liu [39] has investigated the influence of Nb and Al content on the microstructures and properties of TiAl based alloys. They suggest that the yield stress (σ_y), at 900°C of TiAl alloys follows a Hall-Petch relationship $\sigma_{0.2}=\sigma_0+\kappa_\lambda\lambda^-$

$^{1/2}$, where $\sigma_{0.2}$ is the yield strength, σ_0 and κ_λ are material constants and λ is the lamellar spacing. TiAl alloys strengthen with decreasing Al content and/or an increase in Nb content, but as shown in Figure 2-8, Aluminium content is the main factor which influences lamellar spacing. Decreasing Al content increases α_2 volume fraction (Figure 2-9-a), which results in a linear decrease of the lamellar spacing (Figure 2-9-b), which thereafter results in increasing the strength. As shown in Figure 2-10, and regardless the microstructure the yield stress (σ_y) increases linearly by reducing the Al content. An increase in Nb somewhat increases the lamellar spacing (Figure 2-8), but, as shown in Figure 2-10, high temperature strength is increased. So, it is [39] referred that Nb content influences the σ_0 value in the Hall-Petch equation.
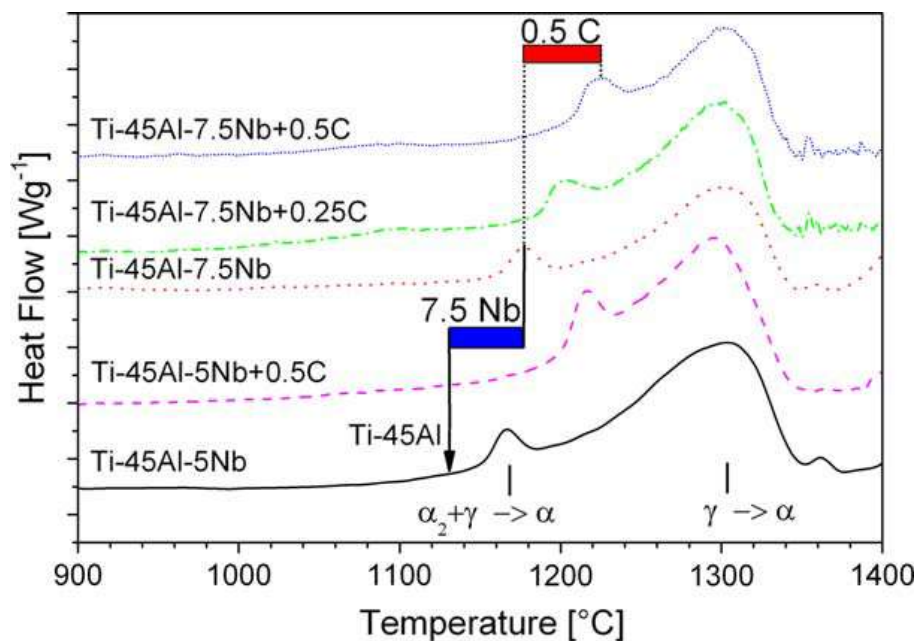
Figure 2-16. Effect of Nb and Carbon content on the equilibria of the TiAl system [57]

The research around high-Niobium containing alloys has been mainly propelled by Helmholtz Zentrum Geesthacht (formerly GKSS) by developing the so-called TNB alloys. The typical formula for those 3rd generation γ-based TiAl alloys is Ti- (45-47) Al – (4-8) Nb and with some small additions (0-1 at %) of Carbon or Boron. Those alloys are considered as the best choice for achieving much higher oxidation and creep resistance and higher temperature strength (up to 1GPa) and microstructure stability and more balanced properties (plastic elongation =2-2.5 %) required for high temperature aircraft engine applications. Those properties (comparable to

Ni-based superalloys) make TNB alloys great candidates for extending high-temperature capabilities to even hotter parts of the turbine engine compared with the 48-2-2 alloys. [11], [18], [39], [40], [45], [59]

Some commonly used TiAl alloys and the influence of alloying elements to each of those alloys are summarised below in Table 2-1.

Table 2-1. Summary of commonly used TiAl alloys and influence of alloying elements

Alloy name	Composition (at. %)	Influence of alloying elements	Classification by Generation	Other classification	Reference(s)
GE 48-2-2	Ti-48Al-2Cr-2Nb	Al: determines initial phase and phase transformations during solidification, influences microstructural features (e.g. α_2 volume fraction), ductility and strength Cr: reduces α- transus temperature, increases ductility in two phase alloys Nb: increases oxidation and creep resistance	2nd	Conventional	[41]
Howmet	Ti-48Al-2Mn-2Nb	Al, Nb: as above Mn: reduces α- transus temperature, increases ductility in two phase alloys	2rd	Conventional	[66]
Lockheed-Martin 45XD™	Ti-45Al-2Nb-2Mn-0.8 vol. % TiB$_2$	Al, Nb, Mn: as above TiB$_2$: for grain refining of cast microstructure	2nd	Conventional	[42], [61]
ABB-2	Ti47Al-2W-0.5Si	Al: as above W: increases high temperature strength and oxidation resistance, improves creep properties in near lamellar microstructures Si: improves creep strength through precipitation hardening and increases oxidation resistance	2nd	Conventional	[38]
ABB-23	Ti-45Al-2W-0.5Si-0.5B	Al, W, Si: as above B: for grain refining of cast microstructures	2nd	Conventional	[38]
GKSS TAB	Ti-47Al-1.5Nb-1Mn-1Cr-0.2Si-0.5B	Al, Nb, Mn, Cr, Si and B: as above	2nd	Conventional	[47]
Gamma MET PX (GMPX)	Ti-45AI-5Nb-0.2B-0.2C	Al and B: as above Nb: increases oxidation and creep resistance and at high concentrations (> at. %) also, increases high temperature strength C: improves high temperature strength and creep resistance by precipitation hardening of finely distributed carbides when heat-treating wrought alloys	2nd	Conventional	[48]
N/A	Ti-46Al-8Nb	Al and Nb: as above	3rd	Massively transformed	[55]
N/A	Ti-46Al-8Ta	Al: as above Ta: producing fine microstructures from massively transformed gamma at lower cooling rates (air cooling) than Nb containing, also improves oxidation and creep resistance and increases high temperature strength	4rd	Massively transformed	[55]
TNB	Ti-(45-47)Al-(4-8)-Nb-(0-1) C, B	Al, Nb, C and B: as above	3rd	High Niobium	[19], [43], [44], [49]
TNM	Ti-(42-45)Al-(3-5)Nb-(0.1-2) Mo-(0.1-1) B	Lower aluminium content and relatively high amount of β-stabilisers (i.e. Nb and Mo) shifts solidification path via a β phase, resulting in fine microstructures and improved wrought processing capability and balanced mechanical properties when appropriately heat-treated	3rd and 4th	β- solidifying	[17], [51]–[54]

2.1.6 Processing and Applications of γ- TiAl based Alloys

Despite the great potential, very limited commercial applications are referred in the literature, largely because of the poor room temperature fracture toughness and the high fatigue crack growth, which are serious limitations, especially for the very conservative aerospace industry. Extruded and forged parts exhibit quite good properties with fine micro-structures, but the cost to form into complex shapes is much higher than Ni-based superalloys. With casting, complex shapes could be achieved with acceptable cost, but typically the resulting properties are unacceptable for demanding applications. Investment cast (IM) parts have been developed for helicopter engines and turbine air foils, but their production cost remains relatively high. Powder metallurgy and injection moulding parts have been developed with acceptable properties, but post- processing is still required to achieve net-shape, which increases the cost to unacceptable values. [9], [17], [18], [32], [38], [40]

There are several steps in the manufacturing route of a TiAl component. Ingot production is always the first step. The most commonly used methods for ingot production include: vacuum arc remelting (VAR), plasma arc remelting (PAM) or induction skull melting (ISM). High quality, reliability and reproducibility of those ingots is key for demanding applications, such as in the aerospace and automotive industry. In particular, chemical and microstructural homogeneity is critical. When those ingots are going to be used for wrought manufacturing routes, HIP is essential to remove internal porosity. In other cases, depending on cooling rates, alloy composition and ingot size, thermal stresses might be generated in the ingots, which can cause cracking. Extra care should be taken to minimise this effect or eliminate it afterwards with appropriate high temperature heat-treatments. In the last decade, a lot of progress has taken place to increase the level of quality control for ingot manufacturing. In the same review article [17] it is noted that the key challenge for the next years would be to develop effective strategies to reduce the cost of ingot manufacturing, including the employment of recycling techniques. [17], [38]

Casting is probably the most cost-effective near-net shape manufacturing route for materials with such bad formability. The choice of alloy composition and specific melting/casting techniques are really important factors for the final resulting properties and specific applications. Alloy composition choice has to be taken in account depending on the required final mechanical properties (application), castability, solidification path and microstructural stability [38]. Usually cast components are assessed for LPT blades and other static, low-risk components [13]. The most common cast alloys include the 2nd generation Ti-48Al-2Cr-2Nb

(GE) [62], Ti-45Al-2Nb-2Mn-0.8 vol. % TiB$_2$ the (Howmet-Pratt and Whitney) [63] and the Ti-47Al-1.5Nb-1Mn-1Cr-0.2Si-0.5B [47]. Typically most of the developed cast alloys include small Boron or Silicon additions for grain refinement [64]–[66]. Solidification path as earlier mentioned in this Chapter for the TNM alloys is important for the phase transformations during cooling and subsequently for the resulting microstructural features and properties. The most promising casting method with acceptable properties until now is investment casting. Other methods have been researched including gravity metal mold casting, centrifugal casting and counter-gravity low pressure casting. All those techniques in accordance to TiAl are explained in detail in the recently published book by Appel [58] and elsewhere [9], [16], [17], [22], [23], [40], [61], [63], [67]–[71]. The only known commercial use of a cast TiAl component is for automotive applications and specifically Mitsubishi who in 1999 were the first to develop investment cast turbocharger wheels [20]. Many other development attempts for commercial applications for aerospace and automotive industry have been performed and tested, but typically the properties are inferior to wrought and/or Ni-based Superalloys.

Wrought manufacturing routes are typically used for many industrial alloys for high demanding applications. Several steps of thermochemical processing such as, rolling, forging and hot extrusion with subsequent machining and heat-treatments might need to take place in order to form the final net-shape component, as well as to optimise microstructures (breakdown of ingot microstructure) and properties. Typically, hot-working for TiAl alloys takes place at temperatures over the brittle-to-ductile transition, much higher than 700 $^{\circ}$C and at low deformation rates [6], [17], [23], [49], [53], [54], [72]. There are obvious benefits over cast components, such as greater chemical and microstructural homogeneity, minimal defects and increased repeatability and reliability. In the last decade several wrought TiAl alloys have been developed with excellent mechanical properties [15], [18], [32], [45], [49], [53], [72]. Industrial and academic research effort has been done to develop the most effective wrought processing steps by GKSS, Rolls Royce Deutschland (formerly BMW Rolls Royce), NASA aerospace vehicles, Plansee AG and others [19], [23], [38], [40], [44], [73]–[75]. On the other hand, despite the superior mechanical properties there are no known wrought commercial applications up to now. This is mainly due to the high processing costs, which are required for capital investment on specialised equipment that can perform at high temperatures[16], [18], [30].

Powder metallurgy (PM) is a well-established manufacturing route for producing metallic components from pre-alloyed or elemental powders. PM routes offer an alternative to ingot

manufacturing routes and the potential to overcome some of the issues related with those methods. With PM, there is the possibility to produce near-net shape components of high quality at acceptable costs. Properties typically [17], [23], [53] are superior to corresponding cast components. This is due to the ability to produce refined, homogenous and segregation and texture free microstructures. In addition, with PM unconventional alloys or composites and porosity controlled structures are possible. The first step for PM is the manufacturing of high quality powders, suitable for the actual PM technique. Both pre-alloyed and elemental powders can be used. Typically, pre-alloyed powders are more expensive and they are manufactured by melting and gas atomising techniques. For reactive, TiAl based alloys the most commonly used manufacturing techniques [38] are: i) the Plasma Inert-Gas Atomisation (PIGA) used by GKSS, ii) the Titanium Gas-Atomiser Process (TiGA) developed by Crucible Materials corporation and iii) the Electrode Induction Gas Atomisation (EIGA) developed by ALD. Powder characteristics (size, particle size distribution, morphology, chemistry, microstructure, porosity, etc.) and quality vary depending on the manufacturing technique and atomisation gas [76].

Several PM processing routes have been evaluated for TiAl based alloys, including Hot Isostatic Pressing (HIP) [40], [53], [73], [77]–[80], Metal Injection Moulding (MIM) [81], Spark Plasma Sintering (SPS) [37], [59], [82], etc. Most of the conventional PM processes require significant post-processing (similar to wrought manufacturing routes) and machining to further optimise properties and/or form the final components [18], [23], [37], [38], [40], which is significantly increases processing costs. MIM is a promising net-shape technique to produce small scale components with minimum post processing, but effort is needed to reduce porosity and contamination [38]. An additional drawback for MIM implantation for TiAl based alloys is the high cost of fine powders required for this process, due to the low yield for fine powders with current powder production methods. SPS TiAl manufacturing has been mainly propelled by Couret [82]–[84]. Both elemental and pre-alloyed powders could be used for this technique. Microstructural manipulation is very flexible with this method. Outstanding tensile properties have been reported for SPS [59], [82], [84] and it is suggested that there is great potential for upscaling and moving towards near-net shape.

2.2 Additive Manufacturing

2.2.1 General Overview

Additive manufacturing (AM), as defined by the ASTM committee F42 on Additive Manufacturing technologies [85], describes a variety of "Processes of joining material to make objects from 3D-CAD models data, usually layer upon layer, in contrast to conventional methods of machining a billet, where material is removed (subtractive manufacturing) ". Historically, there is a large diversity in terminology to describe various processes that can be classified under AM. Other commonly used terms include: i) 3D printing, Freeform or Additive fabrication and Rapid prototyping/manufacturing/tooling. [1], [3]–[5]

Additive manufacturing started with Stereolithography (SLA) in 1986 for building near-net shaped components by curing photosensitive polymer [2], [86]. From this first application, a lot of progress has been made during the last almost 30 years. Nowadays, AM is an established manufacturing route for a wide range of commercial applications and various industries, from the most high-end, such as aerospace, automotive, biomedical and tissue engineering to the most trivial, such as art, food and jewellery. A wide range of materials have been additively manufactured/3D printed from metals and ceramics to human tissues, paper and even food products. Commercial AM platforms cost from a few hundred pounds up to a couple of million pounds. It is out of the scope of this work to review all the different applications and processing of AM, but more information and details can be found in the following review articles and reports [2]–[5].

The focus of this work is on metal based AM techniques that enable the manufacturing of structural components suitable for high-end applications, such as aerospace and automotive. The main metal-based processes referred in the literature could be classified [1], [3], [5] as:

- Powder bed with powder feedstock
- Free-form or metal deposition with wire or powder feedstock, and
- Ultrasonic consolidation of metallic foils

The general principle for all the above AM techniques is schematically shown in Figure 2-17, below. Firstly, a 3D Computer-aided design (CAD) model of the final component needs to be created. Then this 3D model is sliced into several thin 2D layers of user defined thickness. This thickness depends on the platform and required surface finish and varies from several µm to a few mm. Subsequently, the "sliced" file is loaded on the computer of the AM platform. Finally,

each individual layer is fabricated to the desired geometry defined by each 2D slice of the 3D-CAD model, one on the top of the other until the complete manufacture of the final 3D component.
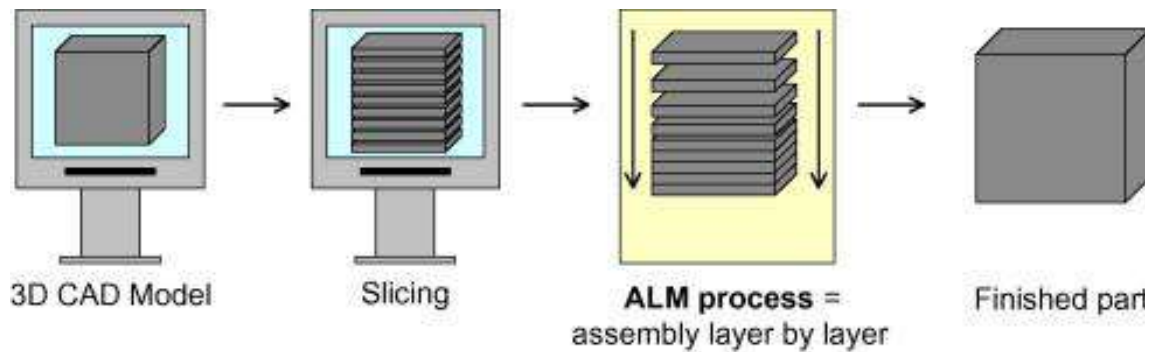
Figure 2-17. Diagram showing schematic sequence of AM processes [3]

In metal deposition or free-form techniques [1], [3], [87] powder or wire is fed and melted on demand on a metallic substrate by a moving robotic hand. Both feeding system and heat source are attached to this robotic hand and both activities are performed simultaneously. Such techniques are used for either 3D digital manufacturing of components or for cladding and repairing applications. In powder bed techniques, a full layer of powder is spread on the metallic substrate, but it is selectively melted only to the desired geometry defined by the 3D-CAD model. In some cases, (i.e. EBM) [6] it is required to pre-sinter the whole powder layer before melting. Both techniques include platforms that use either laser or electron beam as a heat source. Finally, for ultrasonic consolidation (UC) or ultrasonic additive manufacturing (UAM) [88]–[90] metallic foils are welded layer by layer in solid state by applying high frequency ultrasonic vibrations. After consolidation, each layer is formed into the required geometry using a CNC system.

The benefits and challenges for metal based AM implementation are described in various review papers [1]–[5]. Some of the main benefits could be summarised as:

i)   AM is a tool-less, near-net shape process and fully dense (~100% density) structural parts could be fabricated from powder of the parent chemical composition with just only some extra surface finishing (Figure 2-18). Material waste and costs (buy-to-fly ratio) are significantly reduced; less than 10% material waste, when for conventional methods this could be up to 90%.

Figure 2-18. From powder to final part

ii)   AM allows a great freedom of design for fabricating unique structures and features that with other processes would not be possible, as well as fully customisable parts, such as mesh structures (Figure 2-19) and medical implants to fit specific patient body structures (Figure 2-20), respectively.
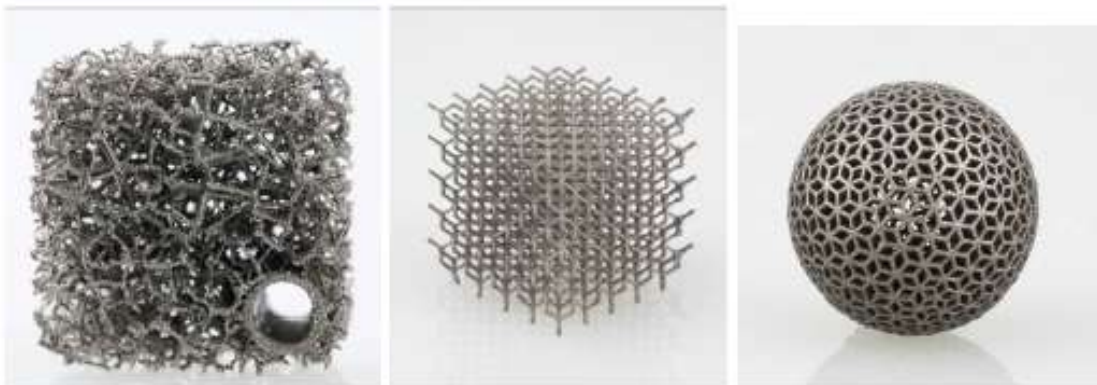
Figure 2-19. Sophisticated mesh structures fabricated by Arcam EBM at the Mercury Centre [3]

Figure 2-20. Chest implant that is able to replicate the intricate structures of the sternum and ribs fabricated by Arcam EBM [91]

iii)   Required parts and manufacturing steps to produce a complete final component are reduced.

iv)   Tooling and post-processing costs, as well as manufacturing lead times are considerably reduced.

v)   It is not required to keep an inventory of semi-finished or finished parts. Components are produced on demand.

The main barriers for AM implementation are related to the extremely high cost of the existing metal-based platforms and secondly to the cost and quality of existing metallic powders. Additionally, AM is still a relatively immature manufacturing route when compared with the well-established conventional manufacturing routes, there are not comprehensive property databases and there is a variability of properties between different builds and/or different platforms. Other concerns are related to the available build sizes, generation of severe thermal stresses and columnar microstructures. [1]–[5]

AM routes have been extensively investigated for processing various metals and alloys for aerospace applications. Due to high material costs, titanium alloys have been the most studied in many near-net shape technologies. The most commonly investigated alloy systems are based on Ti-6Al-4V (ASTM Grade 5&23 ELI), as well as the CP- Ti (ASTM Grade 1&2), although other more exotic systems have been attempted. The research has been mainly done using powder bed, electron and laser beam technologies and properties are reported to be superior to cast and comparable to wrought, which is remarkable for a structure containing defects. [8], [92]

Nickel- based alloys are of great interest for aerospace applications, but maturity of process and available mechanical property databases are limited. Properties currently seem to be lower than wrought. Two alloys remain in focus for near- net shape manufacturing: Inconel 718 and Inconel 625, with the latter being a substitute for IN718 and not requiring any heat treatment. A handful of papers are available on EBM of 718 by Strondl [93] and members of Arcam AB [94] in 2008-09 and more recently by Amato [95] using the SLM system. However, there is no evidence of any single crystal alloys, ODS or even castable alloys (IN713C) that have been attempted on either system.

Work on Aluminium alloys is split equally between castable (Al-Si/Al-Mg) and wrought alloys (Al-Cu/Al-Zn). There is abundance of publications in the literature for attempts mostly with

laser systems, but with EBM and ultra-sonic consolidation as well. Although most of them are just feasibility studies to achieve fully dense deposited material and they lack mechanical property databases. The two EBM feasibility attempts are from Mahale, Cormier and Harrysson [96], and they reported to achieve fully dense material without severe evaporation. The ultrasonic attempts are all for Al3003 alloy and even some increased UTS and elongation are reported, the welding density between consolidated sheets remains low (approximately 70%) [88]–[90]. An SLM paper from Bartkowiak [97], is on Al2021 and Al7075 which are wing skin and wing spar alloys, respectively. No properties are reported, as the resulted samples are just deposited single tracks. Similar attempts from Bartkowiak [97] have been done on AlSi12 and AlSi10Mg. The most complete data are reported by Scmidtke for a modified 5xxx and an Al10SiMg alloy [98].

Other materials of interest for aerospace applications includes intermetallics such as Titanium Aluminide (TiAl) [6], [7], [99]–[103] and Niobium Silicides (Nb-Si) [104]–[106], Mg alloys [107] and refractory metals, such as Tungsten.

2.2.2   Electron Beam Melting (EBM)

In the EBM machine patented by the Swedish company Arcam, melting and consolidation of the layers is performed using the energy of an electron beam. The entire process takes place in a high vacuum chamber. The operational principles of EBM (Figure 2-21) are similar to a Scanning Electron Microscope. Electrons are emitted from a tungsten filament, accelerated through an anode to hit and melt the powder by the transformation of their kinetic energy into heat. Magnetic lenses are used to focus and control the movement of the beam. More details on Arcam EBM operation and principles are given in Section 3.4.1. [6]

EBM has been successfully used for medical, aerospace and automotive commercial applications, mostly for Ti-6V-4Al, CoCr and H13 steel alloys. In addition to the previously mentioned AM benefits, EBM benefits includes [6]–[8]`:

i)   The process is being performed under high vacuum, which leads to very low impurity (H, O, N) pick up

ii)   It is considerably faster and more efficient than laser-based techniques

iii)   Elevated build temperatures are possible, allowing thermal stress release

iv)   Fine microstructures are produced, due to the intrinsic rapid solidification conditions of EBM

v)   Good properties are reported; superior to cast and comparable to wrought

A drawback of the EBM process compared with laser based AM techniques is the poor (rough) surface finish, which requires post machining. [6]–[8]

Figure 2-21. a) ARCAM S12 EBM, b) Layout of electron beam gun column

Most work at Sheffield has been done using the Ti-64 alloy, including the fabrication of lattice or weight optimised structures and components, theme optimisation for better properties or faster building times, etc. [108]–[111]. Feasibility studies have also been performed for processing magnesium and nickel alloys, as well as metal matrix composites. In the PhD thesis of Al-Bermani, [112] characterization and numerical modelling of the electron beam has been performed; investigating how beam velocity, current and focus offset affect the geometry and microstructure of the melt pool by scanning single weld tracks on Ti-64 solid blocks. This approach in studying key beam properties by scanning single weld tracks is very common in this group when developing new materials. Similar experimentation has been used by Stapleton, trying to optimise the hatching parameters for manufacturing MMC components [113].

2.2.3   EBM as an Alternative Processing Route for γ- Titanium Aluminide Alloys

γ-TiAl poor formability probably makes AM the only viable route for manufacturing commercial components with acceptable cost and properties. Most of the AM work on this material has been propelled by Avio on the GE48-2-2 alloy and is therefore by EBM. Published data for mechanical properties are very limited, but have been improved drastically by further process optimization and the utilisation of improved alloy chemistries. Table 2-2 summarises in chronological order the published work and available property data on the AM development of γ-TiAl alloys.

Severe cracking is reported for samples fabricated by blown powder and powder bed laser systems [46], [100], [103]. One should bear in mind that these alloys show very limited elongation and thermal gradients should be minimised if not eliminated. As shown below in Figure 2-22-a) for electron beam welding of TiAl, cooling rate is a very significant factor to achieve a crack-free weld. In this diagram, there are two regions where crack frequency is sharply changing. The first one is at about 800°C and the other at about 600 °C. This crack frequency variability is related [114] to the ability of the material to alleviate thermal induced stresses at different microstructures. This is obvious in Figure 2-22-b) where it shows that crack frequency is closely related to the resulting microstructure and in particular to the remaining undecomposed α phase. Crack-free welds are reported [114] at cooling rates lower than 250°C/s, at which resulting final microstructures contain zero percent of α phase. Furthermore, there is a temperature limit for α decomposition at 600 °C. Below this temperature, cracking is observed during welding even at very slow cooling rates.

Table 2-2. Additive manufacturing developement of γ-TiAl alloys

Alloy	YS (MPa)	UTS (MPa)	Elong. %	Year/Method	Authors	Source
Ti-47Al-2Cr-2Nb				2007/EBM	Cormier et al.	[99]
Ti-47Al2.5V-1Cr		600 - 650	0.6	2007/LMD-blown	Qu and Wang et al.	[115]
Ti-47Al-2Cr-2Nb	1400/ρ			2009/EBM	Murr et al	[100]
Ti-48Al-2Cr-2Nb	353	471	0.1	2010/EBM	Sabbaddini et al. (Avio&Arcam)	[6]
Ti-47Al2.5V-1Cr		550-650	0.3 – 0.6	2010/LMD-blown	Qu and Wang et al.	[103]
Ti-48Al-2Cr-2Nb	353	471	0.1	2011/EBM	Biamino et al. (Avio&Arcam)	[7]
Ti-45Al-2Cr-8Nb	553	609	0.1	2011/EBM	Biamino et al. (Avio&Arcam)	[116]
Ti-48Al-2Cr-2Nb		668		2011/MTT SLM	Lober et al.	[26], [46]
Ti-48Al-2Cr-2Nb				2012/EBM	Hernandez and Murr et al.	[102]
Ti-48Al-2Cr-2Nb				2012/EBM	Schwerdtfeg et al.	[117]
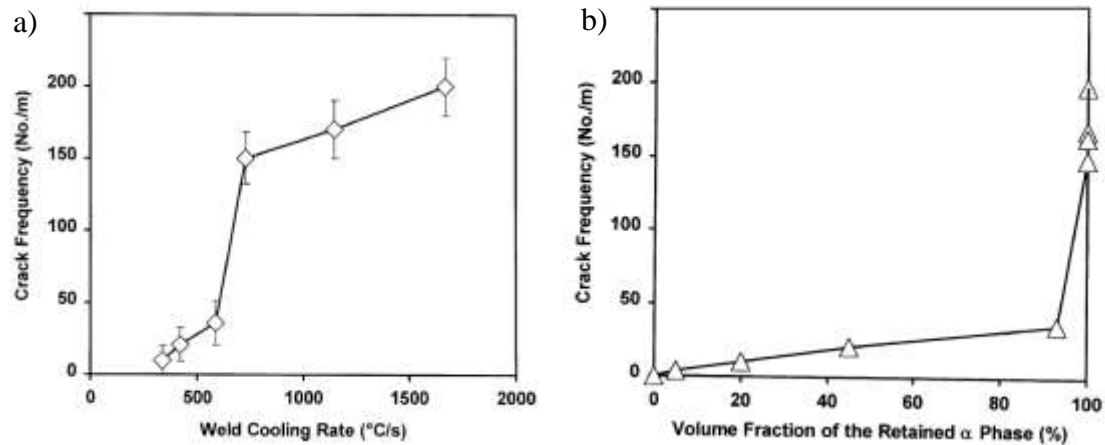
Figure 2-22. Crack frequency vs. a) Weld cooling rate and b) Volume fraction of retained α phase [114]

Guoqing [118] have applied a "composite" electron beam welding technique, which is similar to EBM, in order to optimize resulting microstructures, improve tensile properties and avoid thermal induced cracking. They applied a pre-heating and post-heating treatment by using a

defocused, low energy and high-speed beam to repeatedly scan the surface in order to give a sufficient dwell time and high enough temperature. This increases the decomposition of high temperature α phase to γ phase. A slow cooling rate was used in order to achieve the formation of some lamellar $\alpha_2//\gamma$ structure. The reported resulting microstructure is a fine duplex, with fine γ grains and fine alternating $\alpha_2//\gamma$ lamellar colonies. Tensile properties are reported to improve, following a Hall-Petch relationship similar to what was described previously in Section 2.1.5.

Considering the above we can conclude that EBM seems to be the most promising manufacturing route for fabricating high-end γ-TiAl components for aerospace applications, even compared with similar near net shape AM techniques. The first reported EBM attempt to manufacture γ-TiAl was by Cormier, 2005 [99]. They proved the feasibility of fabricating dense near net shape specimens from pre-alloyed Ti-47Al-2Cr-2Nb, although the final material suffered from high aluminium loss (8 at %) as a result of evaporation. The process parameters were not optimized and they did not have any microstructural control on the final material [99].

The second attempt was by Murr, 2009 [100]. They achieved very dense final material (less than 2% porosity), with a very fine homogeneous duplex microstructure (γ grains~2μm and lamellar spacing~0.6 μm) using the same Ti-47Al-2Cr-2Nb. In contrast to Cormier [99] the aluminium loss was much smaller (1.2 at %). The process parameters were not optimised, as they observed wide melt ridges on the top surface of the samples. Also, they note that they did not have extended z-direction columnar growth, which is the case in most AM processes.

In 2010 collaborative work between AVIO, Italy and Arcam, Sweden was done on the development of γ- TiAl turbine blades fabricated by EBM. The results from the publications are summarised as: The as- built material has a homogeneous very fine near γ- equiaxed microstructure. The process parameters are optimised to have an insignificant Al evaporation loss, even the starting chemistry is somewhat richer in Al. After HIP treatment, the remaining porosity is about 0.2%. A heat treatment is suggested to achieve the desired "optimum", very fine, duplex microstructure with tensile properties comparable to cast and creep comparable to Ni-based superalloys. Oxygen and nitrogen pick up, which are detrimental for properties, are kept very low. All the above results are for the Ti-48Al-2Cr-2Nb (Ti48-2-2 GE alloy) powder feedstock and with a 45-150 μm particle size. [6], [7], [43]

In 2012 Avio performed process development for fabricating high niobium-TiAl alloys, Ti-(45-47)Al-2Cr-8Nb. The reported porosity after HIP treatment is 0.31%, although aluminium

loss remained relatively high at about 3%. As-built microstructure is homogeneous and fine equiaxed. Two different heat treatments were suggested, the first to achieve a coarse fully lamellar microstructure for better creep resistance and the second to give a fine duplex microstructure for optimum fatigue resistance. The high-niobium alloy seems to have better performance for tensile and high temperature oxidation properties (Figure 2-23 and Figure 2-24) compared with the previously mentioned Ti-48-2-2. [116]
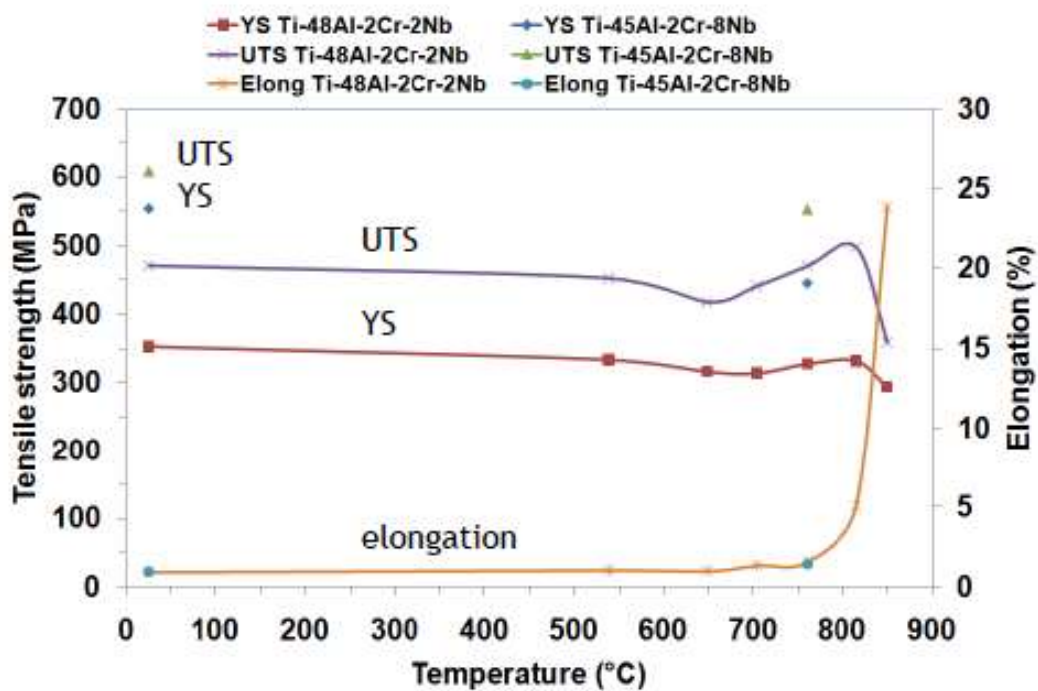
Figure 2-23. Tensile properties comparison of Ti-48Al-2Cr-2Nb (low Nb) and Ti-45-Al-2Cr-8Nb (high Nb) specimens built by EBM and heat-treated to give a fine duplex microstructure [116]
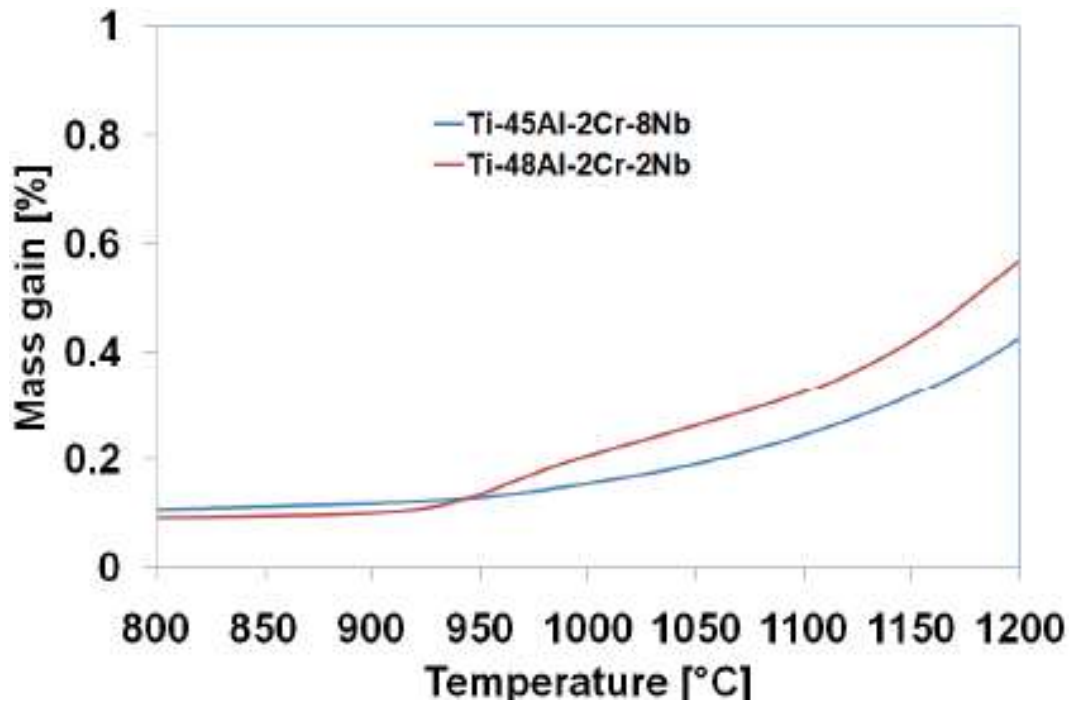
Figure 2-24. Oxidation resistance comparison of Ti-48Al-2Cr-2Nb (low Nb) and Ti-45-Al-2Cr-8Nb (high Nb) specimens built by EBM and heat-treated to give a fine duplex microstructure [116]

2.3 Summary

γ-Titanium Aluminide intermetallics have been extensively investigated for aero-engine and automotive applications, due to their low density and remarkable high temperature properties, as evident in Figure 2-2 and Figure 2-3. However, they exhibit low fracture toughness and room temperature ductility (Figure 2-3-d), which makes processing by conventional routes challenging and costly. TiAl properties are closely related to their intermetallic nature and, also, affected by extrinsic environmental factors. Alloying, processing and post-processing heat-treatments strongly influence the microstructures and mechanical properties of TiAl alloys.

Alloy design development have resulted in several alloy groups through the years. Most of the developed alloys are slightly off- stoichiometric in the Ti-rich area and based on the binary Ti-44-48 at % Al with some extra element additions [18]. Some commonly used alloys and the influence of alloying elements are summarised in Table 2-1. The most balanced properties for the binary alloy, as evident in Figure 2-6, are for an Aluminium content of 48%, in the $\alpha_2 + \gamma$ region.

Duplex microstructure is considered to exhibit the most balanced performance, as evident in Figure 2-13, due to the very fine microstructural features (γ grain size, lamellar grain size and

56

lamellar spacing), following a Hall-Petch strengthening relationship [6], [7], [18], [32]. Where creep resistance and fracture toughness are required, as in high temperature turbine engine parts, fully lamellar microstructure could be more beneficial. It has also been reported [32] that refining the microstructural features of fully lamellar (lamellar grain size and spacing) components could lead to improved elongation and high temperatures strength.

Conventional manufacturing techniques (wrought, cast, powder metallurgy) are well established and the manipulation of microstructure via processing or heat treatment is well documented. Although, TiAl parts with required properties for critical applications, in desired geometry and at acceptable costs is very challenging using any of those manufacturing routes.

AM has been available for several decades and various metals and alloys have been investigated. Due to high material costs, titanium alloys have been the most studied on many near-net shape technologies. The research has been mainly done using powder bed (electron or laser beam) technologies and properties are typically found to be superior to cast and comparable to wrought, which is remarkable for a structure containing defects. [8], [92]

EBM has been successfully used for medical, aerospace and automotive commercial applications, mostly for Ti-6V-4Al, CoCr and H13 steel alloys. Core benefits and disadvantages of EBM processing have been summarised in this work.

γ-TiAl poor formability probably makes AM the only viable route for manufacturing commercial components at acceptable cost and with required properties. Most of the AM work on this material has been propelled by Avio on 48-2-2 alloy and is therefore EBM. Published data for mechanical properties are very limited, but have been improving drastically by process optimization and the utilisation of improved alloys. Table 2-2 summarises in chronological order published work and available properties data on the AM development of γ-TiAl alloys.

Severe cracking is reported for samples fabricated by both blown powder and powder bed laser systems [46], [100], [103] and this is related to thermal induced stresses generated during those processes; as they do not operate at elevated temperatures as in EBM. Cooling rate is a very significant factor to achieve a crack-free weld. Crack-free welds are reported [114] at cooling rates lower than $250\,^{\circ}\mathrm{C/s}$ and at temperatures over $600\,^{\circ}\mathrm{C}$. Below this temperature, cracking is observed during welding even at very slow cooling rates. Taking in account the above we can conclude that EBM seems to be the most promising manufacturing route for fabricating high-end γ-TiAl components for aerospace applications, even in comparison with other similar near-net shape AM techniques.

Some work on high-niobium TiAl (Ti-45Al-2Cr-8Nb) alloy processed by EBM [116] shows (Figure 2-23 and Figure 2-24) improved performance for tensile and high temperature oxidation properties. For our work, a 3rd generation, high niobium TiAl alloy (TNB-TiAl) was developed and this is the 1st AM study in the literature for this alloy. Due to their improved properties (comparable to Ni-based superalloys), TNB alloys are considered as the best choice for extending high-temperature capabilities to even hotter parts of the turbine engine [11], [18], [39], [40], [45], [59].

The methodology followed for the EBM process development for the other TiAl studies is not documented and there is no indication for any focussed effort to perform computational analysis on statistically designed (DOE approach) experiments to relate key process variables (inputs) to component/material properties (outputs) and generate statistical and/or empirical predictive models, as it is aimed for this work. There is no information on key process variables identification either. In some studies [1], [112], but not reported for TiAl process development, numerical heat source modelling, to characterise and simulate the melt pool, has also been proven beneficial for deeper understanding of the effect of process parameters and thermal properties (material specific).

Finally, excess Aluminium evaporation has been identified [6], [7], [43], [99], [100], [116] as an issue during EBM processing of TiAl alloys and Aluminium content is known   [27], [38], [39] to be one of the most important alloying factors affecting microstructures and mechanical properties. Process development is reported [28], [47], [117], [137], [140] to take this in account, but the main solution reported in the literature [28], [47] is to start from powder feedstock with higher Aluminium to compensate the evaporation losses. There is no in-depth investigation of the evaporation phenomena during EBM and the analysis and optimisation is typically based on trying to relate Aluminium loss to energy density [46]; something that has been proven inefficient.

3 METHODOLOGY AND EXPERIMENTAL PROCEDURES

3.1 Introduction

This Chapter explains the methodology and experimental techniques and procedures which were used to accomplish the objectives of this study. Section 3.2.1 emphasises the challenges and methodology for optimising the Arcam EBM process for novel alloys and in particular for the high temperature γ-TiAl alloys. A DOE approach, used throughout this study, is described in Section 3.3. In Section 3.4 some more detailed information about the manufacturing and post-manufacturing processes are described. In Section 3.5 characterisation and the corresponding sample preparation techniques are described. Finally, the MATLAB code developed and the assumptions made for the heat source modelling are explained in Section 3.6.

The manufacturing, sample preparation and analysing of the samples was mainly performed at Mercury Centre, Department of Materials Science and Engineering, The University of Sheffield, UK. An important part of the manufacturing, sample preparation and initial characterisation for the EBM deposited solid samples were performed at the Edward P. Fitts Department of Industrial and Systems Engineering, North Carolina State University, NC, USA during a 45-day period, within an academic collaboration between the above-mentioned institutes. For some of the sample preparation, characterisation and post-manufacturing processes, where required, Mercury Centre subcontracted external industrial and/or academic labs.

3.2 EBM Process Development for Novel Alloys

3.2.1 Challenges

There are numerous process parameters relating to the operation of the Arcam EBM equipment. Arcam provides the end users with the basic operation training (Level 1), standard equipment configuration and process themes for standard materials already developed by Arcam, such as Ti-6Al-4V, CP-Ti and CoCr. Process development for novel alloys require the highest level of training (Level 3) and a greater level of experience with the equipment. Arcam suggests/requires a minimum of 6 months of operation experience after each Level training and

before getting the next one. Approximately 1.5 -2.0 years are needed to get the required Level 3 Certification training for developing the EBM process for novel alloys.

Titanium Aluminide and high temperature alloys, in general, require extremely high build temperatures (>1000 $^{\circ}$C) to be maintained throughout the process [6], [7], [43] and this makes manufacturing very challenging with the standard configuration of the S12 Arcam equipment, which was used for this study. EBM process development for novel alloys is not straightforward. A series of process theme development steps and hardware modifications are required just to achieve a stable process, before the actual process development/optimisation for achieving optimised material and component properties.

The difficulty in retaining a stable process is primarily related to the electron beam nature of the process and the electrical overcharging of the powder bed, which may cause an effect that in Arcam's terminology is defined as a "smoke". The "smoke" effect can be better described as a powder cloud, which occurs due to electrical overcharging of the powder bed and the subsequent powder particles repulsion; this happens due to a combination of insufficient electrical conductivity of the powder bed and inadequate bonding of the powder particles. Conductivity of the powder bed depends on material properties (e.g. material's thermal/electrical conductivity, presence of oxides, etc.), powder characteristics (e.g. packing/apparent density, connectivity of powder particles), build temperature (e.g. dissolving surface oxides, increase of particles connectivity, temperature dependant physical/thermal properties) and effective electrical grounding (i.e. copper wiring) of the powder bed. The "smoke" effect can be eliminated by reducing overcharging and/or increasing sintering. [120]

Typically, two major process steps should be optimised for a stable, "smoke-free", EBM process:

i.   The heating of the starting plate and powder bed to an appropriate, elevated temperature (i.e. build temperature) and

ii. The preheating of each layer of the powder bed (prior to the actual melting step), to slightly pre-sinter the powder particles (i.e. give sufficient bonding, but at the same time the powder should be recoverable) and to maintain the build temperature.

Appropriate build temperature and preheating (degree of pre-sintering) will vary for alloys with different material properties and powder characteristics. For example, a highly conductive material (e.g. copper), with a high packing density and which does not form un-conductive oxides could be processed even without preheating (pre-sintering) at ambient build

temperatures. But usually, this is not the case for Ti and Al containing alloys. Furthermore, high temperature materials (e.g. γ-TiAl intermetallics) will require a higher build temperature and heat input for effective, sufficient sintering. Controlled, elevated and stable temperature throughout the process could, additionally, be beneficial for increased flowability in the weld, dissolving of surface oxides, having a homogeneous microstructure, no heat affected zone, thermal stresses relief, reducing thermal gradients and avoiding unwanted phase transformations. [120]

The degree of sintering influences the subsequent melting steps, as it affects the thermal conductivity of the powder bed. Usually, a more sintered powder bed results in a "smoother" subsequent melting step, but on the other hand an over- sintered powder bed is not ideal, as recycling becomes more difficult and powder quality degrades much faster in terms of shape and even chemistry. Typically, during the EBM process there are more than one (usually two) preheating steps: i) one (softer, process safe) for scanning/sintering the whole surface area of the powder bed (i.e. Preheating 1) and ii) one (harder, melting safe) for scanning/sintering only over the melting area and its closely surrounding surface (Preheating 2). [120]

The third key EBM process step is the actual melting and it is divided in "contours" and "hatching". Contours is the melting of the perimeter of the sliced, 2D component layer in a "multi-beam" scanning mode following a randomised algorithm. Typically, 2 or 3 outer contours are melted. Hatching is the single-beam, snake-type (see Figure 3-9) scanning mode of the internal (within the confines of the contours) of the sliced, 2D component layer. Contours are used for increased resolution and better surface finish and hatching for the bulk melting. Hatching melting is further optimised by applying more sophisticated functions such as for turning and overhanging points (thickness function), applicable for more complex geometries. [120]

Development for each of the 3 key EBM process steps (themes) described in the previous paragraphs includes the optimisation of numerous process parameters, including EB current, velocity, focus offset, line offset, line order, surface temperature, speed function, etc. For each process step the collection of all the relevant, necessary process settings is called a process theme (i.e. heating theme, preheating theme, melting hatching theme and so on). Furthermore other process settings, such as for powder feeding (e.g. powder hopper slot opening, powder raking speed and times of raking, etc.) and other equipment and configuration modifications (e.g. extra thermal insulating of the build chamber, heat resistance thermocouples and

grounding cables, smaller starting plates and extra external cooling of the equipment, etc.) are required when developing a novel alloy, especially when an extremely high building temperature is essential as for γ-TiAl (>1000 ºC). Finally, changing between different materials is a laborious and long-lasting procedure and a strict protocol of thorough cleaning should be followed to eliminate cross-contamination. EBM configuration, process themes and process themes development theory are explained in more detail in Section 3.4.1.

It is obvious that standard EBM development is mainly experimental. AM processes and EBM itself are relatively new and immature techniques compared with the well-established casting and/or forging. There are limited published data in the literature in general and almost none about how to develop novel alloys. There are no prediction models for process parameters or systematic manual for developing new materials. Process development requires experience and research is mainly driven by industry. However, in the literature [121]–[131] there are a some studies and data regarding heat source melting/welding experimental work and modelling, such as for electron beam welding, laser beam welding, etc.

Finally, melting in layers leads to complicated thermal histories. Each individual layer is fully melted and re-melted about 2-3 times and is heat affected during the melting and preheating of the following layers. Heat losses change during the process. In the beginning, they are mainly through radiation from the top surface. As height increases, heat loss through conduction from the surrounding surfaces of the powder bed and start plate is increasing. All this complexity of melting in layers and in conjunction to the numerous process parameters related makes it difficult to directly relate process parameters to outcome material properties and generate process maps. [120], [130]

3.2.2 Methodology

A summary of the process development route followed for this study to develop novel alloys with the Arcam EBM equipment is shown in Figure 3-1.

AM "novel" alloys for aerospace components; EBM process development and material properties

Powder feedstock

Preliminary tests, E_{beam} parametrical studies and process maps

EBM process development and material/process themes optimisation

Post-processing, material properties and further process development

Aerospace components with required properties

- Casting of feedstock with bespoke chemistry and required quality
- Gas-atomisation (powder production method) for required powder characteristics and quality
- Powder specifications
- Sizing to required fraction

- Powder Characterisation
- Define T_{build}
- Define degree-of-sintering
- DOF/Parametrical (key EBM process parameters) studies for
  - Melting response
  - Material properties (e.g. Al loss, micro-hardness, microstructures, etc.)
- Statistical Analysis (prediction) Models
- Analytical prediction Models
- Process maps

- Preheating/Heating process themes development
  - Define Tbuild
  - Define degree-of-sintering
  - Define a "stable" process
- Melting Process themes development and optimisation
  - Surface finish
  - Component density/ Process defects
  - Material properties (e.g. Al loss, microstructures, micro-hardness, etc.)

- HIPing study
- ~~Heat Treatments study~~
- Post-Machining
- Tensile Properties data
- ~~Fatigue properties data~~
- ~~Oxidation data~~
- Identify and resolve main EBM process and material properties issues i.e.
  - Al losses effect on mechanical properties
  - **Al evaporation study** (EBM process themes, vacuum pressure, material physical properties)

Figure 3-1. Chart showing a summary of the EBM process development steps for novel alloys followed for this study. The crossed-out steps weren't performed for this study, but they are suggested for a more complete study

3.2.2.1 Powder Feedstock

Powder feedstock for AM and EBM in specifically should meet some quality standards associated with health and safety [132], the nature of the EBM process and the quality of the final deposited component. Powder is required to be free flowing, which means that the powder should be spherical, with a low amount of satellites and high apparent/packing density (>50%). The typical EBM size fraction for Arcam powders is 44-106 μm for a layer thickness of about 50-70 μm. For this study, a 45-150 μm fraction was decided to be used for increased powder utilisation. Chemistry and purity of the powder is important for the process itself, as well as for the final component quality. Low surface contamination (oxides, nitrides, etc.) improves sintering and melting, increases the conductivity of the powder bed and improves the quality of the final component. O and N are especially known [32] to be detrimental for the ductility of γ-TiAl alloys. [120]

For this study, a gas-atomisation technique and specifically the (EIGA) electrode induction melting gas atomisation method was used to produce pre-alloyed powder with the required characteristics and quality. Atomisation was performed by TLS – Technik GmbH (Germany). The EIGA method is beneficial for high purity as it is a non-contact, crucible-free melting method [38]. The required feedstock for EIGA powder production is solid metal bars. 50 kg of required quality (homogenous, high purity and low oxygen content) and required, bespoke chemistry (Ti-45Al-8Nb-0.2C at %) cast ingots were produced by GfE Metalle und Materialien GmbH (Germany). The as-atomised powder was supplied by the manufacturer (TLS) with specifications for chemistry and powder size distribution (PSD) and with the appropriate material safety data sheet (SDS).

The powder was approved by Arcam for its suitability and safety for using with the equipment. As-received powder was sieved to separate a specific size fraction (45-150 μm) for EBM. The powder used for the preliminary tests (available to the group from a previous project) was from a different batch (Ti-45Al-8Nb at %) and it was purchased from GKSS Forscungszentrum (Germany). The original particle size of this batch was 0-355 μm and it was sieved down to 63-150 μm. No powder specifications were available for this material.

3.2.2.2 Preliminary Tests, Parametrical Studies and Process Maps (Stage 1)

The objective of the 1st process development stage was to perform some targeted, well designed preliminary tests in order to investigate the effect of build temperature and degree ("hardness") of sintering, the melting response (i.e. melting pool geometry, surface finish and evaporation)

and the mechanical/material properties (i.e. micro-hardness, process defects/porosity and microstructures) without the necessity to fully develop/optimise all the process parameters and without extensive hardware modifications and overcoming the complexity of analysing 3D melted components. The idea was to generate and analyse data from this study, as well as to use data obtained within the same academic group and from the literature for different materials processed by electron beam or similar heat sources (i.e. laser beam melting/welding, electron beam welding, etc.), in order to generate process maps and predictive models, which will allow to predict the suitable starting process parameters for novel alloys process development.

The sized powder feedstock was characterised to verify its suitability for EBM processing, as well as to define the material properties baseline before the subsequent manufacturing and post-manufacturing process stages of this study. Characterisation was performed to measurer the:

- Morphology (shape and satellites) by optical microscopy
- Flow rate and Apparent density by using a Hall flowmeter
- Porosity by optical and SEM imaging of powder particle cross-section
- Microstructure by SEM imaging of powder particles cross-section
- Powder size distribution (PSD) by laser diffraction
- True density by Helium measurement, and
- Chemical content by EDX-SEM, ICP and XRF

Single weld tracks were scanned at 3 build temperatures (800-900 °C) on pre-sintered blocks of variable density. Different density for the substrate material would lead to different thermal (i.e. thermal conductivity) properties and the different build temperature would lead to different thermal and physical properties. So, melting on variable density blocks and at different T_{build} will lead to variable melting behaviour (i.e. melt pool geometry, surface finish), density/porosity, cooling rates, microstructure, chemistry and material properties (i.e. micro-hardness). The pre-sintered blocks of variable density were produced by using a Spark Plasma Sintering (SPS) technique and altering the dwell temperature (800-1200 °C). The use of pre-sintered solid blocks (not loose powder) allowed us to introduce a new, "unknown" material in the Arcam EBM equipment overcoming some of the challenges explained in Section 3.2.1. Some of the main benefits of using a solid (pre-sintered) block are:

- Minimum amount of powder is required
- Limited cross contamination risks
- No equipment modifications
- Heating to elevated temperature is only for a short time

- No need for fully trained operator

- Limited concern for health and safety issues related with using metallic powders

- No need to fully understand and/or optimise all the numerous EBM process parameters, but only the chosen ones

SPSed sample characterisation was performed to study the:

- Densification versus dwell temperature by Helium measurement, Archimedes method and Image Analysis

- Microstructural evolution versus dwell temperature by BS-SEM imaging of cross-sectioned SPS samples, and

- Chemical content for contamination (i.e. carbon, oxygen) and other chemistry variations (e.g. Al loss) by EDX-SEM of cross-sectioned SPS samples

Weld track characterisation was performed to study:

- Any cracking, due to thermal stresses by optical microscopy of top surface and cross-sections

- Weld pool geometry (width and depth) by optical microscopy of top surface and cross-section

- Chemical content by SEM-EDX of the cross-section

- Vickers micro-hardness measurements of the cross-section

A response surface method (RSM) design of experiments (DOE) approach under the form of an Optimal Design was implemented to generate the experimental plan for the single weld tracks altering 3 key process parameters/inputs (I_b, v_b and focus offset), to analyse the results (outputs) for weld pool geometry, Al loss, micro-hardness and process defects and finally to generate process maps and statistical analysis models. More details about the DOE approach, specific method and commercial software used are explained in Section 3.3.

3.2.2.3   EBM Process Development and Material/Process Themes Optimisation (Stage 2)

The 2nd stage includes the standard EBM process development and the objective was to develop a stable and optimised (for material and component properties) process. Achieving a stable process was performed by optimising the heating and preheating process themes and the methodology followed to do this is outlined in the appendices.

After a stable process and optimised heating and pre-heating were accomplished, then optimisation of the melting themes (i.e. hatching for this study) was performed. A response

surface method (RSM) design of experiments (DOE) approach under the form of Central Composite Design (CCD) was implemented to generate the experimental plan, analyse the results (outputs) and finally to generate process maps and statistical analysis models. More details about the DOE approach, specific method and commercial software used are explained in Section 3.3. The main parameters (inputs) identified for this optimisation step were **surface temperature**, **speed function**, **focus offset** and **line offset**. The outputs for the analysis and optimisation were: **top surface** quality, minimum **process defects/porosity** (maximum component density) and **Al loss**. Short cylindrical solid blocks were manufactured during this process step and characterised for:

- Top surface quality by visual observation
- Process defects and remaining porosity by optical and BS-SEM imaging of cross-sectioned and polished plane
- Chemical content by EDX-SEM of cross-sectioned polished plane
- Microstructures by BS-SEM imaging of cross-sectioned polished plane, and
- Vickers micro-hardness of cross-sectioned polished plane

3.2.2.4   Post-processing, Material Properties and Further Process Development (Stage 3)

Typically, aerospace components require post-processing for further optimising the as-manufactured components. HIP [43], [78] is typical to eliminate any remaining gas-porosity and/or process related defects large enough to lead to structural failure. Post-machining, for the same reason, is important to eliminate any surface defects, especially for the quite rough surface finish of EBM built components. Finally, customised heat treatments for EBM built components of bespoke chemistry [57], [133] are required to achieve homogenous microstructures. A validation of final component suitability requires a full data base for tensile, fatigue and oxidation properties in the as-built, machined, HIPed and heat-treated condition at different service (room, intermediate and elevated) temperatures. The suggested steps, for this 3rd process development stage, are shown in more details in the appendices.

For this study:

- 1 orientation (Figure 3-2) of tensile specimens was built in two batches of 5 labelled bars (100x15x15 mm) each. Also, a build of 5 standard fatigue (LCF) specimens (Figure 3-3) was attempted, but it failed as there wasn't enough powder to complete the full height. Those semi-finished LCF specimens were used to extract some extra non-

standard tensile specimens, as well as for material characterisation (e.g. microstructures, porosity, etc.).

- A study to optimise the HIP process conditions (time, pressure, temperature and inert atmosphere) was performed and selected specimens were HIPed using those "optimum" process conditions.

- All tensile specimens were machined at standard size and shape prior mechanical testing, and then tested at as-built and as-HIPed conditions at room and elevated temperatures.

- Finally, Aluminium evaporation was identified as one of the most critical issues during the process development. For this reason, an Al evaporation study was performed to better understand the evaporation losses phenomena during vacuum-EBM processing and to find ways to mitigate or even supress this issue.
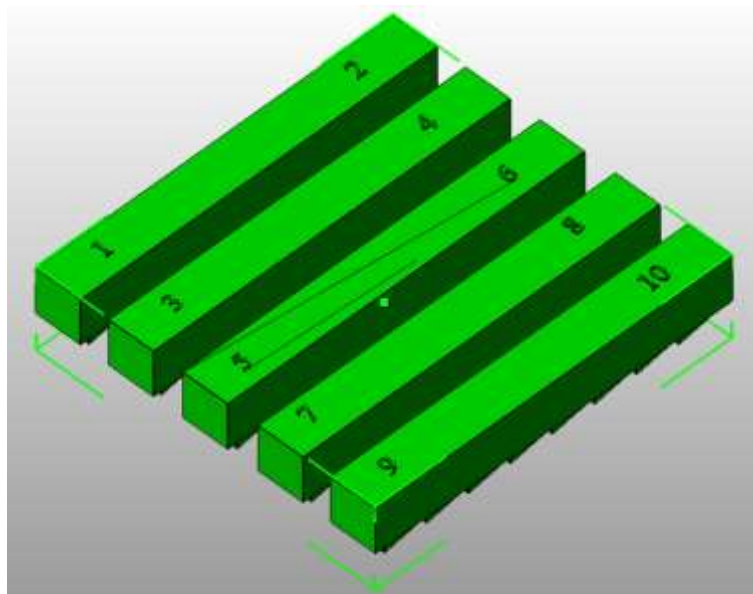
Figure 3-2. stl file used for tensile specimens built by EBM with "optimised" themes
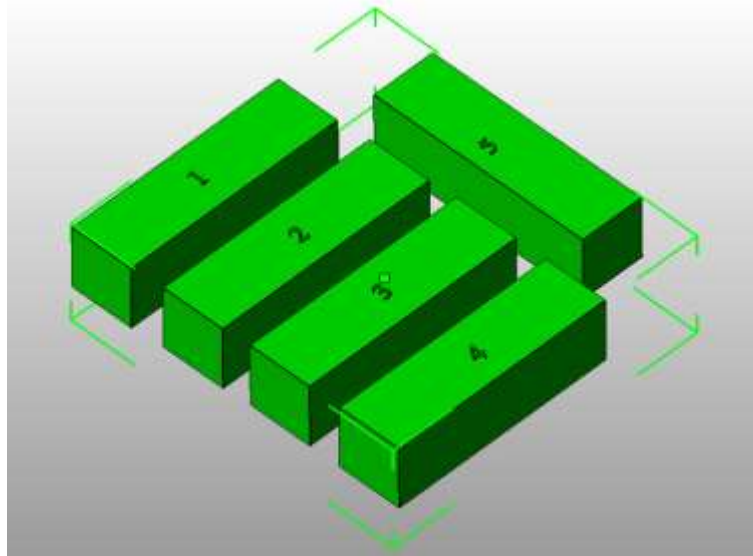
Figure 3-3. stl file used for Low cycle fatigue (LCF) specimens built by EBM with "optimised" themes

3.3 Design of Experiments (DOE)

Design-Expert (version 8.0.7.1) by Stat-Ease (*Stat-Ease Inc. Minneapolis, US*), which is a commercial statistical Design of Experiments (DOE) software, was used to establish the minimum design points that should be tested to have an adequate response surface method (RSM) design [134] under the form of an Optimal Design for the single weld tracks and under the form of Central Composite Design (CCD) for the cylindrical, solid deposited blocks. The same software is also used for the analysis of variance (ANOVA) and the generation of mathematical, prediction models, as well as the graphical representation of the results. A similar RSM - DOE approach under the form of Central Composite Design (CCD) was used in Deffley's PhD thesis [1] investigating the effect of key process variables for two types of commercially available AM systems (powder-bed EOS M270 and blown-powder Trumpf DMD505 on nickel-iron superalloy Inconel 718 and is common to the research group.

RSM is a collection of mathematical and statistical methods used to generate empirical models. The objective is to optimise a response (output variable), which is influenced by several independent variables (input variables) by implementing a well-designed experimental plan. The experimental plan is constituted by a series of tests, aka runs, in which changes are made in the input variables in order to identify the reasons for changes in the output response. [135]

Optimal designs are used to establish the ideal process parameter (optimal up to 5 parameters) window to achieve optimal performance and generated from a random starting point. This makes them more flexible and allow to include additional constraints, be designed for custom

models including block effects, and afford more control to the number of runs in the design. Although, there are compromises for this flexibility. Firstly, the generated design is not consistent and likely to vary if rebuilt even if using the same parameters and the same number of runs. Optimal designs are also slightly less efficient than Box-Behnken and Central Composite designs where those designs could have been used. [136], [137].

For the single weld tracks, 3 numerical continuous factors were used for the experimental plan, including EB **current** (mA), **velocity** (mm/sec) and **focus offset** (mA). The lowest and highest value for each input factor was defined by the user. The **response factors** are **melt track depth** and **width** and **Aluminium loss**. Additionally, the software requires the user to define an anticipated polynomial relationship between response variables and the inputs (factors). For this case, a quadratic polynomial including all the main interaction terms was chosen, as shown in Equation 3.1.

Response = $\beta 0 + \beta 1 * X1 + \beta 2 * X2 + \beta 3 * X3 + \beta 4 * (X1)^2 + \beta 5 * (X2)^2 + \beta 6 * (X3)^2 + \beta 7 * X1 * X2 + \beta 8 * X1 * X3 + \beta 9 * X2 * X3 + \varepsilon$ (Eq. 3.1)

Where X1: EB current, X2: EB velocity, X3: EB focus offset

Using the default settings of the software for a quadratic relationship and 3 input factors the suggested experimental plan was as below:

- 20 experimental points in total, consisting of
  - 10 "Model" points (equals the number of correlation coefficients),
  - 5 "lack-of-fit" points, and
  - 5 "replicate" points (highest leverage points replicated).

Those 20 experimental runs were planned in two different blocks due to experimental convenience reasons (see later in EBM experimental procedure). The selection of the points was done by the software using a default algorithm, which gives the minimum average prediction variance across the region of experimentation. The suggested experimental plan is shown in Table 3-1. The extra 21st experimental point was extracted from the process themes developed by Arcam for the Ti48-2-2 GE alloy and it was kindly provided to us [138]. The experimental plan was repeated for all 3 build temperatures (T_{build}) at 800, 900 and 1000 ^{o}C.

Table 3-1. DOE experimental plan used for single weld tracks

			Coded values			Actual values		
			Factor 1	Factor 2	Factor 3	Factor 1	Factor 2	Factor 3
Std	Run	Block	A:Beam current	B:Beam velocity	C:Focus offset	A:Beam current	B:Beam velocity	C:Focus offset
			mAmper	mm/sec	mAmper	mAmper	mm/sec	mAmper
9	1	1	-0.470	-1.000	-0.100	13.240	500.000	9.000
2	2	1	-1.000	1.000	-1.000	9.000	2000.000	0.000
8	3	1	1.000	-1.000	-0.270	25.000	500.000	7.300
13	4	1	0.100	0.960	0.100	17.800	1970.000	11.000
17	5	1	-1.000	-0.400	1.000	9.000	950.000	20.000
7	6	1	1.000	-1.000	-0.270	25.000	500.000	7.300
19	7	1	-0.100	0.400	1.000	16.200	1550.000	20.000
6	8	1	0.100	-0.100	-0.960	17.800	1175.000	0.400
10	9	1	1.000	0.380	-0.100	25.000	1535.000	9.000
4	10	1	0.100	-0.100	-0.960	17.800	1175.000	0.400
11	11	1	-0.970	-0.100	0.100	9.240	1175.000	11.000
21	12	2	-1.000	1.000	1.000	9.000	2000.000	20.000
14	13	2	0.100	0.960	0.100	17.800	1970.000	11.000
18	14	2	1.000	0.250	1.000	25.000	1437.500	20.000
1	15	2	-1.000	-1.000	-1.000	9.000	500.000	0.000
5	16	2	0.100	-0.100	-0.960	17.800	1175.000	0.400
3	17	2	1.000	1.000	-1.000	25.000	2000.000	0.000
15	18	2	0.280	-0.333	0.300	19.240	1000.264	13.000
12	19	2	-0.970	-0.100	0.100	9.240	1175.000	11.000
16	20	2	-0.250	-1.000	1.000	15.000	500.000	20.000
20	21	1	0.000	0.467	-0.600	17.000	1600.000	4.000

For the solid blocks, a two-factor (Figure 3-4) Box-Wilson Central Composite Design (CCD) was used. Central Composite designs (CCD) are based on 2-level factorial designs; centre and axial points are added to fit quadratic models. Usually, CCD's have 5 levels for each factor, but this can be modified by altering the axial distance (α) to be equal 1.0. In this way a Face-Centred, Central Composite design is generated which has only 3 levels per factor. Typically some centre points are replicated to increase the prediction capability near the centre of the factor space. [135]–[137]

For a 2 factor CCD (Figure 3-4) a minimum of 9 individual runs are required, consisting of:

- 1 centre (0,0) point,

- 4 factorial points at the corners of the square with coded values of 1 and -1, and

- 4 axial points with distance α from the centre. Distance α is user defined and as earlier described it can be larger, smaller, or equal to 1. When it is equal to 1 a face-centred design is generated

In the coded form, all actual values are normalised to be from -1 to 1; -1 being the minimum value and 1 the maximum value of the experimental range. Minimum and maximum actual values are user defined. The 0 and α actual values are calculated and suggested by the software based on the minimum and maximum. The α coded distance, as previously mentioned, is also user defined.

This data normalisation, aka data coding, is a common method used during data post processing to standardise the range of independent variables or features of data. Since the range of values of raw data could significantly vary between different variables, objective functions will not work properly without normalisation. If one of the variables has a broader range of values, the model will be more influenced by this particular variable. Therefore, the range of all variables should be normalized so that each variable contributes approximately proportionately to the regression analysis. [137]
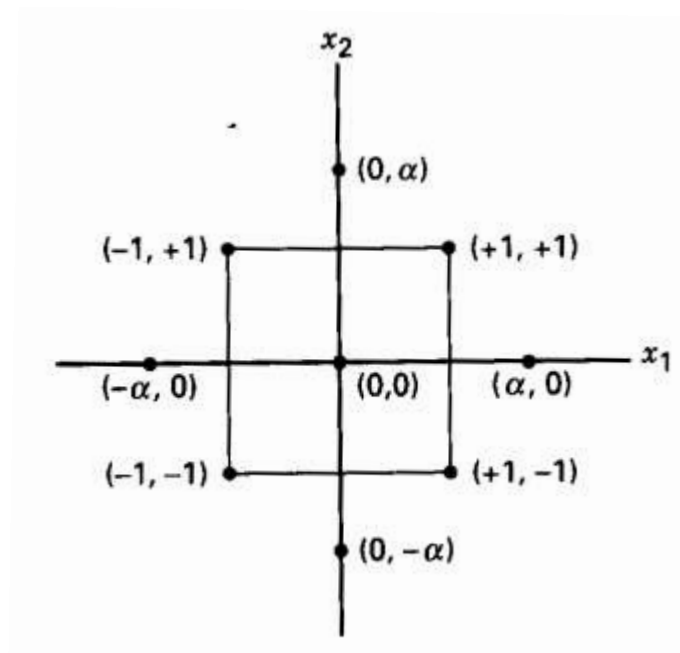
Figure 3-4. 2 factors CCD illustration [1]

Table 3-2 and Table 3-3 show the 2 main DOE experimental plans (actual and coded values) performed to build the cylindrical solid blocks for the EBM process development. For DOE 2 the minimum and maximum user defined values were 4 and 16 and 20 and 44, for focus offset and speed function, respectively. The α value in this case was defined to be equal 1, resulting in a face centred design as previously described. For DOE 3 the minimum and maximum user defined values were 6 and 14 and 32 and 56, for focus offset and speed function, respectively. The α value in this case was defined to be equal 1.5.

Table 3-2. DOE (DOE-2) experimental plan used for depositing EBM solid cylindrical blocks, α was chosen to be equal to 1.

			Coded values		**Actual values**	
			Factor 1	**Factor 2**	Factor 1	Factor 2
Std	Run	Space Type	A: Focus offset (mA)	B: Speed Function	A: Focus offset (mA)	B: Speed Function
9	1	Center	0	0	10.00	32.00
6	2	Axial	α	0	16.00	32.00
8	3	Axial	0	α	10.00	44.00
5	6	Axial	-α	0	4.00	32.00
7	8	Axial	0	-α	10.00	20.00
2	4	Factorial	1	-1	16.00	20.00
4	5	Factorial	1	1	16.00	44.00
3	7	Factorial	-1	1	4.00	44.00
1	9	Factorial	-1	-1	4.00	20.00

Table 3-3. DOE (DOE-3) experimental plan used for depositing EBM solid cylindrical blocks

Std	Run	Space Type	Coded values Factor 1 A: Focus offset (mA)	Actual values Factor 2 B: Speed Function	Coded values Factor 1 A: Focus offset (mA)	Actual values Factor 2 B: Speed Function
5	1	Axial	-α	0	4.00	44.00
3	2	Factorial	-1	1	6.00	56.00
1	3	Factorial	-1	-1	6.00	32.00
8	4	Axial	0	α	10.00	60.00
2	5	Factorial	1	-1	14.00	32.00
4	6	Factorial	1	1	14.00	56.00
7	7	Axial	0	-α	10.00	28.00
6	8	Axial	α	0	16.00	44.00
9	9	Center	0	0	10.00	44.00

3.4 Manufacturing and Post Manufacturing Processes

3.4.1 Electron Beam melting (EBM)

Arcam S12 (Figure 3-5) was the main equipment used for this study, both at the University of Sheffield and at NCSU, USA. The process themes were developed at NCSU and all the bulk samples were produced there. All the single weld tracks and Aluminium loss study were performed using the S12 system at the University of Sheffield. In principle, the two systems are identical and there should be a very good transferability of process parameters between them.

Figure 3-5 shows an image of the equipment at the University of Sheffield. An industrial control computer with an LCD touchscreen and a keyboard, as well as all the electronic switches, circuits and controls of the system are at the top, left-hand side compartment of the equipment. A high voltage (HV) unit is at the bottom, left-hand side compartment. The electron beam gun is at the top, right-hand side and just below is the build chamber. Both the electron beam gun and build chamber are under high vacuum during operation. A series of rough pumps,

turbo pumps and various valves and gauges are placed behind the gun and chamber area to vacuum down as required.

Figure 3-5. Arcam S12 EBM equipment at the University of Sheffield used for this study

The basic layout of the electron beam gun and the build chamber are shown below in Figure 3-6. Electrical current passes through a tungsten filament, which is placed in a grid cup, in order to heat it up to a high temperature (over 2000 ℃). At those temperatures electrons are emitted from the tungsten filament and then accelerated through the gun by applying a high electric potential tension (high voltage) between the grid cup (cathode) and the anode. The voltage of the EBM system is 60 kV. The accelerated electrons pass through a series of lenses (electromagnetic coils), before they hit and melt the surface of the powder bed, in order to focus and drive the electron beam as required by the CAD model and the process parameters. The melting of the powder takes place when the high kinetic energy of the electrons is transformed into thermal energy as they slow down and penetrate the surface of the powder bed. [6], [120]
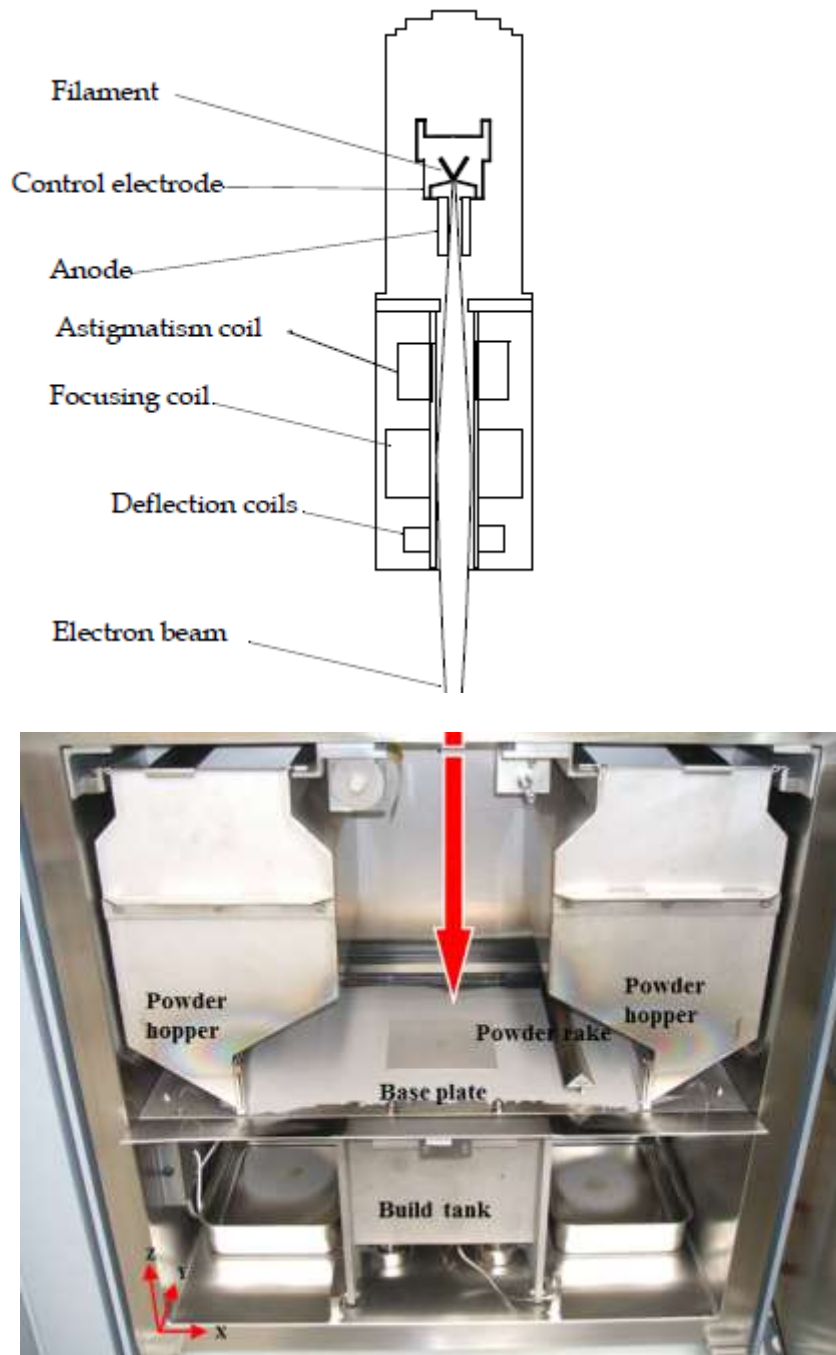
Figure 3-6. Electron beam gun sketch and build chamber envelope [120]

For any AM processes [6], [120], the components are designed by using an appropriate 3D-CAD software and usually in an STL format and further processed by using other software(s) (typically Materialise Magics) to:

- Fix any numerical errors (e.g. flipped triangles, planar holes, bad edges, etc.)
- Place and orientate the components,

- Scale for shrinkage, and

- Generate supports for any overhanging surfaces. - Supports are essential to facilitate effective heat conduction (powder is not as heat conductive as solid), but should be easily removable from the main object.

Then using Arcam special software (EBM build assembler) the component(s) are sliced in 2D layers of user defined thickness and saved in an abf (Arcam sliced mode) format. Finally, the abf file is uploaded into the EBM control software at the pc of the EBM equipment. EBM control software controls all the functions for:

- setting up the process,

- simulating the build,

- controlling the hardware,

- running the build

- and logging machine and process parameters.

The Arcam S12 EBM process set up and operating sequence in more details is outlined in the apprentices. Below a quick definition/explanation [120] of some of the identified key process parameters for heating, preheating and hatching themes is presented. Those parameters and themes were the ones used in this study for the process development for Titanium Aluminide alloys and are referred to throughout this thesis.

- Beam current is the number of electrons in the beam and it is controlled by the control electrode. Typically, current is not constant during the process, but it fluctuates between a given range defined by the user. The current at a specific moment is a function of several factors.

  o For heating and preheating themes, the user can insert a value (mA) for minimum, maximum and average current. When a specific theme starts (e.g. preheating) the beam always starts with the minimum current value and gradually increases (ramps up) to reach the maximum one. The speed of this increase as well as the total time the beam will scan the powder bed depends on the average current value.

  o For the hatching melt theme, the user can insert a value (mA) for current and maximum current. If the automatic power calculation option is disabled, the given current and speed will be used for the melting. If automatic power calculation is enabled the current and speed will take values only allowed by the chosen speed

function (see below) and it depends on sophisticated calculations and functions in order to keep a constant melt pool depth during the process.

- Beam speed is the speed that the beam scans the powder bed in order to heat, preheat or melt.
    - o For the heating and preheating themes, the user can insert a value (mm/sec), which is the actual speed used during the process for those themes.
    - o For the hatching melt theme, the user can insert a value (mm/sec), but as similarly explained for current the actual value used depends on the speed function and if the automatic power calculation option is enabled or not.
- Focus offset is a user defined current value (mA) that used at the focusing electromagnetic coils to focus the electron beam; as shown in Figure 3-7 a 0 value brings the focal point of the beam just on the surface of the powder bed, a positive value above it and a negative below it. Increasing the absolute value of the focus offset current results in a less focused electron beam with less energy density. Selecting the right focus offset current value is empirical and there is no clear trend between focus offset and beam diameter. No information was given by the machine manufacturer about this. Studies investigating the relationship between the focus offset current value and the resulting weld track width are shown in the PhD thesis of Al-Bermani [112].
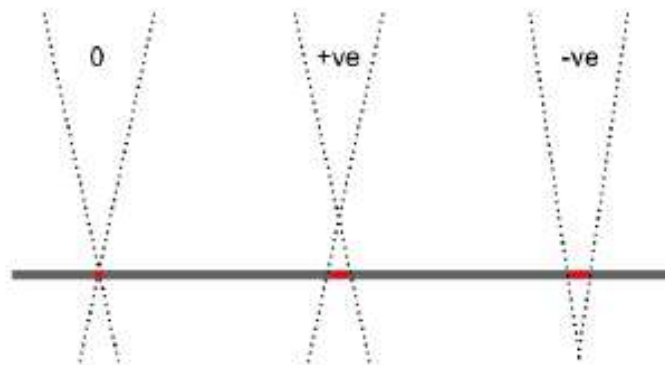
Figure 3-7. Focus offset illustration [120]

- Speed function is a user defined process parameter for the hatching theme and it gives the combination of beam speed and current for keeping a constant melt pool depth when melting the same material. The lower the speed function the higher the melt pool depth would be. As mentioned above speed function is used only when the automatic power

calculation option is enabled. The auto calculation function determines the right combination of speed and current at a certain moment, but always the 2 values are chosen from the given speed function (Figure 3-8).

- Surface temperature function was developed from Arcam when they were first developing the EBM equipment for melting tool steels. The values are arbitrary for other materials, but it was the temperature to be maintained during one layer for tool steels in ºC.

- Line offset is the distance in mm of two adjacent lines (Figure 3-9) during hatching melting.

- Number of repetitions is applicable for heating and pre-heating themes and it is the number of times the powder bed surface in the STL box will be scanned.
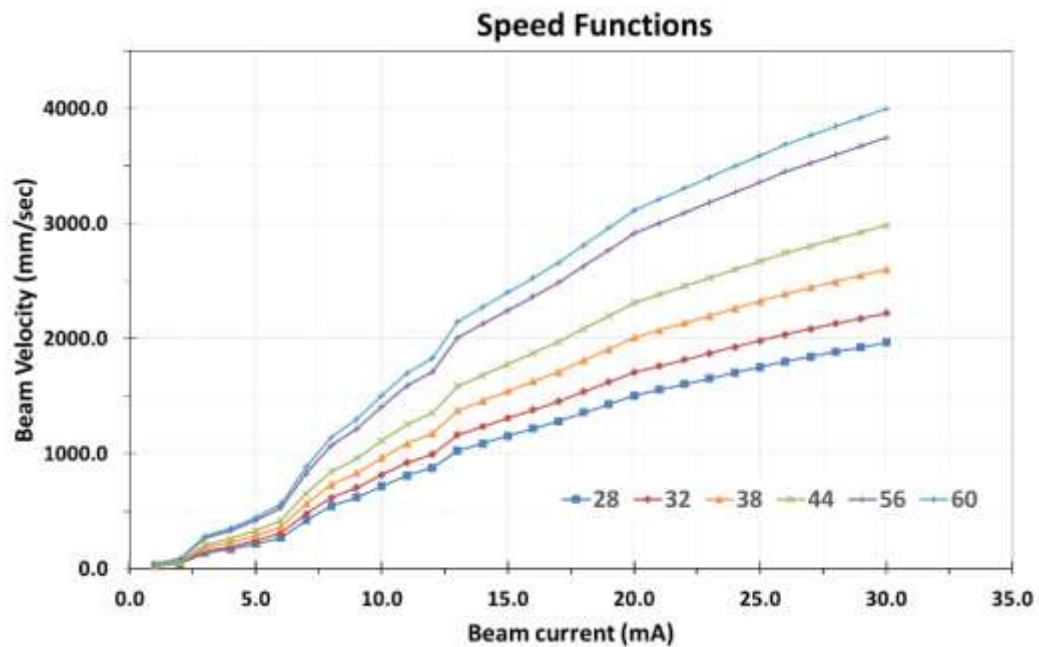
Figure 3-8. Graph showing the beam versus current relationship for various speed functions (raw data provided by Arcam)
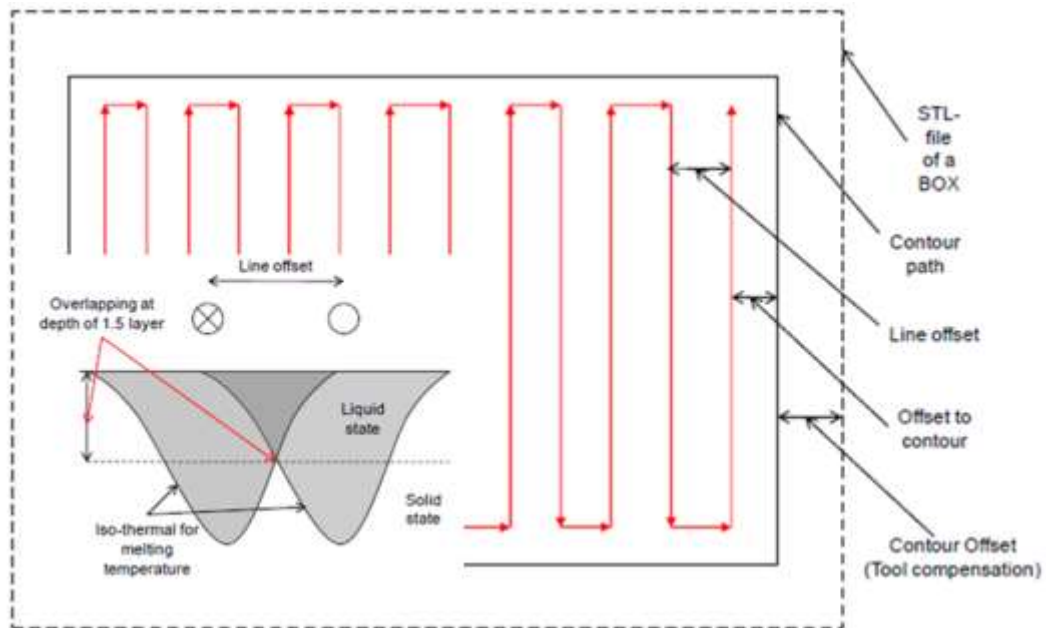
Figure 3-9. Illustration of hatching scanning mode [120]

3.4.1.1 Single-EBM Weld Tracks on Spark Plasma Sintered (SPS) samples

As mentioned in the DOE experimental Section 3.3, 21 weld tracks were planned for the experimental plan. Those runs were scanned on pre-sintered solid samples fabricated by spark plasma sintering (SPS) using similar feedstock (Ti-45Al-8Nb) powder. SPS is an advanced manufacturing, hot pressing technique, which can achieve very rapid consolidation of ceramic and metallic parts from powder feedstock, using high DC electric current, as a heating medium, passing through a graphite mould and a hydraulic system for applying the pressure [139], [140].

Based on literature data for SPS fabricated high niobium TiAl alloys [59], it was decided to fabricate pre-sintered samples of five different, individual dwell temperatures (800, 900, 1000, 1100 and 1200 ºC) for 10 minutes each in an Argon environment. In this way samples of variable density were produced. The heating and cooling rate was 100ºC/min. A 16kN pressure was immediately applied in one step at 600ºC during heating and remains constant until 600ºC during cooling. A typical diagram for this procedure is shown in Figure 3-10 for the 1000ºC holding temperature.
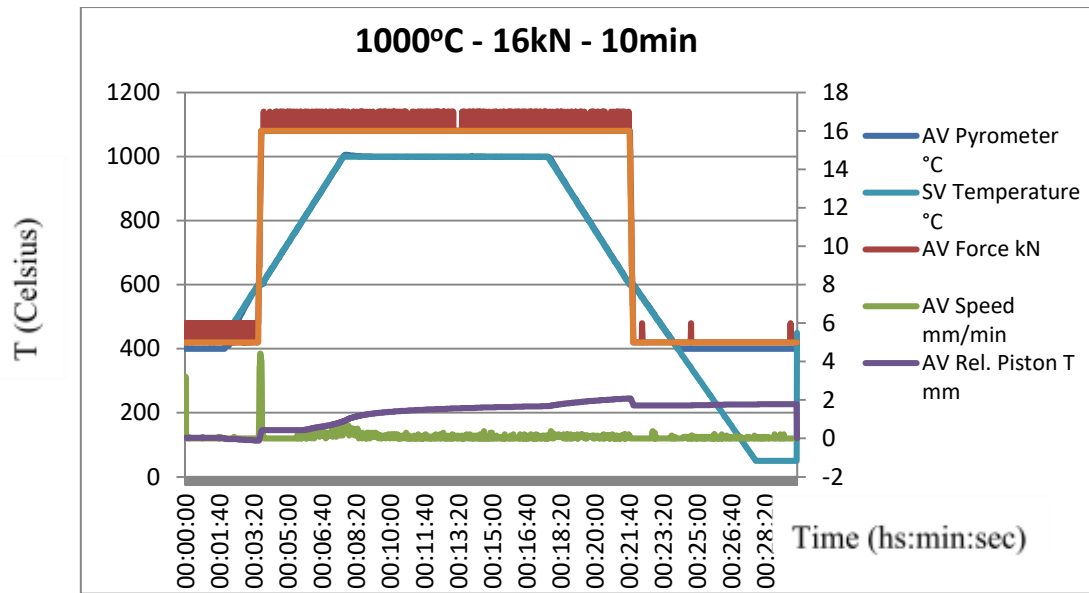
Figure 3-10. Typical diagram of SPS procedure for 1000 ºC holding temperature

The fabrication of the samples was performed using the FCT Systeme GmbH (FCT Group, Germany) spark plasma sintering (SPS) furnace, shown in Figure 3-11.

Figure 3-11. The FCT Systeme GmbH SPS machine at the University of Sheffield used for this study

Samples of 20 mm diameter were fabricated using the graphite mould shown in Figure 3-12. For each sample 6.40 grams of powder were weighed and poured in the mould. The amount of powder used was calculated in a way to attain samples of 5mm height, for a theoretical 100% densification (ρTiAl ≈ 4.1 g/cm^3).

Figure 3-12. SPS graphite mold

The resulting samples were manually ground down using 120 SiC grinding paper to achieve maximum possible flatness and to get rid of the graphite sheet layer. Figure 3-13 a and b shows the resulted, ground, samples fabricated at the 800 and 1000ºC dwell temperature. 3 Weld tracks are scanned on each sample. 7x samples are required for the 21 runs (weld tracks) for the experimental design for each of the 5 variable density batch of samples. 3 different build temperatures are tested at 800, 900 and 1000 ºC. For each build temperature 35 samples are required (7 samples x 5 dwell temperatures x 3 T$_{build}$).
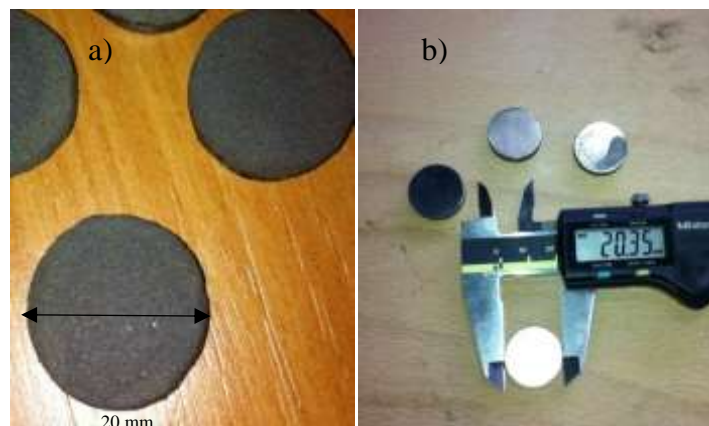
Figure 3-13. SPS fabricated samples a) 800 ºC and b) 1000 ºC holding temperatures

To achieve a homogenous build temperature, the top surface of the pre-sintered samples and the starting plate should be at the same, even height. For this reason, as well as to scan as many samples as possible at the same time a Ti-64, 150x150x20 mm plate (Figure 3-14) with 24 holes (20.40 mm in diameter and 10mm height) was built in the EBM Arcam machine with standard Ti-64 themes. The plate was ground down to be flat as possible, from both top and bottom sides. The centre of the top, shown in Figure 3-14, surface of the plate was used as the datum point, measured against the machine powder rake and set as the melt plane for the electron beam, where a zero focus offset of the beam produces the highest intensity beam anywhere over the working area. Some loose powder was placed in the holes, under the pre-sintered samples to help with the levelling. The goal was for the top surface of each sample to be levelled with the starting Ti-64plate. Extra ceramic insulating plates were placed onto the standard heat shield provided by Arcam as shown in Figure 3-15-a.

Figure 3-14. Sample holder base plate a) as built and b) ground to be flat and SPS-1000 samples placed in the holes
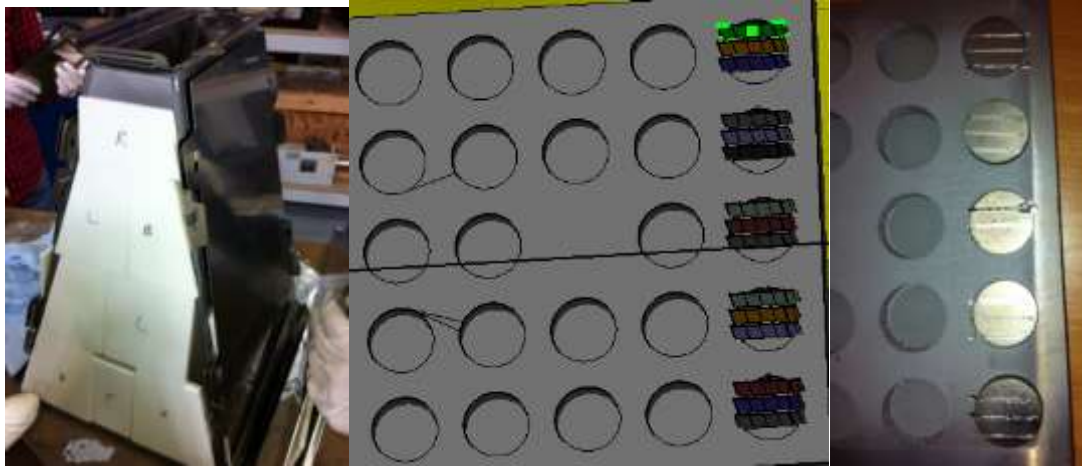
Figure 3-15. a) Ceramic, extra insulating plates placed onto heat shield, b) STL- file of the sample holder with the dummy wafer supports (15 weld tracks) and c) resulting weld tracks

3.4.1.2   Single-layer EBM Melting on Spark Plasma Sintered (SPS) samples

A single layer was melted on pre- sintered samples at 3 different vacuum pressures (i.e. 10^{-2}, 10^{-3} and 10^{-4} mbar). The heating, pre-heating and melting themes were identical for the 3 trials and derived from the layer-by-layer process development, which is described in the next Section 3.4.1.3 and the results are discussed in Chapter 4.

To build the pre-sintered samples the same SPS equipment and methodology, described in the previous section (3.4.1.1), were used. Larger samples of 80 mm diameter were built this time. For each sample 103 grams of powder was weighed and poured in the mould. The amount of powder used was calculated in a way to attain samples of 5 mm height, for a theoretical 100% densification (ρTiAl $\approx$ 4.1 g/cm^3). The dwell temperature for those samples was 800 ^{o}C and it was chosen to achieve slight bonding between the powder particles and to simulate the degree of sintering that takes place during EBM preheating. The resulting samples were manually ground down using 120 SiC grinding paper to achieve maximum possible flatness and to get rid of the graphite sheet layer.

Each sample was placed in the middle of a levelled and centred 150x150 mm base plate. Then the base plate and sample were moved down the height of the SPSed cylindrical sample (5 mm). The machine was vacuumed down to 5x 10^{-4} mbar as during the typical EBM process. Controlled vacuum (CV) EBM process parameter was changed as required for each of the 3 trials. When the start button was pressed the heating, preheating and melting sequence took place as during the typical EBM process, but with the chosen vacuum pressure. The build was set to stop after 3 layers. So, each SPSed sample was preheated and melted 3 times. After each

84

layer, the sample was moved down 70 μm. The melted surface was set to be a square of 40x40 mm. The same configuration of heat shield with the extra insulating ceramic plates was used as shown for the single weld tracks (Figure 3-15).

3.4.1.3   EBM Process Development

The EBM process development was performed as below.

1. "Smoke" tests on cold powder to define safe (smoke free) process parameters (i.e. beam speed, minimum, maximum and average current, line offset, line order and focus offset) for heating and preheating process themes.

2. Heating base plate tests to define heating theme process parameters and build temperature for achieving adequate degree of sintering under the base plate.

3. Initial preheating and melting trials to define preheating process theme parameters for a stable process.

4. Further optimised preheating process theme parameters. The powder bed should be sintered enough not to smoke during preheating or melting, but powder should be recoverable and with zero or very limited chemical content variation (e.g. Al loss) or shape degradation.

5. Deposited a short, cylindrical sample and observed through the window to roughly optimise the hatching theme process parameters for a smooth, homogeneous, dense melting. At this stage issues such as delamination between layers, swelling due to overheating or insufficient melting are easy to be solved just by altering main process parameters.

   o Starting process themes and functions for this study were provided by NCSU and from their development for the Ti-4822 GE alloy.

   o Standard themes for contours, turning points and thickness functions were used as provided (not changed) throughout the study

   o Process development was based only on hatching melting (bulk melting) quality

   o A cross section of this sample was analysed for porosity, microstructure and chemical analysis

6. Finer optimisation performed by applying a CCD DOE plan for selected process parameters for the hatching theme.

   o Process themes and parameters from previous step were used as the centre point

   o A 2 factor CCD for speed function and focus offset were used for the 1st DOE

- o Details for the DOE plan is shown in Section 3.3.
- o The deposited samples were assessed/tested for remaining process defects/porosity, microstructure, micro hardness, chemical content, and surface finish quality (smoothness and resolution).

7. A new tighter CCD DOE was performed based on the results from the previous step. At this step, a 3rd factor was introduced.
   - o Surface temperature process parameter was changed every 5 mm. Surface temperature (ST) of 1200, 1400 and 1600 were used for this study.
   - o Details for the DOE plan is shown in Section 3.3.
   - o The deposited samples from the 2nd DOE were assessed/tested for remaining process defects/porosity, microstructure, micro hardness, chemical content and surface finish quality (smoothness and resolution).

8. Optimal process themes, derived from previous steps, for higher density samples (lower remaining process defects and porosity), with smoother surface quality, lower Al loss and finer microstructure were used for building tensile bars and low cycle fatigue (LCF) samples.
   - o 2 Builds (batches 1 and 2) of 5 tensile bars and
   - o 1 build of 5 LCF (Batch 3) bares were attempted.

3.4.2 Hot Isostatic Pressing (HIP)

The HIP study was performed using the HIP furnace at the University of Sheffield. Three 15x15x15 mm samples were sectioned from one of the tensile bars of batch 2 (2nd Tensile bars build). One of those samples was HIPed at 1100 ^{o}C, 100 MPa for 4 hours and a second one at 1200 ^{o}C, 100 MPa for 4 hours; both under Argon environment. The third sample was kept in the as- built condition. After SEM and optical microscopy observation of the 2 HIPed and the one as-built sample it was found that the 1200 ^{o}C, 100 MPa, 4 hours cycle gave the best results. The rest of the tensile bars and the semi-finished LCF samples were sent to the University of Birmingham for HIP treatment at 1200 ^{o}C, 150 MPa for 4 hours.

3.4.3 Post-Machining and Tensile Testing

As built and as HIPed tensile bars and LCF samples were machined into British (BS) and ASTM standard tensile specimens and tested for tensile properties at Special Testing Ltd

(UKAS accredited lab) at room temperature (RT), and higher temperature at 700 and 900 °C. High (elevated) temperature specimens (ASTM E21 2009) are longer than the room temperature ones (ASTM E8n13a and BS EN 2002-1-2005). Each tensile bar (batch 1 and 2) can be machined into 2 room temperature or 1 elevated temperature tensile specimens. A total of 5 Batch-1 and 4 Batch-2 were machined. The 5th bar from Batch 2 was used for the HIP study as was described earlier. From the 5 LCF samples only 3 of them survived after machining and each one could be machined in 1 room or 1 elevated temperature tensile specimens. Table 3-4 shows the machining and tensile testing plan performed for this study.

Table 3-4. Machining and tensile testing plan

	As Built	HIPed	Total
RT	3 (2xB1+1B3)	6 (2B1+2B2+2B3)	**9**
700 °C	-	3 (2B1+1B2)	**3**
900 °C	-	3 (1B1+2B2)	**3**
Total	**3**	**12**	**15**

3.5 Sample Preparation and Characterisation Techniques

Several characterisation techniques have been used to determine the quality of the final parts manufactured by EBM. Table 3-5 lists the characterisation performed on either powder or bulk samples as well as the method and the equipment utilised. The measurements and methods are explained in this subsection.

Table 3-5. Powder and bulk specimen characterisation techniques used for this study

Matter State	Measurement	Method	Equipment
POWDER	Particle Size Distribution	Laser Diffraction	Coulter LS130 PSA
	Flowability	Hall Flow	Hall Flowmeter
	Apparent (bulk) Density	Apparent Density Cup	Hall Flowmeter
	Particle Density	Helium Pycnometry	Micromeritics AccuPyc II 1340
	Particle Morphology & Microstructure	Optical Microscope & BS-SEM	Polyvar optical microscope & FEI Inspect F FEG-SEM
	Chemical analysis	SEM-EDX	JEOL 6400
		Ti, Al, Mo, Cr, Zr, Fe and Cu by XRF FETI Nb, B, Si, Ni and Y by ICP-OES C, O, N, H by LECO	AMG analytical lab (external)
BULK	Bulk Density	Archimedes	High accuracy balance from METTLER TOLEDO
	Macrostructure	Optical microscope & BS-SEM	Polyvar optical microscope & FEI Inspect F FEG-SEM
	Microstructure	BS-SEM	FEI Inspect F FEG-SEM
	Chemical analysis	SEM-EDS	JEOL 6400
		Ti, Al, Mo, Cr, Zr, Fe and Cu by XRF FETI Nb, B, Si, Ni and Y by ICP-OES C, O, N, H by LECO	AMG analytical lab
	Micro-hardness	Vickers	Struers Durascan

3.5.1　Metallic Powder Characterisation

Powder properties have an important impact on the quality of the final AM components (such as surface finish or mechanical properties). Hence, prior to processing, some features of the metallic powder used in this project were studied and they are explained as follows.

- Particle size distribution (PSD) – For AM processes, PSD is an important parameter with a high influence on the flowability of the powder into the EBM chamber and the surface quality of the final sample. Laser diffraction determines PSD by measuring the angular variation in intensity of light scattered as a laser beam passes through a dispersed powder sample. The angular scattering intensity data is then analysed to calculate the size of the particles. [141]

- Flowability– The time required for a specific powder sample to pass through a discharge orifice is essential to measure the flow rate of the powder. This measurement can be carried out by using a Hall Flowmeter Funnel, as specified in the standard ASTM B213 [142].

- Apparent (bulk) density can be determined by the ratio of a powder mass to a given volume and it can be determined by using cylindrical or square cup as specified in the standard ASTM B212 [141].

- Actual density – A Helium pycnometer is used to determine the true density, or volume, of solid samples (including powder or bulk samples) since helium, which can enter the smallest pores, is used to measure the unknown volume of the material with a known weight. Inert gases (such as helium or nitrogen) are used as the displacement medium. The sample is sealed in the instrument chamber (of known volume), the gas is admitted and then expanded into another precision internal volume. The pressures observed upon filling the sample chamber and then discharging it into a second empty chamber allow computation of the sample solid phase volume. Density calculations are much more accurate and reproducible than the traditional Archimedes water displacement method. [143]

- Particle morphology – Spherical particles are desirable for an ideal AM process. Metallic powder produced by gas atomisation techniques tend to be spherical, which is the most desirable scenario for an ideal AM process. The particle shape was measured by using optical and electron microscopy.

3.5.2 Bulk Sample Characterisation

- Metallographic preparation - All samples were sectioned by using a Struers Minitom cut-off wheel (200rpm), in a way to expose for investigation the cross-section surface, as well as to fit into the 32-mm sample holder of the hot mounting equipment. Conductive Bakelite was used in all cases due to the subsequent SEM characterization. The 800 $^{\circ}$C samples and some powder samples were cold mounted in epoxy resin. The reason was to provide better support to the loose powder particles during grinding and polishing.

  Grinding and polishing were done using a Struers Abramin automatic polishing machine. The first grinding was done using a Struers MD Piano 220 resin bonded diamond disc with segmented surface for 5 minutes, to achieve an optimal flat surface and get rid of the recast layer, after the sectioning part. The result is comparable to a 220 silicon carbide grit finish. Finer grinding was achieved by using a Stuers MD Largo pad with 6 μm diamond suspension, for about 6-8 minutes. Final finishing was achieved by using colloidal silica (0.05 μm silco) mixed 1/1 with water, on a porous neoprene polishing pad for 14 minutes. Silco was poured every minute for the first 10 minutes. For the last 4 minutes, no silco was applied. Instead, the polishing was done by continuously pouring water on the pad.

  All samples were cleaned in an ultra-sound bath in isopropanol and methanol for 10 minutes in each solution, respectively. Krolls's etching solution was applied to some samples, but much better results were achieved with back scattered BS- SEM (Z contrast) imaging on unetched samples.

- Optical and Electron Microscopy Imaging - Microstructure images were taken on etched samples using both a Polyvar optical microscope with an Axiocam camera up to 1000x magnification and an FEI Inspect F FEG-SEM microscope for acquiring secondary electron images and backscattered electron images for the un-etched samples.

- Chemical analysis of powder and bulk samples in this study was performed by

  o SEM-EDX chemical analysis. EDX mapping was carried out at low and high magnification to determine the homogeneity of the samples. A JEOL 6400 was used for EDX quantitative chemical analysis of the samples.
  o Some samples were sent to AMG analytical lab for full chemical analysis as outlined in Table 3-5.

- Hardness Measurements - Vickers hardness (HV0.2) testing was done by using the Struers Durascan, micro-hardness testing equipment at the University of Sheffield.

3.6 Heat Source Modelling

A MATLAB code was developed to analytically solve the modified Rosenthal equation (Equations 3.2 and 3.3) for a moving heat source with a Gaussian distribution [144] and calculating the triple integral (Equation 3.5) for time, x and y space dimensions. The main factors of this equation are shown below, including material properties and process parameters.

$$T[x,y,z] = T_0 + \Delta T \qquad \text{(Eq. 3.2)}$$

$$\Delta T[x,y,z] = \frac{2\alpha\beta P}{\kappa\pi^{3/2}} \cdot \int_0^t \frac{\exp[-2\frac{(x+v_b t)^2 + y^2}{D_b^2 + 8\alpha t} - \frac{z^2}{4\alpha t}}{\sqrt{\alpha t} \cdot aD_b^2 + 8\alpha t)} \cdot dt \qquad \text{(Eq. 3.3)}$$

Where, α: thermal diffusivity, κ: thermal conductivity, β: efficiency parameter, $P = I_b*V$: beam power, I_b: beam current, V: EB gun voltage, v_b: beam velocity, D_b: beam diameter

T_0 is the build temperature (T_{build}). Thermal diffusivity (α) and conductivity (κ) are functions of temperature [145], as shown below in Figure 3-16. Efficiency parameter (β) is a commonly used factor to account for energy losses during beam/material interaction. For electron beam processing (not exclusively for EBM) β values between 0.6-0.9 are reported [112], [122], [130]. Current (I_b) and velocity (v_b) are standard EBM process/beam parameters. Voltage (V) for Arcam EBM equipment is a constant and it is 60 kV. For this study $t = L/v_b$ and L is the scan line length. D_b is the heat source beam diameter, so in this case the electron beam diameter.
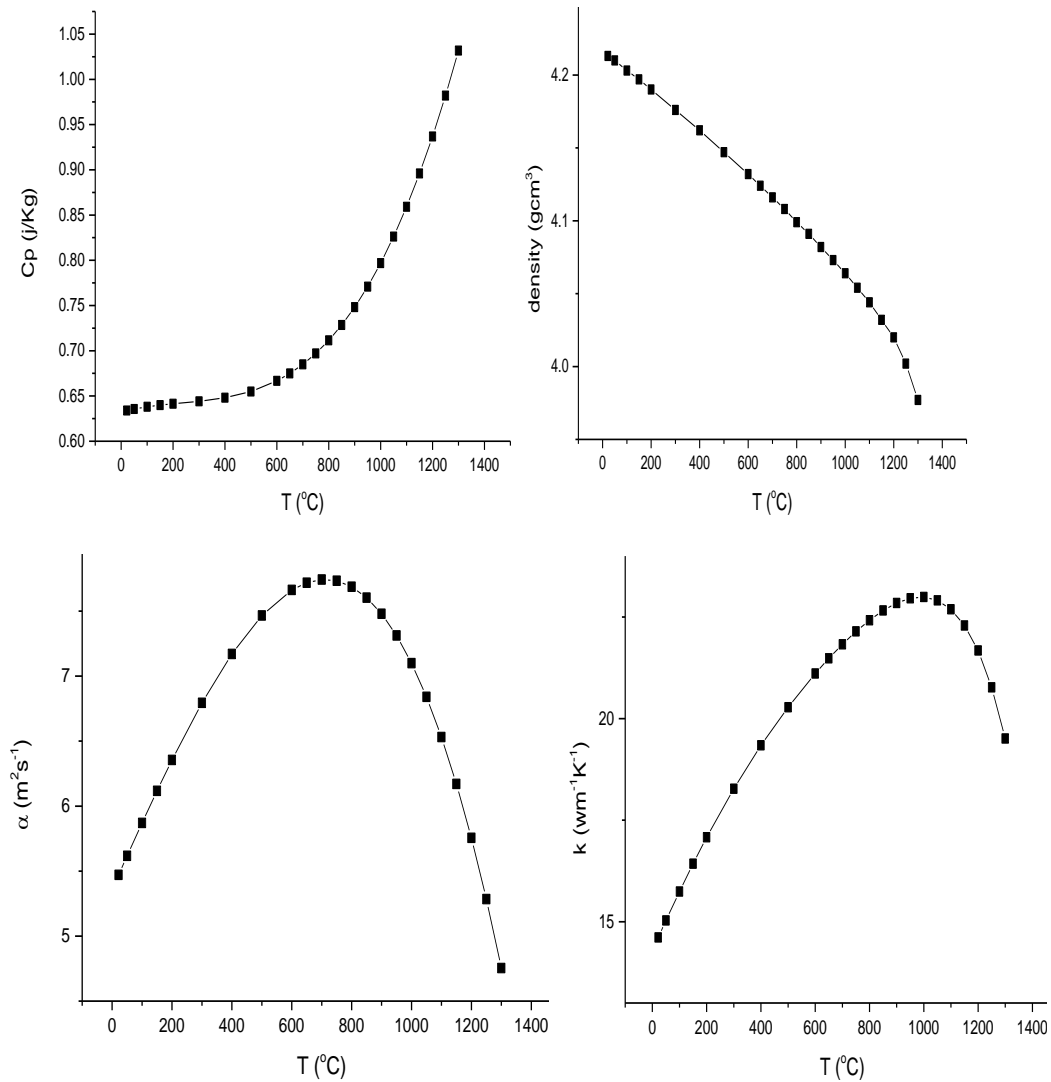
Figure 3-16. a) Thermal capacity, b) density, c) thermal diffusivity and d) thermal conductivity of TiAl8Nb alloys as a function of temperature [145]

For laser beam processing, the beam diameter is a well-defined process parameter [1], which can be adjusted as required. On the other hand, for EBM, beam diameter is not something that readily can be measured and it is controlled by the focus offset. Focus offset, as previously explained (Section 3.4.1), is a user defined current value (mA) used at the focusing electromagnetic coils to focus the electron beam, but do not indicate the actual beam diameter. In some studies [124]–[126], when required for some calculations, the width of the resulting melt pool (thermal footprint) is used as an approximation instead of the actual beam diameter (spot size of the incident beam). However, this way might overestimate the beam diameter when a shallow penetration occurs or underestimate it when a deep (keyhole) penetration mode takes place [126].

The spot size of the incident beam depends only on its energy (i.e. current and voltage) and focus when it hits the solid substrate, and consequently depends on the distance and tilt between the beam source and the substrate. So, spot size is a beam characteristic and independent of the material substrate. On the other hand, the interaction volume of the electron beam with the solid substrate, in addition to beam focus and energy, is also influenced by the density and atomic number of the solid substrate. Finally, the thermal footprint (heat affected zone) will be also affected by the thermal properties of the substrate material and interaction time. [146], [147]

The focus offset (EBM process parameter) effect on beam diameter (thermal footprint) and the electron beam in general is investigated in Chapter 4 and 6. Elmer [126] performed experiments to measure beam diameter for beam currents between 3 – 14 mA. A strong linear relationship (Figure 3-17) is observed between beam current and measured beam diameter. The R^2 for the linear fit is 0.987. The equation (3.4) for the linear fit was used, within the MATLAB code, to estimate the beam diameter as a function of current for all the heat source calculations in this study.

$$D_b = 0.0225*I_b \text{ (mA)} +0.2557 \text{ mm} \quad\quad\quad\quad (Eq. 3.4)$$
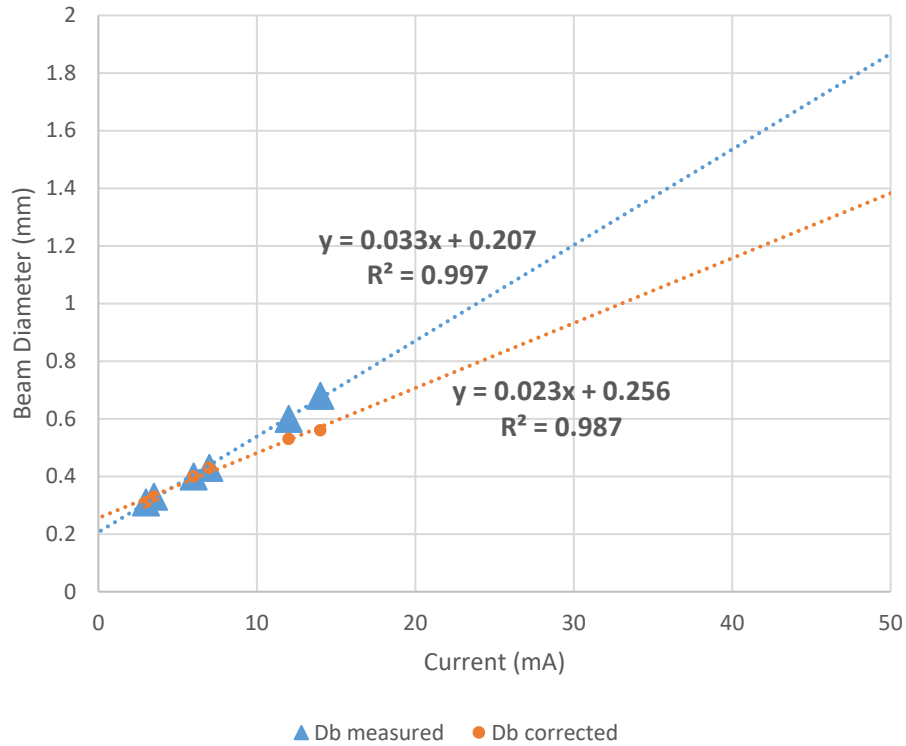
Figure 3-17. Measured focal dimensions (mm) when applying a static electron beam of varying current (mA) on a Tungsten solid block [126]

Analytical solution of the integral of equations (3.2) and (3.3) (for z = 0) could be plotted by MATLAB to show the temperature field (isotherms) around a moving electron beam in the xy plane and an example is shown in Figure 3-18. A code developed and run using MATLAB software was used to calculate the melt pool width and length and to calculate the average surface temperature of a given surface area based on this plot. A modification of the code (for y=0), in a similar way, was used to plot the temperature field in the xz plane (Figure 3-19) and measure the weld pool depth and/or the average temperature at a given area.
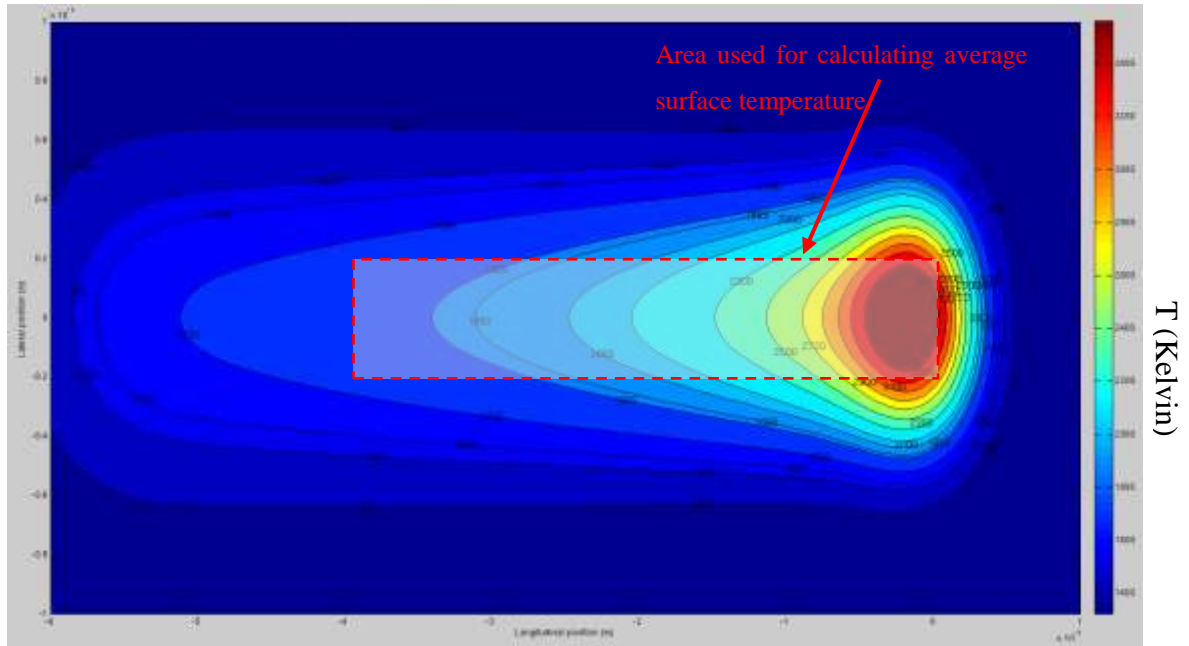
Figure 3-18. Electron beam temperature field (K) at xy plane calculated and plotted using a MATLAB code developed for this study
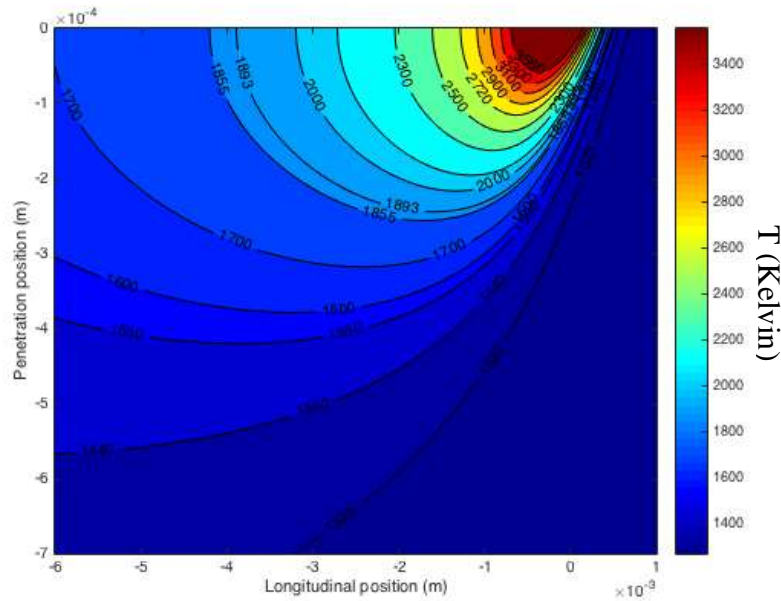
Figure 3-19. Electron beam temperature field (K) at xz plane calculated and plotted using a MATLAB code developed for this study

The temperature (Figure 3-18 and Figure 3-19), as expected, is not the same at every point. The temperature at the centre (very small point) reaches its maximum and rapidly decreases in isothermals as the distance increases from the beam. Depending on the process parameters this

maximum temperature can take extremely high values, but only in a very small point. As shown in Figure 3-21 this could be extremely high and unrealistic. Evaporation depends on surface temperature and apparently would occur at different rates at the different points of the substrate; although the time each point will have a specific temperature is minimum as the temperature rapidly changes with the beam rapidly moving on the substrate. Using the maximum temperature at the centre of the heat field won't take in account the shape (at xy plane) of the beam and this will be misleading for evaporation. For this reason, in this study an average temperature was calculated for a given (larger) surface area (Figure 3-18) and estimated time to also capture the effect of the shape of the beam, by calculating the triple integral (Equation 3.5) for t, x and y.

$$\overline{T} = T_0 + \overline{\Delta T} = T_0 + \frac{2\alpha\beta P}{\kappa\pi^{\frac{3}{2}}} \cdot \int_0^t \int_0^{-x_1} \int_{-y_1}^{y_1} \frac{\exp[-2\frac{(x+v_b t)^2 + y^2}{D_b^2 + 8\alpha t} - \frac{z^2}{4\alpha t}]}{\sqrt{\alpha t} \cdot D_b^2 + 8\alpha t)} \cdot dt \cdot dx \cdot dy \qquad \text{(Eq. 3.5)}$$

Time (t) is calculated by dividing the scan length (L) with the scanning velocity of the beam (v_b). x and y were arbitrarily defined; y to be equal the distance between two adjacent scanned lines, aka line offset (LOF) and x to always be 4 mm. An example of the surface area the average surface temperature is shown in Figure 3-18. The effect of those ambiguous factors (D_b, x1, y1 and t) on the calculated surface temperature was investigated by performing a sensitivity study, shown in Figure 3-20.

The deviation of the calculated surface temperature with only small changes in those factors seems to be quite large. However, care was taken to choose those values in a consistent way which results into realistic temperature values. Besides, the intention of this study was to study the relationship between surface temperature and evaporation losses, rather than trying to give a precise temperature calculation. By realistic; means that the chosen area shouldn't be very small or very large. A very small area wouldn't capture the shape of the melt pool and could give extremely high temperatures. A very large area, much larger than the melt pool, will take in account a lot of noise from the much cooler substrate, which will lead to very low calculated average temperatures. So, in summary the factors were chosen to capture as much of the weld pool, but with not too much noise from the cold substrate. For x_1 (heated area length) 4 mm was used for all the calculations. This was an arbitrary choice and as explained the intention was not to be too far or too close to the electron beam. For y_1 (heated area width) again an

arbitrary choice was made; to be equal to the process parameter of line offset (hatching offset), which is the distance between two adjacent lines during the EBM snake-type (hatching) melting. Eq. 3.4, which was derived from literature data, used to calculate the beam diameter (D_b) for all the temperature calculations for this work. Figure 3-21 shows the difference between the maximum temperature at the centre of the electron beam and the average temperature calculated using our assumptions versus the electron beam diameter. They follow a similar trend; changing the factors to capture a smaller area the average surface temperature can increase up to this maximum temperature, which for a very focused beam could be unrealistically high.
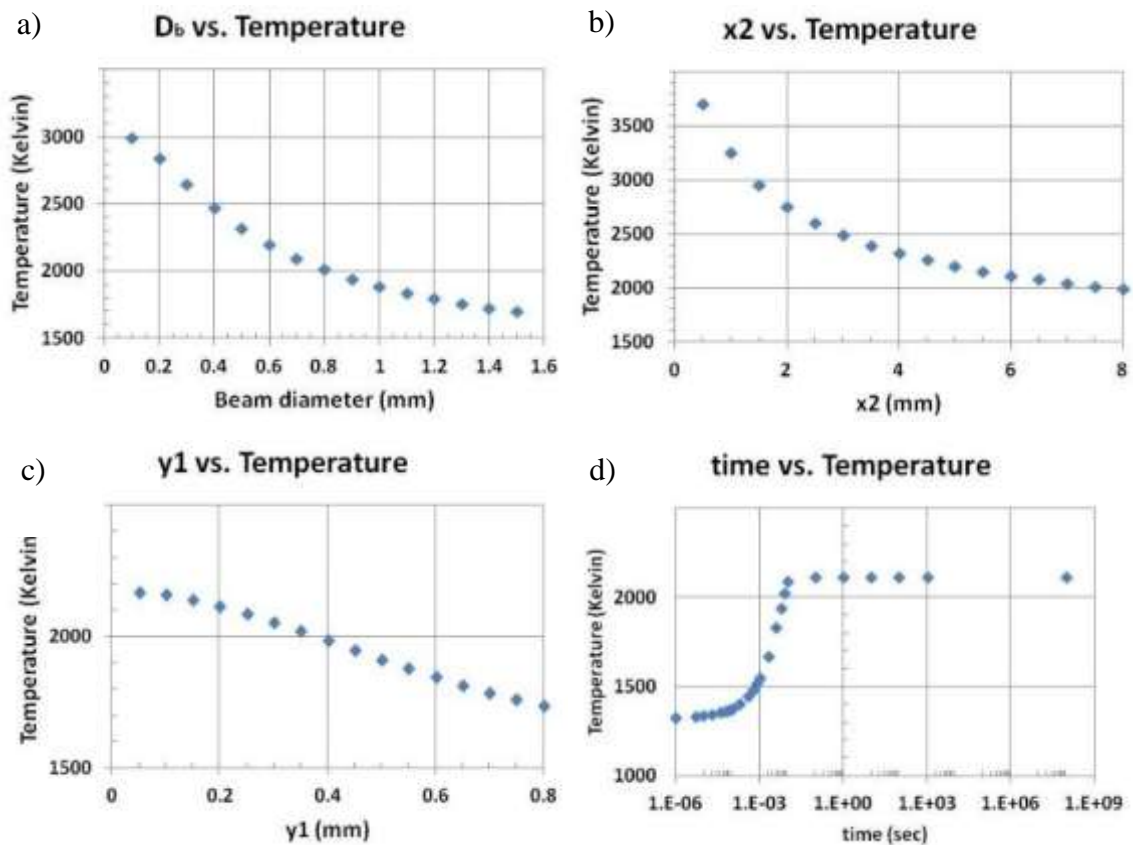
Figure 3-20. Sensitivity study showing the dependence of the calculated average Surface Temperature vs. a) D_b, b) x_1, c) y_1, and d) time
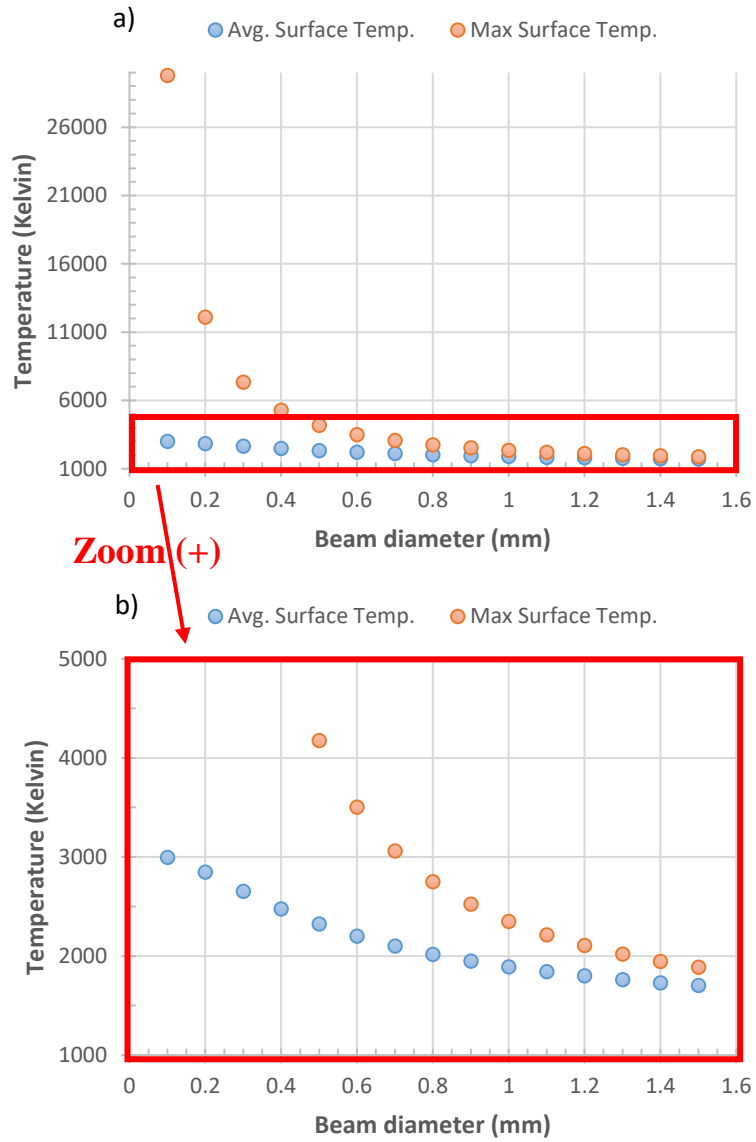
Figure 3-21. Sensitivity study showing the dependence of the calculated average and maximum Surface Temperature vs. D_b. a) full graph, b) zoomed area – part of full graph

4 PRELIMINARY CHARACTERISATION AND PARAMETRICAL STUDIES FOR KEY EBM PROCESS PARAMETERS

4.1 Introduction

This Chapter includes the results and discussion of the main findings from the first step of the methodology for novel alloy process development as described in Chapter 3 and schematically shown in Figure 3-1. Process development for novel alloys is cost and labour intensive and typically takes place in an empirical way. Therefore, there is a necessity for a more quick, cost-effective and scientific approach with reproducible outcome results. The hypothesis for this step is that main EBM process parameters could be rapidly and effectively defined for optimum material properties and process performance, prior to the actual EBM process development, by generating predictive models and process maps relating those main process parameters and specific material properties with melting response and outcome material properties.

A parametrical study of the key electron beam properties (I_b, V_b and focus offset) and T_{build} takes place, by scanning single weld tracks on Spark Plasma Sintering (SPS) fabricated, high-niobium TiAl (Ti-45Al-8Nb at%) samples. SPS in this study is used to rapidly fabricate substrate material of different density using similar feedstock as the subsequent EBM process development. Density is an additional variable factor during EBM AM; from loose, un-melted, un-sintered powder to fully melted and fully dense bulk material. Density/porosity affects specific material (thermal) properties such as conductivity and diffusivity, which in turn affect melting response and other component properties. A DOE approach is used to increase experimentation efficiency. Advanced characterization techniques are applied to the starting powder, SPSed samples and resulting weld tracks to measure density/porosity, melt pool dimensions, Al content, microstructures and micro-hardness. Regression analysis was performed on the measured outputs and statistical models were generated using the DOE software. Existing physical, analytical and empirical models from literature were tested to relate weld pool geometry to specific material (thermal) properties and process parameters.

4.2 Fabrication of high-Niobium Titanium Aluminide Substrates by Spark Plasma Sintering (SPS)

4.2.1 Powder Feedstock used for Parametrical Studies

The feedstock used for the parametrical studies is a Ti-45Al-8Nb (at %) pre-alloyed powder, acquired from GKSS Forscungszentrum (Germany). The particle size distribution of this powder is shown below in Figure 4-1.
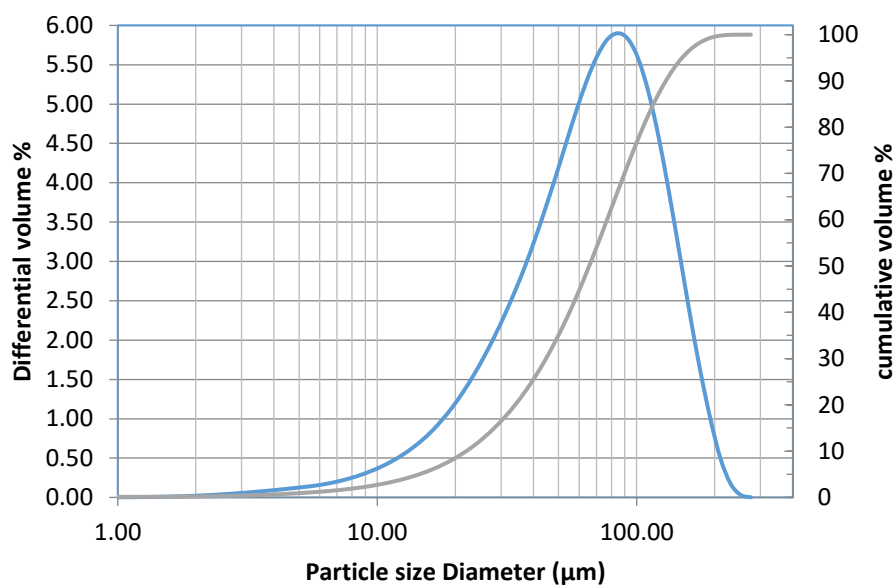
Figure 4-1. Differential and cumulative particle size distribution of powder feedstock used for parametric studies

Flow rate and apparent density measurements were not possible for this powder, as it would not flow through the Hall flow funnel, possibly due to a very good packing density because of the large distribution and number of fines. The true density of the particles was measured by using Helium Pycnometry and it was found to be 4.247 g/cm^3.

Figure 4-2 shows macro- and micrographs of the powder. Particles are mostly spherical with low amount of satellites. A small amount of spherical porosity is observed in some of the particles. Spherical porosity is typical [7], [38], [43], [120] of the gas-atomisation process as a result of argon entrapment. In the higher magnification images of the powder sample some severe cracking is observed in the powder particles. This is expected as a result of the extreme

brittleness of this material and in conjunction with the very rapid solidification conditions of producing the powder feedstock during inert gas-atomisation.
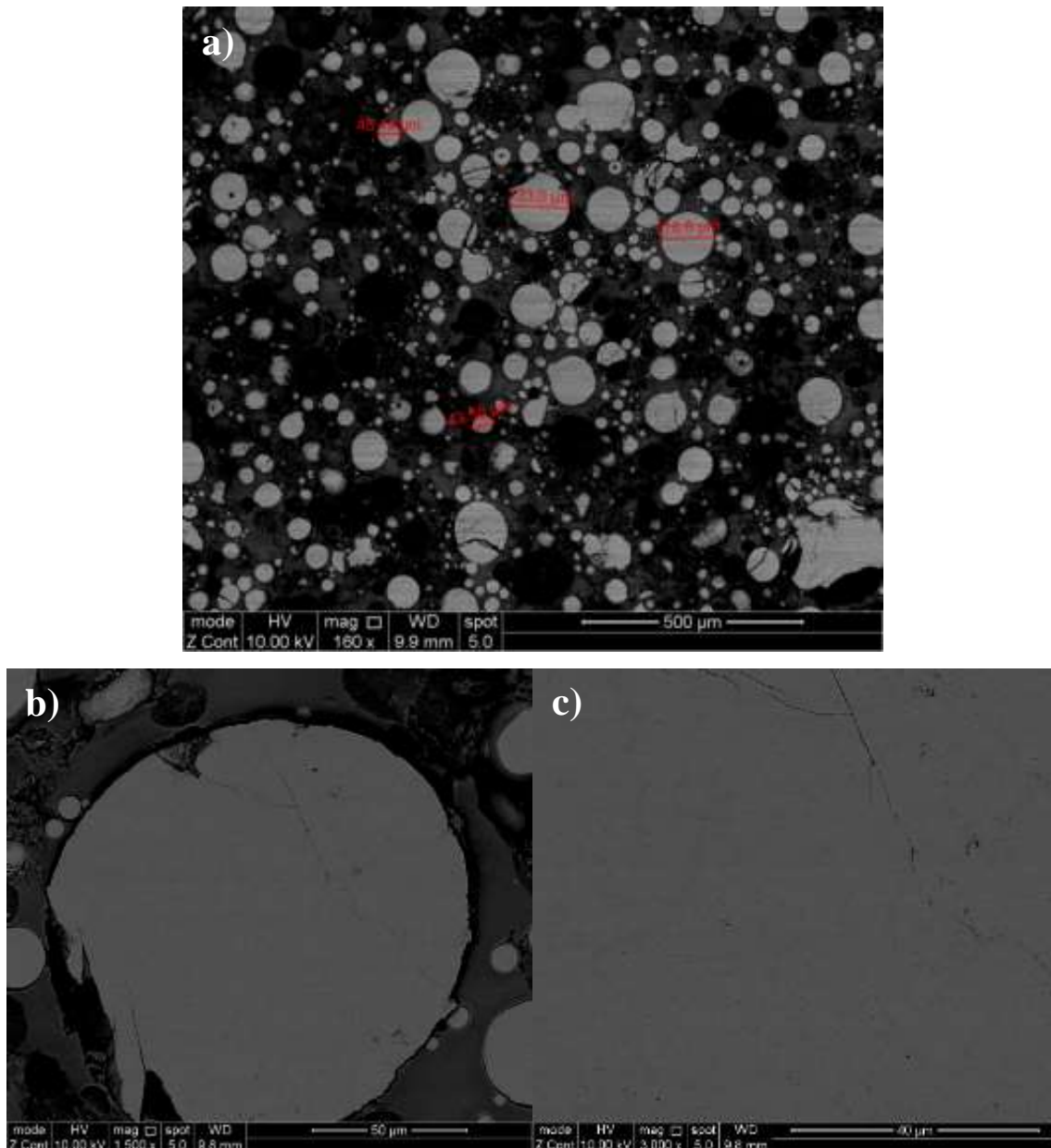
Figure 4-2. Back-scattering SEM images of polished powder particle cross-section at a) 160x, b) 1500x and c) 3000x magnification

The chemical content of this powder was measured by SEM-EDX point analysis and the results (in wt. %) are shown in Table 4-1. Conversion to atomic percent for the average measured chemical content gives 46.14, 45.34 and 8.52 at % for Ti, Al and Nb, respectively which are very close to the nominal chemical content (Ti-45Al-8Nb [at %]). A sample of the same powder

was also sent for full chemical analysis at AMG, as described in Section 3.6.9. The results (in at %) are shown in Table 4-2.

Table 4-1. SEM-EDX chemical analysis (wt. %) of powder feedstock used for parametrical studies

	Al (wt. %)	Ti (wt. %)	Nb (wt. %)	Total (wt. %)
Spectrum 1	29.14	51.87	18.99	100.00
Spectrum 2	28.69	52.40	18.91	100.00
Spectrum 3	28.76	52.59	18.65	100.00
Spectrum 4	28.70	52.35	18.95	100.00
Spectrum 5	29.51	52.26	18.23	100.00
Mean	**28.96**	**52.29**	**18.75**	100.00
Std. deviation	0.36	0.27	0.32	N/A
Max.	29.51	52.59	18.99	N/A
Min.	28.69	51.87	18.23	N/A

Table 4-2. Chemical content (at %) of powder feedstock used for parametrical studies analysed by XRF and LECO

Elements	Ti	Al	Nb	C	O	N	Fe
Chemical Content (at %)	46.32	44.91	8.21	0.191	0.196	0.023	0.049

4.2.2 Spark Plasma sintering (SPS) Fabrication

Scanning single weld tracks on fully dense, pre-manufactured substrates is a common method [1], [8], [113] for studying the effect of key electron or laser beam parameters on melting response and material properties. Typically, wrought and machined, solid, flat, square blocks of similar chemistry are used but with different microstructures and material properties to the powder feedstock that is used for additive manufacturing. In this study, the approach is to use as a substrate, flat samples compacted from the same powder feedstock which will be used during the subsequent EBM process development. The intention is to fabricate substrates of different density/compaction level; from loosely agglomerated powder particles up to fully dense solid samples as described in Section 3.4.1.1.

Figure 4-3 shows the resulting percentage compaction for the different SPS dwell temperatures, which is calculated by dividing the relative piston movement with the initial measured

thickness for each sample. As one would expect, maximum speed and compaction rate are observed when the 16 kN pressure is loaded at 600 °C. Then from this point and up to about 800 °C, a plateau with zero compression is observed. At about 800 °C, a high rate of compression is observed until the maximum (dwell) temperature is reached. The higher the maximum temperature is the higher compression is being achieved. Then another plateau region occurs with lower compaction rate, which becomes flatter as the sintering temperature increases. Finally, a region of high compaction rate and a subsequent steep decrease is observed, more pronounced as the dwell temperature increases, possibly related to the expansion of the graphite mould.
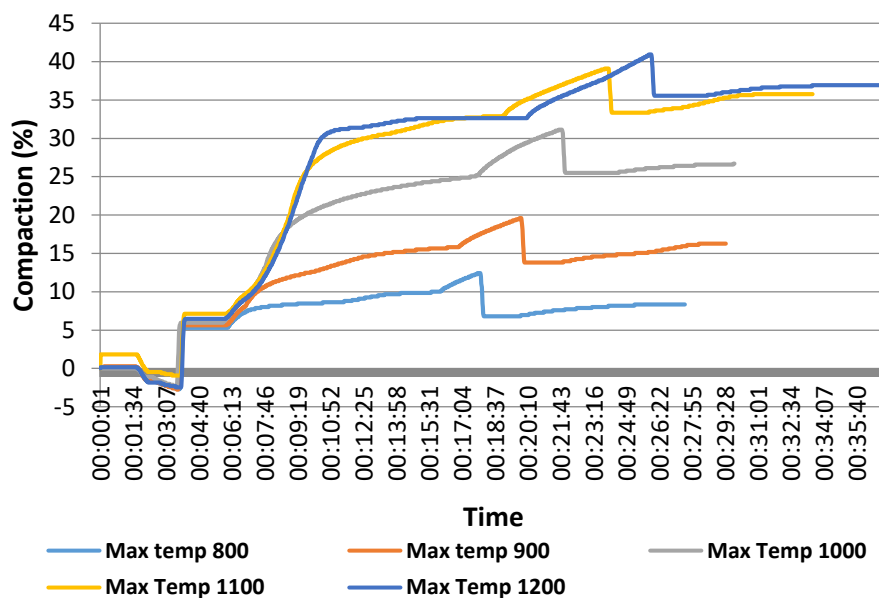
Figure 4-3. Percentage of sample compaction for the different SPS dwell temperatures

4.2.3 Evolution from Powder Feedstock to Fully Dense SPS Fabricated Substrate

Fabrication of pre-sintered substrates of different density by SPS is feasible. The samples compacted at 800 °C dwell temperature are only loosely sintered (Figure 4-5) and they look quite similar to EBM pre-sintered "cake". Those samples could be easily broken into individual particles with a minimum applied force. As shown in Figure 4-4-(b), powder particles are removed during polishing and the macrograph looks similar to the one for a powder sample.
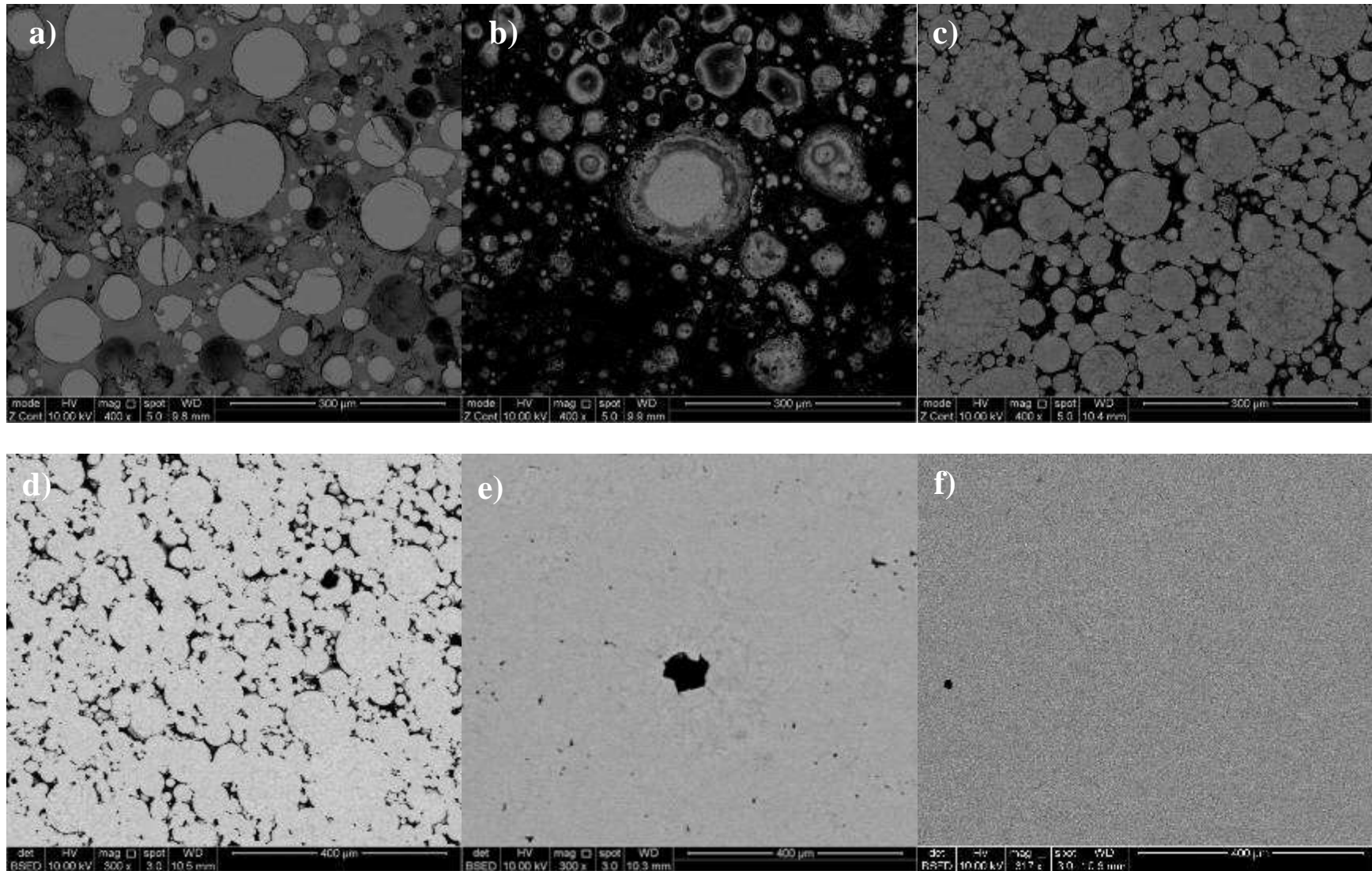
Figure 4-4. Low magnification back-scattering SEM image for a) feedstock powder, b) SPS-800, c) SPS-900, d) SPS-1000, e) SPS-1100 and f) SPS-1200 sample

Figure 4-5. Image of sample fabricated by SPS at 800 °C dwell temperature

Compaction is increased by increasing dwell temperature, as shown in the compaction diagram in Figure 4-3. A plateau region of lower compaction rate is observed after reaching the dwell temperature, which gets flatter with increasing dwell temperature. This is more obvious at 1200 °C, where maximum compaction seems to have been achieved at about 32.5 % and this could be related to the fact that the material gets close to the maximum possible compaction and near to 100% of the theoretical density. This is evident in the low magnification image of Figure 4-4-(f), as well as in the higher magnification images of Figure 4-11, where only some minor small spherical pores could be observed. It is reported [59] that a density of higher than 99.5% can be achieved for dwell temperatures higher than 1100 °C. This agrees with the results of this study (Figure 4-6), where a density higher than 99.9 % is achieved for a dwell temperature of 1200 °C. At 1100 °C the resulting density is between 98-99 %.
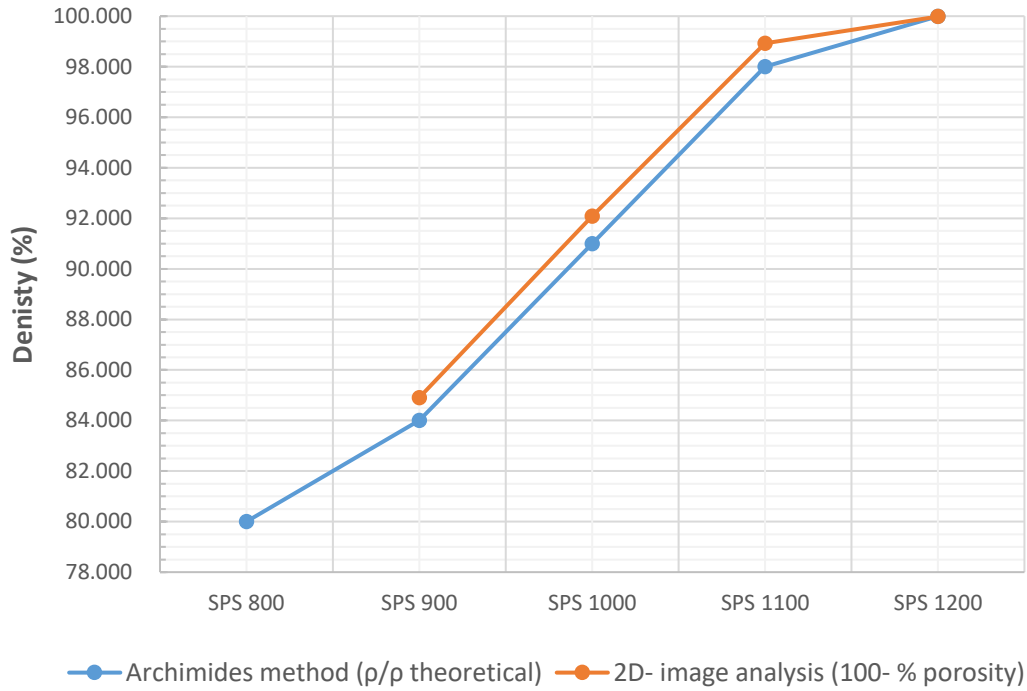
Figure 4-6. Density (%) of SPS fabricated substrates at different dwell temperatures measured with Archimedes' method and 2D- image analysis of low-magnification BS-SEM image taken from polished cross-section

Severe cracks, remaining from powder feedstock (Figure 4-2) and related to rapid solidification and the intrinsic brittleness of the material, are observed in all the SPS fabricated samples up to 1000 ℃ (Figure 4-7, Figure 4-8 and Figure 4-9) dwell temperature. Some smaller line-shaped porosity can be still observed for the SPS fabricated samples at 1100 ℃ (Figure 4-10). For SPS fabricated samples at 1200 ℃ no cracks could be observed. Spherical porosity, due to argon entrapment during gas- atomisation, can be observed to all SPS fabricated samples even in the densest ones fabricated at 1200 ℃. It is reported [6], [7], [43] that this micro-porosity remains even after the EBM consolidation and the subsequent HIP treatment. For the samples fabricated up to 1000 ℃ the interfaces of the individual powder particles are still clearly discrete. Above this temperature, the powder particle interfaces are starting to disappear and the material gets closer to full density.
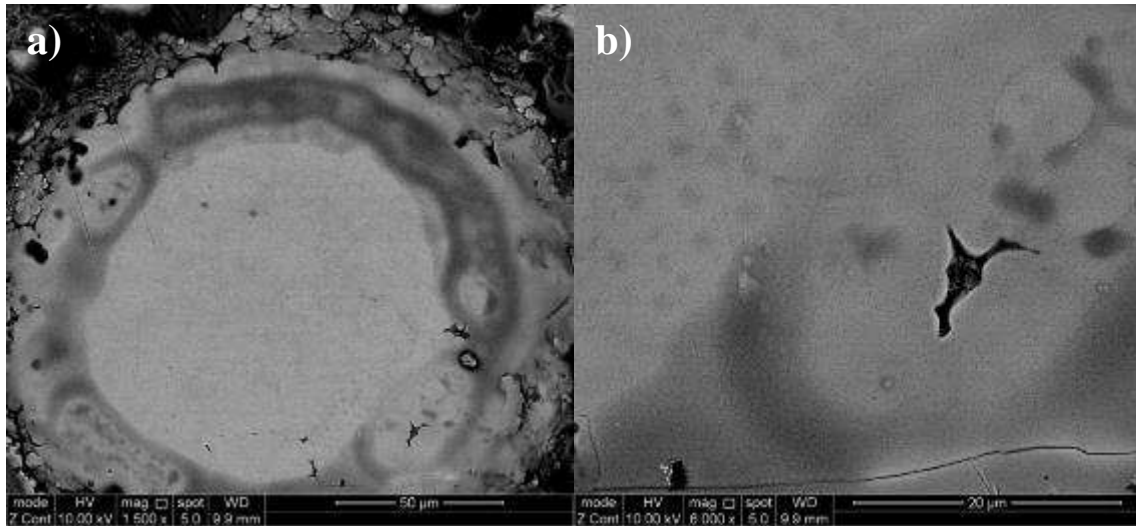
Figure 4-7. High magnification back-scattering SEM images for SPS-800 sample at a) 1500x and b) at 6000x
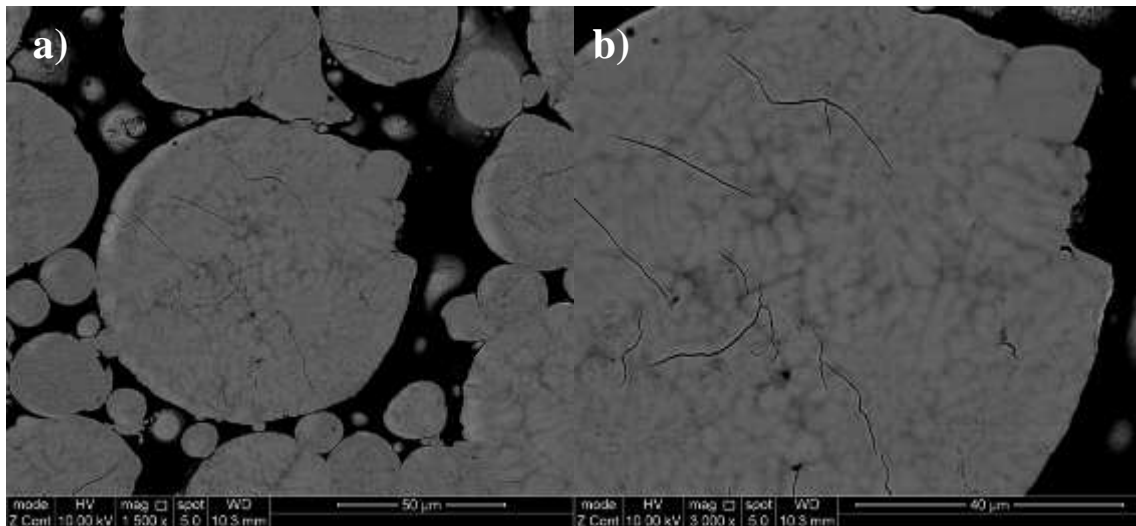
Figure 4-8. High magnification back-scattering SEM images for SPS-900 sample at a) 1500x and b) 3000x
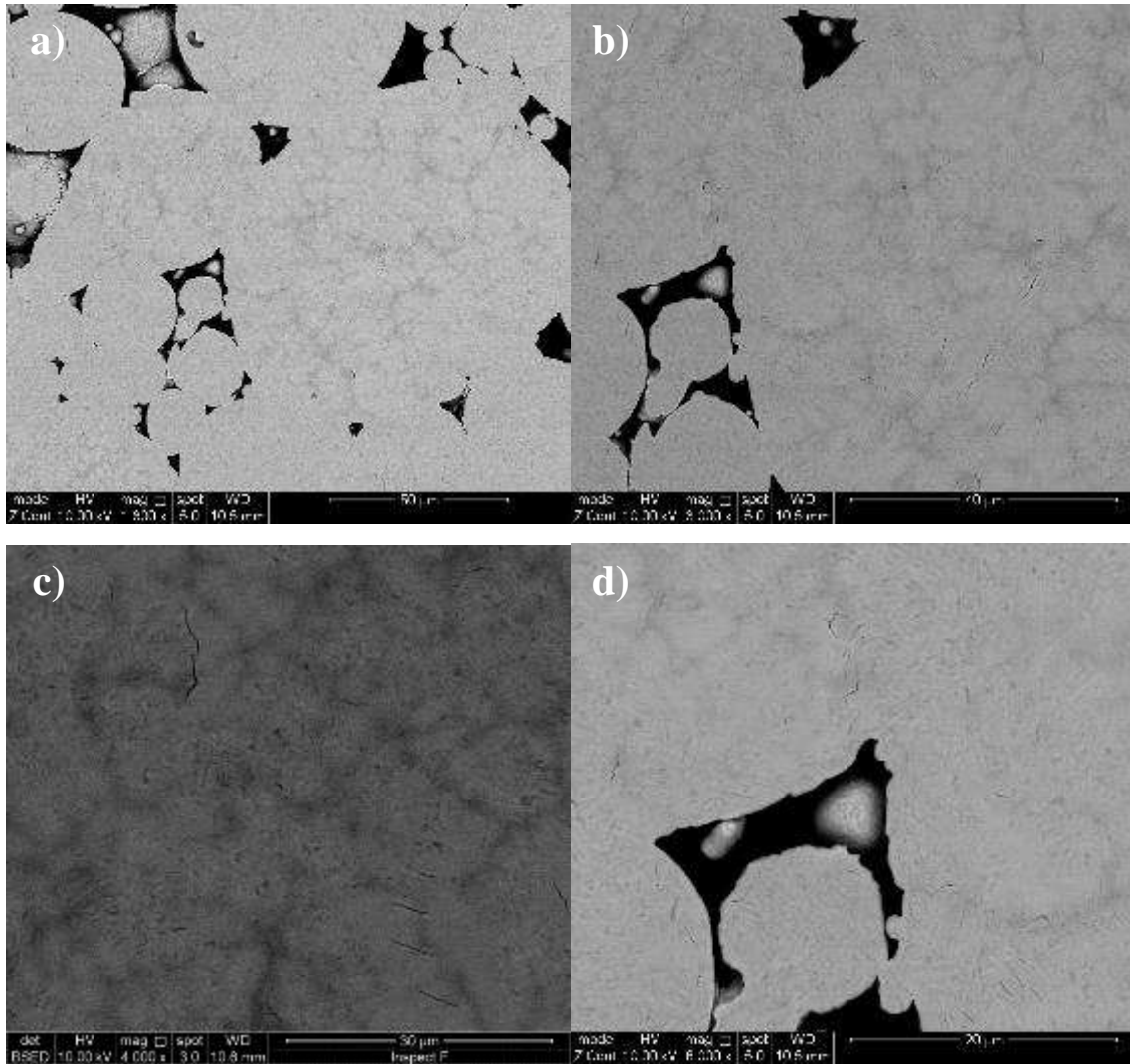
Figure 4-9. High magnification back-scattering SEM image for SPS-1000 sample at a) 1500x, b) 3000x, c) 4000x and d) 6000x
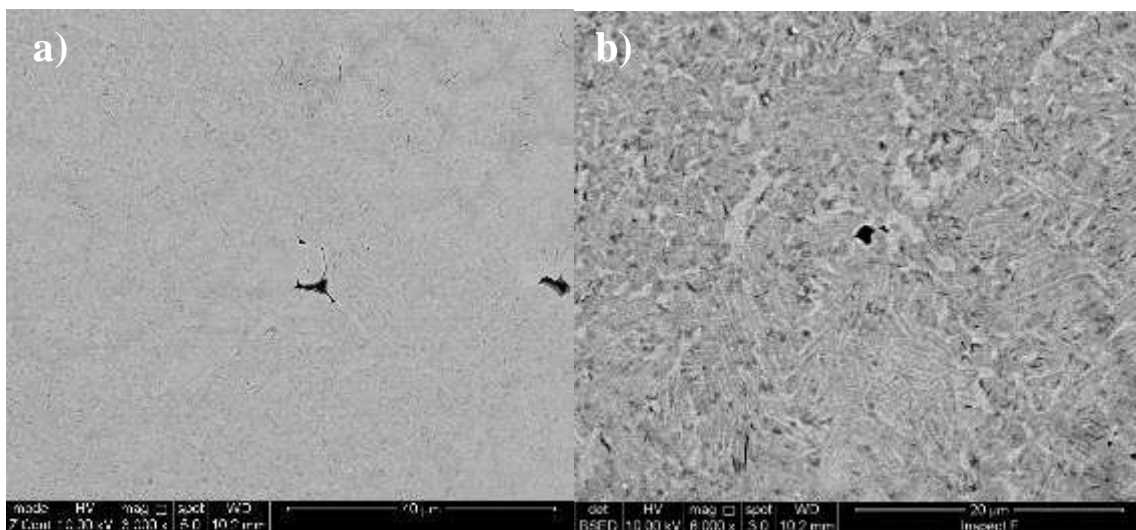
Figure 4-10. High magnification back-scattering SEM image for SPS-1100 sample at a) 3000x and b) at 6000x
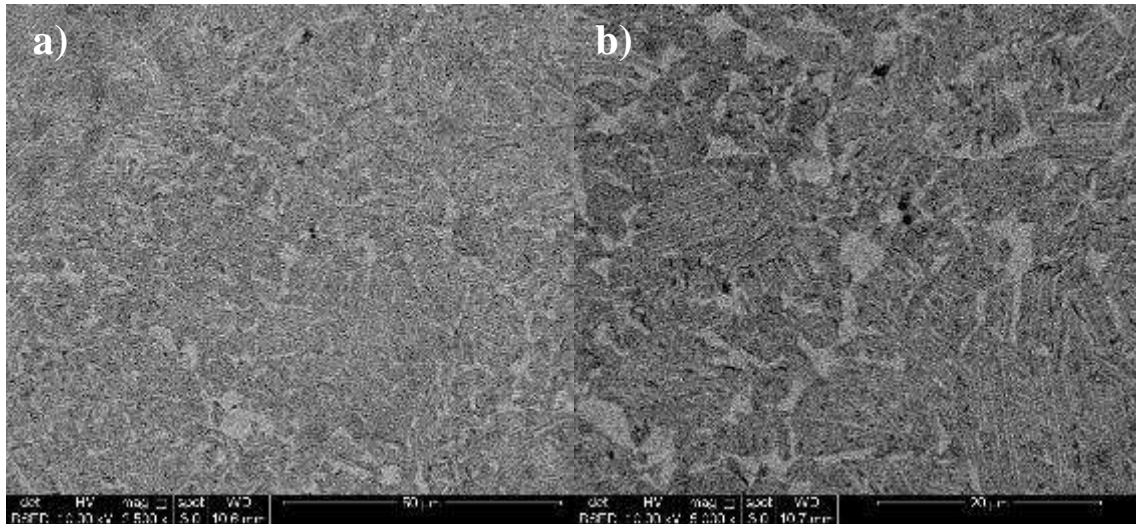
Figure 4-11. High magnification back-scattering SEM image for SPS-1200 sample at a) 2500x and b) at 5000x

The expected microstructures from the literature [59] would be dendritic up to 1000 ºC dwell temperature, which therefore is not any different from what is expected from the parent powder feedstock and as a result of the rapid solidification as earlier mentioned. This microstructure is very clear in Figure 4-8 and for a sintering temperature of 900 ºC. In Figure 4-9-(a), the dendritic structure can also be observed for the 1000 ºC dwell temperature. Nonetheless at higher magnifications of the same image some γ grains and lamellar structure formation in the interdendritic regions can be observed. For 1100 ºC it is reported [59] that a near-gamma microstructure would be formed in all the grains. Instead, in the high magnification micrographs of Figure 4-10 formation of a duplex microstructure of γ grains and γ// α_2 lamellas is clearly shown. This duplex microstructure is much clearer in Figure 4-11 and for 1200 ºC dwell temperature.

Chemical content of selected SPS fabricated samples was measured by SEM-EDX point analysis concurrently with the chemical analysis of the single weld tracks. No change in chemical content and in particular no Aluminium loss or Carbon contamination from the graphite mould was observed.

4.3 Melting Response to Key Electron Beam Parameters and Build Temperature

4.3.1 Single EBM Weld Tracks on Spark Plasma Sintered (SPS) Samples

A Design of Experiments (DOE) commercial software (Design-Expert) was used to establish the minimum design points that should be tested to have an adequate response surface method (RSM) design [134], under the form of an Optimal Design as described in Section 3.3. The same software is used for the analysis of variance (ANOVA) and the generation of mathematical, predictive models, as well as the graphical representation of the results. The DOE experimental plan for the 21 suggested single weld tracks is outlined in Table 3-1. Those weld tracks were scanned on the SPS fabricated samples described in Section 4.2 at 3 different build temperatures (T_{build}) at 800, 900 and 1000 ^{o}C, following the methodology described in Section 3.4.1.1.

Figure 4-12 shows an example of the weld tracks scanned at T_{build} of 900 ^{o}C on the samples fabricated at 1000 ^{o}C dwell temperature. Figure 4-13 shows an example of low magnification (50x) optical images taken from the top surface without any metallographic preparation for weld track 14 scanned on samples fabricated at 800, 900, 1000 and 1100 ^{o}C, respectively at T_{build} of 800 ^{o}C. Similar images were taken for all the scanned weld tracks and they are used for checking top surface melting quality (smoothness) and measuring weld track width.

Figure 4-12. Photo images of individual weld tracks scanned at T_{build} of 900 ^{o}C on the samples fabricated at 1000 ^{o}C dwell temperature
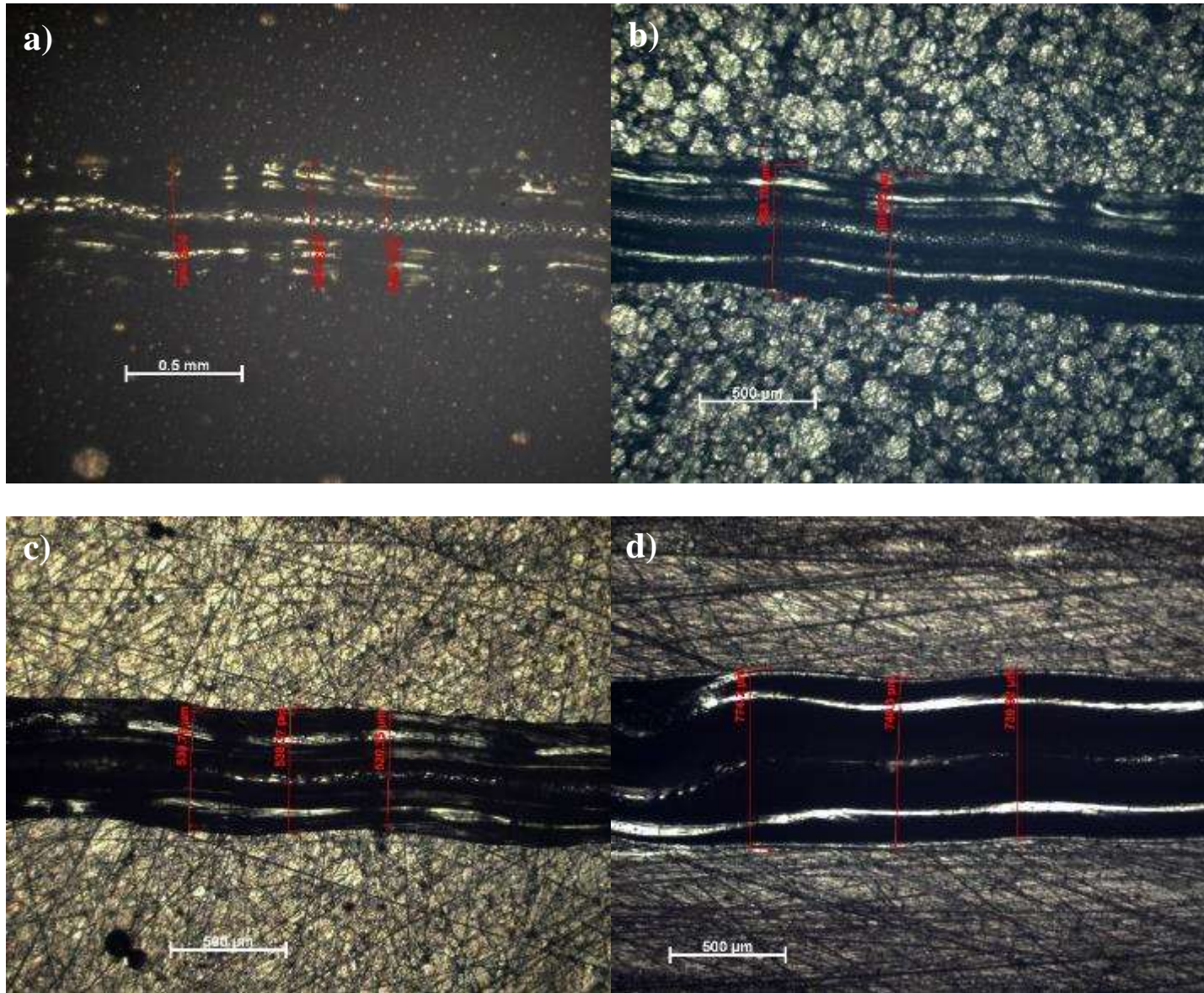
Figure 4-13. Low magnification optical (50x) images of top surface (no metallographic preparation) for weld track 14 scanned on a) SPS800, b) SPS900, c) SPS1000 and d) SPS1100 at 800 ^{o}C T$_{build}$

111
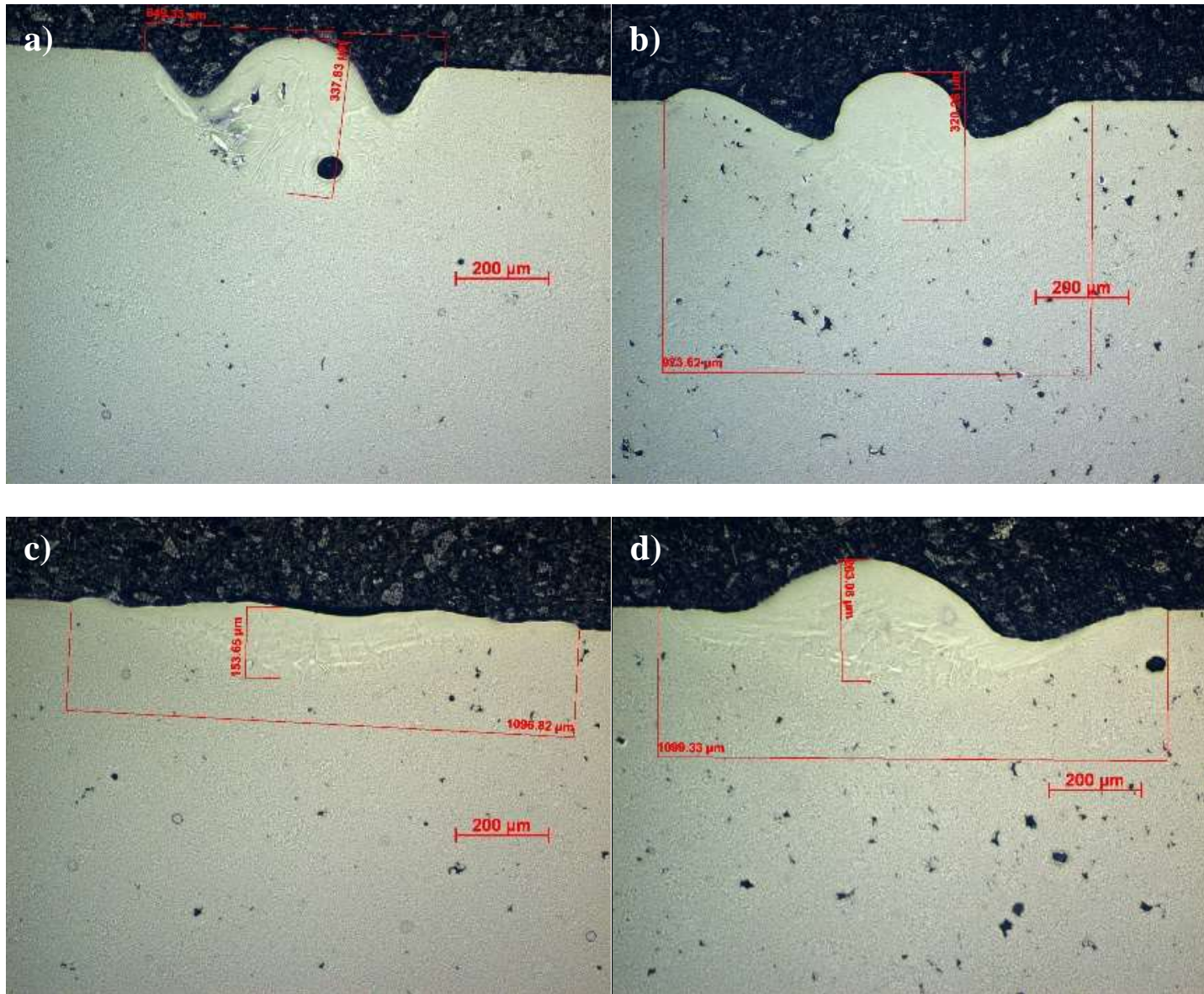
Figure 4-14. Low magnification optical images of polished cross-section for weld tracks a) 15, b) 16, c) 17 and d) 18 scanned on samples fabricated by SPS at 1100 ºC dwell temperature and T$_{build}$ of 1000 ºC

Figure 4-14 shows some examples of low magnification optical images of polished cross-sections for weld tracks a) 15, b) 16, c) 17 and d) 18 scanned on samples fabricated at 1100 °C SPS dwell temperature and T_{build} of 1000 °C. Similar images were taken for all the scanned weld tracks and they were used for measuring the weld pool geometry (width and depth). The melt pool profile analysis for all the weld tracks is covered in detail in the following sections of this chapter. Specifically, the melt pool profile (depth over width) related to energy density is discussed in section 4.4 and shown in Figure 4-20.

4.3.2 Melt Pool Width Analysis

Weld pool geometry data (width and depth) were analysed using the Design-Expert software to find the most accurate models to explain their relationship with the process parameters. For both weld track width and depth, a linear regression fitting seems to be adequate. Table 4-3 shows the results for the analysis of variance (ANOVA) for the weld tracks scanned on the samples fabricated at a dwell temperature of 900 °C and a build temperature of 800 °C. The different terms on this table are showing if the model and which terms are significant. Model F-value of 26.68 implies that the model is significant. There is only a 0.01% chance that an F-value this large could occur due to noise. Values of "Prob > F" less than 0.0500 indicate the model terms which are significant. In this case A and C (EB current and focus offset) are the significant model terms for weld track width. Values greater than 0.1000 indicate that the model terms are not significant. In this case, it seems that EB scanning velocity is not a significant factor affecting melt pool width. The "Lack of Fit F-value" of 0.79 implies that the Lack of Fit is not significant relative to the pure error. There is a 65.37% chance that a "Lack of Fit F-value" this large could occur due to noise.

Table 4-3. ANOVA for Response Surface Linear model for weld tracks scanned on samples fabricated at 900 ºC SPS dwell temperature at 800 ºC T$_{build}$

Analysis of variance table [Partial sum of squares - Type III]						
	Sum of			**Mean**	**F**	**p-value**	
Source	**Squares**	**df**	**Square**	**Value**	**Prob > F**	
Model	6.845E+005	3	2.282E+005	26.68	< 0.0001	significant
A-Beam current	*6.090E+005*	*1*	*6.090E+005*	*71.20*	*< 0.0001*	significant
B-Beam velocity	*154.26*	*1*	*154.26*	*0.018*	*0.8948*	not significant
C-Focus offset	*1.274E+005*	*1*	*1.274E+005*	*14.89*	*0.0014*	significant
Residual	1.368E+005	16	8552.90			
Lack of Fit	*86976.62*	*11*	*7906.97*	*0.79*	*0.6537*	*not significant*
Pure Error	*49869.71*	*5*	*9973.94*			
Cor. Total	8.213E+005	19				

Table 4-4 shows the R squared fitting terms for this model. A high (0.8334) "R-Squared" value indicates a good fitting between actual and predicted values. "Pred. R-Squared" of 0.7359 is in reasonable agreement with the ""Adj. R-Squared"" of 0.8021. The difference of less than 0.2 is desirable. "Adeq. Precision" measures the signal to noise ratio. A ratio greater than 4 is desirable. The ratio of 16.904 indicates an adequate signal.

Table 4-4. R squared fitting terms for weld pool width model for weld tracks scanned on samples fabricated at 900 ºC SPS dwell temperature at 800 ºC T$_{build}$

R-Squared	0.8334
Adj. R-Squared	0.8021
Pred. R-Squared	0.7359
Adeq. Precision	16.904

The diagnostic plot of normal residuals (Figure 4-15-a) indicates that the residuals follow a normal distribution, with just some moderate scatter. No definite patterns like an "S-shaped" curve, are observed. The good fitting of the predicted vs. actual values plot (Figure 4-15-b) indicates, as previously explained, that linear regression is adequate to explain the relationship between weld pool geometry and process parameters. Figure 4-16 shows the relationship between width and the

individual process parameters. Width linearly increases with increasing beam current and focus offset, but it seems to be relatively unaffected by beam velocity.
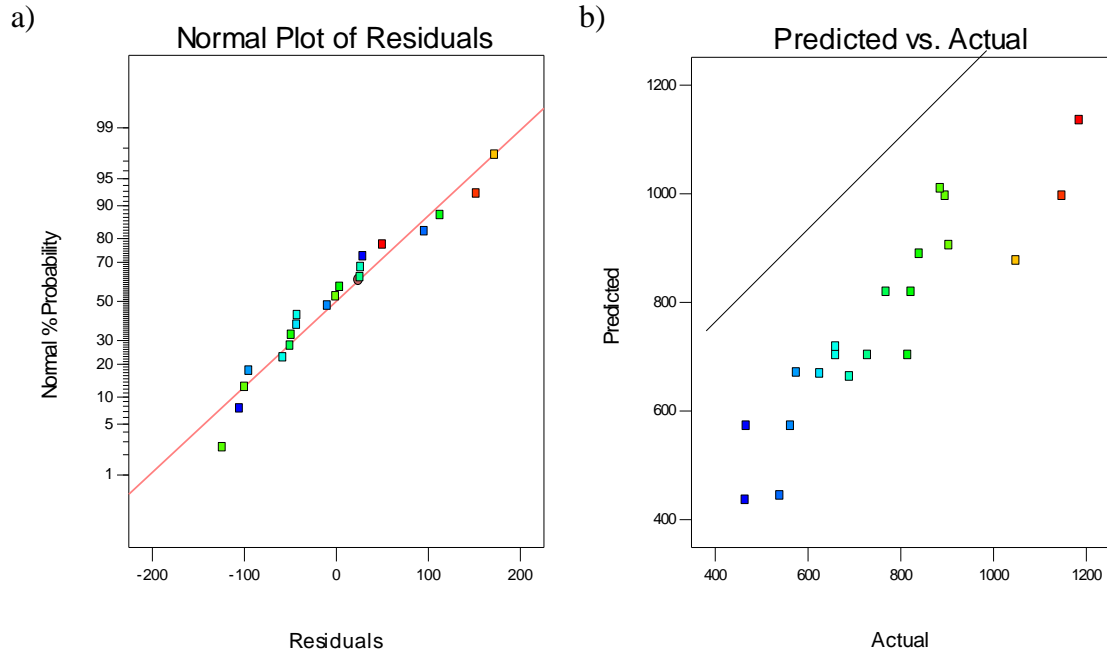
Figure 4-15. Diagnostic plots of a) normal residuals and b) predicted vs. actual fit for weld pool width model for weld tracks scanned on samples fabricated at 900 °C SPS dwell temperature at 800 °C T$_{build}$
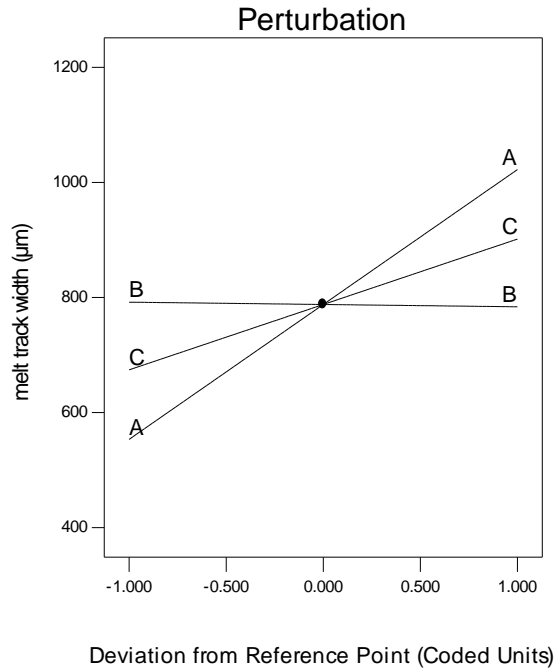
Figure 4-16. Perturbation graph showing the relationship between individual process parameters and weld pool width for weld tracks scanned on samples fabricated at 900 °C SPS dwell temperature at 800 °C T$_{build}$. Where A: beam current, B: beam velocity and C: focus offset, as shown in Table 4-3

The equation (Eq. 4.1) in terms of actual factors can be used to make predictions about the response for given levels of each factor. Here, the levels are specified in the original units for each factor. But this equation cannot be used to determine the relative impact of each factor because the coefficients are scaled to accommodate the units of each factor and the intercept is not at the centre of the design space. Equation (Eq. 4.2) in terms of coded factors can be used to make predictions about the response for given levels of each factor. By default, the high levels of the factors are coded as +1 and the low levels of the factors are coded as -1. This equation is useful for identifying the relative impact of the factors by comparing the factor coefficients.

Melt track width (actual factors) = 182.77 + 29.31 * A -0.0054 * B + 11.36 * C   (Eq. 4.1)

Melt track width (coded factors) = 787.90 + 234.45 * A - 4.02 * B + 113.62 * C   (Eq. 4.2)

Where A: beam current, B: beam velocity and C: focus offset.

116

Similar analysis, as described in this section, was performed for all the different combinations of build temperature and SPS dwell temperature. The results of the ANOVA analysis, R-Squared terms and diagnostic plots is similar for all the models to the one described for the weld pool width for weld tracks scanned on samples fabricated at 900 ºC SPS dwell temperature and 800 ºC build temperature. In all cases a linear regression fitting is adequate to describe the relationship between width and process parameters. The analysis of variance implies that all the models are statistically significant and with quite high R^2 terms. A summary of the "R-Squared" term and the individual coded factor coefficients for all the different models are shown in Table 4-5.

In all cases, as also shown in Figure 4-16, current seems to be the most significant factor followed by focus offset. Velocity, in total, seems to have a much lower effect. The standard deviation between the different models is quite high for this factor. Increase of current will increase imported heat energy and EB diameter (Figure 4-19) [126], so melt pool width is expected to be increased as was actually observed in all the individual models. Increase in focus offset reduces the efficiency of the beam, but at the same time will increase the spot size and consequently the melted area will be increased. So, the actual increase of width with this factor is quite rational. Increase of beam velocity is expected to decrease the heat input per second, so weld track width would be expected to decrease. This factor is insignificant from the ANOVA analysis for most of the models, but it will always have a negative effect on melt pool width.

Table 4-5. Summary of Coded Factors for width analysis for all different models

Model	T_{build}	SPS dwell temp.	R^2	Constant	A: Current	B: Velocity	C: Focus Offset
1	800	900	0.83	787.90	234.45	-4.02	113.62
2	800	1000	0.90	807.67	240.36	-97.38	105.91
3	800	1100	0.82	810.16	217.44	-13.04	97.73
4	900	900	0.88	896.14	310.78	-15.88	139.03
5	900	1000	0.85	947.39	386.87	-7.88	202.75
6	900	1100	0.91	854.11	291.15	-53.11	77.56
7	1000	900	0.85	838.74	252.82	-43.81	158.96
8	1000	1000	0.85	814.98	235.89	-78.97	137.51
9	1000	1100	0.84	840.72	256.46	-15.06	70.19
Mean			0.86	844.20	269.58	-36.57	122.58
St. Deviation			0.03	47.14	49.79	31.88	39.43
St. Error			0.01	15.71	16.60	10.63	13.14

4.3.3   Melt Pool Depth Analysis

The analysis of variance (ANOVA- Table 4-6) for depth indicates that the model and all factors are statistically significant for weld pool depth and for weld tracks scanned on samples fabricated at 900 °C SPS dwell temperature and at 800 °C T_{build}. R-Squared factors (Table 4-7) imply the good fitting of the model.

Table 4-6. ANOVA for Response Surface Linear model for weld tracks scanned on samples fabricated at 900 ºC SPS dwell temperature at 800 ºC T_build

ANOVA for Response Surface Linear model						
Analysis of variance table [Partial sum of squares - Type III]						
	Sum of			Mean	F	p-value	
Source	Squares	df	Square	Value	Prob > F	
Model	3.679E+005	3	1.226E+005	37.44	< 0.0001	significant
A-Beam current	*41108.61*	*1*	*41108.61*	*12.55*	*0.0027*	significant
B-Beam velocity	*2.623E+005*	*1*	*2.623E+005*	*80.07*	*< 0.0001*	significant
C-Focus offset	*28538.68*	*1*	*28538.68*	*8.71*	*0.0094*	significant
Residual	52411.64	16	3275.73			
Lack of Fit	*43943.16*	*11*	*3994.83*	*2.36*	*0.1772*	*not significant*
Pure Error	*8468.48*	*5*	*1693.70*			
Cor Total	4.204E+005	19				

Table 4-7. R squared fitting terms for weld pool depth model for weld tracks scanned on samples fabricated at 900 ºC SPS dwell temperature at 800 ºC T_build

R-Squared	0.8753
Adj. R-Squared	0.8519
Pred. R-Squared	0.7814
Adeq. Precision	20.370

The diagnostic plot of normal residuals (Figure 4-17-a) indicates that the residuals follow a normal distribution, with just some moderate scatter. No definite patterns like an "S-shaped" curve are observed. The good fitting of the predicted vs. actual values plot (Figure 4-17-b) indicates, as previously explained, that linear regression is adequate to explain the relationship between weld pool depth and process parameters. Figure 4-18 shows the relationship between depth and the individual process parameters. In this case velocity seems to be the most significant factor. Depth linearly increases with increasing beam current and decreases with increasing velocity and focus offset.
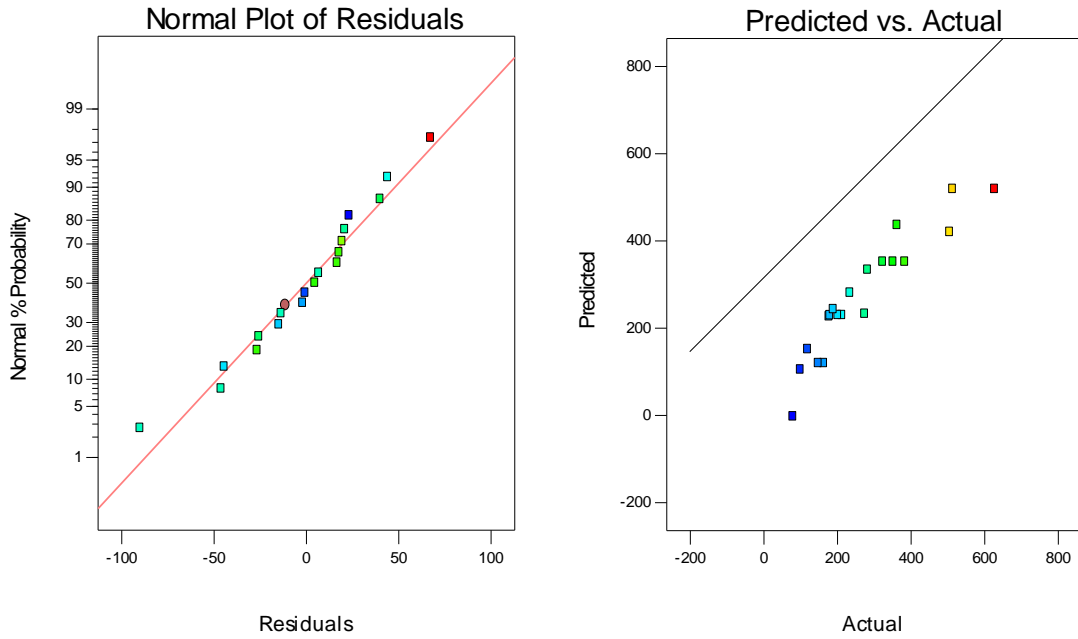
Figure 4-17. Diagnostic plots of a) normal residuals and b) predicted vs. actual fit for weld pool depth model for weld tracks scanned on samples fabricated at 900 ºC SPS dwell temperature at 800 ºC T$_{build}$
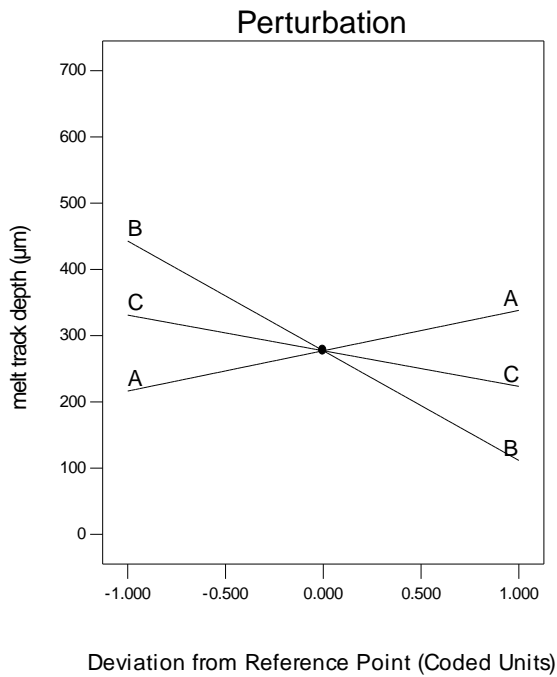
Figure 4-18. Perturbation graph showing the relationship between individual process parameters and weld pool width for weld tracks scanned on samples fabricated at 900 ºC SPS dwell temperature at 800 ºC T$_{build}$, Where A: beam current, B: beam velocity and C: focus offset, as shown in Table 4-6

A summary of the "R-Squared" terms and the individual coded factor coefficients for all the different models is shown in Table 4-8. In all cases a linear regression fitting is adequate to describe the relationship between depth and process parameters. The analysis of variance implies that all the models are statistically significant and with quite high R^2 terms. In all cases and as similarly shown in Figure 4-18 velocity seems to be the most significant factor. Decreasing beam velocity, as described above, is expected to increase heat input per time, so it is quite rational to increase the affected material volume and depth. In the same way decreasing focus offset will increase beam efficiency and consequently it is expected to penetrate deeper into the material. Increasing beam current would be expected to increase the depth, as seems to happen in this case.

Table 4-8. Summary of Coded Factors for depth analysis for all different models

| Model	T_{build}	SPS dwell °C	R^2	Constant	A: Current	B: Velocity	C: Focus Offset
1	800	900	0.88	277.22	60.91	-165.63	-53.78
2	800	1000	0.86	259.55	60.43	-117.45	-26.84
3	800	1100	0.87	267.86	42.01	-146.32	-69.17
4	900	900	0.84	278.32	49.99	-181.65	-43.96
5	900	1000	0.84	242.60	24.78	-157.70	-47.28
6	900	1100	0.76	262.71	42.87	-156.28	-40.47
7	1000	900	0.89	275.31	44.81	-149.99	-44.64
8	1000	1000	0.86	277.03	35.59	-145.10	-55.70
9	1000	1100	0.84	269.74	54.71	-135.64	-62.40

Mean			0.85	267.82	46.23	-150.64	-49.36
St. Deviation			0.03	10.92	11.09	17.14	11.85
St. Error			0.01	3.64	3.70	5.71	3.95

4.4 Melt Pool Geometry Based on Process and Material Properties

As shown in Section 0 for the DOE regression analysis, melt pool width is highly correlated to the heat input (Q) or beam current (I). Focus offset and especially beam velocity seem to have a much

lower effect. Within the experimental window of this study, weld pool depth is mainly affected by beam velocity (v). Similar results can be also observed in Table 4-9 where melt pool width (W) and depth (D) show a very strong correlation to electron beam Power (Q) and beam velocity (v_b), respectively. Those correlation coefficients (r) have been calculated through a statistical multivariate analysis using Pearson's correlation coefficient automatic function in OriginLab software.

In statistics, Pearson correlation coefficient (PCC), also referred to as the Pearson's r or Pearson product-moment correlation coefficient (PPMCC), is a measure of the strength of the linear relationship between two variables X and Y. It can range between +1 and −1. When -1 the variables are correlated by a perfect negative linear relationship, a value of +1 indicates a perfect positive linear relationship and when 0 the two variables are not correlated linearly. [148], [149]

As it can be understood, melt pool width (W) and depth (D) do not depend only on the operational parameters of the process, but also on the material properties of the substrate. The correlation of the melt pool geometry dimensions has been also calculated against their relationship with both EBM operational parameters, as well as material and thermal properties of the substrate. Additionally, the weld pool aspect ratio (depth / (width/2)) and cross-sectional area ($\propto$ width*depth) are also analysed for their correlation with operational parameters and material properties. The half width (width/2) term is used as a reference to the ideal point heat source [124]–[126] which predicts that the aspect ratio (2D/W) of a weld pool is always 1.

In the literature [126] it has been shown that the beam diameter mainly depends on current. The data from an experiment which has been carried out [126] by applying a static electron beam to a Tungsten solid block and measuring the focal dimensions when altering the beam current between 3 -14 mA has been plotted (Figure 4-19) and show a strong linear relationship between beam current and beam diameter. Consequently, it could be anticipated that weld pool width mainly depends on beam diameter and therefore on current, as similarly shown in our results. By increasing the current, the beam diameter increases and therefore the width of the melt pool will also increase. This is also observed in Table 4-11 for the analytical modelling of the melt pool, where melt pool width increases when increasing the beam current. Focus offset is also expected to influence weld pool width by altering the focal dimensions of the electron beam. The Parsons's coefficient shows only a weak correlation between focus offset and weld pool width.

Table 4-9. Pearson's correlation coefficients (r) matrix for weld pool dimensions versus process and material properties

	Description	Units	Source/ Reference(s)	W (m)	D (m)	Cross-sectional area ∝D*W (m²)	Aspect ratio 2D/W	Dim/less Width (v*W/2a) [124]
Q: I*V	Beam Power	W	N/A	**0.7765**	0.3096	0.5442	-0.1092	0.4290
v	Beam velocity	m/sec	N/A	-0.1454	**-0.8021**	**-0.6949**	**-0.7141**	*0.8056*
FO	Beam focus offset	mA	N/A	0.3058	-0.2839	-0.0889	-0.4385	0.1446
E_L: Q/v	Line energy density	J*m^{-1}	N/A	0.5408	**0.8570**	**0.9540**	0.4882	-0.4215
n: $Q*v/(4*\pi*\alpha^2*C_p*\Theta_m*\rho)$	Dim/less operating parameter, n	N/A	[125], [126]	0.3497	-0.4490	-0.2673	-0.5778	**0.9105**
$(Q/k*T_m)*(\alpha/v*W)^{0.83}$	Depth equation from heat conduction theory	m	[131]	*0.2669*	**0.9280**	*0.8619*	*0.7328*	*-0.5906*
E_0: Q/(W*v)	Energy Density	J*m^{-2}	[126]	0.1835	**0.9313**	0.8268	**0.7888**	-0.6573
Q/(D*k*T_m)	Dim/less Depth	N/A	[124]	0.4168	*-0.6395*	*-0.3874*	*-0.7784*	**0.9393**
Where, π=pi, α: thermal diffusivity (m²/sec), C_P: heat capacity (J/kg °C), $\Theta_m = T_m-T_0$ (°C), ρ: density (kg/m³ and κ: thermal conductivity (W/ (m * °C))*								
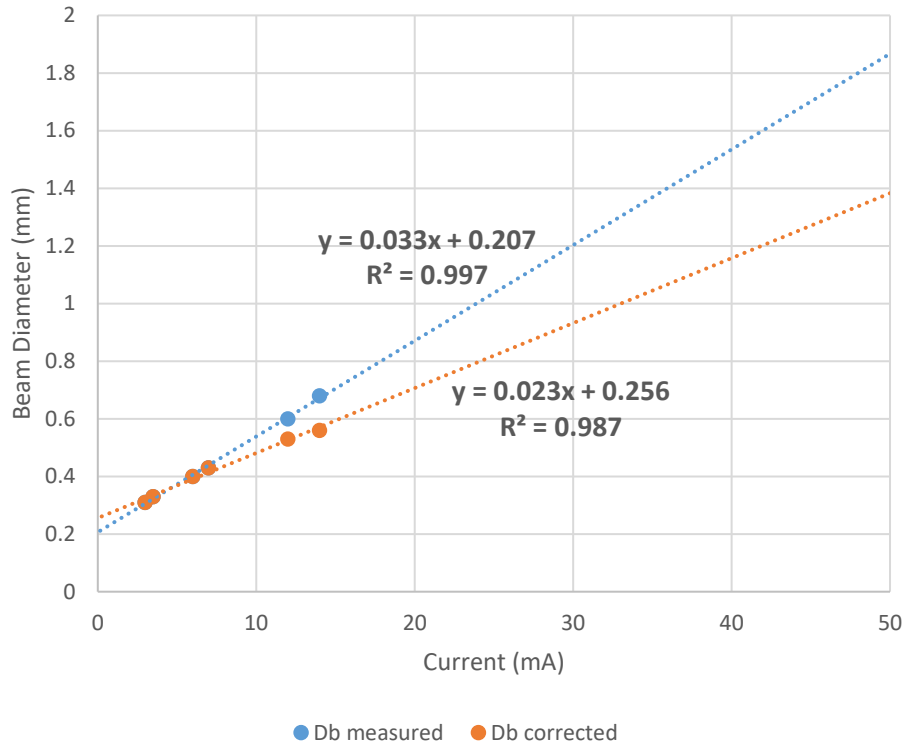
Figure 4-19. Measured focal dimensions (mm) when applying a static electron beam of varying current (mA) on a Tungsten solid block [126]

As shown in Section 4.3.3 and in Table 4-9 melt pool depth (D) is strongly correlated to beam velocity (v). This is also observed in Table 4-10 with the analytical modelling of the melt pool geometry, where melt pool depth obviously increases with decreasing beam velocity. Melt pool depth is more strongly correlated to line energy (Q/v). Line energy (Q/v) also has a very strong positive linear relationship with the cross-sectional area ($\propto$ W*D). On the other hand, the aspect ratio (2D/W) seems to strongly be influenced by beam velocity and not so much by line energy. This shows that the overall melted area remains constant for the same value of line energy (Q/v), regardless of the weld pool shape, which varies with velocity. Focus offset also has a moderate effect on aspect ratio.

There are three main heat source theories in the literature [122], [124]–[126], [144] to model the effect of a moving heat source on a solid substrate; i.e. the point, the distributed and the line heat source and they compute different melt pool geometries. For example, the point heat source model always calculates a weld pool with a perfect half circle shape; width being double the length of the depth (2D/W=1), but, weld pool geometry could vary from shallow and wide to very sharp and deep weld pools. As shown in Figure 4-20, aspect ratio (2D/W) in our results varies from 0.2 for wider and shallow weld tracks and up to 1.9 for deeper and narrower weld tracks.

113

None of the 3 heat source models explains accurately the effect of the electron beam on a metallic substrate across all the range of energy densities (E_0); from very low to very high values. Point and distributed source models assume that the heating effect takes place only on the surface of the substrate [126]. In practise, for high beam power (Q) values (typical for EBM and EBW processing) and relatively low speeds the substrate is evaporating creating a cavity that allows the heat to deposit below its surface. This effect is called the keyhole effect and has been widely investigated in the literature [122], [125], [126]; on the other hand when beam velocity is relatively high this vapour cavity cannot be formed and instead the heat is spread to the surface of the substrate resulting in weld tracks with low depth to width ratio. Those shallow weld tracks are better explained by the line-heat source model [126].

Elmer [126] studied thoroughly this effect and found that there is a transition from shallow to deep penetration as the value of energy density (E_0) increases over a critical E_0 point. This critical point is the energy density when aspect ratio equals and it is different for different materials. For example, it was found to be 10 and 6 J/mm^2 for a 304 SS alloy and for a 2024 aluminium alloy substrate, respectively. For our results (Figure 4-20) this critical point seems to be somewhere in the range between 2-4 J/mm^2. Though, it shall be mentioned that for our study width was used for the corresponding energy density calculations, instead of beam diameter which was used in the literature [126]. Most likely this is an overestimate for the beam diameter value, so the actual energy density values should be somewhat higher than calculated here and the trend would shift towards the right in the graphs in Figure 4-20.

The 2 graphs (Figure 4-20) show the same relationship (E_0 vs 2D/W), but they are colour-mapped, by a) speed velocity (v) and b) beam power (Q) to identify clearer trends and other possible interactions. In Figure 4-20-a, it can be observed a clustering effect for the points having similar speed. As previously shown the aspect ratio (2D/W) increases with decreasing the beam velocity. In Figure 4-20-b, it can be observed that classifying by beam energy (Q) reduces the scatter and clearer trends are shown. Lower beam power, for the same energy density, seems to result in weld tracks with higher aspect ratio, and this most probably is because the speed for those weld tracks is also lower.
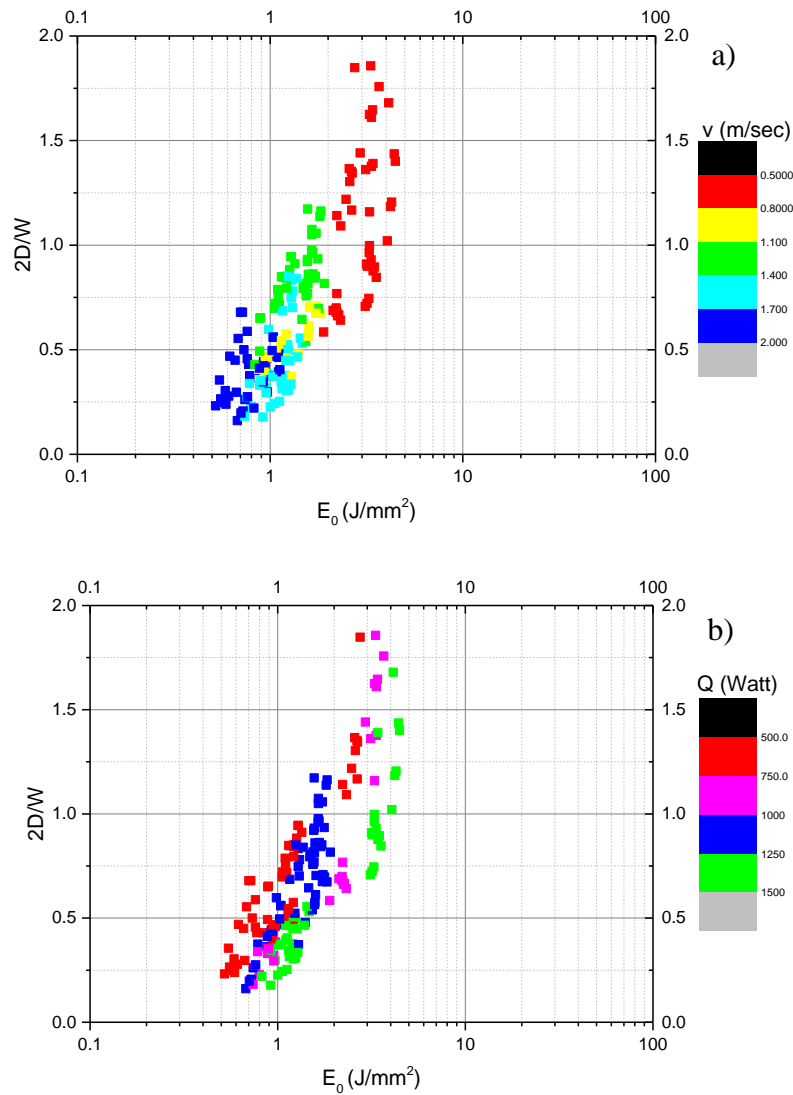
Figure 4-20. Aspect ratio (2D/W) of weld tracks scanned on samples fabricated at various SPS dwell and build temperatures vs. calculated energy density (E₀), colour-mapped a) by speed velocity (v) and b) by beam power (Q)

Other authors [124]–[126], [131] have found very strong correlations between geometrical, operational and material properties. For instance, the non-dimensional analysis (Figure 4-21) shows a very strong correlation between process and material parameters with weld pool geometry for the results from this study; for weld tracks scanned on Ti45Al8Nb substrates of different density and build temperatures, as well as for weld tracks scanned on stainless steel and Inconel substrates using the same EBM system for previous work within the group and for weld tracks scanned on stainless steel and Al alloys from literature data [124], [131]. It is clear from Figure 4-21 that results for completely different alloy families with very different thermal properties fit quite well to the trend when treated in this dimensional manner. This fact allows us to select appropriate electron beam process parameters for required weld pool geometries across materials with different properties without the

need for labour intensive experiments. Figure 4-22 is an expanded insert from Figure 4-21, showing the same non-dimensional analysis for the TiAl EBM data only.
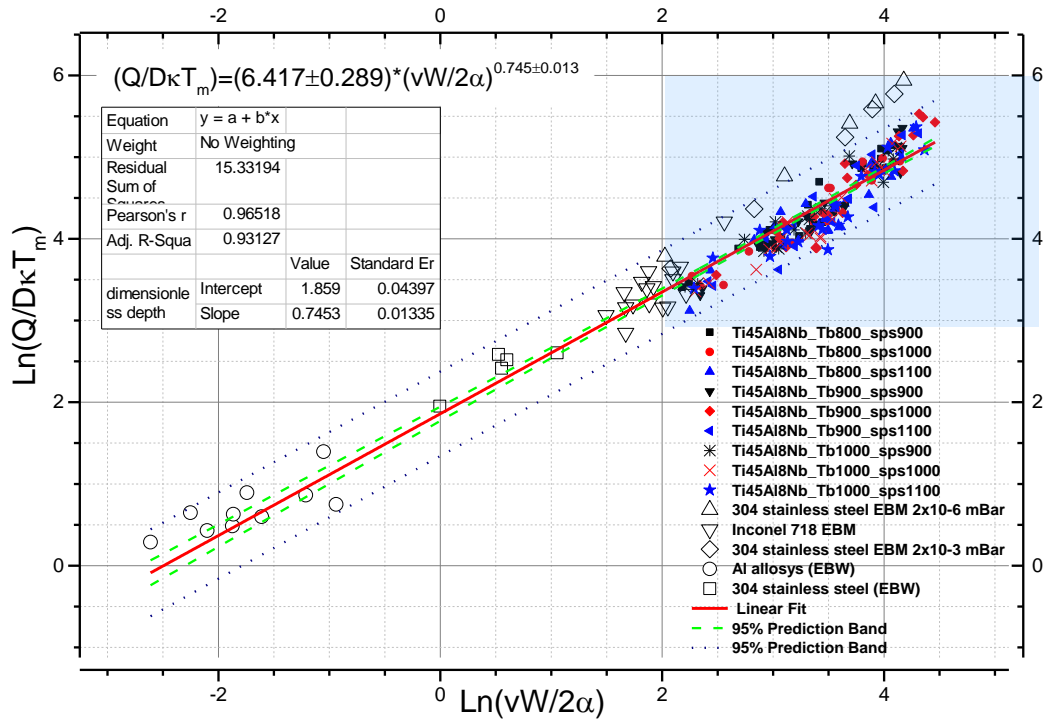
Figure 4-21. Non-dimensional analysis for relating process parameters and material properties to melt pool geometry, where Q: beam power, D: melt pool depth, k: thermal conductivity, T_m: melting temperature, v: beam velocity, W: beam width and α: thermal diffusivity
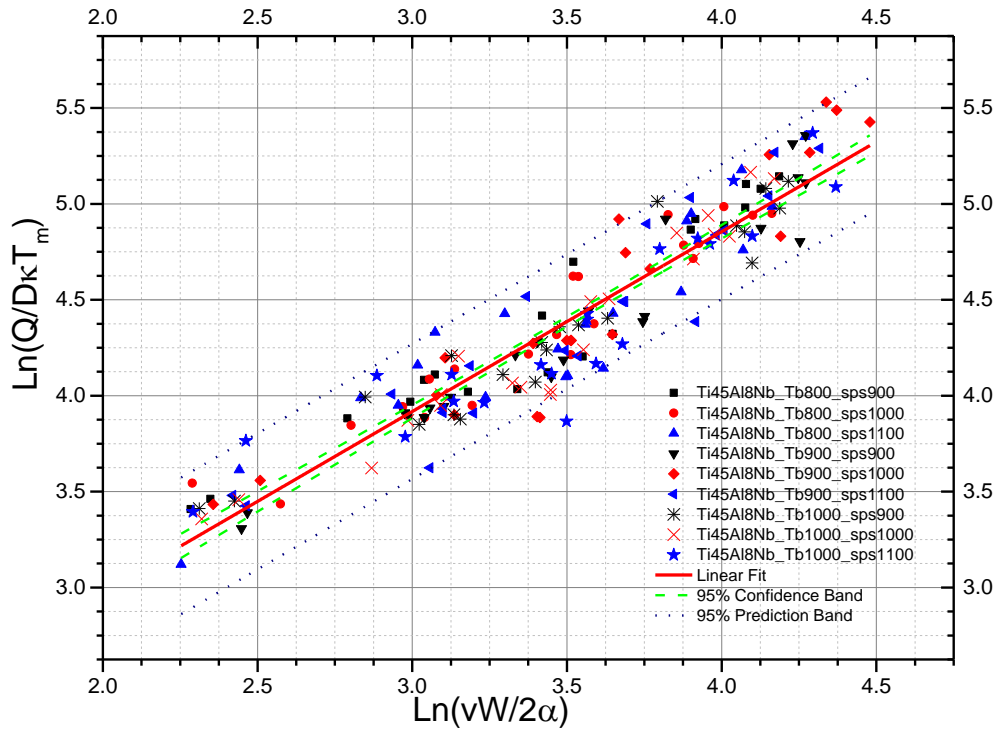
Figure 4-22. Insert for non-dimensional analysis relating process parameters and material properties to melt pool geometry for TiAl EBM data only, where Q: beam power, D: melt pool depth, k: thermal conductivity, T_m: melting temperature, v: beam velocity, W: beam width and α: thermal diffusivity

4.5 Analytical Modelling (modified Rosenthal Equation) for Melt Pool Geometry

A modified Rosenthal equation for moving heat source with a Gaussian distribution [144] was analytically solved by using a MATLAB code developed for this study, as previously described in Section 3.5. The results for Model calculated width, depth and aspect ratio (2D/W) versus the corresponding actual ones for weld tracks scanned at a build temperature of 1000 ℃ on SPS substrates fabricated at 1000 ℃ dwell temperature are presented in Figure 4-23, Figure 4-24 and Figure 4-25. Electron beam efficiency fitting parameter (β) for those calculations was set to be 1 (maximum efficiency). Fitting parameter (β) is a commonly used factor to account for energy losses during beam/material interaction. Typically, for EBM is reported [112], [122], [130] to be between 0.6-0.9.

The analytical model seems to calculate the weld pool geometry quite accurately and especially for depth, showing a high R-Squared term (0.85) for the actual vs. model linear fit. The fits for the width and aspect ratio results are significantly lower, but in any case, there are clear linear trends. From those trendlines for width and depth it seems that the actual values are between 84-88% lower than the model predicted ones. From this fact, one can conclude that the fitting parameter (β) for electron

113

beam efficiency seems to obtain values between 0.84-0.88 for the process window used for the experiments of this work. In Table 4-11 and Table 4-10 are shown some examples of the effect of beam current and speed, respectively on the melting response of Titanium Aluminide substrates.
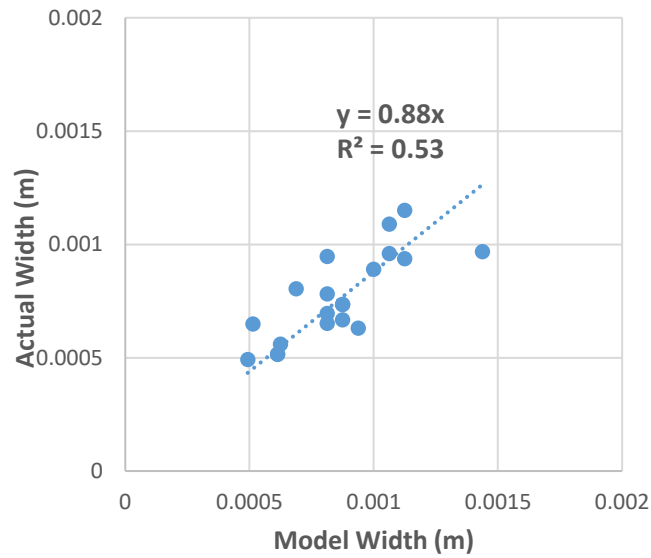
Figure 4-23. Analytical model predicted vs. actual width for weld tracks scanned at 1000 ºC T$_{build}$ on SPS substrates fabricated at 1000 ºC Dwell temperature

Figure 4-24. Analytical model predicted vs. actual depth for weld tracks scanned at 1000 ºC T$_{build}$ on SPS substrates fabricated at 1000 ºC Dwell temperature

Figure 4-25. Analytical model predicted vs. actual aspect ratio for weld tracks scanned at 1000 °C T_{build} on SPS substrates fabricated at 1000 °C Dwell temperature

Table 4-10. Heat source modelling - Effect of EB speed on melting response
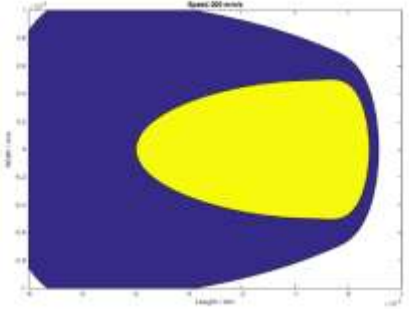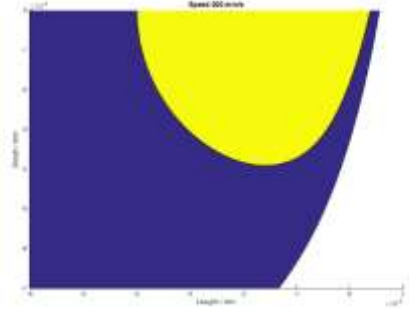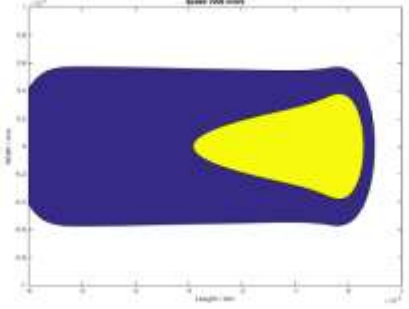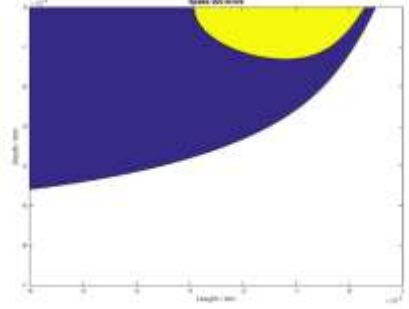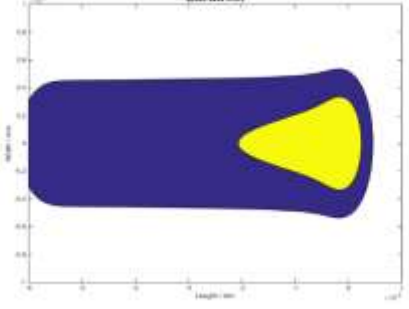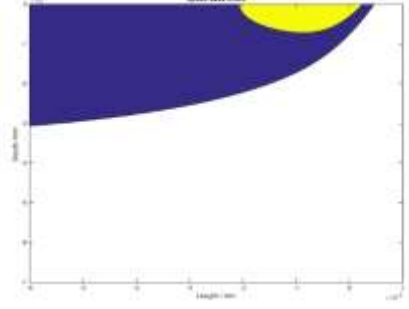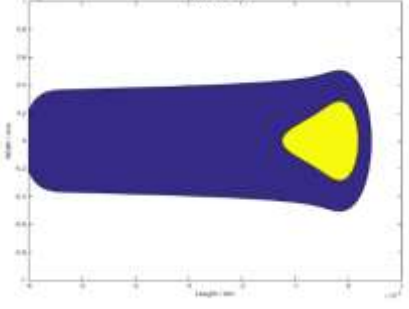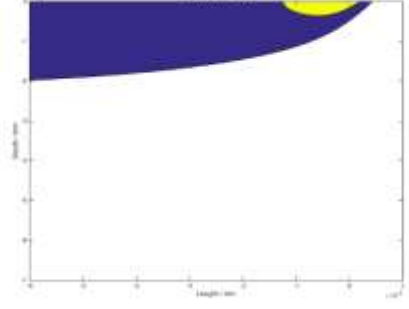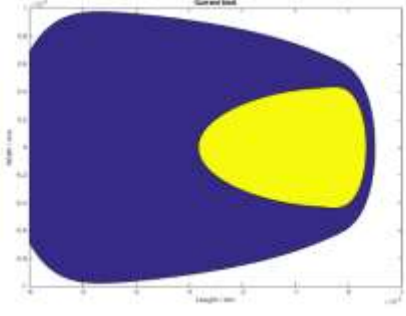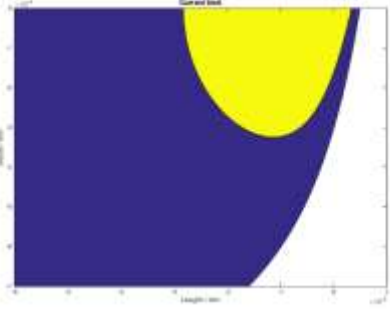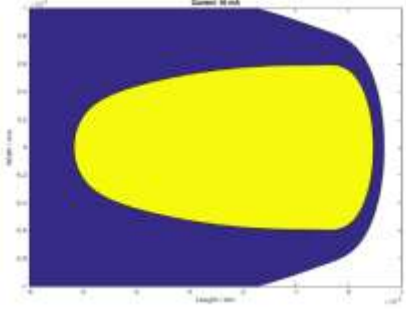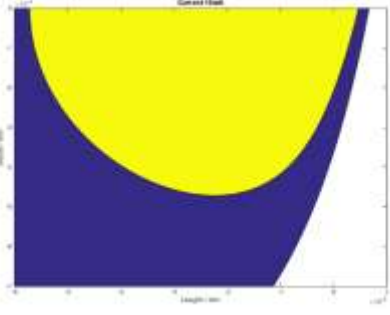
Speed m/sec	Width	Depth
200		
1000		
2000		
4000		

Table 4-11. Heat source modelling - Effect of EB current on melting response

Current (mA)	Width	Depth
5		
10		

4.6 Summary

Substrates of different density were fabricated successfully by SPS; from loosely agglomerated powder particles up to fully dense solid samples. Compaction increased with SPS dwell temperature. Computational analysis and experimental data revealed the effect of key EB process parameters on the melting response of TiAl substrates of known characteristics. Regression analysis of the DOE data was successful in generating statistically significant, predictive models relating key process parameters to melt track width and depth. Statistical multivariate analysis using Pearson's coefficients showed a good agreement with the results from the DOE regression analysis for the effect of key process parameters on melt pool dimensions. Additionally, terms including both operational parameters and material properties (i.e. thermal properties) were statistically analysed against weld pool dimensions; some of those terms showed improved fitting and gave a much better understanding of the physical occurrences taking place during EB melting. Plotting dimensionless terms for melt pool depth and operational parameters for literature data for various materials and experimental data from this study showed a very good fitting; this proves that predictive models and process windows could be generated and used to develop EBM process themes rapidly and efficiently for a required melting response. Analytical heat source modelling (distributed source model) describes weld pool geometry at a quite good level, especially for depth.

5 EBM PROCESS DEVELOPMENT, POST- PROCESSING AND MATERIAL PROPERTIES

5.1 Introduction

This Chapter includes the results and discussion of the main findings from the EBM process development for a Ti45Al8Nb0.2 (TNB-v2) alloy, as well as from the post-processing, mechanical testing and characterisation of EBM as-built and HIPed specimens. The steps and methodology followed are those previously described in Chapter 3 and schematically shown in the process flow chart in Figure 3-1.

The process development has been undertaken using an EBM Arcam S12. Powder feedstock properties are assessed for suitability for the process prior to introduction into the Arcam S12 equipment. Preliminary tests such as "smoke" and sintering tests were performed prior to depositing the first layers. A stable process for preheating and hatching themes was achieved by eye observation through the equipment window and adjusting appropriately the process parameters, in order to have a smooth, relatively dense melt without any "smoking" or "fireworks", which could cause build failure. Further process optimisation for the melting hatching themes was attempted using a DOE approach with reference to as-built top surface quality, process defects and Aluminium loss. Resultant microstructures and micro-hardness results are presented in this Chapter.

Using the optimum themes from the previous step, tensile specimens were manufactured in three builds. Afterwards a study was performed to identify the suitable HIP process parameters to increase as-built component density and eliminate process defects. The optimum conditions were used to HIP some selected as-built tensile specimens. Post-machining was performed to prepare tensile specimens and tensile properties and micro-hardness results are presented for as-built and HIPed specimens at room and elevated temperatures.

5.2 EBM Process Development for a Ti45Al8Nb0.2C Alloy

5.2.1 Powder Feedstock Evaluation

The feedstock used for the EBM layer by layer process development is a Ti-45Al-8Nb-0.2C (at %) pre-alloyed powder. The influence of alloying elements in commonly used TiAl alloys is summarised in Table 2-1. Niobium in general increases the oxidation and creep resistance of TiAl alloys and at high concentrations (>5 at. %) it is used to also increase their high temperature strength [18], [32], [39], [40], [57]. Carbon addition in a small quantity is used to improve high temperature strength and creep resistance by precipitation hardening of finely distributed carbides (P-type (Ti_3AlC perovskites) and H-type (Ti_2A1C hexagonal) carbides) when heat-treating wrought alloys. The P-type carbides, which have a fine needle-like morphology, precipitate homogeneously in the γ-matrix after aging at relatively low temperatures, but tend to be replaced by the coarser and plate shaped H-type precipitates when aging for longer period or at higher ($> 750 \, ^{\circ}C$) temperatures. Those carbides and mainly the P-type, are found to precipitate only in the γ-matrix and this is reported [150] to happen due to the limited solubility of carbon in this phase. [150]–[155]

The as-received powder was sieved to a final size range of 45-150 μm. The particle size distribution of the as-received powder is shown in Figure 5-1.
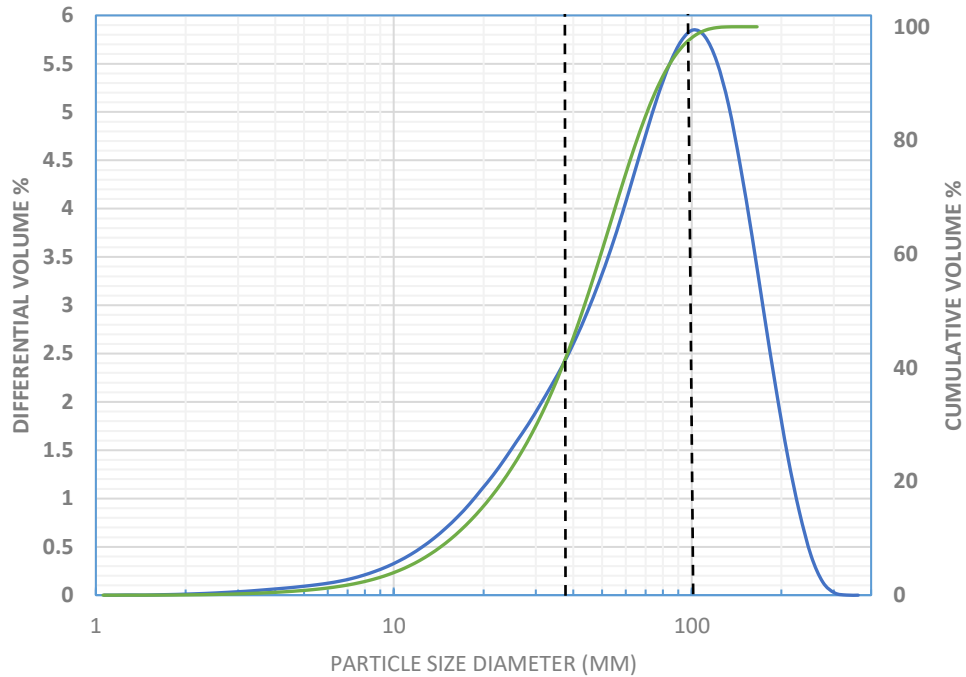
Figure 5-1. Differential and cumulative particle size distribution of powder feedstock used for EBM process development

Figure 5-2 (a) and (b) shows the morphology of the sieved powder; particles are mostly spherical with a low amount of satellites. Only a very few off-size particles could be observed with size similar to the satellite particles (~5 μm). Those fine, off-size particles most probably come from satellites broken from the larger particles. Additionally, a very few non-spherical, elongated particles could be observed. The average Hall flow was measured to be 26.9 seconds, which is comparable with the flowability of standard Ti64 powder supplied by Arcam. Apparent density was measured to be 57.6 %, which is higher than the minimum required of 50%. Consequently, this powder meets the Arcam requirements for a spherical, free flowing and high-packing density powder as described in Section 3.2.2.
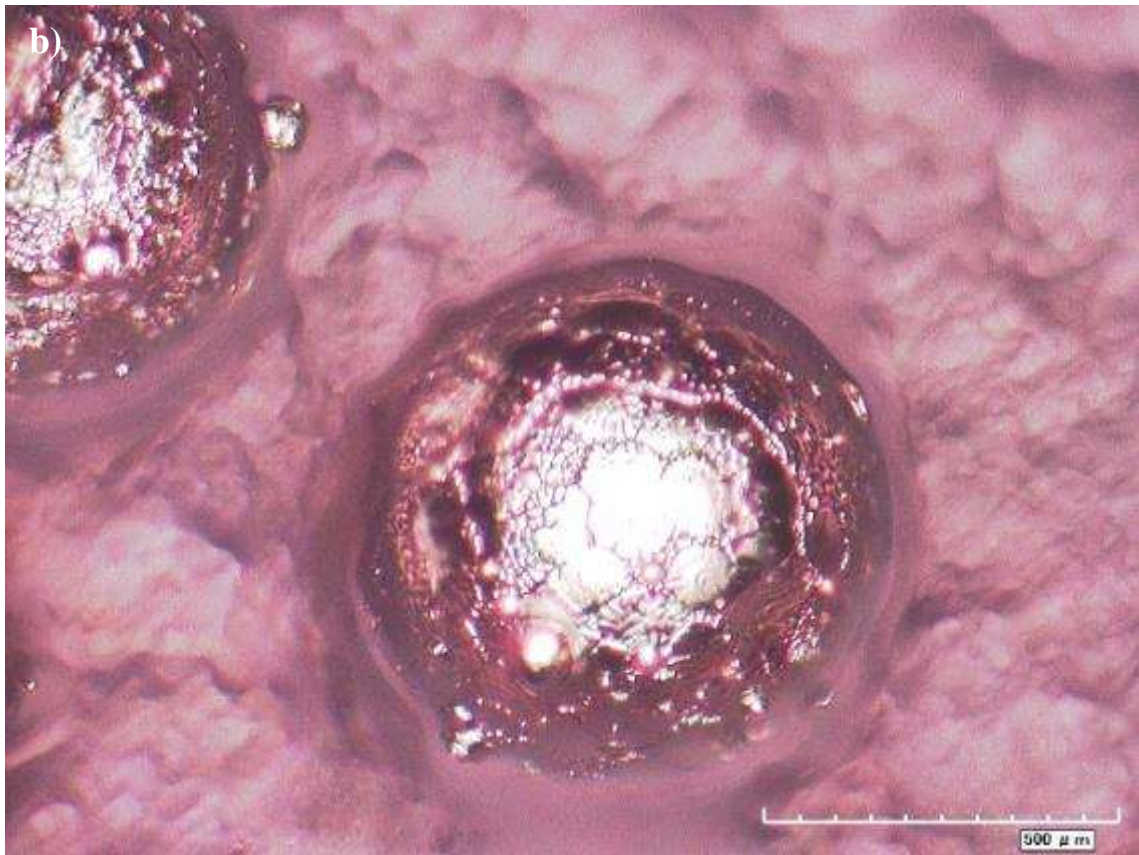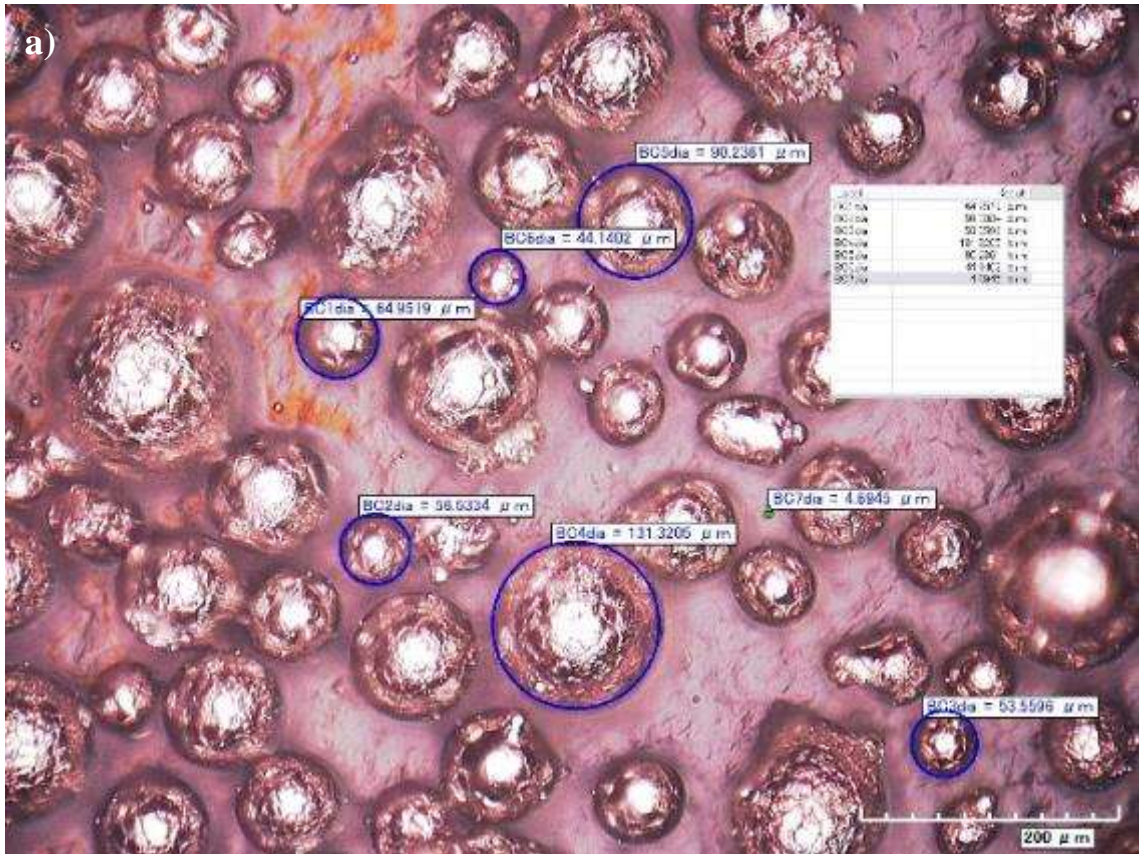
Figure 5-2. Optical images for powder particle morphology at a) 200x and b) 500x

Figure 5-3 shows a cross-section of a powder particle. Some porosity could be observed; but the shape of this porosity is not only spherical, as would be expected due to gas atomisation powder production. The true density of the particles was measured by using Helium Pycnometry and it was found to be 4.251 g/cm^3, which is slightly higher than the powder used for the parametrical studies in Chapter 4.
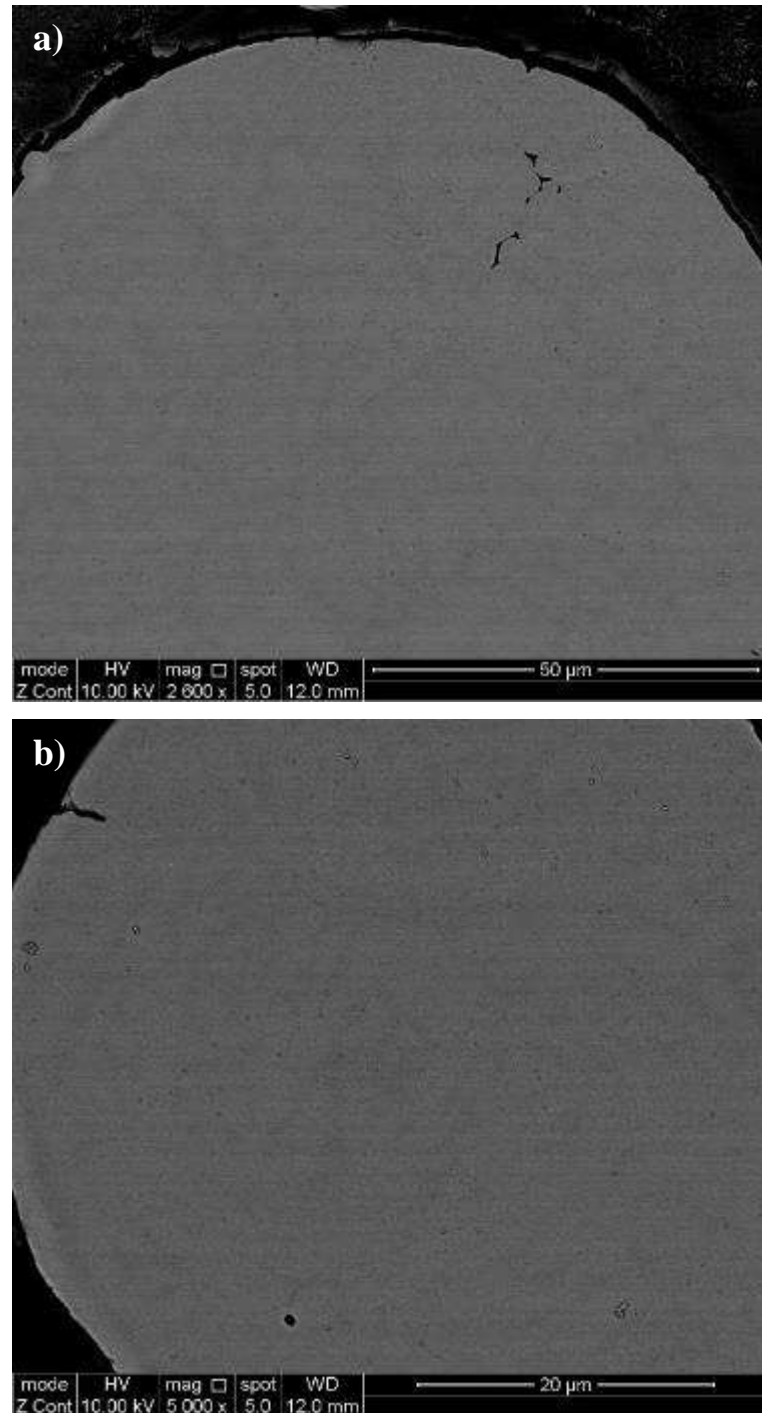
Figure 5-3. Back-scattering SEM images of polished powder particle cross-section

The as-received powder was sent for full chemical analysis at AMG, as described in Section 3.6.9. The results (in at %) are shown in Table 5-1, below.

Table 5-1. Chemical content (at %) of as received powder feedstock

Elements	Ti	Al	Nb	C	O	N	Fe
Chemical Content (at %)	46.58	44.86	8.1	0.18	0.19	0.02	0.04

5.2.2 Heating and Preheating Process Themes Development

As described in more detail in Section 3.2.4 the first important step in EBM process development of a novel alloy is to define a stable process. To do so an appropriate build temperature (T_{build}) and preheating process theme should be defined for the specific material and powder. After performing all the steps described in Section 3.2.4 and by applying some modifications to the Arcam S12 equipment, mainly related to the required high build temperature, a stable process was found to be feasible. The main outcome of this experimental procedure was that a stable build temperature of about 1050-1090 °C was required throughout the process for the specific powder feedstock and base plate dimensions (100x100x10 mm). The layer thickness was set in this study as a constant, 70 µm.

At temperatures below 1000 °C the process was unstable with lots of "arc tripping" and failure occurred as a result of the "smoke" effect described in Chapter 3. Even at temperatures up to 1040 °C the process was not stable for long times and typically failed at a specific build height (~6 mm). The resulting powder "cake" was observed to be very loosely bonded, indicating insufficient sintering. It can be assumed that at this height the loosely sintered powder particles have not enough electrical conductivity and mechanical strength to extract the electrical charge due to the process and withstand the repelling forces caused due to this electrical charging, respectively.

At higher temperatures above 1100 °C the process was very stable, but a significant swelling (Figure 5-4-a) of the top surface of the built specimens, as well as much lower definition of fine features was observed. This is probably due to overheating of the melted surface. In addition, the powder "cake" sinter (Figure 5-4-b) was very hard and the powder could not be readily recycled. A stable temperature between 1060-1070 °C was the optimum for this powder feedstock. The process was stable and the layers were observed to be very smooth during sintering and melting. The only drawback was that the powder cake was still slightly over-sintered, but powder was recoverable (Figure 5-4-c). On this occasion, significant temperature loss (20-30 °C) was observed to take place during the first layers, shifting the process into the "unstable" region, causing failures. To compensate

for this temperature loss the starting build temperature was set to be slightly higher at 1080 ^{o}C and the preheating themes were optimised to keep a stable temperature in the region of 1050 – 1070 ^{o}C for the first 30 minutes of the process.
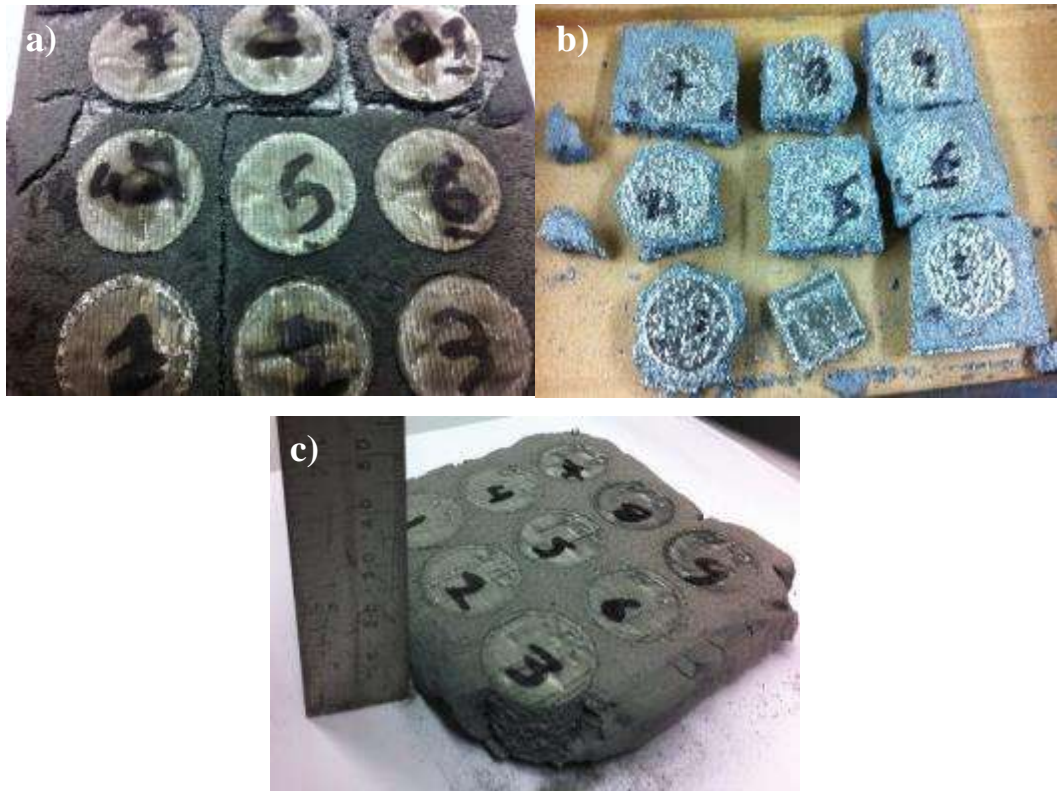
Figure 5-4. Images showing the sintered powder "cake" after various attempts for heating and preheating process themes optimisation

5.2.3   Melting Hatching Process Themes Development

After a stable process was achieved, a DOE approach was used in the form of a Central Composite Design as described in Section 3.3. The DOE experimental plan used for this study is outlined in Table 3-2 and Table 3-3, for DOE-2 and DOE-3, respectively. Using those two experimental plans short cylindrical samples were fabricated by changing two of the key hatching process parameters i.e. speed function and focus offset. In the second experimental plan (DOE 3) the "Surface Temperature" (ST) function was also altered after each 5 mm of build height, as explained in Section 3.4.1.3. Examples of such samples are shown in Figure 5-5. Those samples were assessed for top surface quality, component density and process defects, Al evaporation losses, microstructures and micro-hardness.
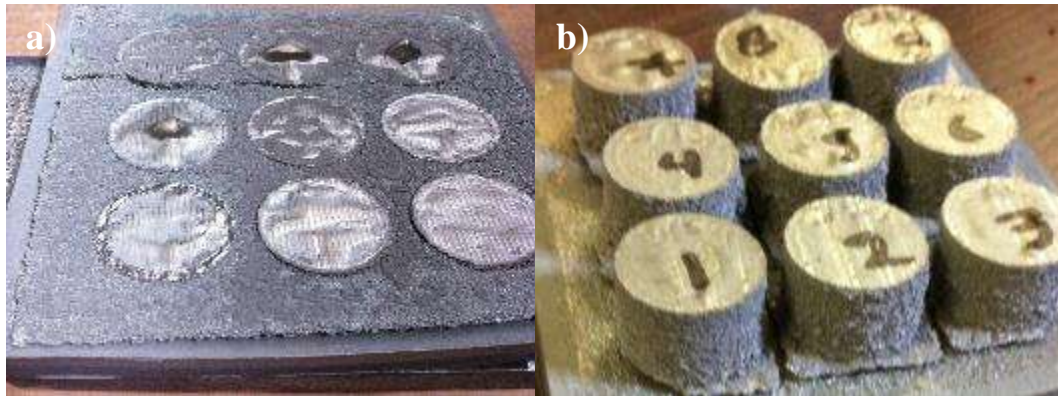
Figure 5-5. Images showing as deposited short samples fabricated for hatching process development for a) DOE-2 and b) DOE-3

5.2.3.1 Top Surface Quality (Swelling)

Surface roughness is a critical factor affecting the performance of a component [156]. Poor as-built surface finish is one of the weaknesses of powder bed AM techniques and it depends on many factors such as powder size, layer thickness, beam power, scan speed, hatching distance, etc [157], [158]. For EBM surface finish is typically coarser compared with laser based AM techniques, due to the coarser powder and layer thickness used [6]–[8]. As shown in Figure 5-5, the roughness on the sides of the components is different and noticeably coarser than on the top surface. The side areas are resulting from contour melting and they are in contact with the sintered "powder cake" during the EBM process. On the other hand, the top surface is resulting from hatching melting of area which is not in contact with the sintered "powder cake" during the EBM process. Only hatching melting was studied for this work and no optimisation effort was made for the contours.
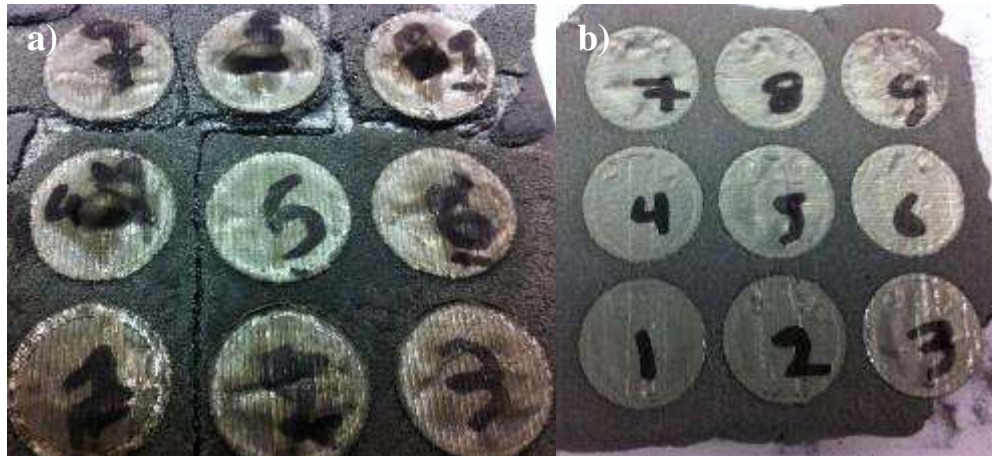
Figure 5-6. Images showing as deposited short samples top surface quality for a) DOE-2 and b) DOE-3

Figure 5-6 shows images of the top surface of the as-built short cylindrical samples for DOE-2 and DOE-3. The surface quality was subjectively assessed by visual observation and using an arbitrary scale with values between 0-6; 0 being the best quality with the flattest/smoothest surface and 6 being the worst quality with swelling similar to what it can be observed for samples 4, 8 and 9 in image Figure 5-6-a). In the selected experimental window, it seems (Figure 5-7-a and Figure 5-8-a) that there is a linear relationship between top surface quality (swelling) and both focus offset and speed function for both DOEs. Both models show adequate fitting (Figure 5-7-b and Figure 5-8-b) with R-Squared values of 0.74 and 0.83, respectively. Speed function in both cases is the most significant factor. Speed function influences line energy and heat input; when lowering the speed function heat input increases, leading to overheating of the melted surface and swelling is more significantly observed at speed functions lower than 32. Optimum surface quality is observed at speed functions higher than 56. Increasing focus offset seems to have a smaller positive effect.
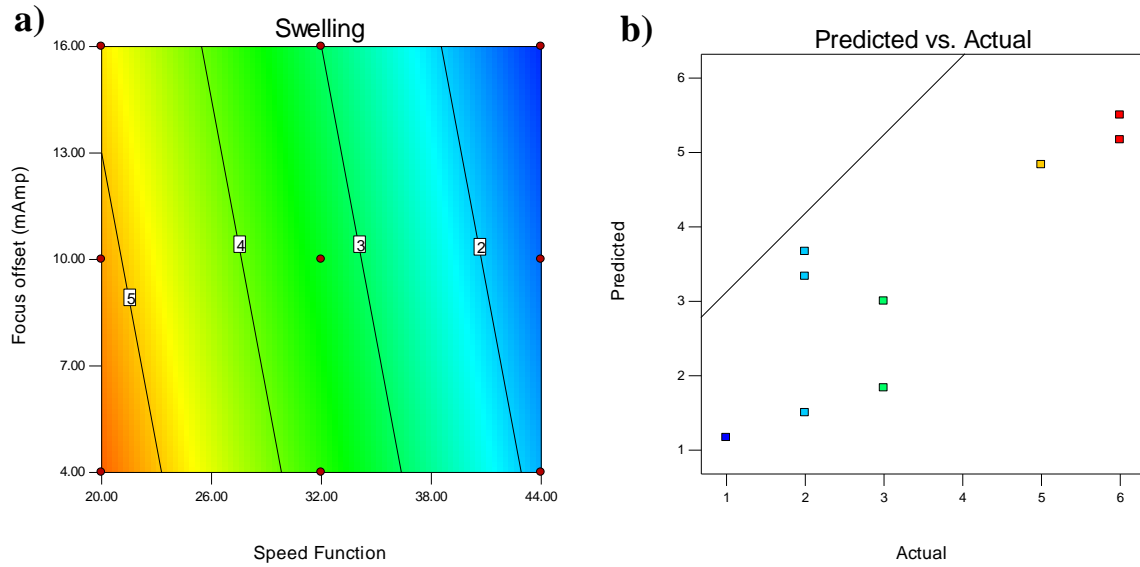
Figure 5-7. a) Contour plot showing focus offset and speed function effect on top surface quality and swelling for DOE-2 and b) diagnostic plot showing predicted vs. actual fit
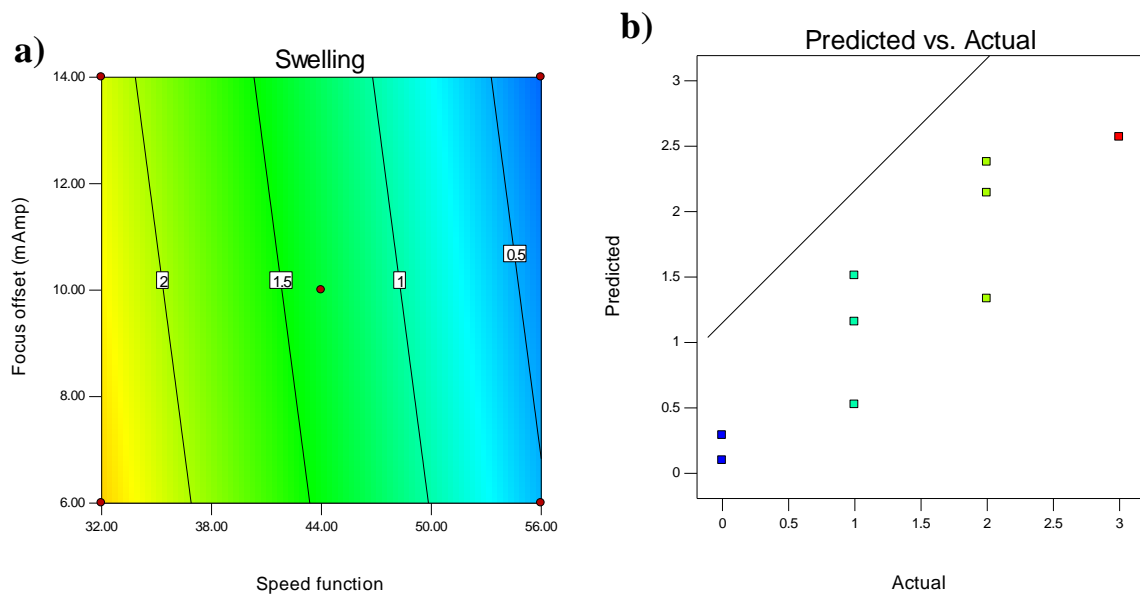
Figure 5-8. a) Contour plot showing focus offset and speed function effect on top surface quality and swelling for DOE-3 and b) diagnostic plot showing predicted vs. actual fit

This subjective assessment was mainly focused on the swelling effect and it was used to define the process window to achieve maximum as-built density but without any swelling. Visual observation is often used to quickly assess the quality of as-built or sectioned EBM specimens in terms of geometrical accuracy and the presence of noticeable defects, such as lack of fusion, delamination and

swelling. Those obvious process defects are attributed on using insufficient or excess energy and such defected samples might not further be tested during a labour-intensive process development. For this work the process development was done in a tight 6 weeks' period and there was no access to more objective and quantitative surface roughness measurement techniques. The obviously swelled samples were not further tested and visual observation was enough to conclude that excess energy was used.

Surface roughness can be quantitively calculated as the relative roughness of a linear profile line or surface area and most commonly is expressed as a single numeric parameter R_a or S_a. R_a for the surface roughness over a profile length, L is defined as:

$$R_a = \frac{1}{L}\int_0^L |f(x)|dx \qquad\qquad \text{Eq. 5.1 [158]}$$

where f(x) is the deviation of surface height at x from the average height over the profile, when the overall profile is assumed to be level. When the height f_n is measured at N locations along the profile length L, the 2D surface roughness can numerically be calculated as:

$$R_a \approx \frac{1}{N}\sum_{i=1}^{N}|f_n| \qquad\qquad \text{Eq. 5.2 [158]}$$

The area surface roughness (S_a) of area A is defined as the average magnitude of the surface profile from the mean plane, when the mean plane is assumed to be level. In this case, with NxM measured deviations $f_{i,j}$ the roughness is approximated as N.

$$S_a \approx \frac{1}{NM}\sum_{i=1}^{N}\sum_{j=1}^{M}\left|f_{ij}\right| \qquad\qquad \text{Eq. 5.3 [158]}$$

Surface profilometers are suitable for measuring surface roughness for most applications. There are two types of surface profilometers; the stylus (contact) type and the optical type. Stylus type work like a phonograph and normally used to measure 2D or large step surface profiles (roughness). For optical type, there is no contact with the surface, measurement speed is very high and this method is especially used to get 3D surface topography and/or small step surface profiles. Optical profilers could have quite high lateral resolution and accurate height resolution and so can be used to measure fine asperities. In nano-level, atomic force microscopes (AFM) and electron scanning microscopes (SEM, TEM) offer even higher spatial resolution and are typically used but can be destructive of the surface, depending on the materials and their small fields of view present difficulty in finding the defects. SEM cannot measure surface roughness quantitatively in conventional modes and AFM cannot measure roughness greater than 10 μm in Z height. [159]

5.2.3.2 Porosity and Process Defects

Porosity and process defects were measured as a percentage of the total surface area of a cross-sectioned and polished plane for selected samples from both DOEs by using image analysis software as described in Section 3.6.10. In both cases the most suitable suggested model (Design-Expert software analysis) to explain the effect of speed function and focus offset on porosity (%) is a two-factor interaction in the form $y = b_1+b_2X_1+b_3X_2+b_4X_1X_2$. R-Squared values are 0.80 and 0.60 for DOE-2 and DOE-3, respectively. It shall be noted that none of the models or factors were found to be statistically significant by the ANOVA analysis. Although, in the selected experimental window it seems that there is a similar trend in both models, as shown in Figure 5-9-a and Figure 5-10-a.

The maximum component density (near to 100%) is observed in the area with speed function lower than 38 and focus offset current higher than approximately 8 mA. In this area increasing speed function and focus offset increases component density. On the other hand, at the same speed function area (<38), when focus offset is below 8 mA, porosity (%)significantly increases with decreasing speed function and focus offset. In the region of higher speed functions (>44) the opposite effect seems to take place, i.e. for focus offset values higher than 8 mA, component density decreases by increasing focus offset and speed function. At focus offset values, lower than 8 mA density seems to increase by increasing speed function and decreasing focus offset even though we don't have enough data in this area to be conclusive in our assertion. Similar results are shown in Figure 5-11, when plotting porosity (%) as a function of line energy density (Joule/m). Porosity seems to decrease with increasing line energy density for the experimental points with high (blue markers) and intermediate (green markers) focus offset values, but seems to increase with increasing line energy density for the experimental points with low (red and yellow markers) focus offset values.

Lowering speed function and focus offset values is expected to have a similar effect on melting response for both process parameters, i.e. increasing melt pool depth and possibly decreasing melt pool width at the same time. As described in more detail in Section 4.4 and also observed in the literature [126] and in Figure 5-11, at high line energy and low speeds (i.e. low speed functions) a deeper penetration tends to take place with a narrower melt pool width. On the other hand, at much higher speeds and lower line energy density values (i.e. high speed functions) a shallower melting tends to occur with the melt pool spreading in a larger width and lower depth. It seems that at low speed function and focus offset values, a deeper and narrow melting pool forms, resulting in inadequate overlapping of adjacent melting hatching lines and subsequently to a lower component density for a given line offset. On the other hand, at high speed function and focus offset values a shallow and wider melting pool seems to be formed, leading to an inadequate consolidation of

neighbouring melting layers and subsequently to a lower component density for a given layer thickness.
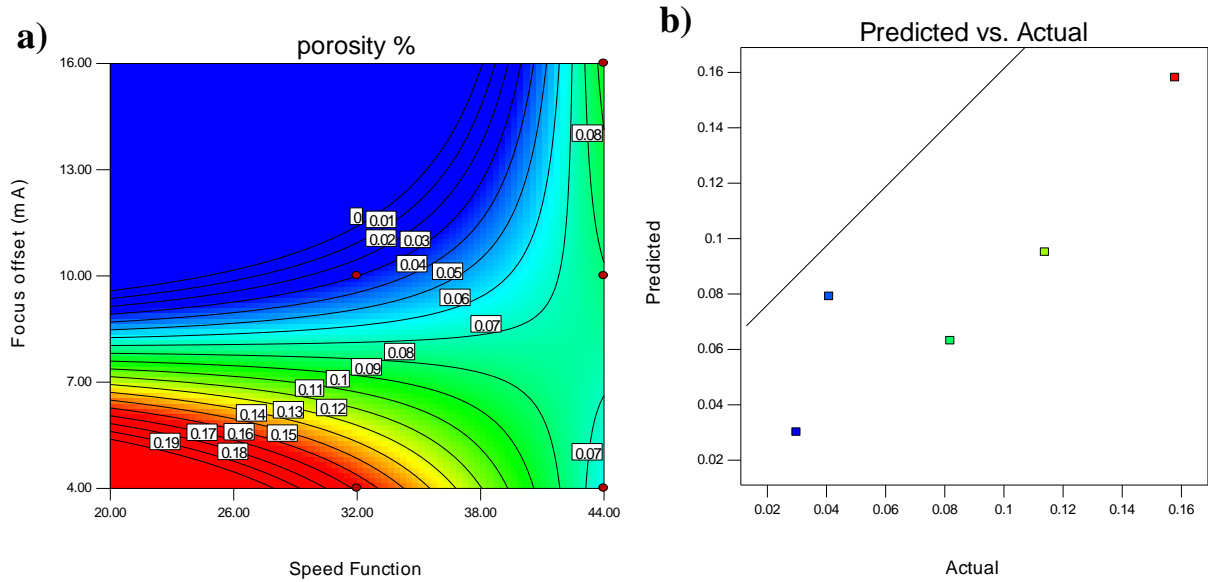
Figure 5-9. a) Contour plot showing focus offset and speed function effect on porosity for DOE 2 and b) diagnostic plot showing predicted vs. actual fit
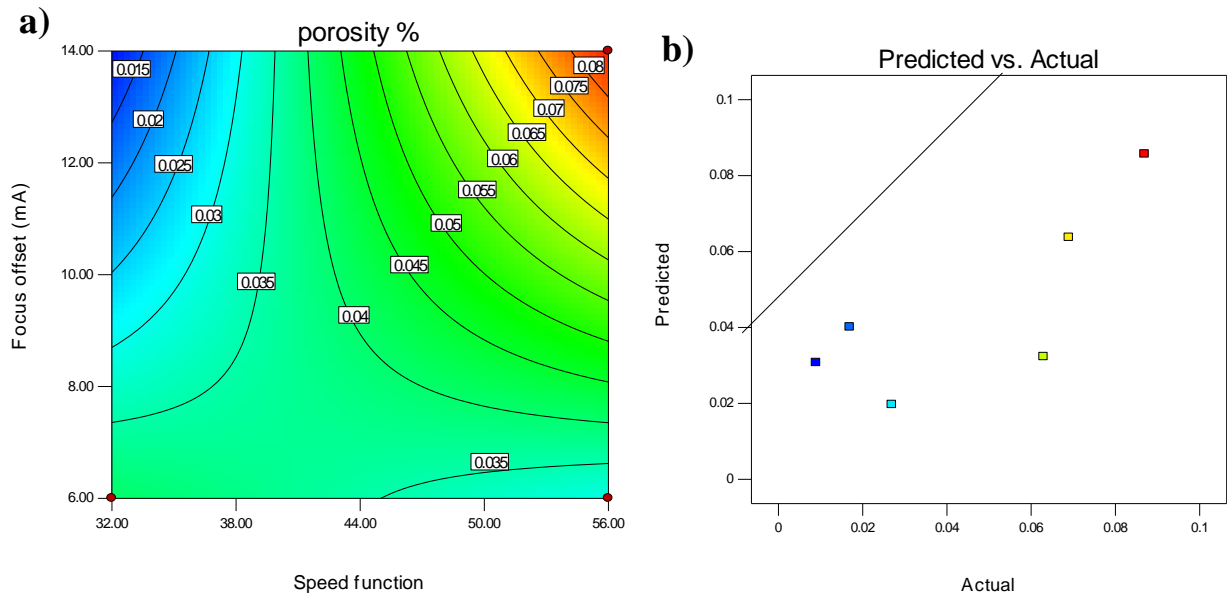
Figure 5-10. a) Contour plot showing focus offset and speed function effect on porosity for DOE 3 and b) diagnostic plot showing predicted vs. actual fit
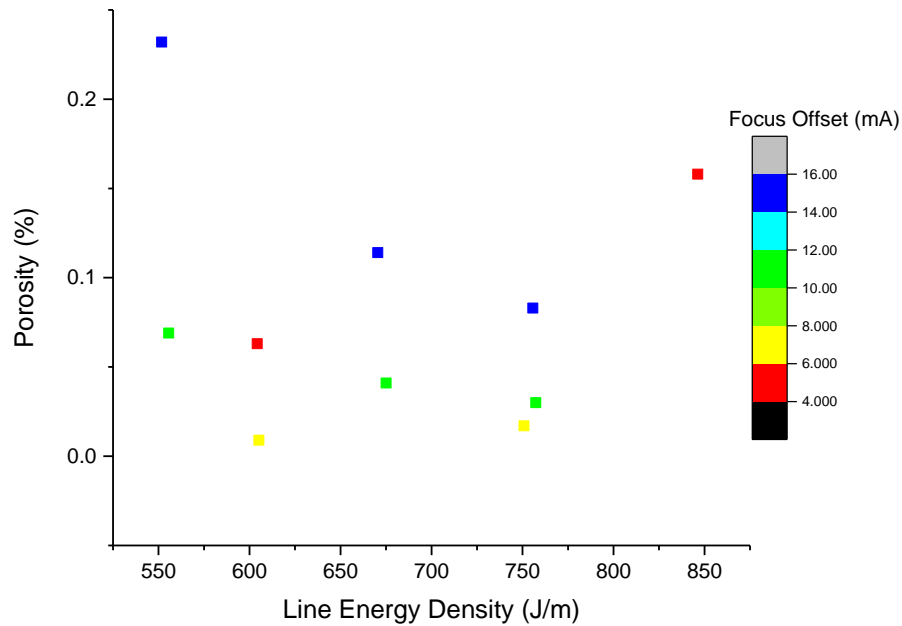
Figure 5-11. Porosity (%) versus line energy density (J/m) colour-mapped by focus offset (mA)

5.2.3.3   Al Evaporation Losses

Chemical content was measured for selected samples to monitor the Al evaporation loss (%). More detailed analysis for the effect of EBM process parameters on Al evaporation loss is presented in the following chapter (Chapter 6). Specifically, in Sections 6.4.1 and 6.4.2 and Figure 6-11, Figure 6-12, Figure 6-13 and Figure 6-14 the effect of focus offset and "Surface Temperature" function, respectively, are described.

From Figure 5-12, it seems that there is a quadratic relationship for focus offset with a minimum for Aluminium loss (%) in the range between 8-10 mA. This quadratic relationship can be explained by considering evaporation behaviour in two areas. In the first area as focus offset increases from low values, evaporation decreased as an effect of decreasing electron beam intensity per surface area. In the area above the range between 8-10 mA the heat affected zone possibly increases (width/depth ratio increases) with subsequent increase of evaporation area, as well as evaporation time as an effect of possible increase of overlapping between the adjacent hatching lines. As one would expect Aluminium loss (%) linearly increases by lowering speed function value, as heat input and subsequently actual surface temperature will increase.

113
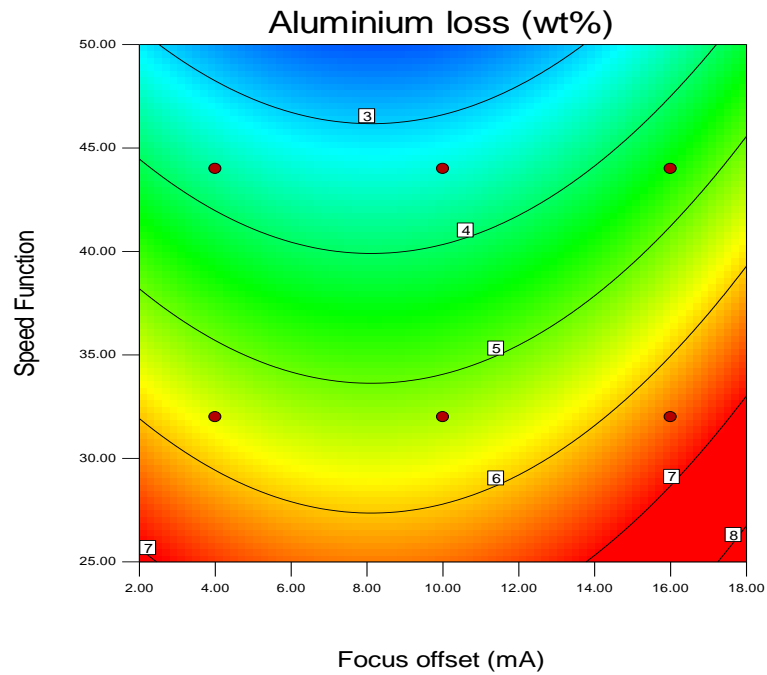
Figure 5-12. Al evaporation losses (at %) as a function of speed function and focus offset

Increase of "Surface Temperature" function (Figure 5-13) increases Al evaporation loss for all the different samples of DOE-3 (Table 3-3) as a result of the actual surface temperature increase. Here, again, it shall be noted that the "Surface Temperature" function was introduced by Arcam when they were first developing the EBM process for tool steels in order to maintain a constant temperature for each layer. "Surface Temperature" function values represent the temperature in Celsius for tool steels but they are arbitrary for other materials. In Figure 5-14 the "Surface Temperature" EBM function values for the samples of DOE-3 are plotted versus the corresponding "Model" calculated surface temperature values. The model estimated temperature for the Titanium Aluminide alloy is higher than what the "Surface Temperature" function indicates and increases at a much lower rate.
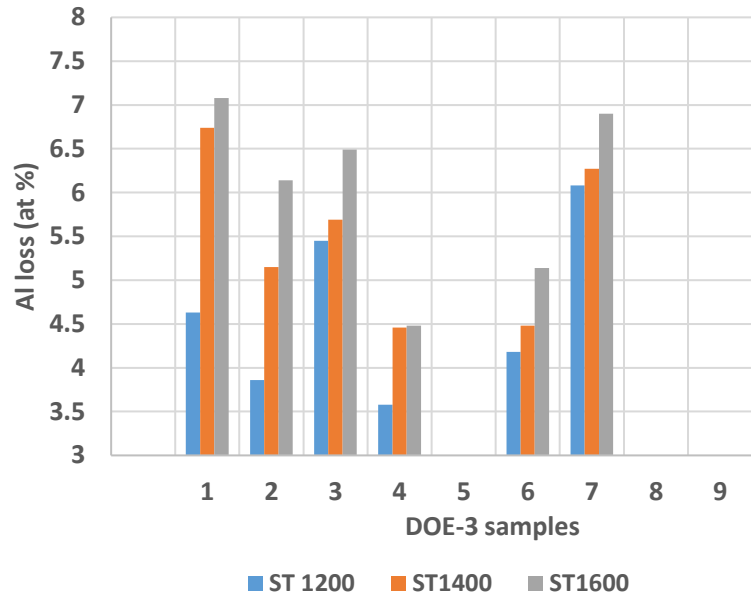
Figure 5-13. Al evaporation losses (at %) as a function of arbitrary "Surface Temperature" (ST) function for DOE-3 samples (Table 3-3)
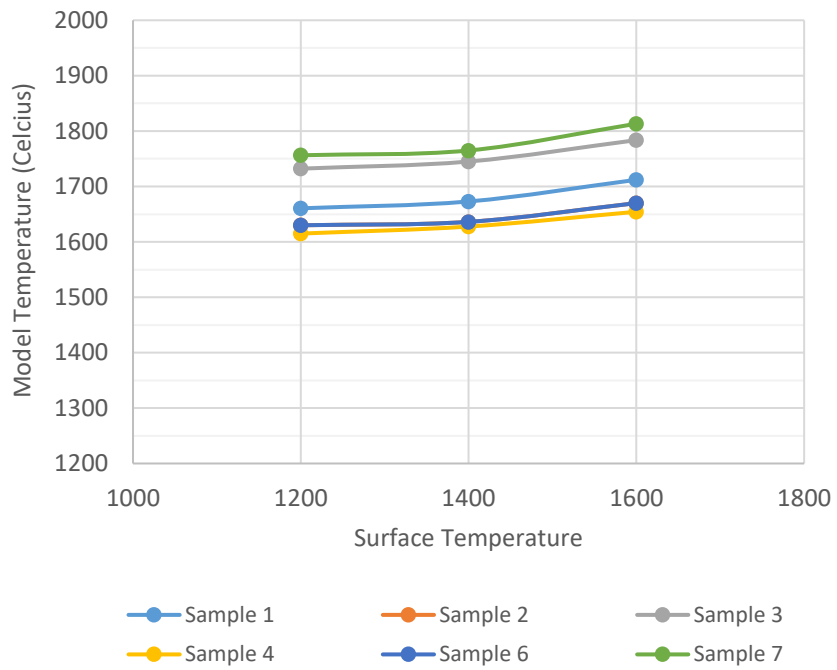
Figure 5-14. "Surface Temperature" EBM function values versus Model calculated surface temperature values for DOE 3

5.2.3.4 *Microstructural Evolution*

BS-SEM images at various magnifications were taken on cross-sections of selected samples. Figure 5-15 shows the microstructures at x1200 magnification for DOE 3 at "Surface Temperature" function 1200 as a function of focus offset and speed function. It is clear that the microstructure coarsens with decreasing speed function. This is related to the expected actual surface temperature increase as the speed function is decreased. The expected surface temperature, as calculated by the heat source modelling MATLAB code and described in Section 3.5, is labelled on each microstructure. Focus offset as more clearly shown in Figure 5-16 does not seem to have an obvious effect on microstructure. On the other hand, microstructure is influenced by changing the "Surface Temperature" function as an effect of some actual surface temperature increase during melting, specifically in Figure 5-17 the microstructure changes from a duplex for ST-1200 to a coarser near lamellar for ST-1400 and finally to an even coarser fully lamellar one for ST-1600, when all other process parameters remain the same.
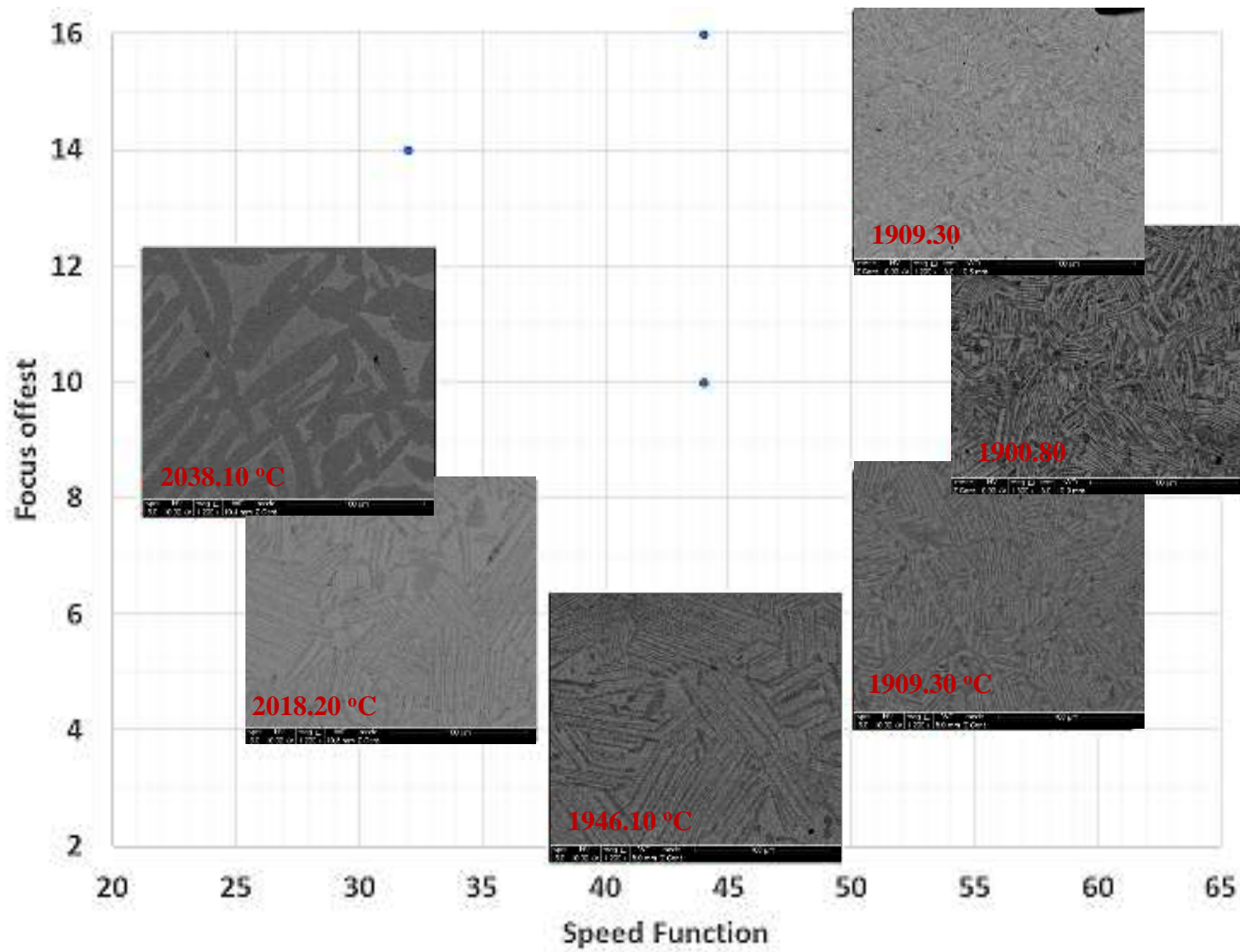
Figure 5-15. Graph showing microstructural evolution as an effect of speed function and focus offset for DOE 3 at ST-1200
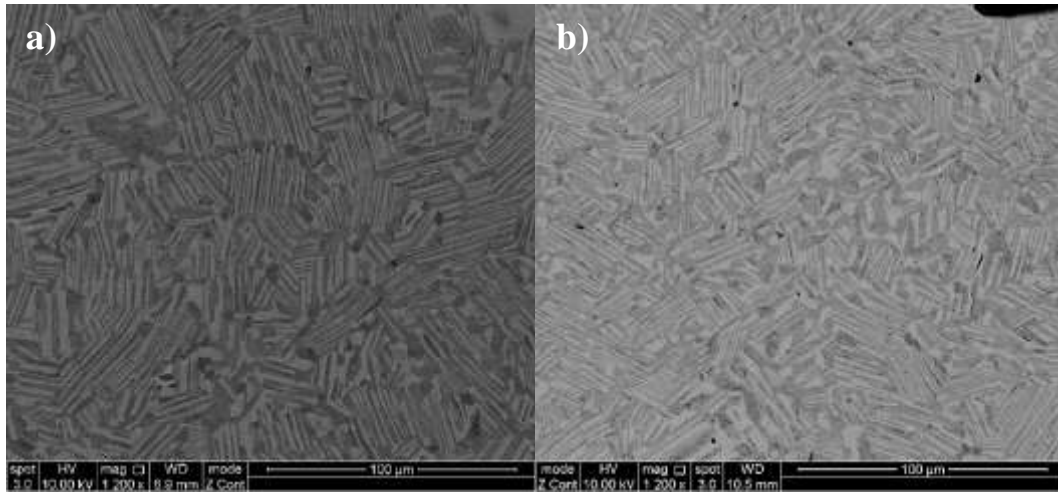
Figure 5-16. BS-SEM microstructures of samples built at speed function 56, ST 1200 and focus offset a) 6 mA and b) 14 mA, respectively
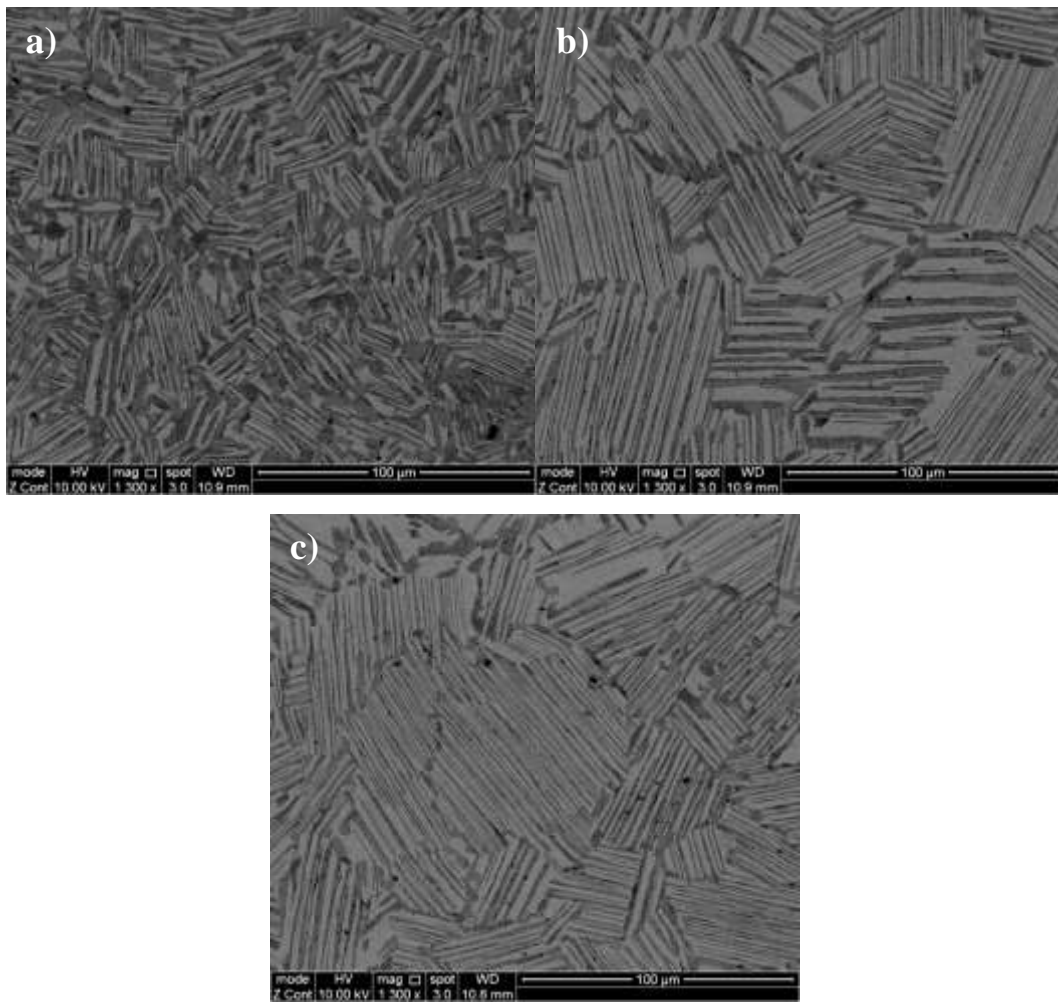
Figure 5-17. BS-SEM microstructures of samples built at speed function 60, focus offset 10 and at a) ST -1200, b) ST-1400 and c) ST-1600 respectively

5.2.4 Powder Quality Deterioration during EBM Processing

Powder quality deteriorates during EBM after each build and especially for the powder that is being used for the pre-sintered "powder cake". As mentioned in Section 5.2.2 and shown in Figure 5-4, pre-sintering was quite hard and powder recovery was quite difficult. In most of the cases the powder cake could not be recycled for the subsequent builds, partly because it was impossible to break it back into individual particles but also because chemistry was adversely affected. Figure 5-18 shows the chemical content variation after each build for the major elements. Aluminium content slightly decreases after each build, but the worst effect is observed in the powder cake with an Aluminium loss of approximately 2.5 at%. Similarly, interstitials (Figure 5-19) increase after each build with the highest increase again being for the powder in the "powder cake". These chemical variations, and especially for Al and O, are possibly related to the low mechanical properties for the as-built and as HIPed specimens presented in Section 5.3.2. The effect of Al content on mechanical properties is shown and analysed in the following chapter (Chapter 6).

	Powder as received	After 1st build	After 2nd build	After 3rd build	"Powder Cake"	Tensile Bar
Ti	46.58	46.36	46.64	46.74	47.86	49.60
Al	44.86	44.88	44.60	44.47	41.95	41.12
Nb	8.10	8.03	8.03	8.00	8.34	8.58
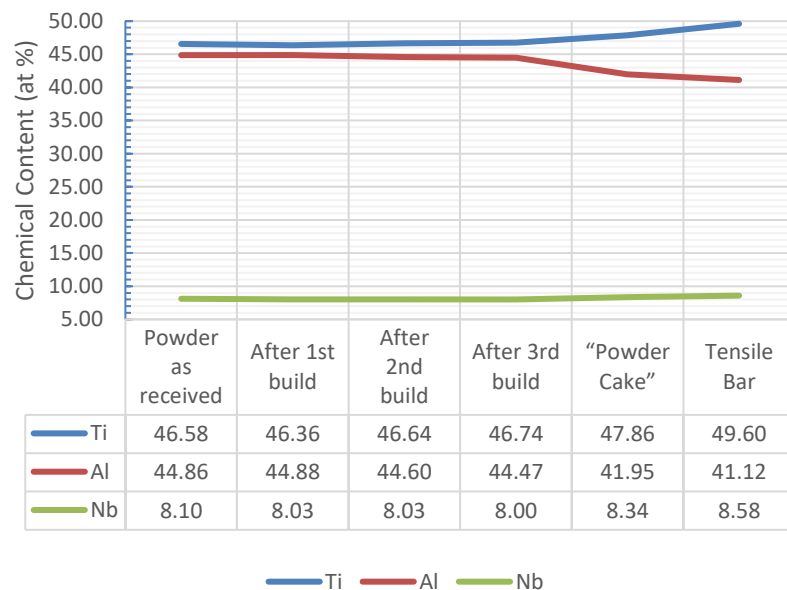
Figure 5-18. Major alloy element content throughout different EBM cycles

	Powder as received	After 1st build	After 2nd build	After 3rd build	"Powder Cake"	Tensile Bar
C	0.18	0.23	0.22	0.25	0.32	0.31
O	0.19	0.27	0.28	0.39	0.48	0.24
N	0.02	0.04	0.04	0.08	0.61	0.03
Fe	0.04	0.14	0.16	0.16	0.15	0.04
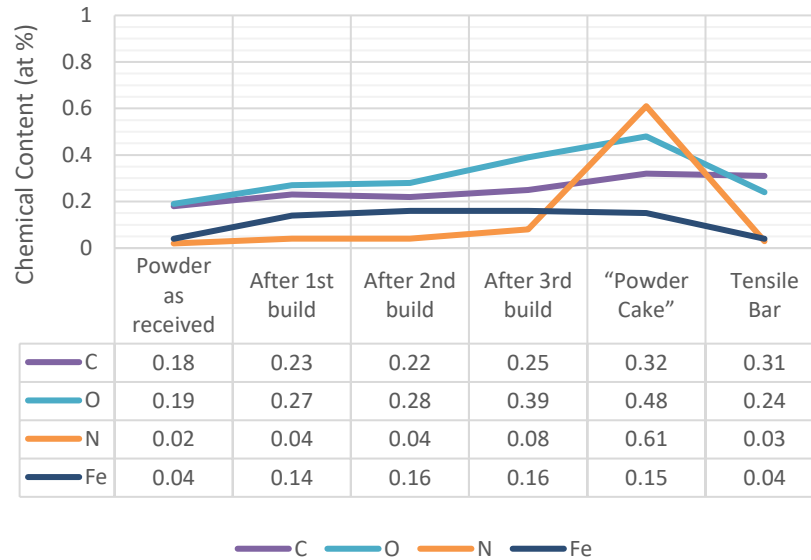
Figure 5-19. Interstitial alloy elements content throughout different EBM cycles

5.3   As-built and HIPed Tensile Bar Characterisation

5.3.1   Densification and Microstructural Evolution during HIP

Tensile specimens were built in 3 "Builds" as described in Section 3.4.1.3 using optimised hatching themes; speed function 38 and focus offset, 10 mA. A tensile specimen from "Build-2" was used for the HIP study. Three small cubes (approximately 15x15x15 mm) were sectioned for this. Two of the samples were HIPed at two different cycles; one for 4 hours, at 150 MPa, at 1100 °C and the second one for 4 hours, at 150 MPa, at 1200 °C. Another sample was used at the as-built condition.

Figure 5-20, Figure 5-21 and Figure 5-22 show the micrographs taken using an optical microscope at a low magnification (50x) for the as- built and the two HIPed samples. In Figure 5-20, as clearly shown in the micrographs at different points of the sample, a relatively high number of pores are observed; both powder and process induced. Process induced porosity, which is mainly observed in Figure 5-20-a and Figure 5-20-c, typically forms due to lack of fusion when applied energy is insufficient for complete melting and consolidation between neighbouring layers and/or adjacent lines during hatching melting [160].

Lack of fusion between neighbouring layers, is mainly observed in Figure 5-20-a, where several elongated, almost linear, process induced pores are located at the same build height and perpendicular to the build direction. It is difficult to define the exact reason for those specific defects, but it seems

to be due to an error during melting a specific or a few neighbouring layers. It could also be related to a raking issue (excess or less powder was spread) or a "smoke" occurrence during one or multiple layers that caused a delay and/or loss of temperature and subsequent inadequate melting and consolidation of the specific layers. The length of those defects is about 200 - 300 μm and the height is less than one layer thickness (70 μm).

Another area with high concentration of process induced pores due to lack of fusion occurs between the contours and the hatching area (Figure 5-20-c). A similar effect has been also observed in other work that has undertaken in the group [161] for the relatively well-established (by means of process themes development) Ti-6Al-4V, but to a much smaller extent. Fully dense EBM Ti64 samples were examined with 3D X-ray Computed tomography and a relatively high concentration of defects and porosity were observed in this exact area between the contours and hatching [161]. The results from those studies reveal the necessity for more research and better understanding of the EBM process and the effects which take place during melting in this area and for further process development and material property optimisation. This is out of the scope of this study, nevertheless those pores could be mainly attributed to lack of fusion at the overlapped melted area between contours and hatching.

Smaller and typically spherical porosity is usually related to gas entrapment [160], which is an intrinsic issue of gas-atomising powder manufacturing techniques. Powder induced porosity, due to gas entrapment, is identified by its high sphericity and it is not possible to eliminate by further process development [162]. The size and frequency depends on the size of the powder particles and the atomising process parameters [162]. Porosity size for this powder particle size (45-150 μm) and atomising method varies between 20 to 70 μm. Powder induced (Argon entrapment) porosity could be observed anywhere in the micrographs. Some examples are shown in Figure 5-20.
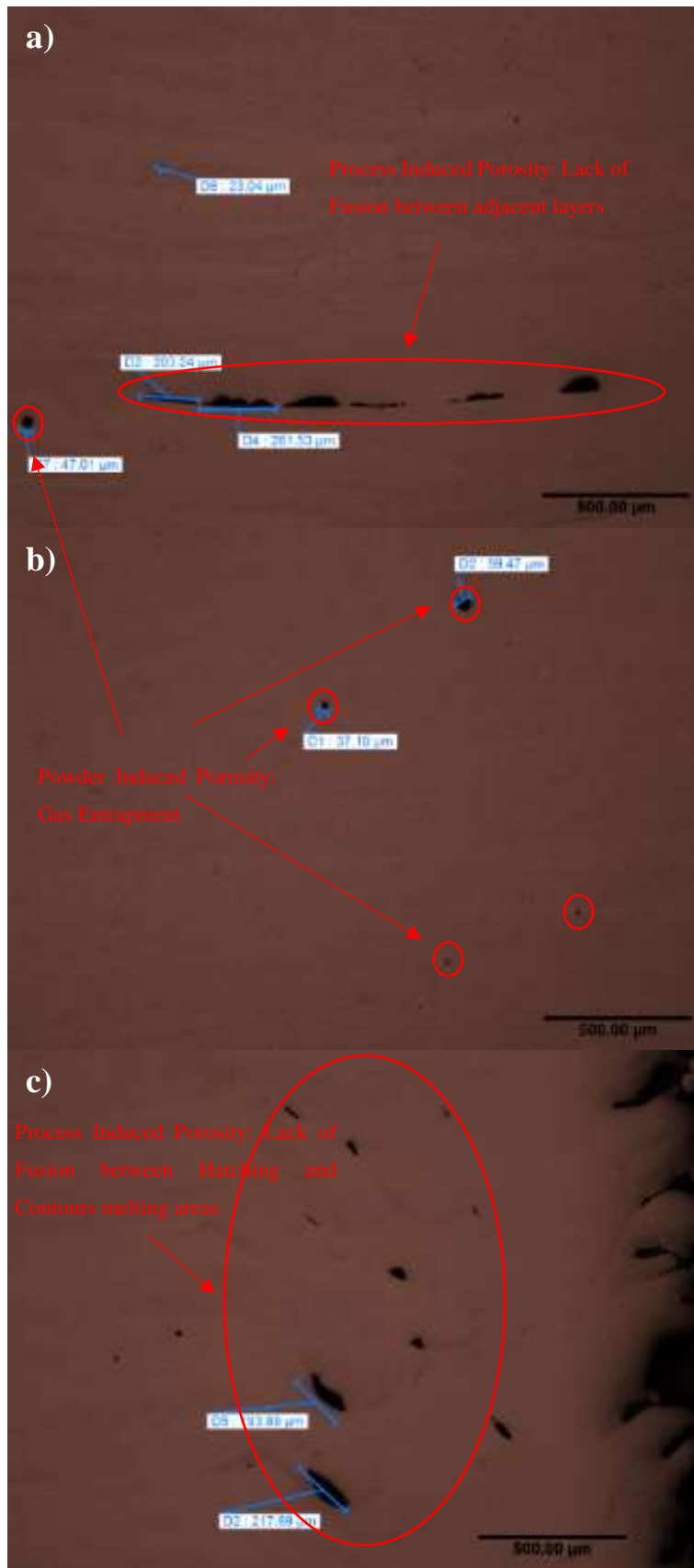
Figure 5-20. Low-magnification (50x) optical micrographs of cross-section of as- built tensile bar specimen a) close to the bottom of the sample, b) at the centre of the sample, and c) at the proximity of the area between the hatching and the contours. Build direction for all micrographs is from bottom to the top

A general comment is that more process theme optimisation could be performed to resolve most of the previously mentioned issues and further increase the as-deposited component density. Other samples which were built with identical process parameters during the process development and were presented in the previous Section 5.2.3 did not show the same high porosity frequency and were almost free of elongated process induced defects. This exposes one of the present AM issues, which is the inconsistency between different "Builds". For this specific sample and as previously described, the almost linear and perpendicular to build orientation process induced defects (Figure 5-20-a) are most likely a result of a random process error which led to lack of fusion during this specific build and only the process induced defects at the proximity of the contours (Figure 5-20-c) are due to insufficient process development. The rest of the spherical porosity is most likely inherent to the atomising process and specific powder feedstock. Consequently, a HIP treatment as similarly used for cast critical aerospace components is also highly recommended for AM manufactured components.

Appropriate HIP conditions (Temperature, time and pressure) shall allow full densification of the components, but at the same time excessive grain coarsening or other microstructural changes should be avoided if not eliminated [43], [80]. A temperature range in the $\alpha+\gamma$ region is typically used. Taking into account the phase diagram for this specific alloy (Figure 2-14, Figure 2-15 and Figure 2-16) and the high Aluminium loss a temperature in the proximity of 1100-1200 $^{\circ}$C seems to be the most promising.

As clearly shown in Figure 5-21, there is clear densification at 1100 $^{\circ}$C. The lack of fusion porosity at the overlap area between the contours and hatching is almost completely closed and the linear process induced defects perpendicular to the build direction are also significantly reduced; but not completely closed. HIP at 1200 $^{\circ}$C seems to be adequate for almost full densification and elimination of the process induced defects and porosity. Only a couple of spherical closed pores seem to survive with a final component density near to 100%. Argon entrapment, as expected, seems to endure from gas atomisation to the final HIPed component.
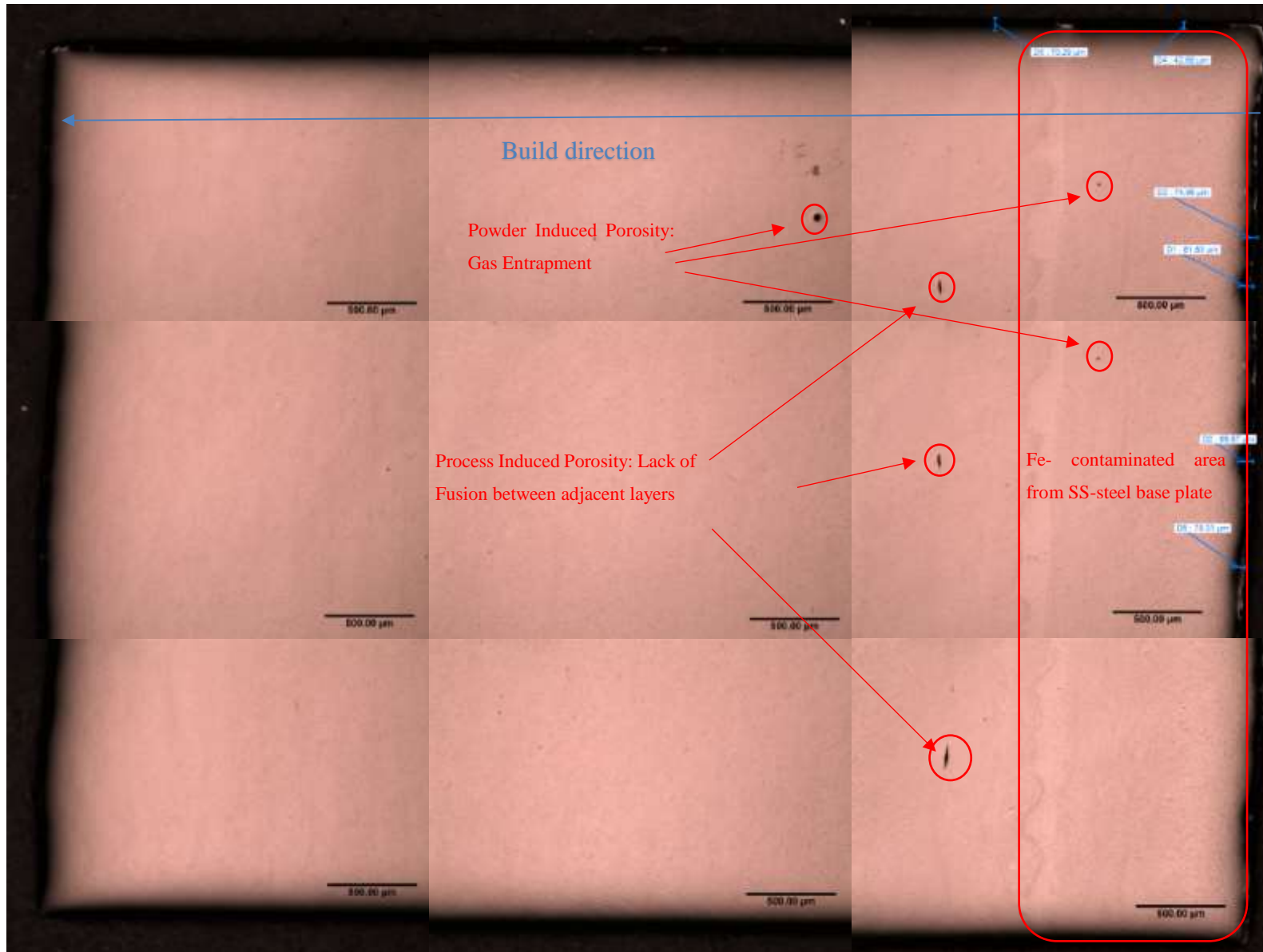
Figure 5-21. Low-magnification (50x) optical micrographs reconstructing the full area of the cross-sectioned surface of HIPed (4 hours, 150 MPa, 1100 ºC) tensile bar specimen; build direction from right to left
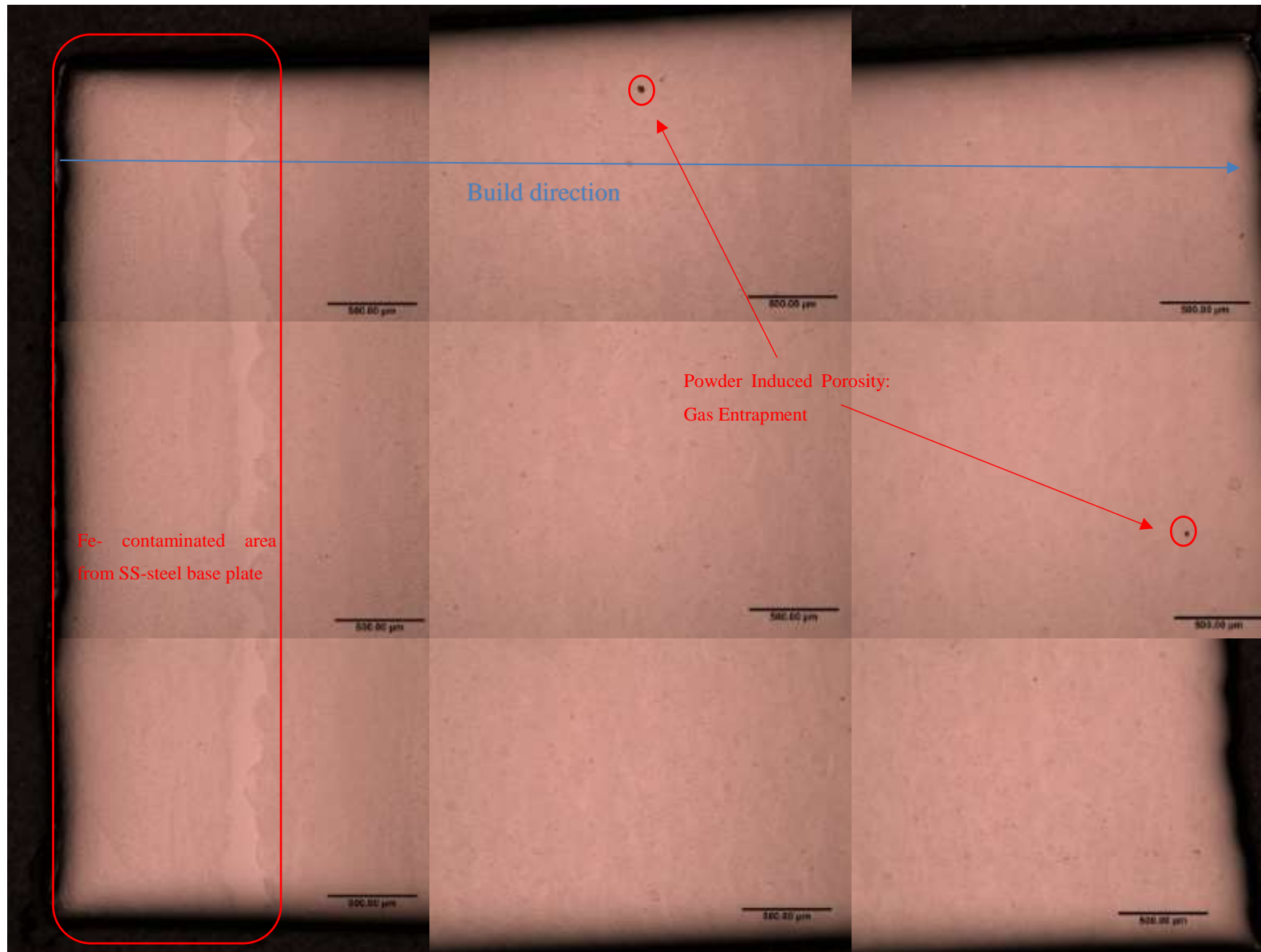
Figure 5-22. Low-magnification (50x) optical micrographs reconstructing the full area of the cross-sectioned surface of HIPed (4 hours, 150 MPa, 1200 ºC) tensile bar specimen; build direction from left to right

113

In Table 5-2, low and high magnification back-scattered SEM images are shown for the as-built and the two HIPed samples. All the images in this table were taken from the centre of the sample, where only hatching melting took place. The as-built microstructure seems to be nearly lamellar consisting mostly of coarse grains of lamellar (alternate $\alpha_2+\gamma$ plates) colonies and some equiaxed finer γ grains. The α_2 colonies are the ones with light grey colour, whereas the γ colonies are the ones with dark grey colour.

In literature [6], [7], [43] the typical as-built EBM microstructure is referred to be near gamma, which consists mainly of γ equiaxed fine grains with some α_2 precipitates. Apparently, the starting (original) chemistry of the alloy used for this work is of a lower Aluminium content (Ti45Al8Nb0.2C at %) compared with the standard GE (Ti48Al2Cr2Nb at %), which is typically used in the other AM attempts. This fact in combination with the relatively high Aluminium evaporation loss which took place during the process, shifted the alloy nearer to the eutectoid composition (~40 at %) and subsequently to a higher amount of eutectoid phase formation. Additionally, an additively layer melted component undergoes:
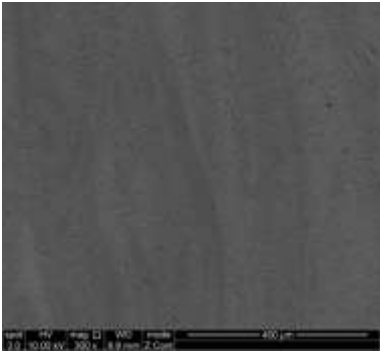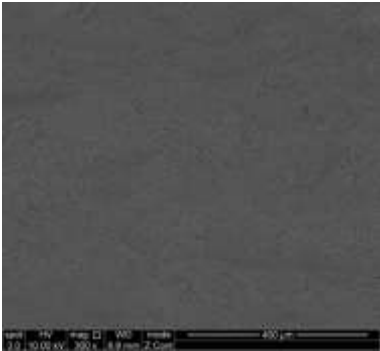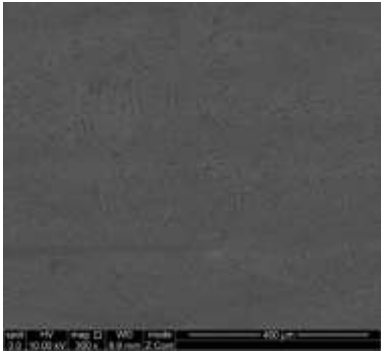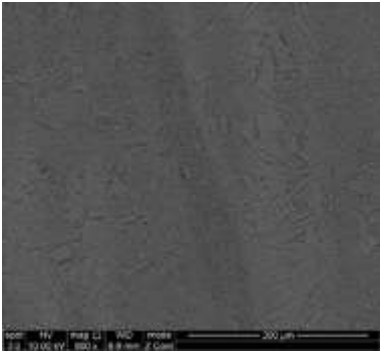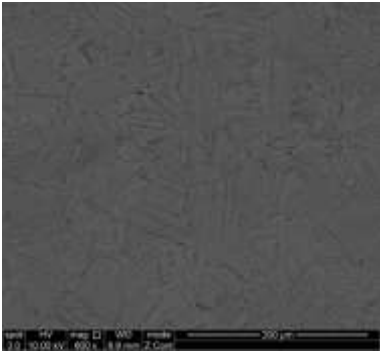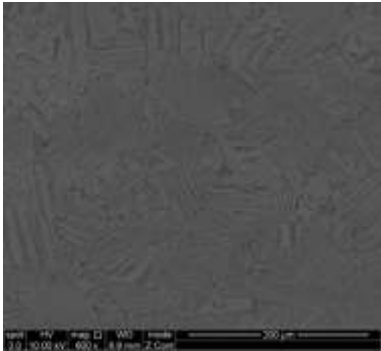
- a thermal cycling as each layer is melted multiple times, and
- an "in-situ" heat treatment due to the elevated build temperature throughout the EBM process
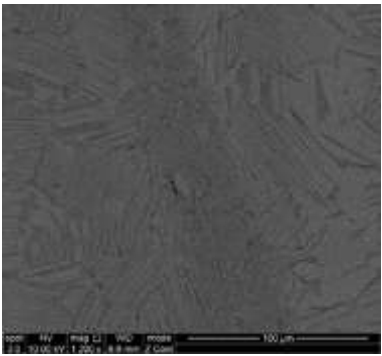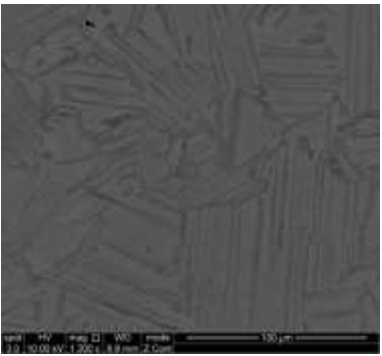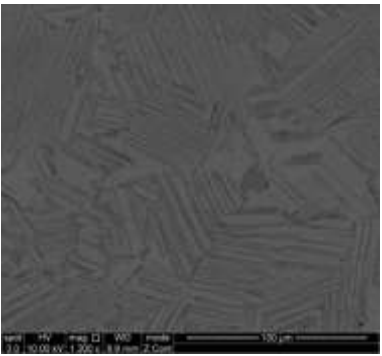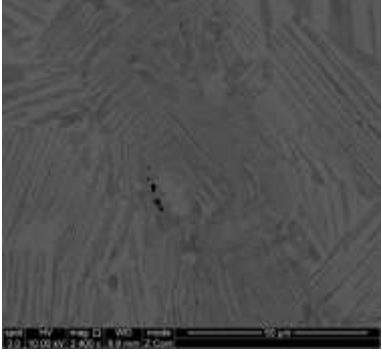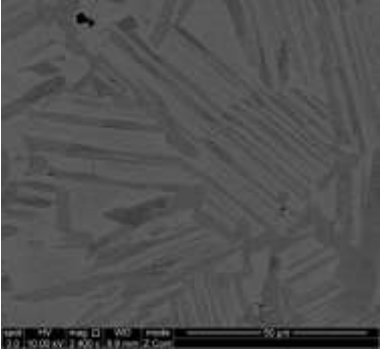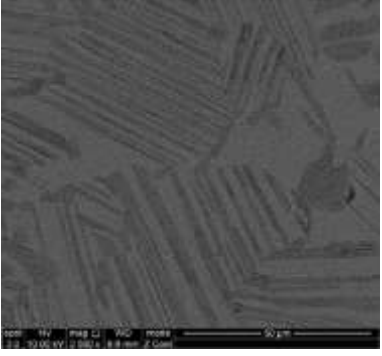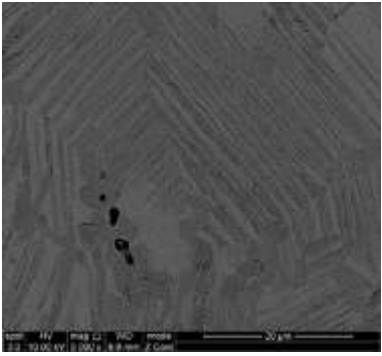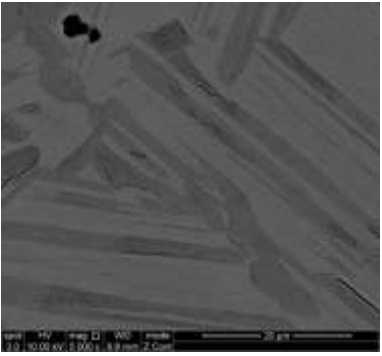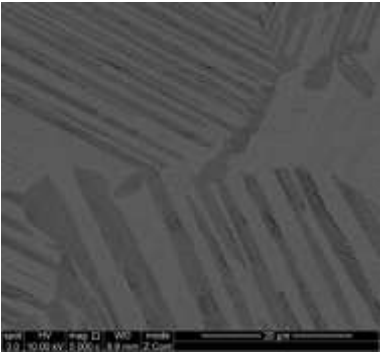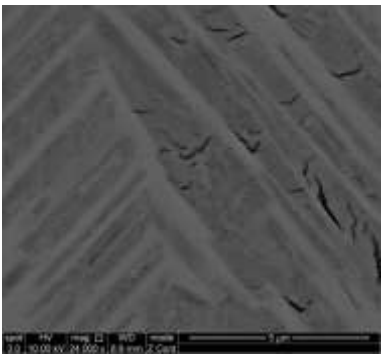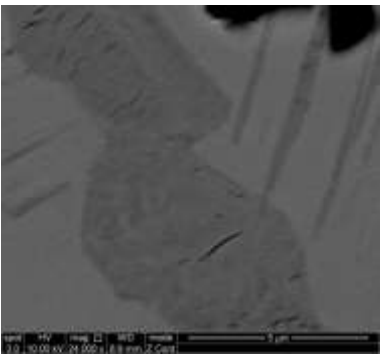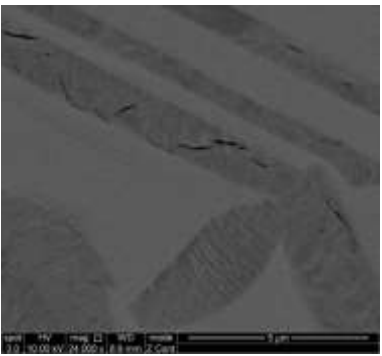
Near gamma microstructures are typical after heat treatments below the eutectoid temperature (~ 1100 °C) and in the $\alpha_2+\gamma$ region. Fully lamellar microstructures are typical after heat treatments over the α-transus and in the α region. Nearly lamellar and duplex microstructures are typical after heat treatments in the α+γ region, the former at higher temperatures nearer (below) to the α-transus and the latter at lower temperatures closer (above) to the eutectoid (Figure 2-14). The other attempts in the literature [6], [7], [43] use a T_{build} approximately at 1000 °C, obviously much lower than the eutectoid. In this work, the T_{build} was kept at approximately 1080 °C, still lower than the eutectoid or the α-transus., but the temperature on the top surface of the powder bed during the process, in both cases, could be much higher than what the thermocouple reads at the bottom of the start plate.

The as-HIPed microstructures look slightly coarser than the as-built, but they are still nearly lamellar, consisting mostly of $\alpha_2//\gamma$ colonies and some γ grains. HIPed microstructures seem to be more homogenous than the as-built microstructures. The microstructures of the two HIPed samples at 1100 and 1200 °C are almost identical, so it can be assumed that no further grain growth takes place within this delta of temperature increase. In conclusion, HIP at 1200 °C is more efficient than at 1100 °C for reducing porosity and process defects and without the cost of further grain coarsening;

the sample is almost free of porosity, other than the closed spherical porosity due to argon entrapment and the microstructure seems to be more homogeneous than the as-built one. Thus, all the remaining tensile specimens were HIPed under those conditions.

Table 5-2. Low and high magnification back scattered-SEM images for as-built, HIPed at 1100 ºC and at 1200 ºC tensile bar specimens

Magnification	As-built	HIPed at 1100 ºC	HIPed at 1200 ºC
50x			
300x			
600x			

Mag.	As-built	HIPed at 1100 °C	HIPed at 1200 °C
1200x			
2400x			
5000x			
24000x			

161

At high magnification (>5000x) and especially at 24000x some microcrack looking features are observed, located only in the γ colonies and being evident in all samples; both before and after the HIP processing. HIP do not seem to affect those features, but they seem to be slightly larger and more in number in the as-built sample and at the same level for the two (1100 and 1200 $^{\circ}$C) HIPed samples. Therefore, if those are microcracks, they either pre-exist the HIP process and could be attributed to solidification cracking during the EBM process or they are resulting during and because of the metallographic preparation, i.e. sectioning and/or grinding/polishing. It is known [34] that the γ phase is more brittle than the α$_2$, so this could explain the fact that they are only located in this phase.

5.3.2 Tensile Properties and Micro-hardness

In Table 5-3, Table 5-4, Table 5-5 and Table 5-6 the results of tensile testing performed during this work are presented. Rectangular tensile specimens were deposited using "optimised" process EBM parameters in 2 "Builds". A 3rd "Build" was intended to deposit some fatigue samples, but it did not complete due to powder shortage. "Build" 3 specimens were incomplete and defective, but some non-standard tensile specimens were machined and tested. Three of the machined tensile specimens were tested in the as-built condition at room temperature (RT). The rest of the specimens were HIPed at "optimum" HIP conditions (1200 $^{\circ}$C, 150 MPa, 4 hours), prior to machining and testing at RT and elevated temperatures (700 and 900 $^{\circ}$C).

RT tensile testing (Table 5-3) for the as-built and machined EBM specimens results to an average UTS of 777.50 MPa and 0 % ductility. All those specimens were characterised as defective, as they all fractured prior to the 0.2 % proof stress being reached. "Build" 3 specimens were not considered for the average calculations, as they exhibit very different tensile properties. RT tensile testing of the HIPed and machined (Table 5-4), EBM deposited tensile specimens results in an average UTS of 773.94 MPa, 0.38 % average elongation and 748.08 MPa of 0.2 % proof stress. In Table 5-5 and Table 5-6 the results for tensile testing at elevated temperatures (700 and 900 $^{\circ}$C) are shown.

Table 5-3. Tensile Bars - As Built & Machined - BS EN 2002-1-2005 (RT)

Samples	0.2 Proof (MPa)	UTS (MPa)	Elongation (%)	Comments
"Build" 1.1a	0.00	755.00	0.00	Defective**
"Build" 1.1b	0.00	800.00	0.00	Defective**
"Build" 3.1	*0.00**	*395.00**	*0.00**	*Defective***
Mean	0.00	777.50	0.00	N/A
Standard deviation	0.00	31.82	0.00	N/A
Standard error	0.00	22.50	0.00	N/A

*Not considered for mean calculation   **** Tensiles fractured prior to 0.2% proof stress being achieved**

Table 5-4. Tensile Bars – HIPed and Machined - ASTM E8n13a (RT)

Samples	0.2 Proof (MPa)	UTS (MPa)	Elongation (%)	Comments
"Build" 1.2a	758.42	765.32	0.00	N/A
"Build" 1.2b	723.95	792.90	0.00	N/A
"Build" 2.1a	751.53	758.42	0.00	N/A
"Build" 2.1b	758.42	779.11	1.50	N/A
"Build" 3.2	*575.71**	*820.48**	*N/A**	*Defective****
"Build" 3.3	*N/A**	*799.79**	*0.00**	*Defective***
Mean	748.08	773.94	0.38	N/A
Standard deviation	16.41	15.29	0.75	N/A
Standard error	8.21	7.64	0.38	N/A

*Not considered for mean calculation   **** Tensiles fractured prior to 0.2% proof stress being achieved**

*** Obvious defect or porosity prior to testing

Table 5-5. Tensile Bars - HIPed and Machined - ASTM E21 2009 (Elevated Temperature – 700 ºC)

Samples	0.2 Proof (MPa)	UTS (MPa)	Elongation (%)	Comments
"Build" 1.3	*N/A*	*N/A*	*N/A*	*Defective***
"Build" 1.4	544.69	606.74	3.00	N/A
"Build" 2.2	565.37	696.37	3.00	N/A
Mean	555.03	651.55	3.00	N/A
Standard deviation	14.63	63.38	0.00	N/A
Standard error	10.34	44.82	0.00	N/A

** Tensiles fractured prior to 0.2% proof stress being achieved

Table 5-6. Tensile Bars – HIPed & Machined - ASTM E21 2009 (Elevated Temperature – 900 ºC)

Samples	0.2 Proof (MPa)	UTS (MPa)	Elongation (%)	Comments
"Build" 1.5	375.76	575.71	N/A	Defective***
"Build" 2.3	358.53	510.21	N/A	Defective***
"Build" 2.4	*N/A*	*N/A*	*N/A*	*Defective*****
Mean	367.15	542.96	N/A	N/A
Standard deviation	12.19	46.32	N/A	N/A
Standard error	8.62	32.75	N/A	N/A

*** Obvious defect or porosity prior to testing **** Sample failed during machining

RT ductility do not seem to improve after HIP, but most of the samples could withstand the tensile testing up to 0.2 % proof stress and one out of the six samples showed some relatively high ductility, with an elongation of 1.5%. However, the standard error for the average ductility for Machined and HIPed samples is quite high and equal to the value of the average itself (0.38%). The highest elongation, as expected, is noticed for the tensile testing at the elevated temperature of 700 ºC, but this was not observed for the samples tested at 900 ºC, which do not show any ductility. It is obvious

that there is some inconsistency of mechanical properties; this is an issue of AM techniques, especially at the early stages of new alloy development and indicates that possibly more process optimisation is required. Even though in general there is some slight improvement of RT tensile behaviour after HIP, which could be related to the EBM process induced porosity reduction, as well as to some homogenisation of the microstructure that took place during HIP, as shown in Section 5.3.1.

RT tensile properties, and specifically elongation, are lower than expected for this alloy and as discussed later in this section this could be mainly attributed to the high Aluminium evaporation loss and to some Oxygen pick up. Figure 5-23 shows the elongation and UTS for extruded and heat treated Ti45Al-8Nb-0.2C specimens at various temperatures [163]. The RT ductility is over 2% and RT UTS is around 900 MPa. At 700 $^{\circ}$C, elongation is about 2.5% and at 750 $^{\circ}$C could reach up to 5-9%. UTS decreases at about 700 and 600 MPa for 700 and 750 $^{\circ}$C, respectively. Literature data (Table 5-7) for EBM deposited Ti-48-2-2 and Ti-45-8-2 samples shows that HIPed and heat-treated specimens with limited Aluminium loss (approximately 0.5 % Al loss) have an increased (up to about 1.0 %) elongation. RT elongation of the as- built specimens is still quite low and near to 0 (0.014-0.182%). RT elongation for TiAl alloys in general is quite low (typically less than 2-3%) and depends on many factors such as microstructure (i.e. equiaxed, fully lamellar, duplex, etc.), microstructural features (size of equiaxed and lamellar grains, inter-lamellar spacing, volume fractions and direction of lamellas, etc.), porosity, Aluminium and other third alloying (Cr, Nb, Ta, Mo etc.) or interstitial (O, N, H, C) element content [17], [18], [32], [39], [163]. Therefore, the manufacturing route (cast, forged, etc.), subsequent HIP and heat treatments are very important factors for the resulting mechanical properties and ductility specifically.

Table 5-7. Tensile properties of literature EBM deposited specimens

Samples	0.2 Proof (MPa)	UTS (MPa)	Elongation (%)	Young's Modulus (GPa)
Ti4822- As-built - RT [43]	N/A	337.843	0.182	261.518
Ti4822- HIPed - RT [43]	N/A	639.742	1.246	152.213
Ti4582- As- built- RT [116]	445	553	0.014	N/A
Ti4582- HIP&HT (fine duplex)- RT [116]	555	609	1	N/A
Ti4582- HIP&HT (fine duplex)- 760 ºC [116]	445	553	1.4	N/A
Ti4822- As built- RT [6], [7]	353	471	0.01	N/A
Ti4822- HIP&HT (fine duplex)- RT [6], [7]	353	471	1	N/A
Ti4822- HIP&HT (fine duplex)- 760 ºC [6], [7]	328	470	1.57	N/A
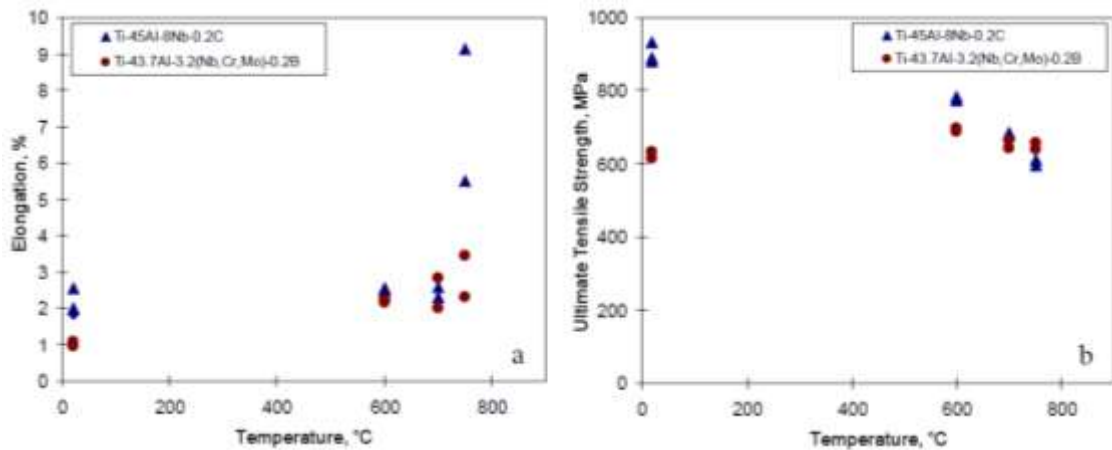
Figure 5-23. Tensile properties versus temperature for Ti-43.7Al-3.2(Nb, Cr, Mo)-0.2B (cast, HIPed and heat treated) and Ti45Al-8Nb-0.2C (extruded and heat treated) alloys, a) for elongation (%) and b) for UTS (MPa) [163]

Tensile testing is not the easiest route to collect comprehensive mechanical property data to analyse, as it is expensive and needs labour intensive experiments to build, machine and test the appropriate samples. Furthermore, for the quite brittle Titanium Aluminide alloys it is not straightforward to get

useful results to compare, as the sample could fail before reaching the 0.2 % proof stress or even during machining. Vickers hardness is a more cost effective and straightforward way to collect a large amount of data for statistical analysis. It also gives the freedom of localised analysis to relate hardness to local features of the material such as microstructure, porosity and in particular for this Chapter to Aluminium content.

Average hardness (Figure 5-24) for the tensile specimens was not significantly influenced by HIP. Although, there was a slight (in the standard error limit) softening effect with increasing HIP temperature, probably because of the slight grain coarsening and some relief of thermal stresses, as shown in 5.3.1. This softening effect is more clearly observed for the SPSed samples in this work (Al loss was 0% for those samples); when dwell temperature increased from 900 to 1200 $^{\circ}$C the microstructure transformed from dendritic to near-gamma over 1000 $^{\circ}$C, then to duplex over 1100 $^{\circ}$C and finally the microstructural features slightly coarsened up to 1200 $^{\circ}$C (Section 4.2.2). Literature data [43] for $HV_{0.2}$ of as –built and HIPed Ti-48-2-2 samples (with limited Al loss) shows the same softening behaviour after HIP, but their values are much higher than for our corresponding EBM deposited samples. In fact, the literature data hardness is closer to the SPSed samples from our study, fabricated at dwell temperatures between 900-1000 $^{\circ}$C. The as-built microstructure (fine equiaxed and fine duplex) for this work [43] is much finer compared with our corresponding EBM (nearly lamellar) results and more similar to the SPSed microstructures shown in Section 4.2.2. Hardness testing of samples from EBM deposited and HIPed blade provided to us from Arcam showed much lower hardness results. We do not have much information about the process parameters and/or further post-processing (heat treatments) for those samples, but their microstructures are much coarser and with a much higher amount of lamellas, compared with the published results [43] for smaller specimens developed by Arcam. In conclusion, it seems that microstructure influences hardness quite significantly, with coarser microstructures have lower hardness.
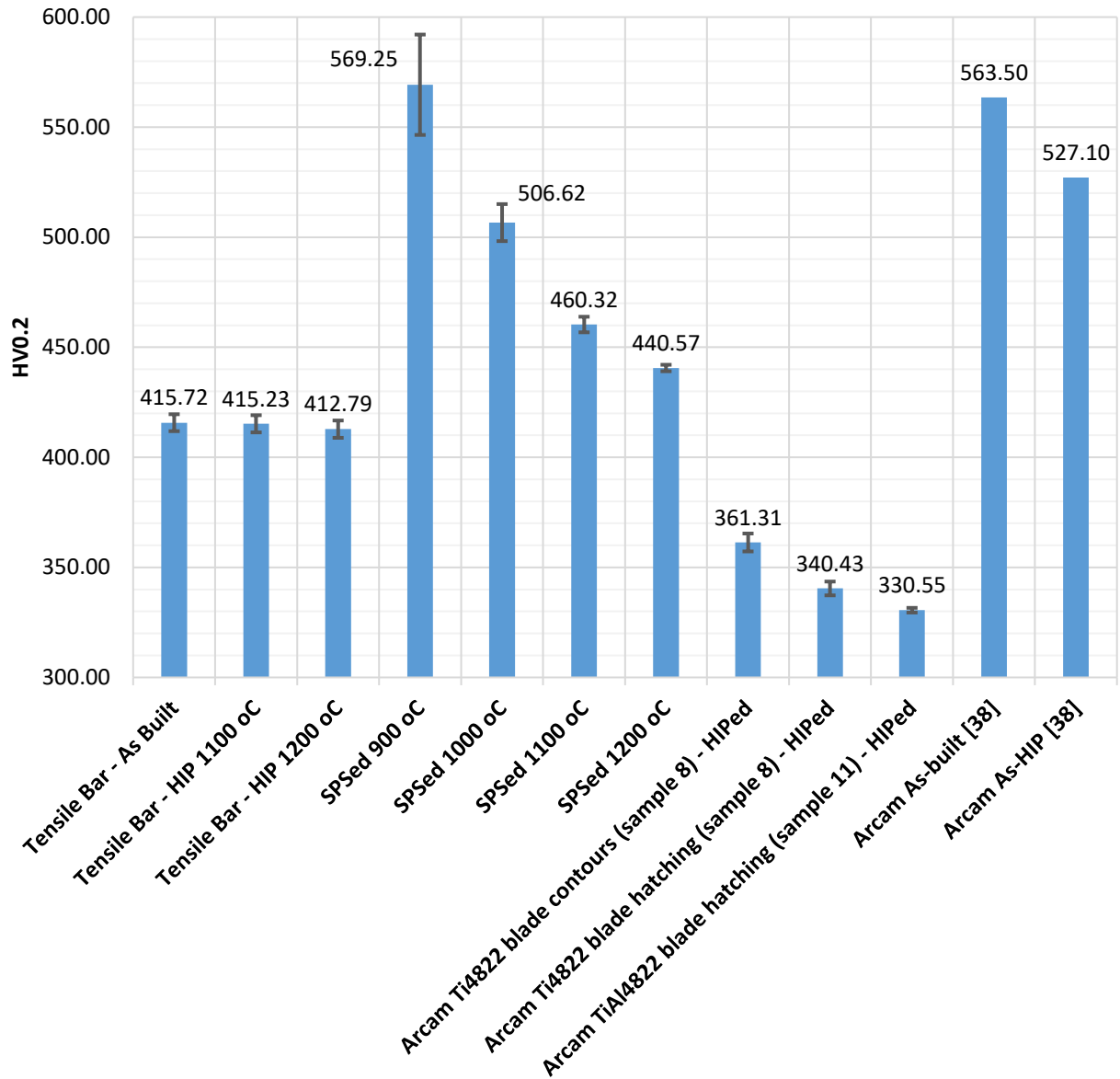
Figure 5-24. Vickers hardness of TiAl based specimens

In summary, the as-built samples were improved after HIP, as process induced defects were significantly reduced and this was also manifested by slightly improved RT tensile behaviour. However, the mechanical properties are inferior than reported for Ti-45Al-8Nb-0.2C wrought samples [163] or EBM and post-processed (HIPed and heat-treated) Ti-48-2-2 and Ti45-8-2 alloys [6], [7], [43], [116]. There is also inconsistency in the RT elongation for the HIPed samples. Only one out of four samples showed some ductility. Additionally, the as- built microstructure is different than reported in the literature [6], [7], [43], [116]; coarser and nearly lamellar instead of the finer duplex microstructure. As shown in Figure 5-18 and Figure 5-19, there was also a significant

Aluminium evaporation loss and some increase of the content of interstitials, especially for oxygen and carbon. As discussed in the following three paragraphs, those chemical variations are all found to affect the microstructure (α_2 volume fraction and lamellar spacing) and therefore the mechanical properties. In addition, the higher build temperatures (1080 $^{\circ}$C) used for this work could be associated to the resulting coarser (compared with the literature) and nearly lamellar as-built microstructures.

Excess Aluminium loss (3.35 at%) and higher build temperatures (1080 $^{\circ}$C) used for our EBM work, could be associated with the resulting coarser and nearly lamellar as-built microstructures. Liu [39] has investigated the influence of Nb and Al content on the microstructures and properties of TiAl based alloys. They suggest that the yield stress (σ_y), at 900°C of TiAl alloys follows a Hall-Petch relationship $\sigma_{0.2}=\sigma_0+\kappa_\lambda\lambda^{-1/2}$, where $\sigma_{0.2}$ is the yield strength, σ_0 and κ_λ are material constants and λ is the lamellar spacing. TiAl alloys strengthen with decreasing Al content and/or an increase in Nb content, but Aluminium content is the main factor which influences lamellar spacing. When the Al content decreases the α_2 volume fraction increases (Figure 5-25-a), which results in a linear decrease of the lamellar spacing (Figure 5-25-b). A decreased lamellar spacing has a hardening effect on TiAl based alloys. As shown in Figure 5-26Figure 2-10, and regardless the microstructure the yield stress (σ_y), at 900°C increases linearly by reducing the Al content. [39]
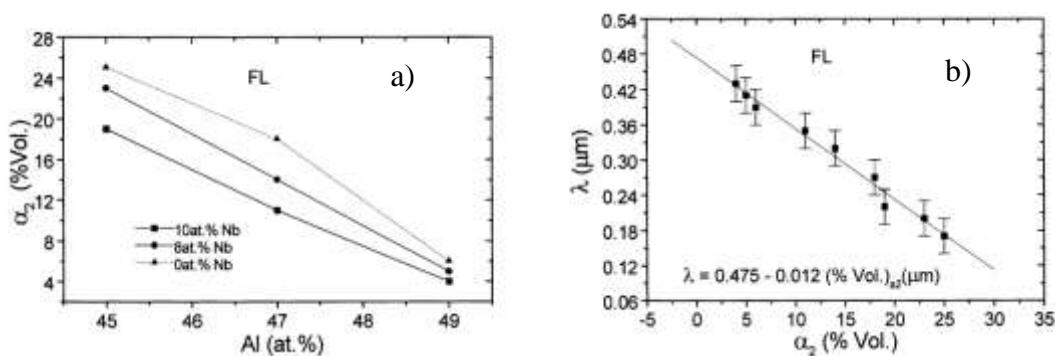
Figure 5-25. a) Effect of Nb and Al contents on the volume fraction of α_2 phase and b) Statistic relationship between lamellar spacing and the volume fraction of α_2 [39]
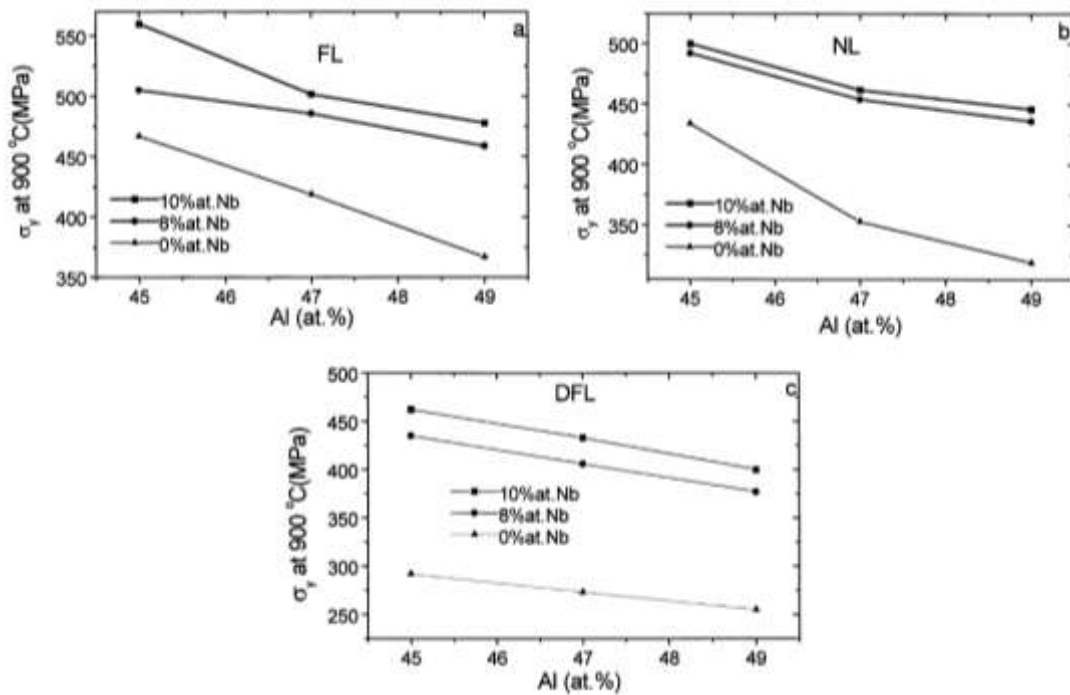
Figure 5-26. Effect of Nb and Al on the high temperature strength of TiAl alloys; for a) fully lamellar (FL), b) nearly lamellar (NL) and c) degraded fully lamellar (DFL) microstructures [39]

In a similar way [164], an increase in Oxygen content could lead in increasing the α_2 volume fraction (Figure 5-27-a) and therefore in a decrease of the lamellar spacing (Figure 5-27-b), which thereafter has an effect in mechanical properties, as shown in Figure 5-27-c and Figure 5-27-d. The effect of oxygen on microstructures and mechanical properties might vary depending on the applied heat treatment. The oxygen content (Figure 5-19) for the tested tensile bars was 0.24 at% and was increased from 0.19 at% which was for the starting virgin powder. In wt. ppm, the Oxygen content increased from 710 to 900 ppm. As per specification from the manufacturer (GfE) [165], the Oxygen content for the forged ingots shall be below 800 wt. ppm. Apparently, this is slightly over specification and as shown in Figure 5-27-c and Figure 5-27-d, this level of increase could influence the mechanical properties. [164]

Finally, the tensile bar has an increased carbon content of 870 wt. ppm (0.31 at%), which is 160 wt. ppm over the supplier's (GfE) [165] specification limits, i.e. 570±200 wt. ppm. The original carbon content of the powder feedstock was in specification limits, i.e. 0.18 at% (510 wt. ppm). As shown in Figure 5-28-b, this increase could influence the hardness of the alloy. It seems (Figure 5-28-a) that carbon, also, influences the α_2 volume fraction and therefore the lamellar spacing (λ), which is a critical parameter in the Hall-Petch ($\sigma_{0.2}=\sigma_0+\kappa_\lambda\lambda^{-1/2}$) relationship [166].
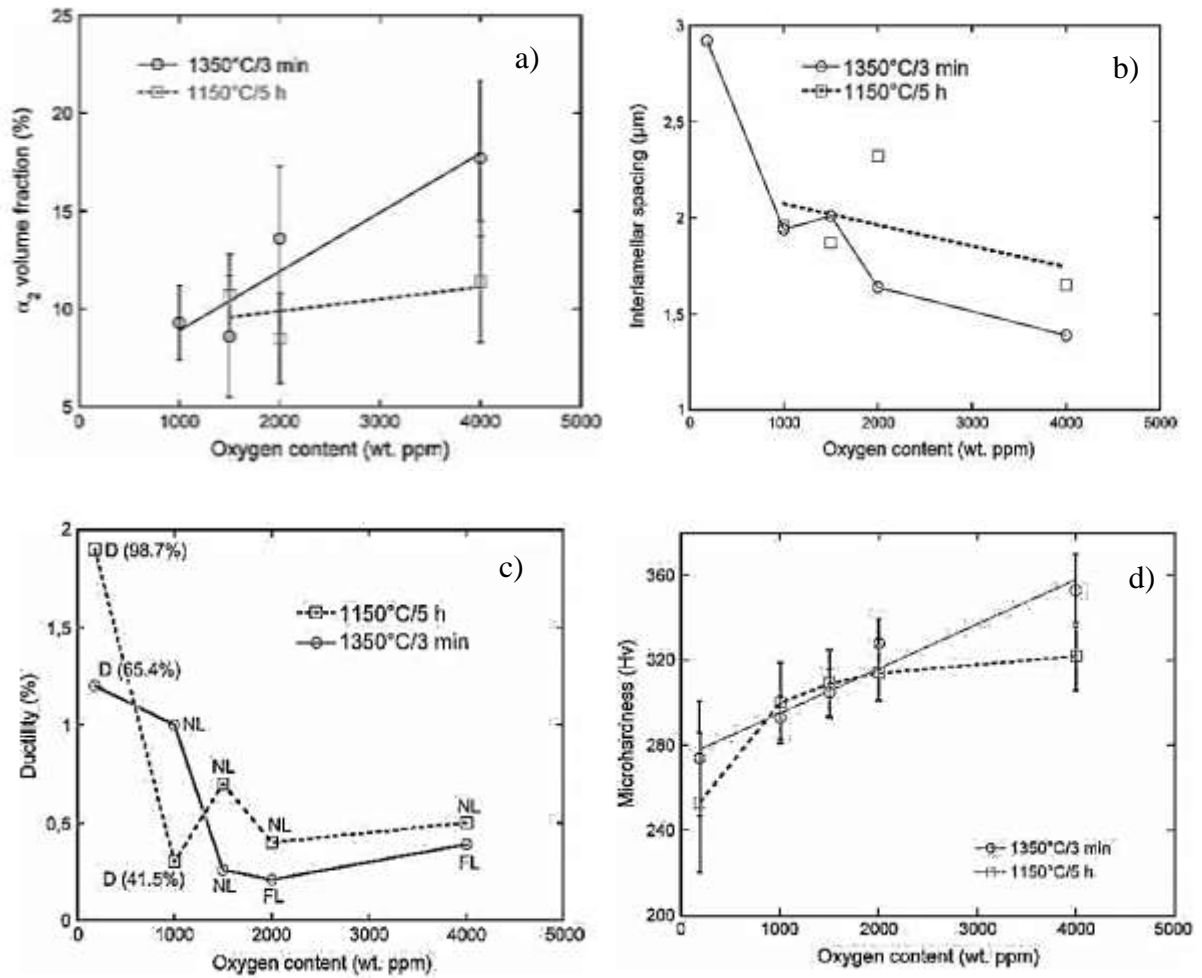
Figure 5-27. Effect of Oxygen content (wt. ppm) on a) the volume fraction of α₂ phase, b) the interlamellar spacing (µm), c) the ductility (%) and d) the micro-hardness (HV), of a Ti-48Al-2Cr-2Nb alloy heat-treated in two different heat treatments [164]
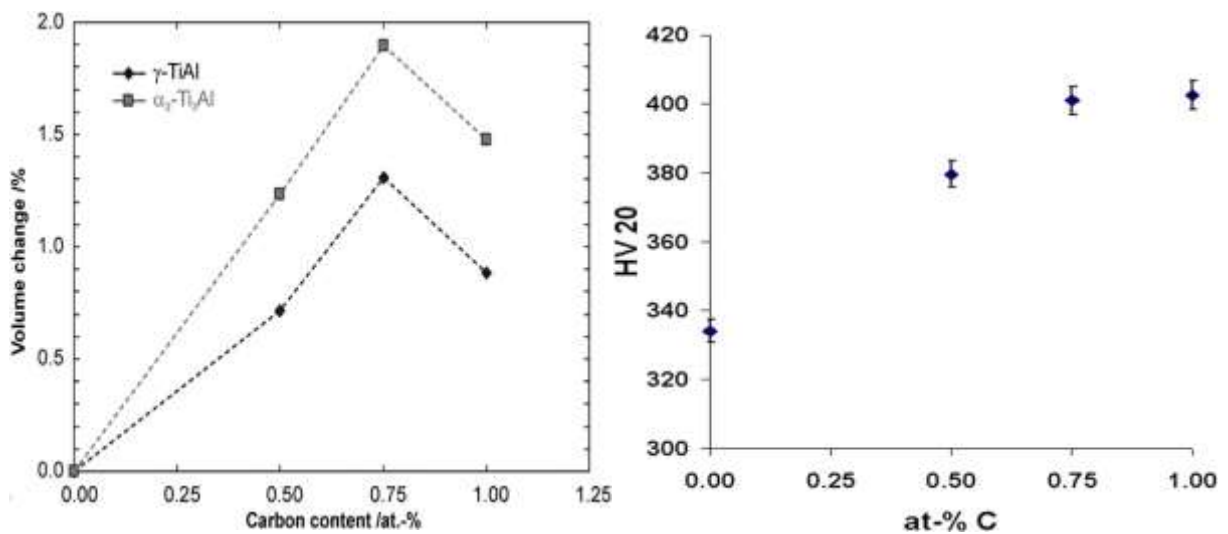
Figure 5-28. Effect of Carbon content (at %) on a) the volume fraction of α₂ and γ phases, and b) the micro-hardness (HV), of a Ti-45Al-5Nb-xC alloy [166]

171

5.4   Material Properties Dependence on Aluminium (%) Content

High Aluminium evaporation loss was observed to be one of the main issues, during the process development of the Titanium Aluminide intermetallics. It is well known from the literature [27] that Al content is probably the most critical factor affecting the microstructures and mechanical properties of γ-based TiAl alloys and the slightest shift in the phase diagram could be highly detrimental (Figure 2-6) [27]. This was, also, shown in Figure 5-25 and Figure 5-26 and discussed in Section 5.3.2.

Of course, as also discussed in Section 5.3.2, there are other significant factors that could affect the microstructures and mechanical properties of TiAl alloys and therefore their hardness. In this work, Oxygen and Carbon pick up were also identified as factors that could affect the hardness of TiAl based alloys. Those 2 chemical variations are most likely related to contamination during the powder handling process, i.e. setting up the machine and recycling the powder and not to the varied process themes. In a more industrial environment, this could be more efficiently controlled by better housekeeping and if possible by implementing a complete "closed-loop" handling process for the powder. Apparently, this was not possible and out of the scope for a research environment; there were no dedicated powder handling equipment and the available powder was very limited to discard any possibly contaminated parts of it. On the other hand, the Al variation is strongly correlated to the process parameters.

In this Section, the focus is to investigate this relationship between mechanical properties (specifically micro-hardness) and the varied, due to the EBM process, Aluminium content. A comprehensive study of Vickers micro-indentation hardness was performed for most of the samples manufactured for this work; including SPS manufactured samples at different dwell temperatures, single weld tracks, cylindrical EBM deposited solid blocks, single layer melted samples and tensile specimens. At the same time, chemical analysis for Aluminium content, using various techniques depending on the sample, was performed for most of the samples.

Micro-indentation results in general show (Figure 5-29, Figure 5-30, Figure 5-31, Figure 5-32 and Figure 5-33) the tendency for increasing hardness (HV) as the Aluminium content is decreasing from the starting 45% and this is in accordance with literature data [28], where the Vickers hardness shows a minimum at about 50% Aluminium content for the binary alloy. This tendency is more evident for the average Vickers hardness of the single layer melted pre-sintered (SPS) samples study (Figure 5-29), where the only process parameter changed was chamber pressure.

172
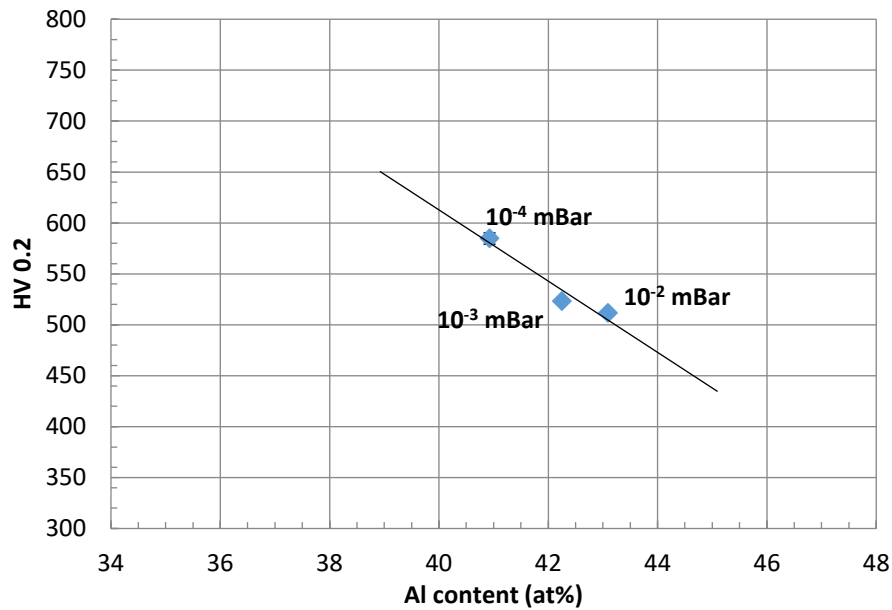
Figure 5-29. Average Vickers hardness versus average Aluminium content for a single layer melted on SPS fabricated samples at different chamber pressures

Aluminium content, for all the individual samples (Figure 5-30, Figure 5-31 and Figure 5-32), increases up to the original 45 at %, as the distance from the surface is increased; at the same time Vickers hardness decreases. The higher the chamber pressure, the lower the corresponding measured Aluminium loss (%) is. In Figure 5-29, the average Aluminium content was measured by EDX-SEM area analysis in the area between 0 and 210 μm from the surface, which corresponds to about 3 EBM layers (3x 70 μm). Average Vickers Hardness was measured in the same area. For Figure 5-30, Figure 5-31 and Figure 5-32, Aluminium content was measured by EDX-SEM point analysis from 0 to approximately 600 μm with a 50 μm step.
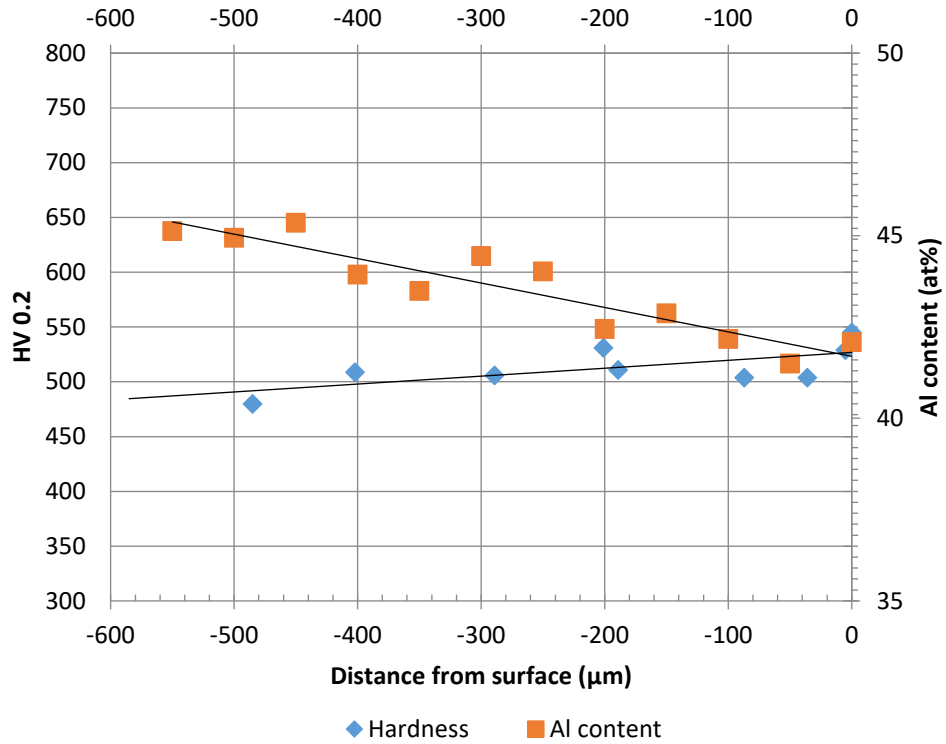
Figure 5-30. Vickers hardness and Aluminium content variation versus the distance from surface during a single layer melting of SPS fabricated samples at 10^{-2} mBar chamber pressure
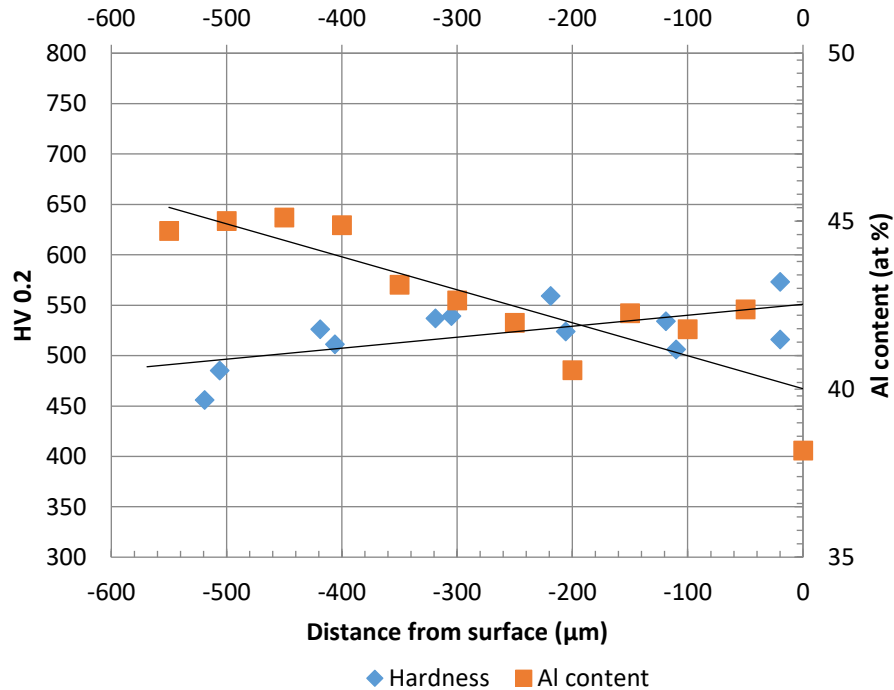
Figure 5-31. Vickers hardness and Aluminium content variation versus the distance from surface during a single layer melting of SPS fabricated samples at 10^{-3} mBar chamber pressure
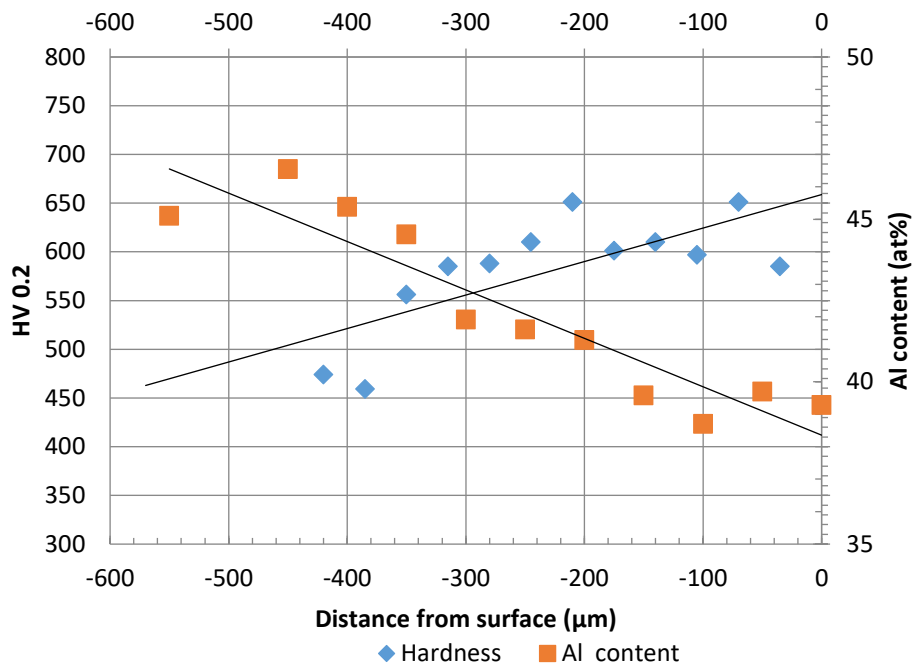
Figure 5-32. Vickers hardness and Aluminium content variation versus the distance from surface during a single layer melting of SPS fabricated samples at 10^{-4} mBar chamber pressure

A similar relationship between Aluminium content and Vickers hardness could also be observed for the EBM deposited solid blocks in Figure 5-33. Of course, in this case there is some relatively high scattering, which is quite reasonable as further factors could influence the hardness of those samples, such as varying microstructure, porosity and process defects; also, resulting from the varied process parameters. As previously discussed, Oxygen and Carbon pick up has been found to affect the hardness of TiAl alloys, although those variations are related to powder handling contamination and are not expected to fluctuate with process parameters. Regardless this scatter, a clear trend is observed; Vickers micro-hardness increases when Aluminium content decreases. Additionally, the hardness results for the as-built and HIPed tensile bars fit very well within these results and slightly lower than the overall trendline. Finally, the results for the SPS fabricated samples from the same feedstock also fit quite well, but sit slightly above the overall trendline.
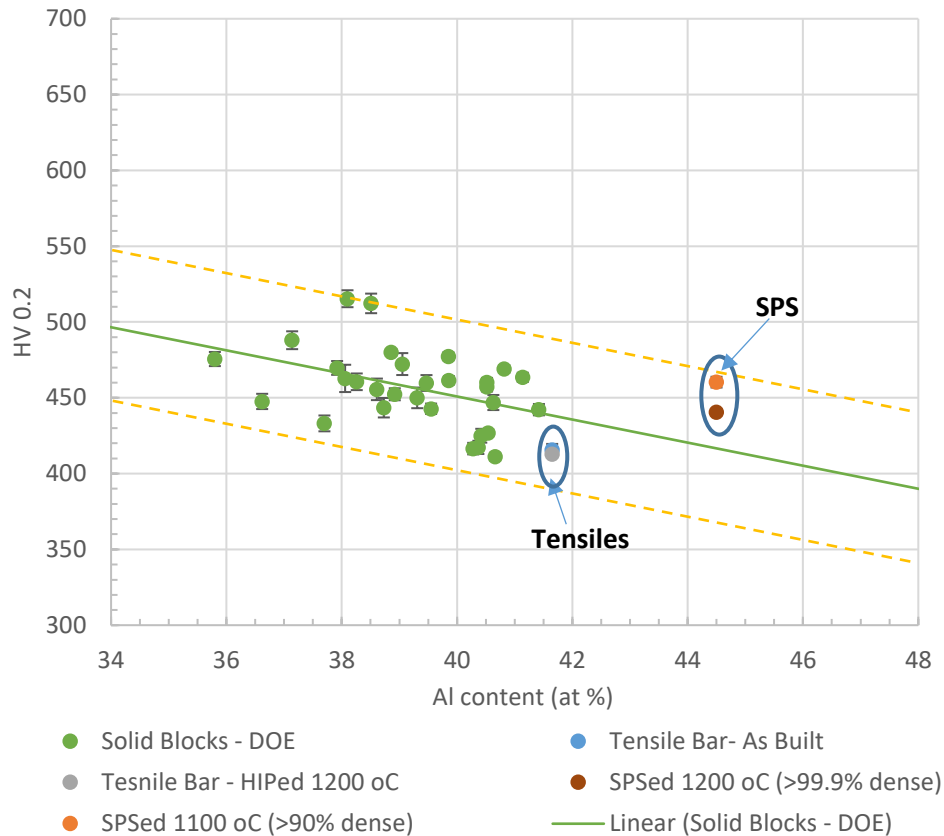
Figure 5-33. Measured avearge Vickers hardness versus measured Al content

5.5 Summary

Arcam EBM process themes were developed for fabricating simple geometries from a 45-150 µm TNB-TiAl alloy powder feedstock and a 70 µm layer thickness. A build temperature of 1050-1090 ºC was identified for a stable process. Design of Experiments (DOE) approach was successfully used to optimise melting process themes for surface finish, component density and Aluminium evaporation loss. The most significant points obtained from the DOE analysis are summarised below.

- Speed function was the most significant factor for top surface quality, where the optimum surface quality was observed at speed functions higher than 56. In contrast, increasing focus offset showed a smaller linear positive effect.

- Aluminium evaporation had a strong linear relationship with speed function (Aluminium loss decreases with increasing speed function) and a quadratic relationship with focus offset, showing a minimum in the range between 8-10 mA.

- Maximum density (minimum process defects) was found for low values of speed function and high values of focus offset, and vice versa.

- Microstructure was significantly influenced by speed function and surface temperature; it got coarser with decreasing speed function and/or increasing surface temperature, as actual surface temperature was calculated to increase.

Post-processing was performed to eliminate defects and remaining porosity from the bulk and surface by Hot Isostatic Pressing (HIP) and machining. Optimum HIP conditions were identified at 1200 °C, 150 MPa, for 4 hours. Only some spherical closed pores survived which originated from powder feedstock, possibly due to Argon entrapment during gas-atomisation. Microstructural analysis and mechanical properties were investigated for the as-built and HIPed specimens at room and elevated temperatures. Mechanical properties were only slightly improved by HIP as a result of porosity reduction, process defect elimination and microstructure homogenisation. However, properties were found to be worse than expected and this is mainly related to the chemical variations occurred to the tensile bar during the EBM process, i.e. i) excess Al evaporation, and ii) Oxygen and Carbon pick up. Those chemical variations, all found to affect the microstructure (α_2 volume fraction and lamellar spacing) and therefore the mechanical properties. In addition, the higher build temperatures (1080 °C) used for this work could be associated to the resulting coarser (compared with the literature) and nearly lamellar as-built microstructures.

Aluminium content, as reported in the literature [27], is probably the most critical factor affecting the microstructures and mechanical properties of TiAl-based alloys and the slightest shift in the phase diagram could be detrimental. Oxygen and Carbon pick up were also identified as critical factors that could affect the hardness of TiAl based alloys. Those latter chemical variations are most likely related to contamination during the powder handling process, i.e. setting up the machine and recycling the powder and not to the varied process themes. In a more industrial environment this could be more efficiently controlled by better housekeeping and if possible by implementing a complete "closed-loop" handling process for the powder. On the other hand, the Al variation is strongly correlated to the process parameters. A comprehensive study was performed for most of the samples manufactured for this work; which regardless the, expected in some cases, high scatter shows a very clear trend relating the varied Aluminium content to the HV hardness.

6 EVAPORATION PHENOMENA AND IMPEDING PRESSURE DURING ELECTRON BEAM MELTING

6.1 Introduction

Aluminium evaporation has been identified as one of the most critical issues during the EBM process development of Titanium Aluminides and Aluminium content is strongly related to mechanical properties and micro-hardness. The physics behind evaporation of pure elements and alloys was studied and the effect of process parameters and in specific the effect of surface temperature and applied chamber pressure on evaporation were investigated. Average surface temperature was calculated, as described in Section 3.6, by integrating the modified Rosenthal equation for a moving heat source with a Gaussian distribution. Impeding pressure for Aluminium evaporation versus surface temperature was estimated using experimental results and literature data. Finally, additional process parameters and phenomena affecting evaporation are discussed and some conclusions are drawn on reduction of evaporation loss in Arcam EBM processing.

6.2 Volatilisation and Impeding Pressure during Vacuum- EBM processing

6.2.1 Evaporation Rates for the Ti45Al8Nb Alloy System

Aluminium evaporation loss is a function of more factors than just surface temperature. Heating time, applied vacuum pressure and material properties should be also considered. Evaporation rates for Al, Ti and Nb in vacuum at a large range of temperatures may be calculated using Langmuir's equation [167]–[169].

$$J = \frac{x_{i\gamma_i}p_v^i}{\sqrt{2\pi M R_g T}} \qquad \text{(Eq. 6.1)}$$

Where x_i is the molar fraction of each component i, γ_i is the activity coefficient of i, p_v is the partial pressure of i, R_g is the ideal gas constant, T the absolute temperature and M the molar mass of the evaporating species.

Partial pressures (p_v) for pure elements Al, Ti and Nb at different temperatures can be calculated using the Clausius-Clapeyron or Antoine's equation; with the latter being derived from the Clausius-Clapeyron equation. In this work, Antoine's equation (Eq. 6.2) was used, which is a simple three parameter fit to experimental vapour pressures measured over a restricted temperature range and

this is considered to be a more accurate estimation. Antoine's coefficients (A, B and C) for different elements at different temperature ranges are to be found in Langes's Handbook of Chemistry [170].

$$LogP = A - \frac{B}{T+C} \qquad \text{(Eq. 6.2)}$$

Activity coefficients (γ_i) for Aluminium and Titanium in TiAl binary and TiAlNb ternary alloys at different temperatures were calculated from interpolating and extrapolating the fitting trends of literature data extracted from various literature sources [171]–[177] and shown in Figure 6-1 and Figure 6-2 for Aluminium and Titanium, respectively.
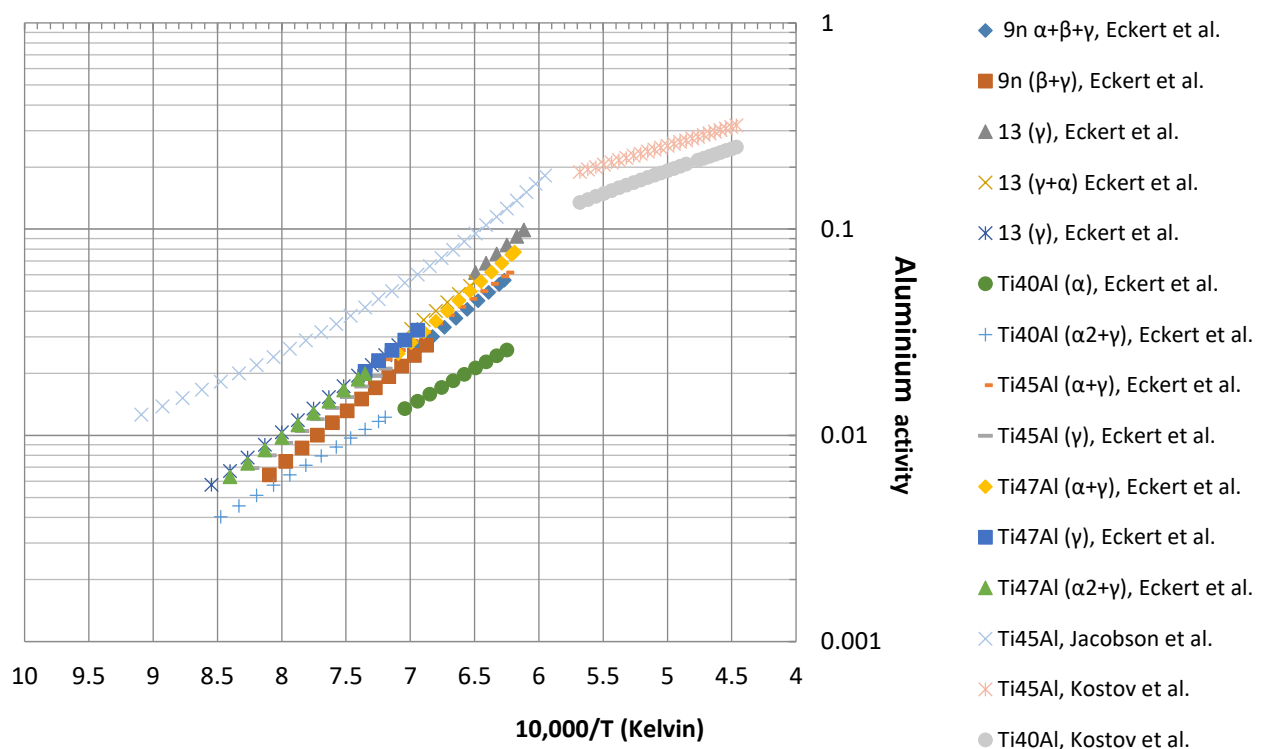
Figure 6-1. Literature data for Aluminium activity versus 10000/T (K) for various TiAl based alloys [171]–[177]
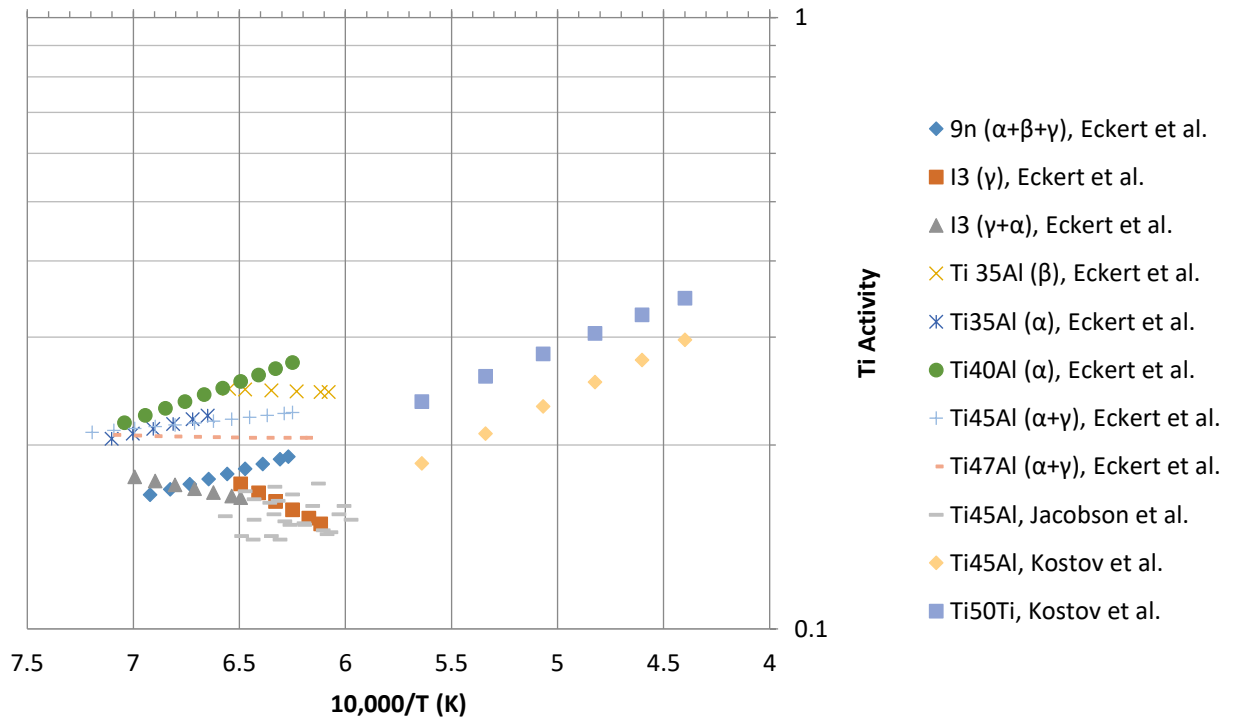
Figure 6-2. Literature data for Titanium activity vs. 10000/T (K) for various TiAl based alloys [171]–[177]

Evaporation rates versus temperature for each individual element in the Ti45Al8Nb alloy are shown in Figure 6-3 and they were calculated using Equation 6.1. x_i is 0.47, 0.45 and 0.08 for Ti, Al and Nb respectively. Activities for Aluminium and Titanium versus temperature were calculated by using the equations (Eq. 6.3- Eq. 6.8) extracted from the data in Figure 6-1 and Figure 6-2. Activity for Nb was assumed to be 1. Molar mass (M) is 92.91, 26.98 and 47.87 g/mole, for Nb, Al and Ti, respectively. R_g is a constant, 8.31 J*K^{-1} *mol^{-1}.

$\gamma_{Al} = (8.0162*10\text{^}-5)*EXP(0.0045988*T(K))$:T=1100 -1700 K, for Ti45Al   (Eq. 6.3)

$\gamma_{Al} = 0.00026943*T(K)-0.28512$: T > 1633 K, for Ti45Al   (Eq. 6.4)

$\gamma_{Al} = (9.580048*10\text{^}-29)*T(K)\text{^}8.38623985$: T=1100 – 1700, for Ti45Al   (Eq. 6.5)

$\gamma_{Al} = (2.4007*10\text{^}-4*T(K))-(2.8795*10\text{^}-1)$: T > 1633 K, for Ti40Al   (Eq. 6.6)

$\gamma_{Ti} = 0.0318149585*EXP(0.000986624845*(T(K))$: T=1100-1750 K, for Ti45Al   (Eq. 6.7)

$\gamma_{Ti} = 0.000221594445*(T(K)-0.206162166$: T > 1750 K, for Ti45Al   (Eq. 6.8)

For identical or quite similar alloy systems, in this case gamma-TiAl alloys, higher calculated average surface temperatures per surface area and longer heating times would give higher evaporation rate values, which would lead to higher Aluminium losses.
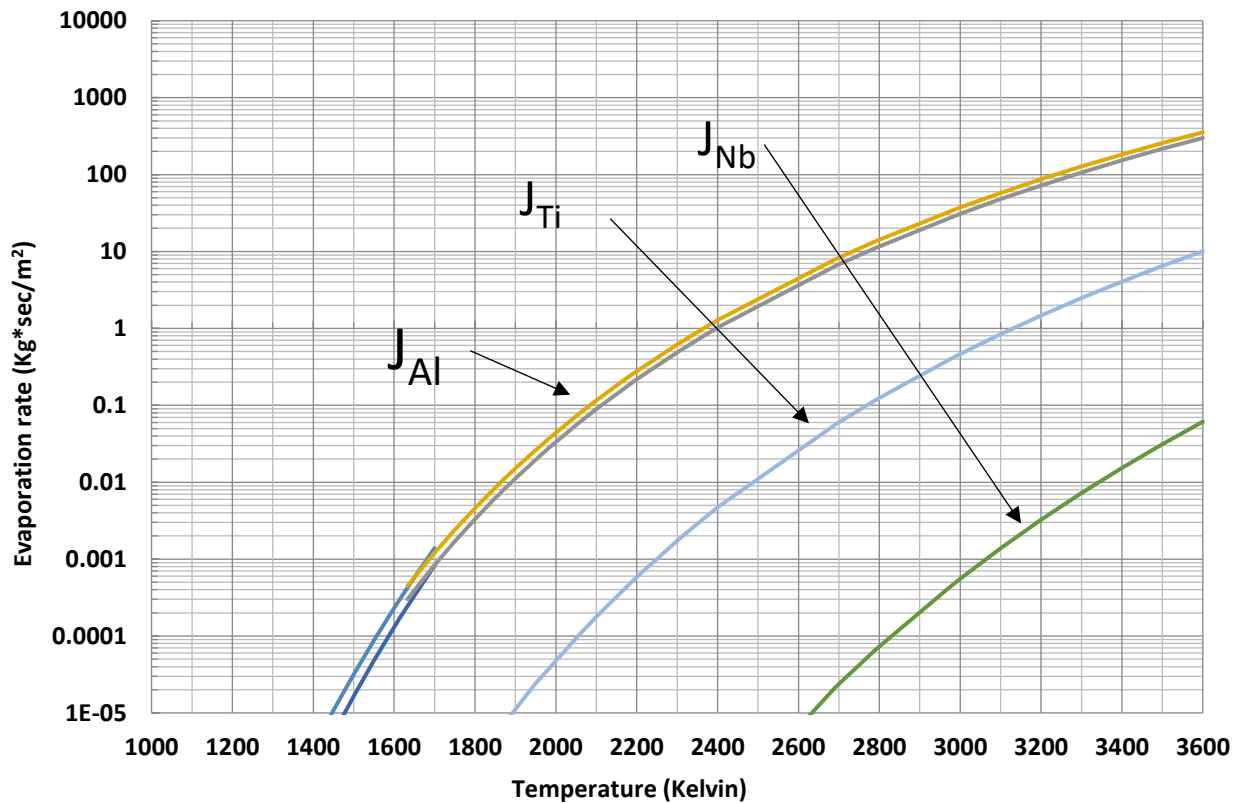
Figure 6-3. Calculated evaporation rates for Ti, Al and Nb versus temperature for the Ti45Al8Nb alloy system

The relative evaporation rates (Figure 6-4) of $ER_{Al/Ti}$ and $ER_{Al/Nb}$ are drastically reduced with increasing temperature, but even at 3000 ºC degrees they remain quite high, separated by over two orders of magnitude. Consequently, it can be anticipated that the main variation in chemical content would result from Aluminium evaporation losses. This is quite clear in Figure 6-5, where the Aluminium loss is the main chemistry variation throughout the process development accomplished by a simultaneous increase in the Titanium content. Nb content is slightly increased in the alloy, as well, as might be anticipated. So, it is verified that the Aluminium evaporation rate is much higher than the ones of Ti and Nb.
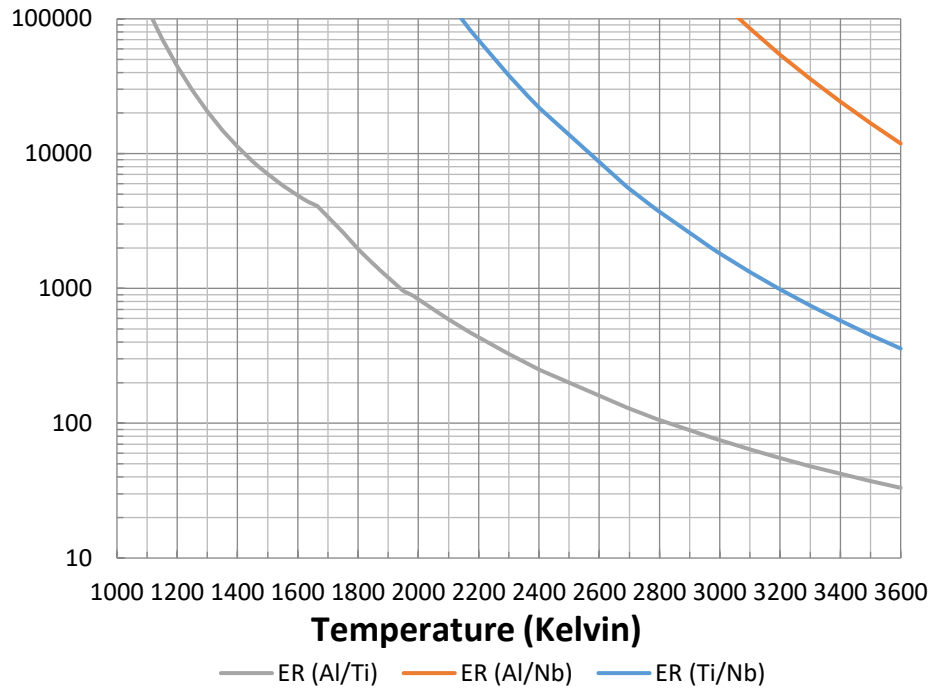
Figure 6-4. Estimated evaporation ratio versus temperature (K) for Al, Ti and Nb for Ti45Al8Nb alloy system

Major alloy elements chemical content

	Powder as received	After 1st build	After 2nd build	After 3rd build	"Powder Cake"	Tensile Bar
Ti	46.58	46.36	46.64	46.74	47.86	49.60
Al	44.86	44.88	44.60	44.47	41.95	41.12
Nb	8.10	8.03	8.03	8.00	8.34	8.58
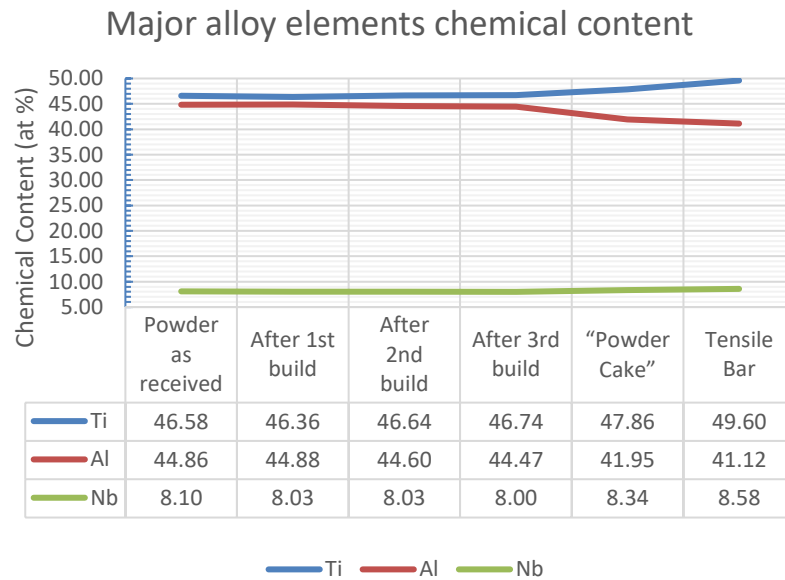
Figure 6-5. Major alloy element content throughout the process development

Another observation from Figure 6-5 is that evaporation, actually also takes place at temperatures below the melting point and during the preheating of the powder bed. The calculated temperature for preheating is approximately 1700 K and about 150 K lower than the melting point. Aluminium sublimation is an established phenomenon in the literature [178], [179] and further to its dependence

182

on temperature and the partial pressure of the individual element, this depends also on the chamber pressure. The importance of chamber pressure can be observed in Figure 6-6 for the single layer melting study at three different chamber pressures. The depth of the re-melted area decreases with decreasing chamber pressure and because at lower chamber pressures the total evaporation rate from the top surface is expected to be higher.
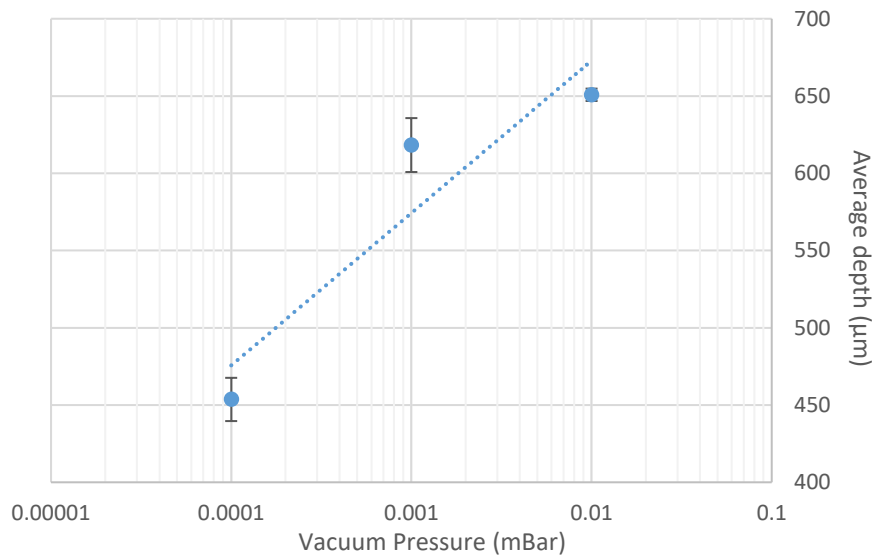
Figure 6-6. Depth of remelted area versus chamber pressure

6.2.2 Aluminium Evaporation Losses (%) during EBM Processing of a Ti45Al8Nb Alloy

Integration of the Modified Rosenthal equation for a moving heat source with a Gaussian distribution [144] was performed using a MATLAB code developed for this work, as explained in more detail in Chapter 3. Temperature isotherms/fields can be calculated around a moving heat source of known process parameters (e.g. current, speed, etc.); along the surface and the depth of a base material of known material (thermal) properties. As earlier discussed in this chapter, evaporation mainly occurs on the surface of the heated material. Using this assumption, the average surface temperature on a given surface area around the electron beam was calculated for:

- Single EBM weld tracks
- Single EBM melted layer at 3 different chamber pressures
- EBM deposited solid blocks
- EBM deposited tensile bars, and
- EBM literature data [99], [119]

Very clear and almost parallel to each other fitting trends, relating measured Al (at %) losses to calculated average surface temperatures (Kelvin) can be observed in Figure 6-7. As expected, those trends show that Al loss % increases with increasing surface temperature. Heating time is not considered for those calculations. For a given calculated average surface temperature it seems that decreasing chamber pressure would increase Al evaporation losses.

Aluminium loss for the single weld tracks (orange squares) sits lower than EBM literature data for similar chamber pressure and surface temperature. This is due to the fact that as the heating time during preheating and subsequent hatching melting for the samples in the literature is anticipated to be much longer than the preheating and scanning of the single weld tracks in this study. Additionally, single weld tracks were scanned at a build temperature of 900 $^\circ$C, when most of the samples in the literature were deposited at a build temperature slightly higher than 1000 $^\circ$C.

During the process development of the cylindrical deposited samples (dark red squares) the chamber pressure used was approximately 5×10^{-4} mBar, which is more than one order of magnitude lower than the standard controlled vacuum (CV-EBM) EBM mode at 2×10^{-3} mBar. As clearly shown in Figure 6-7, this results in a higher Aluminium loss during those experiments, compared with the literature data at corresponding surface temperatures. After realising this issue with the CV-EBM mode this was fixed and the tensile bars (light red squares) were built under standard chamber pressure conditions, 2×10^{-3} mBar. Indeed, Aluminium loss in the melting hatching area is reduced and the results sit closer to the trendline of the EBM literature data. On the other hand, Al loss in the pre-heating area of the tensile specimens builds (light red square on the left side of the graph at approx. 1670 Kelvin) sit much higher than the expected trendline for a chamber pressure of 2×10^{-3} mBar. This is attributable to long heating times during preheating that are not taken in account in this calculation.

The Aluminium loss results for the single layer melted substrates study (green triangles markers) are quite consistent with the ones for the tensile bars at the same chamber pressure, 2×10^{-3} mBar. Aluminium loss is lower for a higher chamber pressure and higher for a lower chamber pressure (black and purple tringle markers) as might be expected. As mentioned in Section 6.2.1 and in Figure 6-5 and Figure 6-6 evaporation of volatile elements could take place even at temperatures much lower than the melting point and this depends on heating time and chamber pressure.
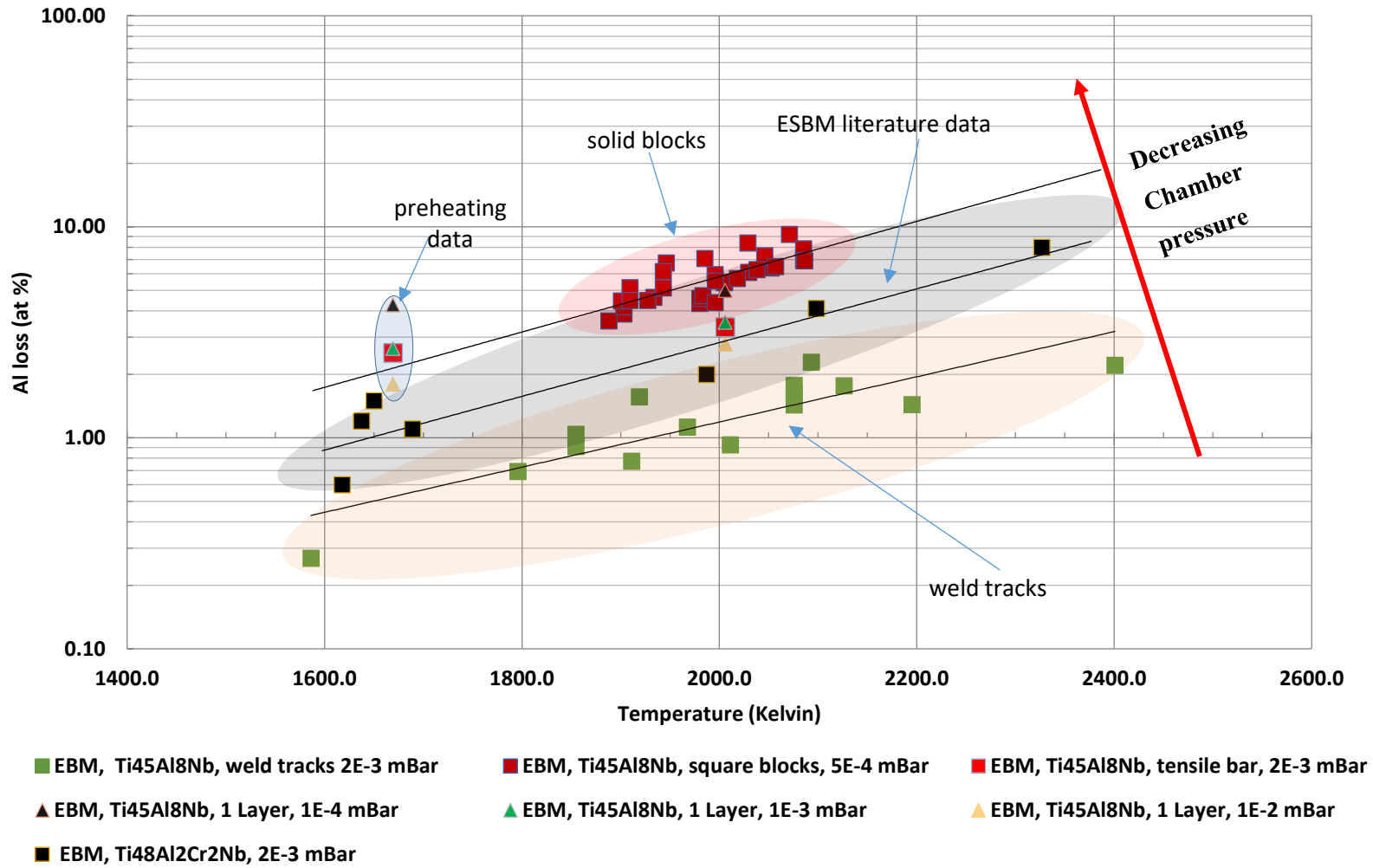
Figure 6-7. Al loss (at %) versus calculated surface temperature for electron beam melted samples

Knowing all the relevant process parameters and material properties (Eq. 6.1) we may calculate the evaporation rates for all the individual constituent elements. Average surface temperatures calculated with the MATLAB code are used to calculate all temperature related parameters (e.g. partial pressures and activities). In those calculations heating times are taken into account as well. Aluminium evaporation rates were calculated for:

- Single EBM weld tracks
- Single EBM layer (x 3 times) at 3 different chamber pressures
- EBM deposited solid blocks
- EBM deposited tensile bars
- EBM literature data [99], [119]
- Induction melting casting literature data [178] for various chamber pressures and heating times, and
- Metal Injection moulding literature data [179]

As might be expected and indeed is clearly shown in Figure 6-8 there is a clear correlation between actual, measured Aluminium loss (at %) and the Model calculated evaporation rates. The alloy system (γ-TiAl) is similar for all data in the graph and the heating times during EBM are not that long to significantly affect the resulting trendlines compared with the ones in Figure 6-7. Though heating times and material properties are quite important and they were accounted for in the calculations for this graph. This should explain and predict Aluminium loss more accurately for those specific data and alloys and it could be a more "global" representation for different processes and even alloy systems. This is quite obvious for the literature data of induction melting casting [178] and metal injection moulding [179], where melting temperature is being kept constant and the only varying process parameters are heating time and chamber pressure. For those literature data temperature and heating time are not estimated/calculated, but are precisely measured experimental data. There is a clear trend of increasing Aluminium loss as the Aluminium evaporation rate is increasing as an effect of the increasing heating time for those literature data. Once more the Aluminium loss trendline is shifted to higher levels as chamber pressure is decreased.
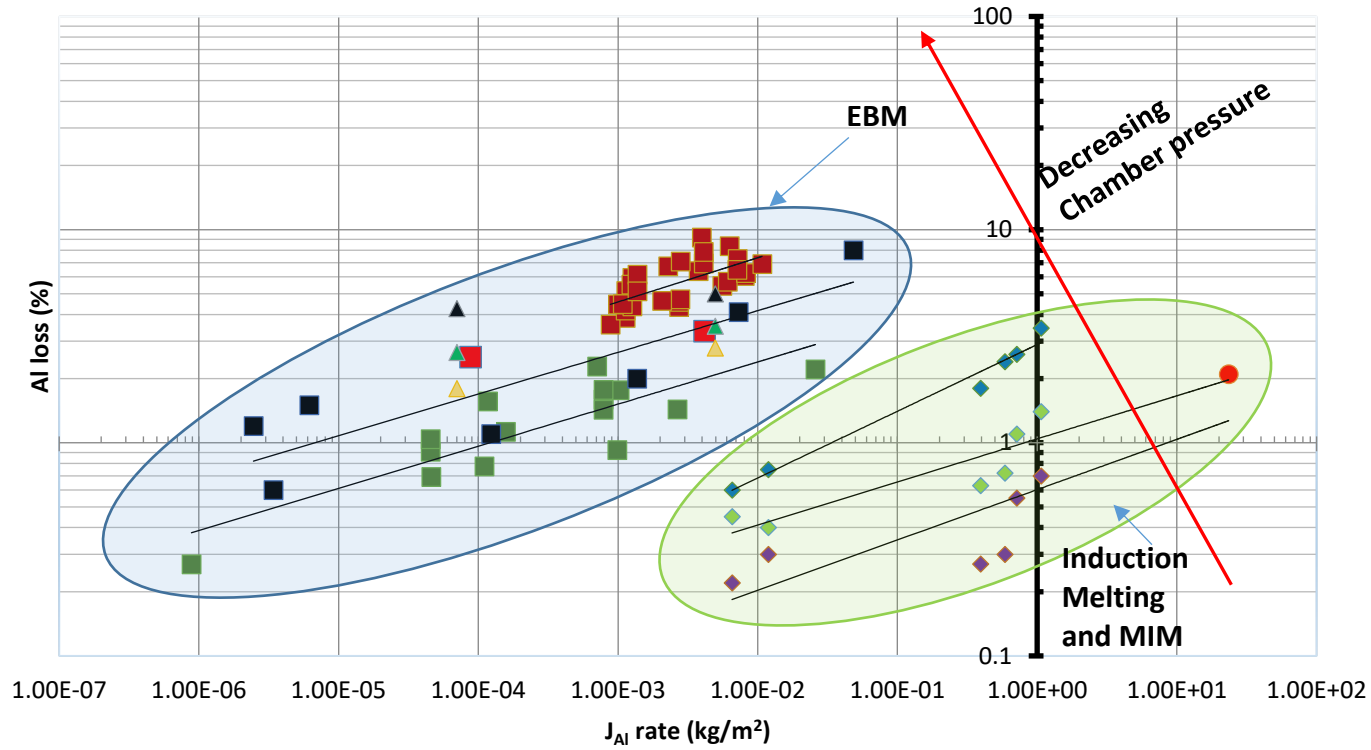
Figure 6-8. Al loss (at %) vesrsus calculated Al evaporation rate, J_{Al} (kg/m^2)

It is clear from the trendlines exhibited in both figures (Figure 6-7 and Figure 6-8) that the use of a heat source model to estimate the average surface temperature and the evaporation rate, rather than the frequently used line energy index [119], seems to be a much more comprehensive way to explain Aluminium evaporation losses during vacuum- EBM of Titanium Aluminide alloys. Line energy indicates the total imported energy quite precisely, but cannot explain and predict how this energy is being distributed on the powder bed in terms of melt pool dimensions and temperature fields in general, and cannot account for the physics behind evaporation by itself.

6.2.3 Impeding Chamber Pressure for Suppressing Al Evaporation loss (%) during EBM Processing of a Ti45Al8Nb alloy

An obvious conclusion from the discussion in this chapter is that evaporation is a function of material properties, surface temperature, heating time and chamber pressure. Obviously, material (thermal) properties cannot be altered for a given alloy, but surface temperature and heating time and subsequently evaporation rate could be easily controlled by altering process parameters. However, in the case of additive manufacturing and EBM specifically, when "lowering" the process (beam related) parameters which affect evaporation, densification of the deposited sample might also be reduced. Additionally, as discussed, evaporation occurs even at temperatures much lower than the melting point, so it is inevitable that volatile elements, which are present in high temperature alloys will evaporate during the process. Another way to control and reduce evaporation is by increasing chamber pressure. Impeding pressure for suppressing evaporation is a well-established phenomenon and it is has also been investigated for Ti-Al and Ti-Al-Nb alloy systems for investment casting [169], [180].

To study this, a single layer was melted under fixed conditions (identical to the optimised hatching themes for tensile specimens) for 3 different chamber pressures (10^{-2}, 10^{-3} and 10^{-4} mBar) and chemical analysis (EDX-SEM) was performed on the cross-section for both the melting hatching area, as well as at the preheating area. Average Aluminium loss and standard error are plotted for each one of those single preheating and melting runs versus the applied chamber pressure (Figure 6-9). Once more a strong relationship between Aluminium loss and chamber pressure can be observed; a logarithmic relationship in this case, where the higher the applied chamber pressure the lower the Aluminium loss for a given surface temperature. Increase in surface temperature increases Aluminium loss as similarly shown in the previous

graphs (Figure 6-7 and Figure 6-8). The Aluminium loss results for the tensile bars that were built with identical process parameters under controlled vacuum (2×10^{-3} mBar – yellow dashed line) fit quite well in the same trend for both the hatching melting and pre-heating area.
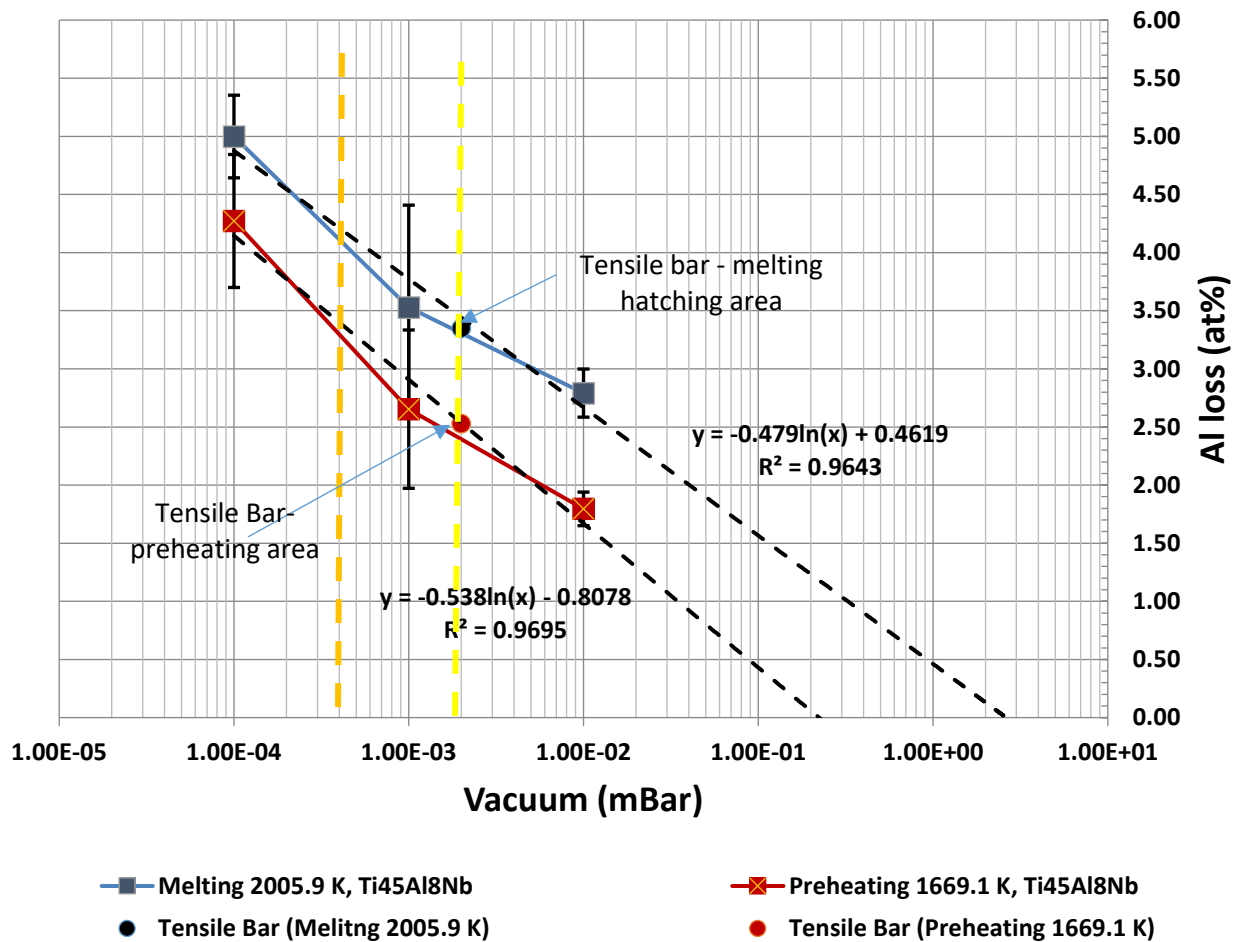
Figure 6-9. Al loss (at %) versus applied vacuum pressure

Extrapolating both logarithmic trends for a 0 % Aluminium loss we can estimate an impeding pressure for both melting and preheating temperatures. The estimated impeding pressures are 1.26 and 0.12 mBar, respectively. Those impeding pressures are plotted in Figure 6-10 with literature data [169], [178]–[180] and estimations for impeding pressures at various temperatures for binary and ternary gamma- based alloys, as well as with the partial pressure calculations for Ti, Al and Nb for Ti45Al8Nb alloys. The blue horizontal dashed line indicates the CV-EBM pressure (2×10^{-3} mBar). Guo [169] experimentally indicated that a sufficient impeding pressure during induction skull melting of Ti25Al25 Nb should be higher than a

factor of 8.1 times the partial pressure of Aluminium. The red dotted lines in the figure are calculated by multiplying the estimated Aluminium partial pressure (upper and lower limit) from our study for the Ti45Al8Nb alloy system by the 8.1 factor. Guo [180] in a more recent study calculated numerically and generated predicting equations for the impeding pressures of binary Ti-xAl alloys with Al content from 25 to 50 at% and temperatures from 1800 to 2000 Kelvin. The linear relationship of impeding pressure versus temperature for the binary Ti45Al from this study [180] is extrapolated and also plotted (black dotted line) in Figure 6-10.
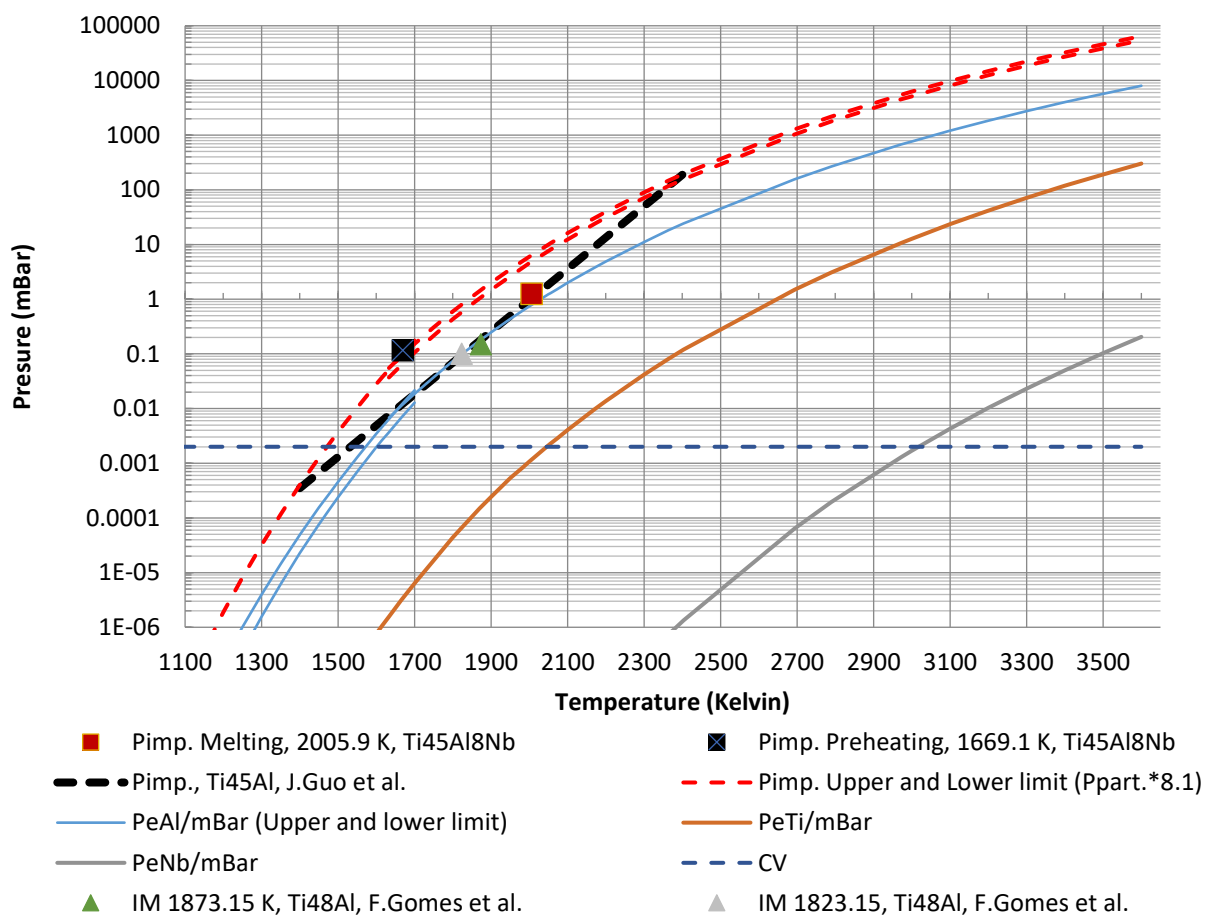
Figure 6-10. Impeding and partial presures versus temperature for Titanium Aluminides

The results for impeding pressures calculated from this study for melting and pre-heating, as well as the ones from literature are quite consistent and a successful impeding pressure at a given temperature should be at least higher than the partial pressure of the most volatile element; Aluminium in this case. The higher the surface temperature, the higher the chamber pressure should be to supress effectively Aluminium evaporation losses. From this graph, it is

quite clear that the suggested Arcam controlled vacuum pressure is not high enough to supress Aluminium evaporation at temperatures higher than about 1500-1600 K for this specific alloy system. This also explains the even higher evaporation losses for the builds that were performed at even lower chamber pressure.

6.3 Effect of Secondary EBM Process Parameters on Aluminium Loss

6.3.1 Aluminium Evaporation Losses Dependence on the Arbitrary "Surface temperature" EBM function

It is unknown how an appropriate Surface Temperature function is selected during novel alloys development by Arcam. The suggested surface temperature for TiAl by Arcam (during Level 3 EBM training) was ST-1600. The suggested Surface Temperature function from a previous TiAl development being performed at NCSU was ST-1200. For the process development for this study, as discussed in more detail in Chapter 5, 1200, 1400 and 1600 values were used. Surface Temperature function was developed during the first years of the Arcam EBM process and it was applicable for tool steels in order to keep a constant average surface temperature during each layer. For other alloys, the value of this process parameter is somewhat arbitrary. In general, a higher "Surface Temperature" value tends to use a higher beam current and speed combination for a given speed function.

The "Surface Temperature" function was not considered for the calculations of the surface temperature with the MATLAB code and for the subsequent calculations of the Aluminium evaporation rates. However, the actual current and speed values during the EBM process for the different "Surface Temperature" values were extracted from the log files and were taken into account. As shown in Figure 6-11, actual, measured Aluminium loss (at %) is higher for a higher value of the "Surface Temperature" function value. This is obviously a source for deviation and justifies, somewhat, the scattering in Figure 6-8 and Figure 6-7 in Section 6.2.2 regarding Aluminium loss.

The possible reason for this discrepancy is that the increase of "Surface Temperature" function, in addition to actually increasing the surface temperature, also changes the heat mode from a deeper and localised penetration [126] to a more spread and shallow surface melting, as an effect of the increase of electron beam speed. A larger area would increase the actual evaporation area, as well as the evaporation time by increasing the possible overlap between

adjacent hatching lines. This effect was shown in Chapter 4, where aspect ratio (2D/W) of weld pool geometry of single weld tracks significantly varies with beam speed and line Energy (E_0), with Pearson's correlation coefficients of -0.7141 and 0.7888 (Table 4-9), respectively and is also shown in Figure 4-20.
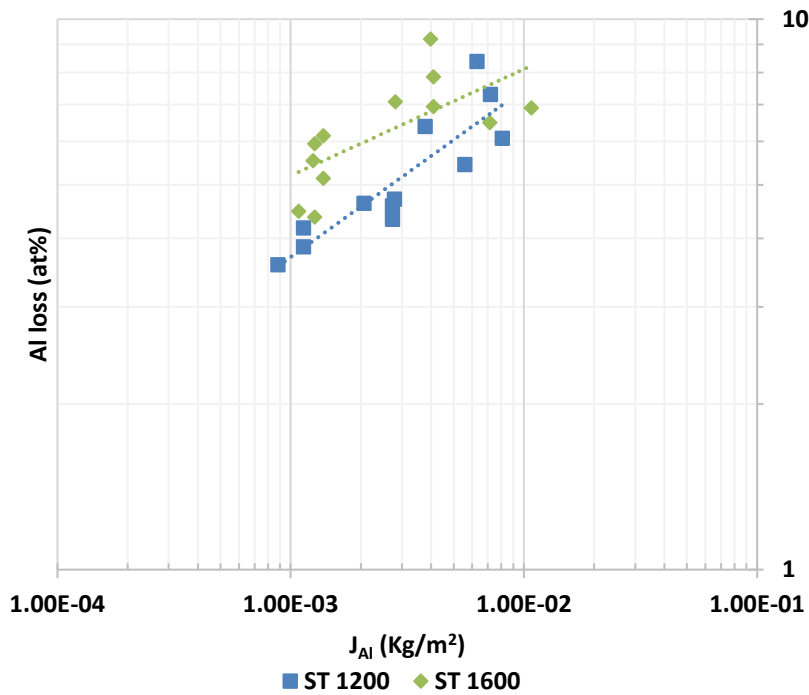
Figure 6-11. Al loss (at %) vs. Al evaporation rate (J_{Al}) for different "surface temperature" process parameters

6.3.2 Aluminium Evaporation Losses Dependence on Focus Offset EBM Process Parameter

Another important process factor that has been also investigated on the previous chapters is focus offset. Focus offset is expected to have a significant impact in both temperature fields and possibly on heating mode. A smaller focus offset is expected to reduce the beam diameter, but with increased intensity. A larger focus offset is expected to decrease the intensity of the electron beam, but it will affect a larger area. As previously discussed, a larger heat affected area increases both the actual evaporation area as well as the evaporation time by increasing the possible overlap between adjacent hatching lines.

In reality a quadratic relationship is observed with a minimum Aluminium loss (Figure 5-12, Figure 6-13 and Figure 6-14) in the range between 8-10 mA for focus offset. Aluminium loss linearly increases with reducing speed function value and increasing calculated surface temperature and calculated evaporation rate, respectively. All three models show a good fit. This quadratic relationship can be explained by considering evaporation behaviour in two areas. In the first area as focus offset increases from a low starting value, evaporation decreases as a result of decreasing electron beam intensity per surface area. In the area above the range 8-10 mA the heat affected zone possibly increases (width/depth ratio increases) with subsequent increase of evaporation area, as well as evaporation time rises because of an increase in overlap between adjacent hatching lines.
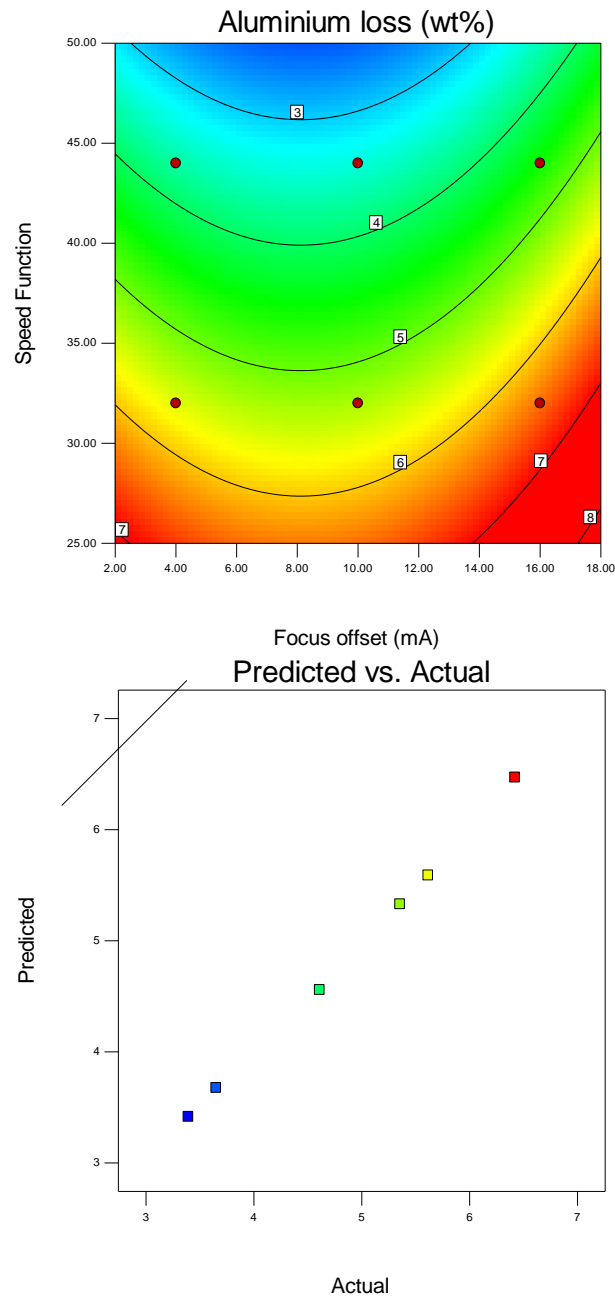
Figure 6-12. Al evaporation losses (at %) as a function of speed function and focus offset, b) diagnostic plot (predicted vs. actual) for the fitted Al evaporation losses measurements
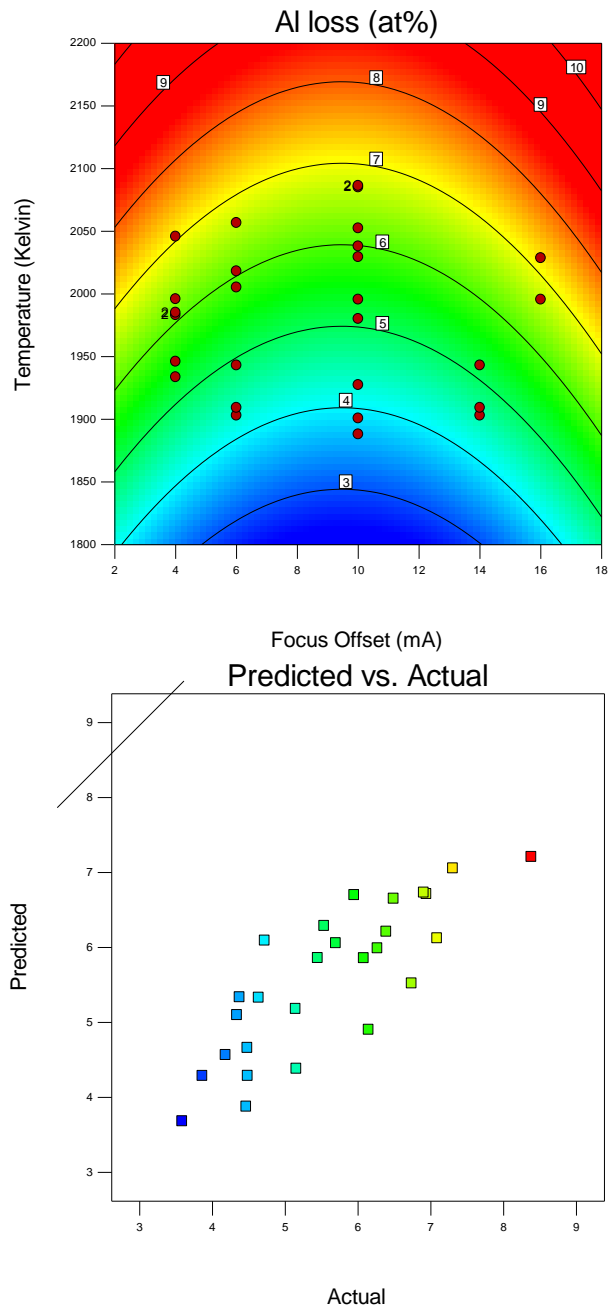
Figure 6-13. Al evaporation losses (at %) as a function of calculated surface temperature (Kelvin) and focus offset, b) diagnostic plot (predicted vs. actual) for the fitted Al evaporation losses measurements
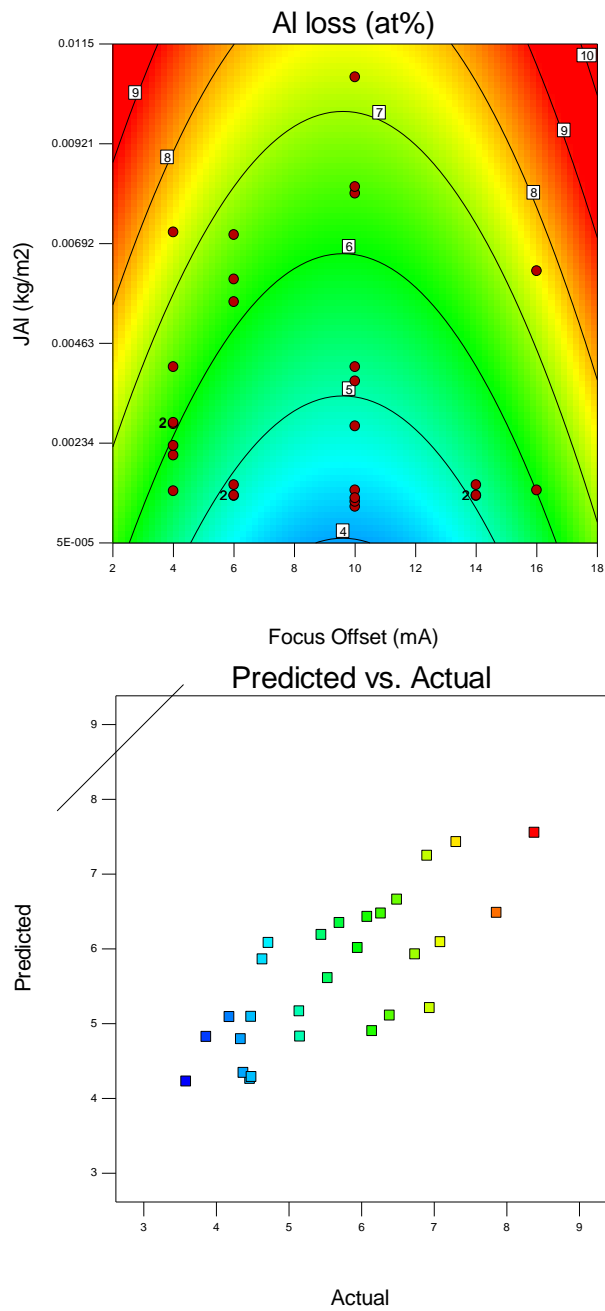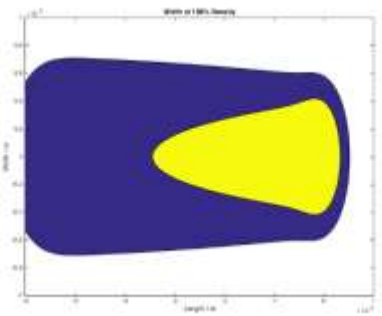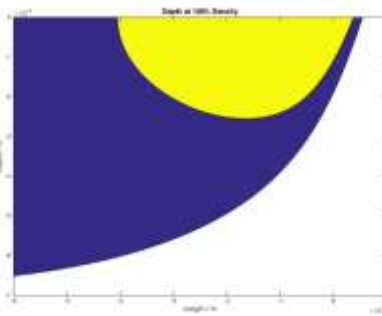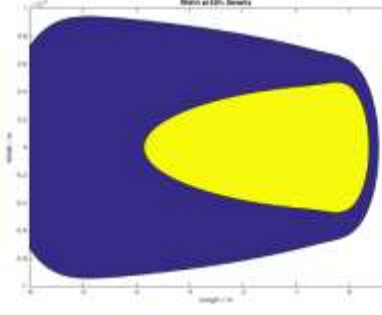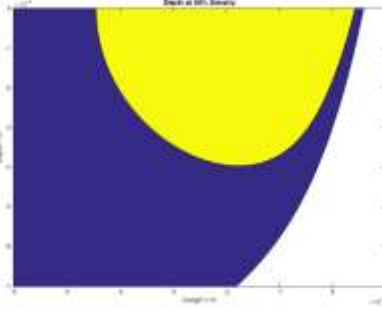
Figure 6-14. a) Al evaporation losses (at %) as a function of calculated Al evaporation rate (J_{Al}: kg/m^2) and focus offset, b) diagnostic plot (predicted vs. actual) for the fitted Al evaporation losses measurements

6.3.3 Aluminium Evaporation Losses Dependence on Density of the Substrate Material

During the EBM process, a scanning (melting or preheating) electron beam interacts with a substrate of varying density. Densification of the substrate depends on the preheating or melting process parameters of the previous layers. For example, when preheating or melting on overhanging surfaces the substrate is of much lower density than melting and preheating on already melted and almost fully dense substrates. Thermal properties of a specific material such as thermal conductivity (k) and thermal diffusivity (α) are functions of density. Melting/preheating on less dense substrates increases surface temperature and subsequently evaporation is expected to increase. Melt pool depth and length are increasing with decreasing density, but melt pool width remains almost unchanged (Table 6-1). Additionally, evaporation has been suggested to increase with increased level of porosity (φ), due to the increase of exposed surface area [130].

Table 6-1. Heat source modelling - Effect of substrate density on melting response

	Width	Depth
Density 100%		
Density 50%		

Aluminium loss was measured for weld tracks scanned on different levels of density/porosity substrates manufactured by SPS at different dwell temperatures. In Figure 6-15, Aluminium

loss (at %) versus calculated surface temperature is plotted for single weld tracks scanned on samples prepared by SPS at 900 and 1000 ºC dwell temperature, respectively, the resulting density is about 83 and 91 %, respectively. As expected from the discussion in the previous paragraph, Aluminium loss is higher for the weld tracks scanned on the more porous substrate, with all other process parameters being fixed. This obviously is an additional source for deviation and justifies scattering of the trendlines, which are presented in Section 6.2.2 of this chapter regarding Aluminium loss.
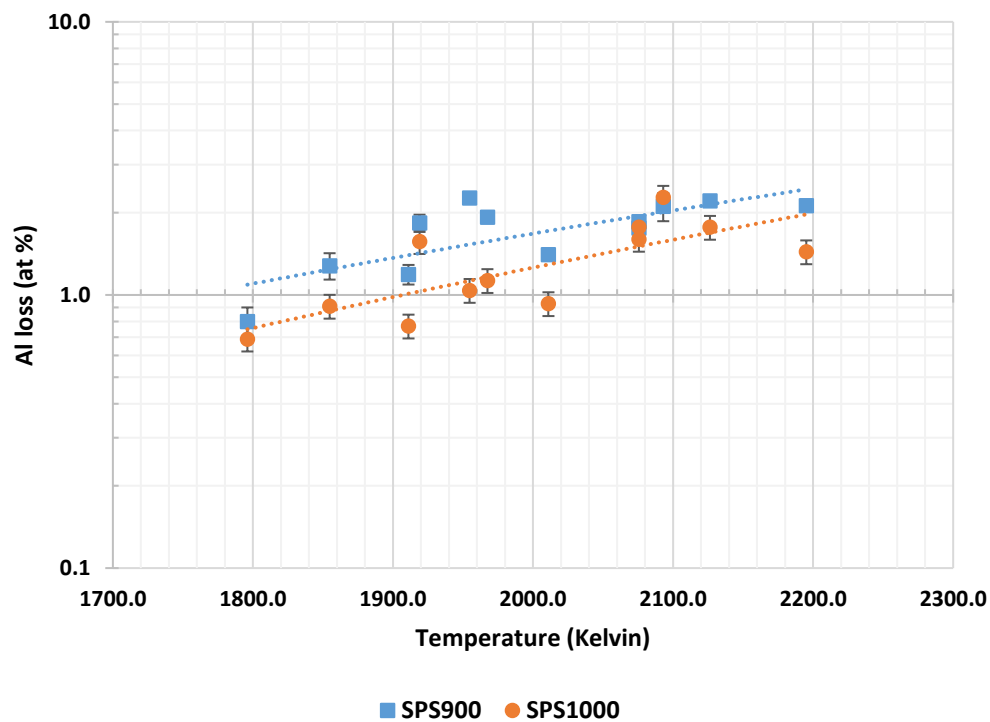
Figure 6-15. Al evaporation losses (at %) for single weld tracks scanned on SPSed base material of different resulting density

6.4 Summary

High Aluminium evaporation loss has been observed as one of the main issue during the process development of Electron Beam Melting of Titanium Aluminides. A heat source model was used to estimate the average surface temperature when scanning a TiAl substrate with an electron beam. This surface temperature was used to estimate Al evaporation rate. Actual measured Aluminium loss for the experimental data from this study and literature data for EBM and other vacuum processes were plotted against surface temperature and evaporation rate with very good fitting. Aluminium evaporation loss versus chamber pressure showed a logarithmic

trend; those trends were extrapolated for a 0 % Al loss in order to estimate impeding vacuum pressures for melting and preheating temperatures and the results were found to be very consistent with literature data and a successful impeding pressure at a given temperature was found that should be at least higher than the partial pressure of the most volatile element; Al in this case.

To conclude, evaporation per surface area during EBM processing of a metallic substrate mainly depends on surface temperature, heating time and chamber pressure and is a function of material specific properties and operational parameters. The main parameters affecting evaporation have been identified.

7 CONCLUSIONS AND FURTHER WORK

The investigations carried out in this work are best summarised into three sections. Firstly, preliminary characterisation and parametrical studies for key EBM process parameters, discussed in Chapter 4, gave an insight into identifying key process parameters and their effect on the melt pool by both statistical/empirical and analytical heat source modelling. EBM process development, post-processing, resulting microstructures and material properties were discussed in Chapter 5. Finally, the evaporation phenomena and impeding pressure during EBM were investigated in Chapter 6. The main findings from these chapters are summarised here, conclusions are drawn and further future work is suggested.

7.1 Preliminary Characterisation and Parametrical Studies for Key EBM Process Parameters

- The scanning of single weld tracks on solid substrates of variable density fabricated by Spark Plasma Sintering is an effective methodology to investigate the effect of the electron beam on melt pool geometry when varying key process parameters.
- Statistically designed experiments were used successfully to accurately fit empirical and statistical models relating weld track geometry to key process parameters.
  - For weld track width, current was found to be the most significant factor, followed by focus offset.
  - For depth, velocity and line energy (E_L: Q/v) were found to be the most significant factors.
  - The overall volume of the melt pool depends on line energy (E_L: Q/v), regardless of the weld pool shape, which varies with velocity and energy density (E_0)
  - Weld pool (Depth/Width) aspect ratio increases by increasing energy density (E_0) or decreasing the velocity
- Process parameters and resulting weld pool geometry dimensions for different alloy families with different thermal properties (from this work and literature data) fit very well in a logarithmic trend when normalised and treated in a non-dimensional manner.
- Weld pool geometry is well explained by analytical heat source modelling using a fitting parameter of $\beta = 0.84$-0.88. The β parameter incorporates the effect of beam efficiency.

7.2 EBM Process Development, Post- Processing, Resulting Microstructures and Material Properties

- A stable build temperature between 1050-1090 °C is required throughout the process for the specific powder feedstock, base plate dimensions (100x100x10 mm) and layer thickness (70 µm).

- Statistically designed experiments were used successfully to accurately fit empirical statistical models relating the effect of key EBM process (hatch) theme variables selected response variables.

  o For top surface quality, speed function was found to be the most significant factor.

  o Aluminium evaporation has a strong linear relationship with speed function (↑SF, ↓Al loss), while a quadratic relationship seems to occur with focus offset, showing a minimum in the range between 8-10 mA.

  o Maximum density (minimum process defects) is expected for low values of speed function and high values of focus offset or vice versa.

  o Speed function and surface temperature process parameters significantly influence microstructural evolution.

- The microstructure of tensile bars, built with optimised parameters, was found to be nearly lamellar, consisting mainly of coarse grains of lamellar (alternate $\alpha_2+\gamma$ plates) colonies and some equiaxed finer γ grains. This is in contrast with the literature, where near gamma microstructures, consisting mainly of γ equiaxed fine grains with some α_2 precipitates are reported. This is related to chemistry variations (mainly high Al evaporation loss) during the process and the higher build temperature used for this study.

- Hot Isostatic pressing (HIP) at 1200 °C, 150 MPa, for 4 hours was effective to achieve near full densification by eliminating process induced porosity (e.g. lack of fusion). Only a few spherical closed pores survived, related to gas entrapment (powder induced porosity), which is an intrinsic issue of gas-atomising powder manufacturing techniques and it is not possible to eliminate by further EBM process development.

- Post-HIP microstructures look slightly coarser, but more homogenous than the as-built microstructure.

- Mechanical properties only slightly improved after HIP. This slight improvement is related to the reduction of process induced porosity and microstructural homogenisation.

- Mechanical properties are lower than expected for this material (Ti-45Al-8Nb-0.2C) or other TiAl-based alloys manufacture by EBM. This is related to the resulting not optimised microstructure (no heat treatment), to a significant Aluminium evaporation loss and some increase of the content of interstitials, especially for oxygen and carbon. Those chemical variations are all found to affect the microstructure (α_2 volume fraction and lamellar spacing) and therefore the mechanical properties.

- Oxygen and Carbon pick up are related to contamination during the powder handling process, i.e. setting up the machine and recycling the powder and not to the varied process themes. A more careful powder handling procedure and constant monitoring of the powder are suggested to ensure that the composition remains within specification.

- Aluminium content variation is strongly correlated to the process parameters and is identified as one of the main issues for the EBM process development of TiAl-based alloys. Comprehensive study of micro-indentation hardness results versus Aluminium content shows a strong and clear relationship and this is in accordance with literature data.

7.3 Evaporation Phenomena and Impeding Pressure during Electron Beam Melting of a Ti45Al8Nb0.2C Alloy

- Evaporation rates for Ti, Al and Nb versus temperature for the Ti45Al8Nb alloy system were successfully calculated by using known equations and data from the literature.

- Average surface temperatures during EBM process were calculated by integrating a modified Rosenthal equation for a moving heat source with a Gaussian distribution and subsequently used to calculate evaporation rates.

- Estimated surface temperatures and evaporation rates were successfully plotted against measured actual Aluminium evaporation (at %) data from EBM process from this work showing very clear trends. Literature data for EBM processing, Induction Melting casting and Metal Injection Moulding for γ-TiAl based alloys also fit very well in those trends. A clear finding is that an increased chamber pressure could reduce the Aluminium evaporation.

- Impeding pressures for eliminating the Aluminium evaporation loss for melting and preheating EBM process themes were estimated and show a good correlation with literature data. A successful impeding pressure, at a given temperature, should be at least higher than the partial pressure of the most volatile element; Aluminium in this case.

- Evaporation per surface area during EBM process mainly depends on surface temperature, heating time and applied chamber pressure and is a function of material specific properties and operational parameters. The main EBM process parameters affecting evaporation has been identified and discussed in Chapter 6.

7.4 Further Work

7.4.1 Melting (Hatch) theme
- Not all EBM process variables were investigated in this study. Further parametrical studies could be performed investigating the effect of additional key process parameters on melting response, as well as on further required response variables (e.g. hardness, microstructures, etc.).

- Specifically, line (hatching) offset and layer thickness are identified as very important process parameters for further development of melting process themes.

7.4.2 Preheating Theme
- The preheating process theme developed during this study results in a slightly over-sintered powder bed. Due to time limitations during the process development step, such a "harder-sintered" powder bed was preferred, as it was safer for process stability. Though, for optimum powder recovery and minimum powder quality deterioration a softer sintering shall be investigated.

- Equipment modifications for reducing heat losses from the powder bed during EBM processing might help in reducing the required heat input during preheating and subsequently softer sintering could be easier to achieve.

7.4.3 Reduce Aluminium Evaporation

- Further process development shall be done on reducing or even eliminating Al evaporation loss.

- Process theme development shall aim to reduce surface temperature and heating time per surface area.
  - A suggested way is by increasing speed function and/or reducing overlapping between adjacent scanned lines during hatching melting (i.e. increase line offset).
  - Moreover, considering the results from the parametrical studies in **Chapter 5** increasing speed function shall be accompanied by very low values of focus offset in order to achieve required high component density with minimum porosity and process defects.

- As suggested from the results in **Chapter 6**, increasing chamber pressure could effectively decrease or eliminate evaporation.
  - An Argon environment could be used to achieve the required impeding pressure.
  - Trials shall be done under such an environment to verify the results from **Chapter 6,** as well as to test the effect on the EB efficiency and stability.

- If evaporation can't be effectively supressed with process theme development or by increasing chamber pressure a starting powder of higher Aluminium content shall be considered to compensate for the Aluminium loss of the selected process window.

7.4.4 Other Process Themes development

- After achieving the optimum process windows for heating, preheating and melting hatching, for simple geometries, further process theme development shall be carried out:
  - To optimise the contours themes
  - To optimise the turning points and thickness functions for hatching melting
  - To scale up process themes for more complex geometries,
  - To consider extra steps of preheating and melting themes, and
  - To develop process themes for support structures

7.4.5   Heat Treatments

- A study for designing customised heat treatments for the EBM as-built components of the bespoke chemistry shall be carried out to achieve the suitable microstructure depending on application and required performance.

8 BIBLIOGRAPHY

[1] R. J. Deffley, "Development of Processing Strategies for the Additive Layer Manufacture of Aerospace Components in Inconel 718," The Univesrsity of Sheffield, 2012.

[2] G. N. Levy, R. Schindel, and J. P. Kruth, "Rapid Manufacturing and Rapid Tooling With Layer Manufacturing (Lm) Technologies, State of the Art and Future Perspectives," *CIRP Annals - Manufacturing Technology*, vol. 52, no. 2, pp. 589–609, 2003.

[3] J. Hunt, "Additive manufacturing; Overview of key technologies and markets," Sheffield, 2012.

[4] D. L. Bourell, M. C. Leu, and D. W. Rosen, "Roadmap for Additive Manufacturing: Identifying the Future of Freeform Processing," 2009.

[5] K. V. Wong and A. Hernandez, "A Review of Additive Manufacturing," *ISRN Mechanical Engineering*, vol. 2012, pp. 1–10, 2012.

[6] S. Sabbadini, O. Tassa, P. Gennaro, and U. Ackelid, "Additive manufacturing of gamma titanium aluminide parts by electron beam melting," *TMS Annual Meeting*, vol. 1, pp. 267–274, 2010.

[7] S. Biamino, A. Penna, U. Ackelid, S. Sabbadini, O. Tassa, P. Fino, M. Pavese, P. Gennaro, and C. Badini, "Electron beam melting of Ti-48Al-2Cr-2Nb alloy: Microstructure and mechanical properties investigation," *Intermetallics*, vol. 19, no. 6, pp. 776–781, 2011.

[8] S. S. Al-Bermani, M. L. Blackmore, W. Zhang, and I. Todd, "The Origin of Microstructural Diversity, Texture, and Mechanical Properties in Electron Beam Melted Ti-6Al-4V," *Metallurgical and Materials Transactions A*, vol. 41, no. 13, pp. 3422–3434, 2010.

[9] E. A. Loria, "Gamma titanium aluminides as prospective structural materials," *Intermetallics*, vol. 8, no. 9–11, pp. 1339–1345, 2000.

[10] T. Noda, "Application of cast gamma TiAl for automobiles," *Intermetallics*, vol. 6, no. 7–8, pp. 709–713, 1998.

[11] B. F. Appel, U. Brossmann, U. Christoph, S. Eggert, P. Janschek, U. Lorenz, J. Müllauer,

M. Oehring, and J. D. H. Paul, "Recent Progress in the Development of Gamma Titanium Aluminide Alloys," *Advanced Engineering Materials*, vol. 2, no. 11, pp. 699–720, 2000.

[12] F. H. Froes, C. Suryanarayana, and D. Eliezer, "Synthesis, properties and applications of titanium aluminides," *Journal of Materials Science*, vol. 27, no. 19, pp. 5113–5140, 1992.

[13] Y.-W. Kim, "Intermetallic alloys based on gamma titanium aluminide," *Jom*, vol. 41, no. 7, pp. 24–30, 1989.

[14] D. M. Dimiduk, "Gamma titanium aluminide alloys—an assessment within the competition of aerospace structural materials," *Materials Science and Engineering: A*, vol. 263, no. 2, pp. 281–288, 1999.

[15] P. A. Bartolotta and D. L. Krause, "Titanium aluminide applications in the high speed civil transport," *Gamma Titanium Aluminides*, vol. 209071, pp. 3–10, 1999.

[16] E. A. Loria, "Quo vadis gamma titanium aluminide," *Intermetallics*, vol. 9, no. 12, pp. 997–1001, 2001.

[17] H. Clemens and S. Mayer, "Design, Processing, Microstructure, Properties, and Applications of Advanced Intermetallic TiAl Alloys," *Advanced Engineering Materials*, vol. 15, no. 4, pp. 191–215, 2013.

[18] X. Wu, "Review of alloy and process development of TiAl alloys," *Intermetallics*, vol. 14, no. 10–11, pp. 1114–1122, 2006.

[19] J. Lapin, "TiAl-based alloys: Present status and future perspectives," in *18th International Metallurgical & Materials Conference Proceedings*, 2009, pp. 19–21.

[20] T. Tetsui, "Development of a TiAl turbocharger for passenger vehicles," *Materials Science and Engineering A*, vol. 329–331, pp. 582–588, 2002.

[21] W. Shouren, G. Peiquan, and Y. Liying, "Centrifugal precision cast TiAl turbocharger wheel using ceramic mold," *Journal of Materials Processing Technology*, vol. 204, no. 1–3, pp. 492–497, 2008.

[22] M. T. Jovanović, B. Dimčić, I. Bobić, S. Zec, V. Maksimović, M. Jovanovic, B. Dimcic, I. Bobic, S. Zec, V. Maksimovic, M. T. Jovanović, B. Dimčić, I. Bobić, S. Zec, and V.

Maksimović, "Microstructure and mechanical properties of precision cast TiAl turbocharger wheel," *Journal of Materials Processing Technology*, vol. 167, no. 1, pp. 14–21, 2005.

[23] K. Kothari, "Manufacturing Techniques for Titanium Aluminide Based Alloys and Metal Matrix Composites," University Maryland, 2010.

[24] "GEnx Engine | Boeing 787 Dreamliner & 747-8 | GE Aviation." [Online]. Available: http://www.geaviation.com/commercial/engines/genx/. [Accessed: 17-Jan-2016].

[25] B. P. Bewlay, M. Weimer, T. Kelly, A. Suzuki, and P. R. Subramanian, "The Science, Technology, and Implementation of TiAl Alloys in Commercial Aircraft Engines," *MRS Proceedings*, vol. 1516, pp. 49–58, 2013.

[26] L. Löber, "Selective laser melting of Titanium Aluminides," in *4th International Workshop on Titanium Aluminides*, 2011.

[27] E. P. George, M. Yamaguchi, K. S. Kumar, and C. T. Liu, "Ordered Intermetallics," in *Annual Review of Materials Science*, vol. 24, no. 1, 1994, pp. 409–451.

[28] G. Sauthoff, "Intermetallics," *Weinheim*, 1995. [Online]. Available: http://books.google.co.uk/books?id=Oe_POhzOIQkC&pg=PA63&lpg=PA63&dq=sau thoff+intermetallics&source=bl&ots=2XVUG96K31&sig=16Yl3BIijd3d3kbblyNUlIq NQ3E&hl=en&sa=X&ei=TqmFT_2kIYL80QX6luHjBw&ved=0CCgQ6AEwAQ#v=o nepage&q=sauthoff intermetallics&f=false. [Accessed: 07-Apr-2012].

[29] N. Cinca, C. R. C. Lima, and J. M. Guilemany, "An overview of intermetallics research and application: Status of thermal spray coatings," *Journal of Materials Research and Technology*, vol. 2, no. 1, pp. 75–86, 2013.

[30] A. Lasalmonie, "Intermetallics: Why is it so difficult to introduce them in gas turbine engines?," *Intermetallics*, vol. 14, no. 10–11, pp. 1123–1129, 2006.

[31] N. S. Stoloff, C. T. Liu, and S. C. Deevi, "Emerging applications of intermetallics," *Intermetallics*, vol. 8, no. 9–11, pp. 1313–1320, 2000.

[32] S. Djanarthany, J.-C. Viala, and J. Bouix, "An overview of monolithic titanium aluminides based on Ti3Al and TiAl," *Materials Chemistry and Physics*, vol. 72, no. 3, pp. 301–319, 2001.

[33] CALPHAD, "Titanium-Aluminum (Ti-Al) Phase Diagram," *Computational Thermodynamics*, 2011. [Online]. Available: http://www.calphad.com/titanium-aluminum.html. [Accessed: 20-Mar-2012].

[34] M. R. Yang and S. K. Wu, "The improvement of high-temperature oxidation of Ti-50Al by anodic coating in the phosphoric acid," *Acta Materialia*, vol. 50, no. 4, pp. 691–701, 2002.

[35] M. Dettenwanger, F. & Schütze, "Isothermal Oxidation of alpha2-Ti3Al," *Oxidation of Metals*, vol. 54, no. 1, pp. 121–138, 2000.

[36] R. G. Reddy, X. Wen, and M. Divakar, "Isothermal oxidation of TiAl alloy," *Metallurgical and Materials Transactions A*, vol. 32, no. 9, pp. 2357–2361, 2001.

[37] M. Thomas and M.-P. Bacos, "Processing and Characterization of TiAl- based Alloys : Towards an Industrial Scale," *Aerospace Lab*, no. 3, pp. 1–11, 2011.

[38] F. Appel, D. H. Paul, and M. Oehring, *Gamma Titanium Aluminide Alloys: Science and Technology*. John Wiley & Sons, 2011.

[39] Z. C. Liu, J. P. Lin, S. J. Li, and G. L. Chen, "Effects of Nb and Al on the microstructures and mechanical properties of high Nb containing TiAl base alloys," *Intermetallics*, vol. 10, no. 7, pp. 653–659, 2002.

[40] R. Gerling, H. Clemens, and F. P. P. Schimansky, "Power Metallurgical processing of Intermetallic Gamma Titanium Aluminides," *Advanced Engineering Materials*, vol. 6, no. 1–2, pp. 23–38, 2004.

[41] P. Bartolotta, J. Barrett, T. Kelly, and R. Smashey, "The use of cast Ti−48Al−2Cr−2Nb in jet engines," *Jom*, vol. 49, no. 5, pp. 48–50, 1997.

[42] J. M. Larsen, B. D. Worth, S. J. Balsone, and J. W. Jones, "An Overview Of Structural Capability Of Available Gamma Titanium Aluminide Alloys," *Gamma Titanium Aluminides*, pp. 821–833, 1995.

[43] S. F. Franzén and J. Karlsson, "γ-Titanium Aluminide Manufactured by Electron," Chalmers University of Technology, 2010.

[44] W. Voice, "The future use of gamma titanium aluminides by Rolls-Royce," *Aircraft Engineering and Aerospace Technology*, vol. 71, no. 4, pp. 337–340, 1999.

[45]   W. E. Voice, M. Henderson, E. F. J. Shelton, and X. Wu, "Gamma titanium aluminide, TNB," *Intermetallics*, vol. 13, no. 9, pp. 959–964, 2005.

[46]   J. Loeber, L., Biamino, S., Ackelid, U., Sabbadini, S., Epicoco, P., Fino, P., Eckert, "Comparison of selective laser and electron beam melted titanium aluminides," in *22nd Annual International Solid Freeform Fabrication Symposium - An Additive Manufacturing Conference, SFF 2011*, 2011, pp. 547–556.

[47]   F. Appel, M. Oehring, and R. Wagner, "Novel design concepts for gamma-base titanium aluminide alloys," *Intermetallics*, vol. 8, no. 9–11, pp. 1283–1312, 2000.

[48]   Bacos M.P., Morel A., Naveos S., Bachelier-Locq A., Josso P., and Thomas M., "The effect of long term exposure in oxidising and corroding environments on the tensile properties of two gamma-TiAl alloys," *Intermetallics*, vol. 14, pp. 102–113, 2006.

[49]   F. Appel, M. Oehring, J. D. H. Paul, C. Klinkenberg, and T. Carneiro, "Physical aspects of hot-working gamma-based titanium aluminides," *Intermetallics*, vol. 12, pp. 791–802, 2004.

[50]   A. El Chaikh, F. Appel, and T. K. Heckel, "Characterization of the Damage Mechanisms of a High-Strength," *Technology*, pp. 1–21, 2012.

[51]   V. Güther, C. Rothe, S. Winter, and H. Clemens, "Metallurgy, Microstructure and Properties of Intermetallic TiAl Ingots," *BHM Berg- und Hüttenmännische Monatshefte*, vol. 155, no. 7, pp. 325–329, 2010.

[52]   M. Schloffer, B. Rashkova, T. Schöberl, E. Schwaighofer, Z. Zhang, H. Clemens, and S. Mayer, "Evolution of the ω phase in a β-stabilized multi-phase TiAl alloy and its effect on hardness," *Acta Materialia*, vol. 64, pp. 241–252, 2014.

[53]   M. Schloffer, F. Iqbal, H. Gabrisch, E. Schwaighofer, F. P. Schimansky, S. Mayer, A. Stark, T. Lippmann, M. Göken, F. Pyczak, and H. Clemens, "Microstructure development and hardness of a powder metallurgical multi phase γ-TiAl based alloy," *Intermetallics*, vol. 22, pp. 231–240, 2012.

[54]   V. Imayev, T. Oleneva, R. Imayev, H. J. Christ, and H. J. Fecht, "Microstructure and mechanical properties of low and heavy alloyed γ-TiAl + α2-Ti3Al based alloys subjected to different treatments," *Intermetallics*, vol. 26, pp. 91–97, 2012.

[55]   H. Saage, A. J. Huang, D. Hu, M. H. Loretto, and X. Wu, "Microstructures and tensile

properties of massively transformed and aged Ti46Al8Nb and Ti46Al8Ta alloys," *Intermetallics*, vol. 17, no. 1–2, pp. 32–38, 2009.

[56] V. T. Witusiewicz, A. A. Bondar, U. Hecht, T. Y. Velikanova, and S. Rex, "The Al–B–Nb–Ti system," *Journal of Alloys and Compounds*, vol. 465, no. 1–2, pp. 64–77, 2008.

[57] H. F. Chladil, H. Clemens, H. Leitner, A. Bartels, R. Gerling, F. P. Schimansky, and S. Kremmer, "Phase transformations in high niobium and carbon containing γ-TiAl based alloys," *Intermetallics*, vol. 14, no. 10–11, pp. 1194–1198, 2006.

[58] F. Appel and M. Oehring, "γ-Titanium Aluminide Alloys: Alloy Design and Properties," in *Titanium and Titanium Alloys*, 2005, pp. 89–152.

[59] Y. H. Wang, J. P. Lin, Y. H. He, Y. L. Wang, and G. L. Chen, "Fabrication and SPS microstructures of Ti-45Al-8.5Nb-(W,B,Y) alloying powders," *Intermetallics*, vol. 16, no. 2, pp. 215–224, 2008.

[60] B. Matijasevic and J. Banhart, "Improvement of aluminium foam technology by tailoring of blowing agent," *Scripta Materialia*, vol. 54, no. 4, pp. 503–508, 2006.

[61] Larsen, DE, Christodoulou, L, "Investment-cast processing of X D TM near- γ titanium aluminides," *Materials Science and Engineering*, vol. A144, pp. 45–49, 1991.

[62] F. H. Froes, "Structural intermetallics," *Jom*, no. September, pp. 6–17, 1989.

[63] D. Larsen, "Status of investment cast gamma titanium aluminides in the USA," *Materials Science and Engineering: A*, vol. 213, pp. 128–133, 1996.

[64] L. Zhao, P. Au, J. Beddoes, and W. Wallace, "Method to procuce fine-grained lamellar microstructures in gamma titanium aluminides," *US Patent 5,653,828*, 1997.

[65] X. Nguyen-Dinh, "Titanium aluminide alloys containing boron, chromium, silicon and tungsten," *US Patent 5,908,516*, 1999.

[66] Y.-W. Kim and D. M. Dimiduk, "Progress in the understanding of gamma titanium aluminides," *Jom*, vol. 43, no. 8, pp. 40–47, 1991.

[67] J. . Kuang, R. . Harding, and J. Campbell, "Microstructures and properties of investment castings of γ-titanium aluminide," *Materials Science and Engineering: A*, vol. 329–331, pp. 31–37, 2002.

[68] M. M. Keller, P. E. Jones, W. J. Porter, and D. Eylon, "The Development of Low-Cost

TiAl Automotive Valves," *Jom*, vol. 49, no. 5, pp. 42–44, 1997.

[69] R. A. Harding, M. Wickins, H. Wang, G. Djambazov, and K. A. Pericleous, "Intermetallics Development of a turbulence-free casting technique for titanium aluminides," *Intermetallics*, vol. 19, no. 6, pp. 805–813, 2011.

[70] K. Liu, Y. C. Ma, M. Gao, G. B. Rao, Y. Y. Li, K. Wei, X. Wu, and M. H. Loretto, "Single step centrifugal casting TiAl automotive valves," *Intermetallics*, vol. 13, no. 9, pp. 925–928, 2005.

[71] A. Choudhury and M. Blum, "Economical production of titanium-aluminide automotive valves using cold wall induction melting and centrifugal casting in a permanent mold," *Vacuum*, vol. 47, no. 6–8, pp. 829–831, 1996.

[72] M. Takeyama and S. Kobayashi, "Physical metallurgy for wrought gamma titanium aluminides Microstructure control through phase transformations," *Intermetallics*, vol. 13, no. 9, pp. 993–999, 2005.

[73] G. Wegmann, R. Gerling, and F. P. Schimansky, "Temperature induced porosity in hot isostatically pressed gamma titanium aluminide alloy powders," *Acta Materialia*, vol. 51, pp. 741–752, 2003.

[74] G. Das, W. Smarsly, F. Heutling, U. Habel, C. Kunze, and D. Helm, "Development of Gamma TiAl for Aerospace Engines," in *4th International workshop on titanium aluminides*, 2011.

[75] H. Zhu, T. Wei, D. Carr, R. Harrison, L. Edwards, W. Hoffelner, D. Seo, and K. Maruyama, "Assessment of Titanium aluminide alloys for high-temperature nuclear structural applications," *Jom*, vol. 64, no. 12, pp. 1418–1424, 2012.

[76] I. E. Anderson and R. L. Terpstra, "Increased process uniformity in gas atomisation," *Metal Powder Report*, vol. 57, no. 6, p. 58, Jun. 2002.

[77] T. Sawatzky, H. Saari, and D. Laurin, "The Effect of Multi-Stage HIP and Aging Treatments on the Microstructure and Mechanical Properties of Powder Metallurgy Beta Gamma TiAl-4Nb-2Mo Alloy," *Structures and Materials*, pp. 5–9, 2012.

[78] R. Simpkinsii, M. Rourke, T. Bieler, and P. Mcquay, "The effects of HIP pore closure and age hardening on primary creep and tensile property variations in a TiAl XD^{TM} alloy with 0.1wt.% carbon," *Materials Science and Engineering: A*, vol. 463, no. 1–2, pp.

208–215, 2007.

[79] H. B. Yu, D. L. Zhang, Y. Y. Chen, P. Cao, and B. Gabbitas, "Synthesis of an ultrafine grained TiAl based alloy by subzero temperature milling and HIP, its microstructure and mechanical properties," *Journal of Alloys and Compounds*, vol. 474, no. 1–2, pp. 105–112, 2009.

[80] U. Habel and B. J. McTiernan, "HIP temperature and properties of a gas-atomized gamma-titanium aluminide alloy," *Intermetallics*, vol. 12, no. 1, pp. 63–68, 2004.

[81] C. X. Cui, B. M. Hu, L. C. Zhao, and S. J. Liu, "Titanium alloy production technology, market prospects and industry development," *Materials & Design*, vol. 32, no. 3, pp. 1684–1691, 2011.

[82] H. Jabbar, J.-P. Monchoux, F. Houdellier, M. Dollé, F.-P. Schimansky, F. Pyczak, M. Thomas, and A. Couret, "Microstructure and mechanical properties of high niobium containing TiAl alloys elaborated by spark plasma sintering," *Intermetallics*, vol. 18, no. 12, pp. 2312–2321, 2010.

[83] T. Voisin, J.-P. Monchoux, M. Hantcherli, S. Mayer, H. Clemens, and A. Couret, "Microstructures and mechanical properties of a multi-phase β-solidifying TiAl alloy densified by spark plasma sintering," *Acta Materialia*, vol. 73, no. 1, pp. 107–115, 2014.

[84] X. Lu, X. B. He, B. Zhang, L. Zhang, X. H. Qu, and Z. X. Guo, "Intermetallics Microstructure and mechanical properties of a spark plasma sintered $Ti-45Al-8.5Nb-0.2W-0.2B-0.1Y$ alloy," *Intermetallics*, vol. 17, no. 10, pp. 840–846, 2009.

[85] ASTM International, "Committee F42 on Additive Manufacturing Technologies," *Committee F42 - AM Technologies*, 2014. [Online]. Available: http://www.astm.org/COMMITTEE/F42.htm. [Accessed: 10-Feb-2016].

[86] B. Van Der Schueren and J. P. Kruth, "Powder deposition in selective metal powder sintering," *Rapid Prototyping Journal*, vol. 1, no. 3, pp. 23–31, 1995.

[87] L. Shepeleva, B. Medres, W. D. Kaplan, M. Bamberger, and a. Weisheit, "Laser cladding of turbine blades," *Surface and Coatings Technology*, vol. 125, no. 1–3, pp. 45–48, 2000.

[88] D. R. Foster, M. J. Dapino, and S. S. Babu, "Elastic constants of ultrasonic additive manufactured Al 3003-H18," *Ultrasonics*, vol. 53, no. 1, pp. 211–218, 2013.

[89]   D. Schick, S. Suresh Babu, D. R. Foster, M. Dapino, M. Short, and J. C. Lippold, "Transient thermal response in ultrasonic additive manufacturing of aluminum 3003," *Rapid Prototyping Journal*, vol. 17, no. 5, pp. 369–379, 2011.

[90]   D. E. Schick, R. M. Hahnlen, R. Dehoff, P. Collins, S. S. Babu, M. J. Dapino, and J. C. Lippold, "Microstructural characterization of bonding interfaces in Aluminum 3003 blocks fabricated by ultrasonic additive manufacturing," *Welding Journal*, vol. 89, no. 5, pp. 105–115, 2010.

[91]   "3D Printing Gives Cancer Patient New Ribs and Sternum in First-of-Its-Kind Surgery | 3DPrint.com." [Online]. Available: http://3dprint.com/95371/3d-printed-ribs-and-sternum/. [Accessed: 10-Feb-2016].

[92]   M. Koike, K. Martinez, L. Guo, G. Chahine, R. Kovacevic, and T. Okabe, "Evaluation of titanium alloy fabricated using electron beam melting system for dental applications," *Journal of Materials Processing Technology*, vol. 211, no. 8, pp. 1400–1408, 2011.

[93]   A. Strondl, R. Fischer, G. Frommeyer, and A. Schneider, "Investigations of MX and γ′/γ ″precipitates in the nickel-based superalloy 718 produced by electron beam melting," *Materials Science and Engineering A*, vol. 480, no. 1–2, pp. 138–147, 2008.

[94]   X. Zhao, J. Chen, X. Lin, and W. Huang, "Study on microstructure and mechanical properties of laser rapid forming Inconel 718," *Materials Science and Engineering: A*, vol. 478, no. 1–2, pp. 119–124, 2008.

[95]   K. N. Amato, S. M. Gaytan, L. E. Murr, E. Martinez, and P. W. Shindo, "Microstructures and mechanical behavior of Inconel 718 fabricated by selective laser melting," *Acta Materialia*, vol. 60, pp. 2229–2239, 2012.

[96]   T. Mahale, D. Cormier, O. Harrysson, and K. Ervin, "Advances in Electron Beam Melting of Aluminum Alloys," *International Solid Freeform Fabrication Symposium*, pp. 312–323, 2007.

[97]   K. Bartkowiak, S. Ullrich, T. Frick, and M. Schmidt, "New developments of laser processing aluminium alloys via additive manufacturing technique," *Physics Procedia*, vol. 12, no. PART 1, pp. 393–401, 2011.

[98]   K. Schmidtke, F. Palm, A. Hawkins, and C. Emmelmann, "Process and mechanical properties: Applicability of a scandium modified Al-alloy for laser additive

manufacturing," *Physics Procedia*, vol. 12, no. PART 1, pp. 369–374, 2011.

[99] D. Cormier, O. Harrysson, T. Mahale, and H. West, "Freeform Fabrication of Titanium Aluminide via Electron Beam Melting Using Prealloyed and Blended Powders," *Research Letters in Materials Science*, vol. 2007, pp. 1–4, 2007.

[100] L. E. Murr, S. M. Gaytan, F. Medina, E. Martinez, J. L. Martinez, D. H. Hernandez, B. I. Machado, D. A. Ramirez, and R. B. Wicker, "Characterization of Ti–6Al–4V open cellular foams fabricated by additive manufacturing using electron beam melting," *Materials Science and Engineering: A*, vol. 527, no. 7–8, pp. 1861–1868, 2010.

[101] M. Filippini, S. Beretta, L. Patriarca, G. Pasquero, and S. Sabbadini, "Defect tolerance of a gamma titanium aluminide alloy," *Procedia Engineering*, vol. 10, pp. 3677–3682, 2011.

[102] J. Hernandez, L. E. Murr, S. M. Gaytan, E. Martinez, F. Medina, and R. B. Wicker, "Microstructures for Two-Phase Gamma Titanium Aluminide Fabricated by Electron Beam Melting," *Metallography, Microstructure, and Analysis*, vol. 1, no. 1, pp. 14–27, 2012.

[103] H. P. Qu, P. Li, S. Q. Zhang, A. Li, and H. M. Wang, "Microstructure and mechanical property of laser melting deposition (LMD) Ti/TiAl structural gradient material," *Materials and Design*, vol. 31, no. 1, pp. 574–582, 2010.

[104] B. P. Bewlay, M. R. Jackson, J. . Zhao, and P. R. Subramanian, "A Review of Very-High-Temperature Nb-Silicide – Based Composites," *Metallurgical and Materials Transactions*, vol. 34A, pp. 2043–2052, 2003.

[105] R. Dicks, F. Wang, and X. Wu, "The manufacture of a niobium/niobium-silicide-based alloy using direct laser fabrication," *Journal of Materials Processing Technology*, vol. 209, no. 4, pp. 1752–1757, 2009.

[106] C. A. Brice, K. I. Schwendner, S. Amancherla, H. L. Fraser, and X. D. Zhang, "Characterization of laser deposited niobium and molybdenum silicides," in *Solid Freeform and Additive Fabrication*, 2000, vol. 625, pp. 31–36.

[107] B. Zhang, H. Liao, and C. Coddet, "Effects of processing parameters on properties of selective laser melting Mg-9%Al powder mixture," *Materials & Design*, vol. 34, pp. 753–758, 2012.

[108] W. van Grunsven, E. Hernandez-Nava, G. Reilly, and R. Goodall, "Fabrication and Mechanical Characterisation of Titanium Lattices with Graded Porosity," *Metals*, vol. 4, no. 3, pp. 401–409, 2014.

[109] C. Smith, I. Todd, and M. Gilbert, "Utilizing additive manufacturing techniques to fabricate weight optimized components designed using structural optimization methods," *Solid Freeform Fabrication Symposium*, pp. 879–894, 2013.

[110] E. Hernandez-Nava, C. J. Smith, F. Derguti, S. Tammas-Williams, F. Leonard, P. J. Withers, I. Todd, and R. Goodall, "The effect of density and feature size on mechanical properties of isostructural metallic foams produced by additive manufacturing," *Acta Materialia*, vol. 85, pp. 387–395, 2015.

[111] A. Amendola, E. Hernndez-Nava, R. Goodall, I. Todd, R. E. Skelton, and F. Fraternali, "On the additive manufacturing, post-tensioning and testing of bi-material tensegrity structures," *Composite Structures*, vol. 131, pp. 66–71, 2015.

[112] Al-Bermani, SS, "An Investigation into Microstructure and Microstructural Control of Additive Layer Manufactured Ti-6Al-4V by Electron Beam Melting," The University of Sheffield, 2011.

[113] D. Stapleton, "Manufacture of Metal Matrix Composites by Additive Layer Manufacture – A Feasibility Study," The University of Sheffield, 2011.

[114] M. C. Chaturvedi, Q. Xu, and N. L. Richards, "Development of crack-free welds in a TiAl-based alloy," *Journal of Materials Processing Technology*, vol. 118, no. 1–3, pp. 74–78, 2001.

[115] Y. D. Wang, H. B. Tang, Y. L. Fang, and H. M. Wang, "Microstructure and mechanical properties of laser melting deposited 1Cr12Ni2WMoVNb steel," *Materials Science & Engineering A*, vol. 527, no. 18–19, pp. 4804–4809, 2010.

[116] S. Biamino, "High niobium containing TiAl alloy produced by electron beam melting," in *4th International Workshop on Titanium Aluminides*, 2011.

[117] J. Schwerdtfeger, R. F. Singer, and C. Körner, "Influencing the microstructure of TiAl during selective electron beam melting," in *5th International Symposium on High-Temperature Metallurgical Processingth International Workshop on Titanium Aluminides*, 2012.

[118] C. Guoqing, Z. Binggang, L. Wei, and F. Jicai, "Crack formation and control upon the electron beam welding of TiAl-based alloys," *Intermetallics*, vol. 19, no. 12, pp. 1857–1863, 2011.

[119] J. Schwerdtfeger, R. F. Singer, and C. Körner, "Gamma TiAl by selective electron beam melting : Microstructure and Aluminium loss Research interests," 2013.

[120] U. Ackelid, M. Svensson, and A. Ab, "EBM Level 2 and 3 training notes." 2012.

[121] T. K. Heckel and H. J. Christ, "Thermomechanical fatigue of the TiAl intermetallic alloy TNB-V2," *Experimental Mechanics*, vol. 50, no. 6, pp. 717–724, 2010.

[122] Y. Wang, P. Fu, Y. Guan, Z. Lu, and Y. Wei, "Research on modeling of heat source for electron beam welding fusion-solidification zone," *Chinese Journal of Aeronautics*, vol. 26, no. 1, pp. 217–223, 2013.

[123] D. Dye, O. Hunziker, and R. C. Reed, "Numerical analysis of the weldability of superalloys," *Acta Materialia*, vol. 49, no. 4, pp. 683–697, 2001.

[124] H. Giedt and L. N. Tallerico, "Prediction of Electron Beam Depth of Penetration," *Welding Research Supplement*, pp. 299–305, 1988.

[125] T. W. Eagar and N. S. Tsai, "Temperature fields produced by traveling distributed heat sources," *Welding Journal*, vol. 62, no. 12, pp. 346–355, 1983.

[126] J. W. Elmer, W. H. Giedt, and T. W. Eager, "The Transition from Shallow to Deep Penetration during Electron Beam Welding," *Welding Journal*, vol. 69, no. 5, pp. 167–176, 1990.

[127] K. N. Lankalapalli, J. F. Tu, and M. Gartner, "A model for estimating penetration depth of laser welding processes," *Journal of Physics D: Applied Physics*, vol. 29, pp. 1831–1841, 1996.

[128] Y. Luo, J. Liu, and H. Ye, "An analytical model and tomographic calculation of vacuum electron beam welding heat source," *Vacuum*, vol. 84, no. 6, pp. 857–863, 2010.

[129] S. Rouquette, J. Guo, and P. Le Masson, "Estimation of the parameters of a Gaussian heat source by the Levenberg–Marquardt method: application to the electron beam welding," *International Journal of Thermal Sciences*, vol. 46, pp. 128–138, 2007.

[130] N. Shen and K. Chou, "Thermal Modeling of Electron Beam Additive Manufacturing

Process: Powder Sintering Effects," in *ASME 2012 International Manufacturing Science and Engineering Conference*, 2012, no. MSEC2012-7253, p. 287.

[131] N. Taniguchi, "The energy-beam processing of materials," pp. 150–162, 1989.

[132] U. Ackelid, "Arcam Level 2-3 Training EBM Safety," 2012.

[133] M. Terner, S. Biamino, D. Ugues, S. Sabbadini, P. Fino, M. Pavese, and C. Badini, "Phase transitions assessment on γ-TiAl by Thermo Mechanical Analysis," *Intermetallics*, vol. 37, pp. 7–10, 2013.

[134] D. C. Montgomerey, "Design and Analysis of Experiments," 2009.

[135] R. F. Gunst, "Response Surface Methodology: Process and Product Optimization Using Designed Experiments," *Technometrics*, vol. 38, no. 3, pp. 284–286, 1996.

[136] "Design-Expert (version 8.0.7.1), Stat-Ease Inc. Minneapolis, US, help_content."

[137] C. Croarkin and P. Tobias, "NIST/SEMATECH e-handbook of statistical methods," *Retrieved January*, 2014. [Online]. Available: http://www.itl.nist.gov/div898/handbook. [Accessed: 28-Mar-2012].

[138] "Arcam e-mail conversation, Arcam AB, support@arcam.com." .

[139] FCT systeme GmbH, "Spark Plasma Sintering Technology." [Online]. Available: http://www.fct-systeme.de/en/content/Spark_Plasma_Sintertechnologie/~nm.19~nc.40/SPS-Technology.html.

[140] "FCT-Systeme SPS furnace operation training, Sheffield 2012." .

[141] ASTM International, "B212-13: Standard Test Method for Apparent Density of Free-Flowing Metal Powders Using the Hall Flowmeter Funnel 1," vol. 99, no. Reapproved 2006, pp. 1–4, 2013.

[142] ASTM, "Standard Test Methods for Flow Rate of Metal Powders Using the Hall Flowmeter," *Astm*, vol. i, pp. 213–216, 2015.

[143] ASTM, "ASTM B923-10: Standard Test Method for Metal Powder Skeletal Density by Helium or Nitrogen," *ASTM International*, vol. c, pp. 10–13, 2015.

[144] M. Gäumann, C. Bezençon, P. Canalis, and W. Kurz, "Single-crystal laser deposition of

superalloys: Processing-microstructure maps," *Acta Materialia*, vol. 49, no. 6, pp. 1051–1062, 2001.

[145] D. Egry, I., Brooks, R., Holland-Moritz, "Thermophysical Properties of Titanium Aluminides - the European IMPRESS Project," *International journal of Thermophysics*, vol. 28, pp. 1026–1036, 2007.

[146] W. Bolse, B. Schattat, and A. Feyh, "Modification of thin-layer systems by swift heavy ions," *Applied Physics A: Materials Science and Processing*, vol. 77, no. 1, pp. 11–15, 2003.

[147] R. Ubic, "Electrons and Their Interaction with Matter," pp. 1–18.

[148] P. Ahlgren, B. Jarneving, and R. Rousseau, "Requirements for a cocitation similarity measure, with special reference to Pearson's correlation coefficient," *Journal of the American Society for Information Science and Technology*, vol. 54, no. 6, pp. 550–560, 2003.

[149] S. Williams, "Pearson's correlation coefficient.," *The New Zealand medical journal*, vol. 109, no. 1015, p. 38, 1996.

[150] P.-I. Gouma, K. Subramanian, Y.-W. Kim, and M. J. Mills, "Annealing studies of γ-titanium aluminides alloyed with light elements for creep strengthening," *Intermetallics*, vol. 6, no. 7–8, pp. 689–693, 1998.

[151] C. S. Han, "Microstructure of Carbide Precipitates in L1(2)-Ni3Al and L1(0)-TiAl," *Metals and Materials International*, vol. 2114, no. 2, pp. 151–157, 2008.

[152] L. Wang, H. Gabrisch, U. Lorenz, F. P. Schimansky, A. Schreyer, A. Stark, and F. Pyczak, "Nucleation and thermal stability of carbide precipitates in high Nb containing TiAl alloys," *Intermetallics*, vol. 66, pp. 111–119, 2015.

[153] Z. Wu, R. Hu, T. Zhang, F. Zhang, H. Kou, and J. Li, "Understanding the role of carbon atoms on microstructure and phase transformation of high Nb containing TiAl alloys," *Materials Characterization*, vol. 124, pp. 1–7, 2017.

[154] P. I. Gouma, S. J. Davey, and M. H. Loretto, "Microstructure and mechanical properties of a TiAl-based powder alloy containing carbon," *Materials Science and Engineering: A*, vol. 241, no. 1–2, pp. 151–158, 1998.

[155] W. H. Tian and M. Nemoto, "Effect of carbon addition on the microstructures and mechanical properties of γ-TiAl alloys," *Intermetallics*, vol. 5, no. 3, pp. 237–244, 1997.

[156] P. Edwards and M. Ramulu, "Fatigue performance evaluation of selective laser melted Ti-6Al-4V," *Materials Science and Engineering A*, vol. 598, pp. 327–337, 2014.

[157] F. Calignano, D. Manfredi, E. P. Ambrosio, L. Iuliano, and P. Fino, "Influence of process parameters on surface roughness of aluminum parts produced by DMLS," *International Journal of Advanced Manufacturing Technology*, vol. 67, no. 9–12, pp. 2743–2751, 2013.

[158] G. Strano, L. Hao, R. M. Everson, and K. E. Evans, "Surface roughness analysis, modelling and prediction in selective laser melting," *Journal of Materials Processing Technology*, vol. 213, no. 4, pp. 589–597, 2013.

[159] C. Y. Poon and B. Bhushan, "Comparison of surface roughness measurements by stylus profiler, AFM and non-contact optical profiler," *Wear*, vol. 190, no. 1, pp. 76–88, 1995.

[160] W. J. Sames, F. A. List, S. Pannala, R. R. Dehoff, and S. S. Babu, "The metallurgy and processing science of metal additive manufacturing," *International Materials Reviews*, vol. 61, no. 5, pp. 315–360, 2016.

[161] F. Léonard, S. Tammas-Williams, P. B. Prangnell, I. Todd, and P. J. Withers, "Assessment by X-ray CT of the effects of geometry and build direction on defects in titanium ALM parts," in *Conference on Industrial Computed Tomography*, 2012, pp. 85–93.

[162] R. Gerling, R. Leitgeb, and F.-P. Schimansky, "Porosity and argon concentration in gas atomized gamma-TiAl powder and hot isostatically pressed compacts," *Materials Science and Engineering*, vol. A252, no. 2, pp. 239–247, 1998.

[163] Y. Brechet, F. Louchet, A. Tourabp, and B. Wack, "Microstructure and Mechanical Properties of," vol. 40, no. 4, pp. 857–861, 1992.

[164] M. Lamirand, J. L. Bonnentien, G. Ferrière, S. Guérin, and J. P. Chevalier, "Effects of interstitial oxygen on microstructure and mechanical properties of Ti-48AI-2Cr-2Nb with fully lamellar and duplex microstructures," *Metallurgical and Materials Transactions A: Physical Metallurgy and Materials Science*, vol. 37, no. 8, pp. 2369–2378, 2006.

[165] GfE Metallee und Materiallien, "γ -TiAl TNB-V2 Remelt Stocks," 2010.

[166] H. Gabrisch, A. Stark, F. P. Schimansky, L. Wang, N. Schell, U. Lorenz, and F. Pyczak, "Investigation of carbides in Ti-45Al-5Nb-xC alloys ($0 \leq x \leq 1$) by transmission electron microscopy and high energy-XRD," *Intermetallics*, vol. 33, pp. 44–53, 2013.

[167] S. Akhonin, N. Trigub, V. Zamkov, and S. Semiatin, "Mathematical modeling of aluminum evaporation during electron-beam cold-hearth melting of Ti-6Al-4V ingots," *Metallurgical and Materials Transactions B*, vol. 34, no. 4, pp. 447–454, 2003.

[168] A. Powell, U. Pal, J. van den Avyle, B. Damkroger, and J. Szekely, "Analysis of multicomponent evaporation in electron beam melting and refining of titanium alloys," *Metallurgical and Materials Transactions B*, vol. 28, no. 6, pp. 1227–1239, 1997.

[169] J. Guo, G. Liu, Y. Su, H. Ding, J. Jia, and H. Fu, "Evaporation of multi-components in Ti-25Al-25Nb melt during induction skull melting process," *Trans. Nonferrous Met. Soc. China*, vol. 12, no. 4, 2002.

[170] J. A. Dean, "Handbook of Chemistry," *Pure and Applied Chemistry*, p. 1424, 1999.

[171] M. Eckert, D. Kath, and K. Hilpert, "Thermodynamic activities in the alloys of the Ti-Al-Nb system," *Metallurgical and Materials Transactions A*, vol. 30, no. 5, pp. 1315–1326, 1999.

[172] A. Kostov, B. Friedrich, and D. Zivkovic, "Predicting thermodynamic properties in Ti – Al binary system by FactSage," *Computational Materials Science*, vol. 37, pp. 355–360, 2006.

[173] N. S. Jacobson, M. P. Brady, and G. M. Mehrotra, "Thermodynamics of Selected Ti-Al and Ti-Al-Cr Alloys," *Oxidation of Metals*, vol. 52, no. 5, pp. 537–556, 1999.

[174] A. Kostov, B. Friedrich, and D. Zivkovic, "Thermodynamic calculations in alloys Ti-Al, Ti-Fe, Al-Fe and Ti-Al-Fe," *Journal of Mining and Metallurgy, Section B: Metallurgy*, vol. 44, no. 1, pp. 49–61, 2008.

[175] R. G. Reddy, A. M. Yahya, and L. Brewer, "Thermodynamic properties of Ti-Al intermetallics," *Journal of Alloys and Compounds*, vol. 321, no. 2, pp. 223–227, 2001.

[176] V. T. Witusiewicz, A. Bondar, U. Hecht, and T. Y. Velikanova, "The Al – B – Nb – Ti system IV . Experimental study and thermodynamic re-evaluation of the binary Al – Nb

and ternary Al – Nb – Ti systems," *Journal of Alloys and Compounds*, vol. 472, pp. 133–161, 2009.

[177] V. T. Witusiewicz, A. A. Bondar, U. Hecht, S. Rex, and T. Y. Velikanova, "The Al-B-Nb-Ti system. III. Thermodynamic re-evaluation of the constituent binary system Al-Ti," *Journal of Alloys and Compounds*, vol. 465, no. 1–2, pp. 64–77, 2008.

[178] F. Gomes, J. Barbosa, and C. S. Ribeiro, "Aluminium Evaporation During Ceramic Crucible Induction Melting of Titanium Aluminides," *Materials Science Forum*, pp. 1–6, 2013.

[179] W. Limberg, T. Ebel, F. Pyczak, M. Oehring, and F. P. Schimansky, "Influence of the sintering atmosphere on the tensile properties of MIM-processed Ti 45Al 5Nb 0.2B 0.2C," *Materials Science and Engineering A*, vol. 552, pp. 323–329, 2012.

[180] J. Guo, J. Jia, H. Fu, G. Liu, Y. Su, and H. Ding, "The critical pressure and impeding pressure of Al evaporation during induction skull melting processing of TiAl," *Metallurgical and Materials Transactions A*, vol. 33, no. 10, pp. 3249–3253, 2002.

9 APPENDICES

APPENDIX I. MATLAB Codes

CALCULATION OF AVERAGE SURFACE TEMPERATURE

```
clear all

clc

%1. add constants in the equation

k=22; d=4032000; Cp=0.9; b=0.7;

T0celcious=1050; LOF=0.2E-3; %fo=10;

I=38E-3;      V=14600E-3;

D=(0.0225*(I*1000)+0.2557)/1000;

T0=T0celcious+273.15;

a=k/(d.*Cp); Thm=1893-T0;

P=b*I.*60000; n=P/(4*pi*a*Cp*Thm*d); vdless= a/V;

t0=0;  L=40E-3; t2=L/V;

x1 = 0.0 ;

x2 = -4E-3 ;

y1 = LOF ;

y2 = -LOF ;

% 2. Average Temp area for melting surface

z = 0;

fun2=@(t,x,y)(2.*a.*b.*P./(k.*(pi.^(3/2)))).*exp((-2.*((x+V.*t).^2 +
y.^2)./(D.^2+8.*a.*t))-((z.^2)./(4.*a.*t)))./((a.*t).^0.5.*(D.^2+8.*a.*t));

Tmean_surface=(integral3(fun2,t0,t2,x1,x2,y1,y2) / abs((x1-x2)*(y1-y2))) +
T0
```

DETERMINATION OF MELT POOL WIDTH

```matlab
clear all

clc

%1. add constants in the equation

k=22; d=4032000; Cp=0.9; b=0.9;

T0celcious=1050; LOF=0.2E-3; %fo=10;

I=38E-3;      V=14600E-3;

D=(0.0225*(I*1000)+0.2557)/1000;

T0=T0celcious+273.15;

a=k/(d.*Cp); Thm=1893-T0;

P=b*I.*60000;

t0=0;  L=6E-3; t2=L/V;



x1 = 0.0 ;

x2 = -6E-3 ;

y1 = LOF ;

y2 = -LOF ;



LD= 70E-6;

%2. Isotherms

%steps size and geometry of plate

x_vec = linspace(0.001,-L,200) ;

y_vec = linspace(0.001,-0.001,200) ;

z_vec = 0.000000; %linspace(0.000,-0.000070,10) ;

% Intergration

for loopx = 1 : length(x_vec) ;

    x = x_vec(loopx) ;

    for loopy = 1 : length(y_vec);
```

```matlab
        y = y_vec(loopy) ;

        for loopz= 1 : length(z_vec) %:0.00001:0.0006;

            z = z_vec(loopz) ;



    fun=@(t) (2.*a.*b.*P./(k.*(pi.^(3/2)))).*exp((-2.*((x+V.*t).^2 +
y.^2)./(D.^2+8.*a.*t))-((z.^2)./(4.*a.*t)))./((a.*t).^0.5.*(D.^2+8.*a.*t));

    q=integral(fun,t0,t2);



        s=[x,y,z,q, q+T0];



        total_temp(loopx,loopy) = q + T0 ;

        x_contours(loopx,loopy) = x ;

        y_contours(loopx,loopy) = y ;



        end

    end

end



%3.figure isotherms all



figure

colormap jet;

v = [3560 3300 3100 2900 2720 2500 2300 2100 2000 1893 1855 1700 1600 1550
1440 1323 1193 1100];



[C,h]=contourf(x_contours,y_contours,total_temp,v);

V = [3560 3300 3100 2900 2720 2500 2300 2000 1893 1855 1700 1600 1550 1440
1323 1193];
```

225

```matlab
clabel(C,h,V,'FontSize',13,'Color','k','Rotation',0);



xlabel('Longitudinal position (m)');

ylabel('Lateral position (m)');

colorbar;



%4. Contour Area calc



 figure

 v = [1893 1400]  ;

 [C,h]=contourf(x_contours,y_contours,total_temp,v);



 I = find(C(1,:) == v(1)) ;

 ext_cont = C(1:2,I+1:end)

 z_pos = find(ext_cont(2,:) >= 0)




 Width = 2 * max(ext_cont(2,:))

 length = abs(max(ext_cont(1,:)) - min(ext_cont(1,:)))



 iso_area = 2 * trapz(ext_cont(1,z_pos),ext_cont(2,z_pos))
```

DETERMINATION OF MELT POOL DEPTH

```matlab
clear all

clc

%1. add constants in the equation

k=22.99119; d=4064000; Cp=0.7968; b=0.9;

T0=1000+273.15; I=0.009; V=0.5; fo=0;

a=k/(d.*Cp); Thm=1893-T0;

P=b*I.*60000;

D=(0.0225*(I*1000)+0.2557)/1000;



%2. Isotherms



%steps size and geometry of plate

x_vec = linspace(0.001,-0.006,200) ;

y_vec = 0;%linspace(0.002,-0.002,200) ;

z_vec = linspace(0.000,-0.00070,100) ;



% Intergration

for loopx = 1 : length(x_vec) ;

    x = x_vec(loopx) ;

    for loopy = 1 : length(y_vec);

        y = y_vec(loopy) ;

        for loopz= 1 : length(z_vec) %:0.00001:0.0006;

            z = z_vec(loopz) ;


    fun=@(t) (2.*a.*b.*P./(k.*(pi.^(3/2)))).*exp((-2.*((x+V.*t).^2 +
y.^2)./(D.^2+8.*a.*t))-((z.^2)./(4.*a.*t)))./((a.*t).^0.5.*(D.^2+8.*a.*t));

    q=integral(fun,0,inf);
```

```matlab
        s=[x,y,z,q,  q+T0];


        total_temp(loopx,loopz) = q + T0 ;

        x_contours(loopx,loopz) = x ;

        y_contours(loopx,loopz) = z ;



        end

    end

end


%4.figure isotherms all


figure

colormap jet;

v = [3560 3300 3100 2900 2720 2500 2300 2100 2000 1893 1855 1700 1600 1550
1440 1323 1193 1100];



[C,h]=contourf(x_contours,y_contours,total_temp,v);

V = [3560 3300 3100 2900 2720 2500 2300 2000 1893 1855 1700 1600 1550 1440
1323 1193];

clabel(C,h,V,'FontSize',13,'Color','k','Rotation',0);



xlabel('Longitudinal position (m)');

ylabel('Penetration position (m)');

colorbar;


%5. Contour Area calc
```

```matlab
figure

v = [1893 1400]  ;

[C,h]=contourf(x_contours,y_contours,total_temp,v);



I = find(C(1,:) == v(1)) ;

ext_cont = C(1:2,I+1:end)

z_pos = find(ext_cont(2,:) >= 0)




Width = 2 * max(ext_cont(2,:))

length = abs(max(ext_cont(1,:)) - min(ext_cont(1,:)))


iso_area = 2 * trapz(ext_cont(1,z_pos),ext_cont(2,z_pos))
```

APPENDIX II. Weld tracks data

EBM - Single weld tracks

T_{build}: 1173.15 K, CV-EBM: $2*10^{-3}$ mBar

Sample	Weld track	Current (mA)	Velocity (mm/sec)	Focus offset (mA)	Temperature (K)	Al loss (%)	P^0Al (Pascal)	γ_{Al}	J_{Al} rate (kg/m²s⁻¹)	Time (sec)	J_{Al}*time (kg/m²)
1	2	9.0	2000.0	0.1	1586.2	0.27	4.98	0.12	0.0002	0.005	0.0000009
2	4	17.8	1970.0	11.0	1854.7	0.91	150.20	0.21	0.0090	0.005	0.0000455
2	5	9.0	950.0	20.0	1796.0	0.69	77.80	0.20	0.0044	0.011	0.0000460
2	7	16.2	1550.0	20.0	1911.1	0.77	271.89	0.23	0.0171	0.006	0.0001105
3	9	25.0	1535.0	9.0	2093.0	2.28	1484.77	0.28	0.1085	0.007	0.0007065
3	11	17.8	1175.0	0.4	2075.6	1.60	1278.44	0.27	0.0922	0.009	0.0007846
4	14	25.0	1437.5	20.0	2126.3	1.77	1963.78	0.29	0.1469	0.007	0.0010219
4	15	9.0	500.0	0.1	2011.0	0.93	717.61	0.26	0.0492	0.020	0.0009847
4	17	25.0	2000.0	0.1	1967.4	1.13	475.72	0.24	0.0315	0.005	0.0001575
5	18	19.2	1000.3	13.0	2195.1	1.44	3403.75	0.31	0.2667	0.010	0.0026665
5	20	15.0	500.0	20.0	2400.7	2.21	14596.39	0.36	1.2915	0.020	0.0258295
5	21	17.0	1600.0	4.0	1919.0	1.57	294.58	0.23	0.0187	0.006	0.0001168
6	10	17.8	1175.0	0.4	2075.6	1.43	1278.44	0.27	0.0922	0.009	0.0007846
7	13	17.8	1970.0	11.0	1854.7	1.04	150.20	0.21	0.0090	0.005	0.0000455
7	16	17.8	1175.0	0.4	2075.6	1.77	1278.44	0.27	0.0922	0.009	0.0007846

Sample	Weld track	Temperature (K)	Al loss (%)	Al content	HV0.2	st. Error
1	1	1940.2	0.58	44.42	603.00	6.56
2	4	2170.4	0.91	44.09	475.25	74.59
2	5	1881	0.69	44.31	632.25	10.85
2	7	2189.6	0.77	44.23	604.75	14.67
3	9	2443.52	1.6	43.4	584.00	10.85
3	11	2552.5	2.28	42.72	593.83	9.56
4	14	2798	1.77	43.23	637.71	7.85
4	15	2110.8	0.93	44.07	613.75	9.64
4	17	2563.8	1.13	43.87	636.17	16.70
5	18	2651.3	1.44	43.56	630	6.71317113
5	20	2735.9	2.21	42.79	621.3333	20.333333
5	21	2224	1.57	43.43	605	14.42221
6	10	2443.52	1.43	43.57	604	10.214369
7	13	2170.4	1.04	43.96	622.3333333	7.88106028
7	16	2443.52	1.77	43.23	644.75	22.4067512

APPENDIX III. Solid blocks and tensile bars data

EBM - Solid blocks and Tensile bars

T_{build}: 1343.15 K, Layer thickness: 70 μm, Line offset 0.2 mm, Not controlled Vacuum: ~ 5*10^{-4} mBar, Controlled Vacuum: 2*10^{-3} mBar for Tensile Bars

Run order	Block	Surface Temp.	Focus offset (mA)	Speed function	Current (mA)	Velocity (mm/sec)	Temperature (Kelvin)	Al loss (%)	γ_{Al}	P^0Al (Pascal)	J_{Al} (kg/m²sec⁻¹)	Time (sec)	J_{Al}*time (kg/m²)
1	2	1200	16	32	5.50	280.00	2028.70	8.38	0.266	993.617	0.070	0.1071	0.0075
2	2	1200	10	32	7.79	590.00	2052.50	6.39	0.275	1322.440	0.096	0.0508	0.0049
3	2	1200	10	44	5.73	395.00	1980.20	4.34	0.249	543.248	0.036	0.0759	0.0028
5	2	1200	16	44	5.73	395.00	1980.20	4.58	0.249	543.248	0.036	0.0759	0.0028
6	2	1200	4	32	5.73	290.00	2045.90	7.30	0.272	1186.404	0.085	0.1034	0.0088
7	2	1200	4	44	5.79	400.00	1983.20	4.72	0.250	561.599	0.038	0.0750	0.0028
1	2	1600	16	32	8.56	665.00	1933.7	9.20	0.284	1746.079	0.129	0.0451	0.0058
2	2	1600	10	32	9.32	740.00	1903.1	6.94	0.292	2247.320	0.170	0.0405	0.0069
3	2	1600	10	44	9.26	1000.00	2005.3	4.37	0.263	889.899	0.062	0.0300	0.0019
5	2	1600	16	44	9.26	1000.00	1888.1	5.95	0.263	889.899	0.062	0.0300	0.0019
6	2	1600	4	32	9.32	740.00	1903.1	7.86	0.292	2247.320	0.170	0.0405	0.0069
7	2	1600	4	44	9.38	1020.00	2029.5	5.53	0.264	912.621	0.064	0.0294	0.0019
1	3	1200	4	44	4.86	320.00	1946.10	4.63	0.235	330.566	0.021	0.0938	0.0020
2	3	1200	6	56	5.03	415.00	1909.30	3.86	0.224	217.284	0.013	0.0723	0.0010
3	3	1200	6	32	5.09	250.00	2018.20	5.45	0.260	795.213	0.055	0.1200	0.0066
4	3	1200	10	60	5.03	450.00	1900.80	3.58	0.219	178.535	0.011	0.0667	0.0007
6	3	1200	14	56	5.03	415.00	1909.30	4.18	0.224	217.284	0.013	0.0723	0.0010
7	3	1200	10	28	5.09	220.00	2038.10	6.08	0.269	1077.141	0.077	0.1364	0.0104
1	3	1400	4	44	5.03	330.00	2070.8	6.74	0.239	378.824	0.025	0.0909	0.0022
2	3	1400	6	56	5.21	440.00	2085.2	5.15	0.226	232.029	0.014	0.0682	0.0010
3	3	1400	6	32	5.27	260.00	1995.6	5.69	0.264	904.447	0.063	0.1154	0.0073
4	3	1400	10	60	5.21	460.00	1995.6	4.46	0.223	207.928	0.013	0.0652	0.0008

6	3	1400	14	56	5.21	440.00	2085.2	4.48	0.226	232.029	0.014	0.0682	0.0010
7	3	1400	10	28	5.27	235.00	1996	6.27	0.271	1153.645	0.082	0.1277	0.0105
1	3	1600	4	44	5.84	405.00	1985.20	7.08	0.250	574.501	0.039	0.0741	0.0029
2	3	1600	6	56	6.02	530.00	1943.10	6.14	0.236	346.462	0.022	0.0566	0.0013
3	3	1600	6	32	6.08	325.00	2056.80	6.49	0.275	1307.674	0.094	0.0923	0.0087
4	3	1600	10	60	6.02	570.00	1927.50	4.48	0.231	286.727	0.018	0.0526	0.0010
6	3	1600	14	56	6.02	530.00	1943.10	5.14	0.236	346.462	0.022	0.0566	0.0013
7	3	1600	10	28	6.08	285.00	2086.40	6.90	0.285	1829.609	0.136	0.1053	0.0143
preheating	tensile bar	1200	40	no	38.00	14600.00	1669.1	2.53	0.181	18.372	0.001	0.1027	0.0001
melting	tensile bar	1200	11	38	7.00	565.5	2005.9	3.35	0.258	746.511	0.051	0.0884	0.0045

Run order	Block	Surface Temp.	Al loss (%)	Av. Hardness	st. Error	Al content
1	2	1200	8.38	447.5833333	5.035711838	36.62
2	2	1200	6.39	455.5555556	7.099483014	38.61
3	2	1200	4.34	411.2068966	2.597544933	40.66
5	2	1200	4.58	424.9714286	4.564290646	40.42
6	2	1200	7.3	433.1025641	5.21854304	37.7
7	2	1200	4.72	416.4642857	3.81430132	40.28
1	2	1600	9.2	475.5625	4.660980539	35.8
2	2	1600	6.94	462.7777778	8.99502606	38.06
3	2	1600	4.37	446.8823529	4.983710489	40.63
5	2	1600	5.95	472.2380952	7.237766283	39.05
6	2	1600	7.86	487.9565217	5.890126481	37.14
7	2	1600	5.53	459.75	5.221060208	39.47
1	3	1200	4.63	452.3055556	3.951254461	40.37
2	3	1200	3.86	469.0384615	2.405261327	41.14
3	3	1200	5.45	442.1666667	3.737306559	39.55
4	3	1200	3.58	442.75	3.425018827	41.42
6	3	1200	4.18	463.4857143	3.042555317	40.82
7	3	1200	6.08	417.2941176	4.356683285	38.92
1	3	1400	6.74	460.5555556	5.49233874	38.26
2	3	1400	5.15	477.3428571	2.60966744	39.85
3	3	1400	5.69	449.9444444	6.814194387	39.31
4	3	1400	4.46	426.9166667	2.124077764	40.54
6	3	1400	4.48	457.3142857	3.182306946	40.52
7	3	1400	6.27	443.4444444	6.425574453	38.73
1	3	1600	7.08	469.6944444	4.544981437	37.92
2	3	1600	6.14	480.0333333	1.986777813	38.86
3	3	1600	6.49	512.25	6.464110319	38.51
4	3	1600	4.48	460.2222222	2.893646875	40.52
6	3	1600	5.14	461.5	2.727141651	39.86
7	3	1600	6.9	515.3333333	5.582000552	38.1
melting	tensile bar	1200	3.35			41.65

APPENDIX IV. Single layer melting study data

EBM - 1 layer melting (3 times)

T_{build}: 1343.15 Kelvin, Layer thickness: 70 μm, Line offset 0.2 mm, Surface temp:1200, speed function (melting): 38

Sample	Vacuum Pressure (mBar)	Current (mA)	Velocity (mm/sec)	Focus offset (mA)	Temperature (Kelvin)	Al loss (%)	Standard error	P^0Al (Pascal)	γ_{Al}	J_{Al} (kg/m²sec⁻¹)	Time (sec)	J_{Al}*time (kg/m²)
1 - melting	0.0001	7	565.5	11	2005.9	5.00	0.36	746.511	0.258	0.051396	0.1061	0.005453
2 - melting	0.0010	7	565.5	11	2005.9	3.53	0.88	746.511	0.258	0.051396	0.1061	0.005453
3 - melting	0.0100	7	565.5	11	2005.9	2.79	0.21	746.511	0.258	0.051396	0.1061	0.005453
1 - preheating	0.0001	38	14600.0	40	1669.1	4.27	0.57	18.372	0.181	0.000974	0.0822	0.000080
2 - preheating	0.0010	38	14600.0	40	1669.1	2.65	0.68	18.372	0.181	0.000974	0.0822	0.000080
3 - preheating	0.0100	38	14600.0	40	1669.1	1.80	0.14	18.372	0.181	0.000974	0.0822	0.000080

sample	Vacuum pressure	Al content	Al loss	Average hardness	standard error
1	10^-2 mBar	43.091	1.859	511.3968254	1.49043027
2	10^-3 mBar	42.251	2.699	523.1944444	0.83917704
3	10^-4 mBar	40.926	4.024	584.6606061	5.50603309

Vacuum pressure (mBar)	0.01	0.001	0.0001
1	666.91	495.16	528.91
2	666.68	547.45	466.52
3	654.03	621.36	494.26
4	652.02	651.75	382.26
5	640.6	620.46	411.09
6	656.93	647.71	442.27
7	656.74	664.17	456.13
8	647.15	659.48	459.59
9	641.25	656.09	408.91
10	625.43	618.96	486.15
Av. Penetration depth	650.774	618.259	453.609
stdev	12.6871914	55.1859625	44.2412596
st.error	4.01204221	17.4513336	13.9903147

APPENDIX V. Literature data

EBM - literature data

T_{build}: 1223.15, Controlled Vacuum: $2*10^{-3}$ mBar

Sample	Current (mA)	Velocity (mm/sec)	Line offset (mm)	Layer thickness (μm)	Temperature (Kelvin)	Al loss (%)	P^0Al (Pascal)	γ_{Al}	J_{Al} (kg/m²sec⁻¹)	Time (sec)	J_{Al}*time (kg/m²)
Schwerdfeger et al. 17.9	15.0	6000.0	0.1	70.0	1637.5	1.2	34.327	0.227	0.002	0.00500	0.0000120
Schwerdfeger et al. 17.2	7.5	3000.0	0.1	70.0	1617.7	0.6	4.332	0.113	0.000	0.01000	0.0000016
Schwerdfeger et al. 17.4	8.5	3000.0	0.1	70.0	1650.0	1.5	8.619	0.140	0.000	0.01000	0.0000038
Schwerdfeger et al. 7.6	3.5	300.0	0.2	100.0	1689.2	1.1	16.562	0.175	0.001	0.10000	0.0000905
Schwerdfeger et al. 7.8	10.5	900.0	0.2	100.0	1986.8	2.0	1210.458	0.272	0.093	0.03333	0.0030892
Schwerdfeger et al. 5.8	9.2	500.0	0.2	100.0	2098.3	4.1	3063.481	0.303	0.254	0.06000	0.0152281
Cormier et al.	13.0	500.0	0.2	100.0	2326.7	8.0	42420.156	0.409	4.373	0.06000	0.2623643

Induction melting casting and Metal injection moulding literature data

Sample	Vacuum Pressure (mBar)	Temperature (Kelvin)	Al loss (%)	p^0Al (Pascal)	γ_{Al}	J_{Al} (kg/m^{2}sec^{-1})	time (sec)	J_{Al}*time (kg/m^2)
Gomes et al - Induction melting	0.005	1823.15	0.6	105.9856	0.206	0.00654	1	0.00654
Gomes et al - Induction melting	0.005	1823.15	1.8	105.9856	0.206	0.00654	60	0.392417
Gomes et al - Induction melting	0.005	1823.15	2.4	105.9856	0.206	0.00654	90	0.588625
Gomes et al - Induction melting	0.005	1873.15	0.75	183.0604	0.220	0.011873	1	0.011873
Gomes et al - Induction melting	0.005	1873.15	2.6	183.0604	0.220	0.011873	60	0.712392
Gomes et al - Induction melting	0.005	1873.15	3.45	183.0604	0.220	0.011873	90	1.068588
Gomes et al - Induction melting	0.05	1823.15	0.45	105.9856	0.206	0.00654	1	0.00654
Gomes et al - Induction melting	0.05	1823.15	0.63	105.9856	0.206	0.00654	60	0.392417
Gomes et al - Induction melting	0.05	1823.15	0.72	105.9856	0.206	0.00654	90	0.588625
Gomes et al - Induction melting	0.05	1873.15	0.4	183.0604	0.220	0.011873	1	0.011873
Gomes et al - Induction melting	0.05	1873.15	1.1	183.0604	0.2120	0.011873	60	0.712392
Gomes et al - Induction melting	0.05	1873.15	1.4	183.0604	0.220	0.011873	90	1.068588
Gomes et al - Induction melting	0.01	1823.15	0.22	105.9856	0.206	0.00654	1	0.00654
Gomes et al - Induction melting	0.01	1823.15	0.27	105.9856	0.206	0.00654	60	0.392417
Gomes et al - Induction melting	0.01	1823.15	0.3	105.9856	0.206	0.00654	90	0.588625
Gomes et al - Induction melting	0.01	1873.15	0.3	183.0604	0.220	0.011873	1	0.011873
Gomes et al - Induction melting	0.01	1873.15	0.55	183.0604	0.220	0.011873	60	0.712392
Gomes et al - Induction melting	0.01	1873.15	0.7	183.0604	0.220	0.011873	90	1.068588
Limberg et al. - MIM	0.01	1773.15	2.1	59.49952	0.193	0.003262	7200	23.48801

APPENDIX VI. EBM development steps to achieve a stable process

i. **"Smoke" tests** were performed by EB scanning on "cold" powder. The effect of the main related process parameters for heating and pre-heating (i.e. speed, minimum, maximum and average current, line offset, line order and focus offset) were investigated in order to achieve the appropriate combination for a "smoke" safe pre-heating theme (avoiding overcharging).

ii. Powder bed **sintering tests** were performed. The starting plate and consequently the powder bed beneath the starting plate are heated up to a temperature slightly lower than the expected sintering temperature. Then the powder bed just below the starting plate is checked if it is sintered enough. If not, iterative, T_{build} increasing steps are followed till this is accomplished. Sintering level under the starting plate is important for efficient electrical grounding of the powder bed.

iii. **Stable/safe process** is tested on a simple geometry. Melting (contours and hatching) of a simple geometry is introduced into the process and heating (T_{build}) and preheating themes are tested for suitability to maintain a stable process regarding temperature, sintering smoothness and being smoke-free. All related process parameters are tuned at the same time and optimisation is done by eye observation of the process through the protective glass of the Arcam EBM equipment.

APPENDIX VII. Post-processing, Material Properties and Further Process Development (Stage 3)

1. Build specimens with "optimised" process themes at various orientations for i) tensile, ii) fatigue and iii) oxidation resistance testing.

2. Perform a HIP study for identifying the appropriate process conditions (time, pressure, temperature and inert atmosphere) for eliminating process defects/porosity without extensive grain coarsening of the as-built microstructure and with limited surface oxidation.

3. Perform a HIP cycle on selected specimens with "optimum" process conditions from the previous step.

4. Perform a heat-treatment study for designing/identifying targeted, customised heat treatments for EBM built components of the bespoke chemistry in order to achieve required and homogenous microstructures.

5. Perform post- machining of all samples to remove the rough outer surface, as well as to manufacture the appropriate standard size and shape specimens for the subsequent mechanical testing.

6. Tensile property data of the machined specimens for the as-built and as-HIPed at room, intermediate and elevated temperatures.

7. Fatigue Property data.

8. Oxidation resistance data.

9. Identify and resolve main EBM process and material property issues.

APPENDIX VIII. Arcam S12 EBM process set up and operating sequence

Before starting the build, the basic machine set up includes:

- Thorough cleaning of the electron beam gun and all the surfaces in the build chamber
- Fill in the powder tanks (hopers) with powder
- Preparing the powder bed
    - ~40 mm height of powder is required below the base plate in the build tank
    - Ground wiring should be checked and thermocouple properly attached under the base plate
    - Base plate should be flat (levelled to powder raking) and in the centre of the powder bed
- Vacuum down to 10^{-4} mbar for the vacuum chamber and 10^{-6} mbar for the electron gun
- Turn on the HV unit to ramp up to 60 kV
- Turn the beam on, set it to the centre of the base plate and perform basic beam alignments
- Load the abf file on the PC and apply process themes to the different models as required
- Press play to start the build

After pressing the start button the EBM process runs in the basic following steps

i. Heating of the base (start) plate up to a desired, user defined temperature, referred as the build temperature (T_{build}). The target is for this temperature to be maintained constant throughout the build process. This is achieved by scanning the base plate multiple times in a rectangular raster format with a defocused electron beam at high speeds.

ii. When the desired temperature is achieved the first homogenous, smooth layer of powder is spread on the base plate by raking (typically 3x times) with the powder rake. Powder feeding from the hoppers is gravity driven and the amount of powder spread should be always constant. To control this, powder sensors are fitted in the equipment.

iii. The next step is preheating the powder bed (only in the confines of the base plate) to slightly pre-sinter the powder particles, as well as to maintain the T_{build}. Preheating in the same way with heating is achieved by scanning the powder bed multiple times in a rectangular raster patent with a defocused beam at high speeds.

iv. Then the actual steps of melting the component take place. Melting is divided in contours, hatching and supports (i.e. wafer, volume or pin supports). Contours are melted in a multi-beam method and hatching in a snaking pattern.

v. In some cases, an extra heating step is introduced in order to keep the heat input balance constant for each layer. This or those heating steps take place after the end of all the melting steps or even between melting of the different models (e.g. contours, wafer supports, etc.). Scanning mode and process parameters for these extra-steps are similar to the pre-heating step.

vi. Then the base plate is mechanically moved down at the desired, user defined layer thickness and a new layer of powder is spread on the top of the previous one.

vii. The sequence of spreading (raking) powder, preheating, melting, post-heating, moving down the plate is continuous until the last layer of the CAD model is built. Each layer is melted in a different direction. So, when one layer is melted along the x- axis the subsequent layer is melted along the y- axis and so on.

viii. All the building process runs under a controlled-vacuum (CV-EBM). Controlled vacuum is a function, which pours helium in the vacuum chamber in order to raise the pressure to ~2 x 10^{-3} mbar. Helium gets ionised by the electron beam and the ions help excess charge to be moved away from the powder bed and subsequently reduces "smoke" sensitivity, which was explained in more detail in Section 3.2.1. At the same time, increasing vacuum pressure could reduce evaporation of volatiles.